Some studies on the design of reciprocal and time-modulated non-reciprocal filters for 5G applications

Submitted in partial fulfilment of the requirements
for the award of the degree of
Doctor of Philosophy

by

Prantik Dutta
(Roll No: 701932)

Under the supervision of

Dr. Gande Arun Kumar
(Assistant Professor)

Department of Electronics & Communication Engineering
National Institute of Technology Warangal
Telangana, India - 506004
2023

Some studies on the design of reciprocal and time-modulated non-reciprocal filters for 5G applications

Submitted in partial fulfilment of the requirements
for the award of the degree of
Doctor of Philosophy

by

Prantik Dutta
(Roll No: 701932)

Under the supervision of
Dr. Gande Arun Kumar
(Assistant Professor)

Department of Electronics & Communication Engineering
National Institute of Technology Warangal
Telangana, India - 506004
2023

To my beloved family, remarkable teachers, and treasured friends: Your unwavering presence in my life has filled it with immeasurable joy and gratitude.

Approval Sheet

This thesis entitled **Some studies on the design of reciprocal and time-modulated non-reciprocal filters for 5G applications** by **Prantik Dutta** is approved for the degree of **Doctor of Philosophy**.

Examiners

Research Supervisor

Dr. Gande Arun Kumar
Department of ECE
NIT Warangal, India-506004

Chairman & Head

Prof. P. Sreehari Rao
Department of ECE
NIT Warangal, India-506004

Place:

Date:

Declaration

This is to certify that the work presented in this thesis entitled **Some studies on the design of reciprocal and time-modulated non-reciprocal filters for 5G applications** is a bonafide work done by me under the supervision of **Dr. Gande Arun Kumar** and was not submitted elsewhere for the award of any degree.

I declare that this written submission represents my own ideas and even considered others ideas which are adequately cited and further referenced the original sources. I understand that any violation of the above will cause disciplinary action by the institute and can also evoke panel action from the sources or from whom proper permission has not been taken when needed. I also declare that I have adhered to all principles of academic honesty and integrity and have not misrepresented or fabricated or falsified any idea or data or fact or source in my submission.

Prantik Dutta
Research Scholar
Roll No.: 701932

Place:
Date:

NATIONAL INSTITUTE OF TECHNOLOGY
WARANGAL, INDIA-506004
Department of Electronics & Communication Engineering

CERTIFICATE

This is to certify that the thesis work entitled **Some studies on the design of reciprocal and time-modulated non-reciprocal filters for 5G applications** is a bonafide record of work carried out by **Prantik Dutta** submitted to the faculty of **Electronics & Communication Engineering** department, in partial fulfillment of the requirements for the award of the degree of **Doctor of Philosophy** in **Electronics and Communication Engineering, National Institute of Technology Warangal, India-506004**. The contributions embodied in this thesis have not been submitted to any other university or institute for the award of any degree.

Dr. Gande Arun Kumar
Research Supervisor
Assistant Professor
Department of ECE
NIT Warangal, India-506 004.

Place:
Date:

Acknowledgements

To begin with, my heartfelt appreciation goes to my supervisor, Dr. G. Arun Kumar, for his invaluable guidance, unwavering support, and continuous encouragement throughout this research journey. His expertise, insightful feedback, and mentorship have played a crucial role in shaping the direction and quality of this work.

I would also like to extend my heartfelt thanks to Prof. P. Sreehari Rao, the DSC Chairman and HoD of the Department of ECE, for his valuable guidance, encouragement, and support in the successful completion of this research. I am grateful to the esteemed DSC members, Dr. Amara Prakasa Rao, Dr. Gopi Ram, and Dr. A. V. Giridhar from the Department of EEE, for their valuable insights and suggestions that have significantly enriched the research work.

I would like to acknowledge the contributions of the former HoDs, Prof. L. Anjaneyulu and Prof. N. Bheema Rao, for their support and guidance during the initial stages of this research.

I am grateful to Mr. Y. Suresh Babu (BEL) and Mr. C. Sataiah (BDL) for their assistance in measurements and PCB fabrication. Special thanks to Mr. Bijit Biswas and Mr. Sukhendu Bhanja (SAMEER, Kolkata) for providing substrates and consumables. I also acknowledge the support of the Industrial and Automation Lab and the Central Research Instrumentation Facility (CRIF) at NIT Warangal for providing the necessary resources and research facilities that were indispensable for conducting experiments and obtaining accurate results.

My heartfelt thanks go to all the faculties, fellow scholars, and non-teaching staff members of the department for their support, valuable discussions, and assistance throughout my research journey.

Last but certainly not least, I am deeply grateful to my family members for their unwavering love, understanding, and encouragement. Their constant support and belief in me have been my driving force.

I am truly fortunate to have had the opportunity to work with such exceptional individuals and receive their support and guidance. Their contributions have been invaluable in shaping this thesis and my academic journey as a whole.

Prantik Dutta

Abstract

This research focuses on the development of magnetless non-reciprocal bandpass filtering isolators as an alternative to conventional ferrite-based magnetic components. These conventional components, while essential in electronic systems, are often bulky, expensive, and pose integration challenges. In response, researchers have explored magnetless non-reciprocal devices, particularly in the context of spatio-temporal modulation. By harnessing this phenomenon, these devices can achieve simultaneous filtering and isolation in opposite directions. This work aims to enhance the filtering isolation responses of such spatio-temporally modulated non-reciprocal bandpass filters by proposing optimization strategies and proposing non-conventional coupling matrix synthesis methods to enhance the comprehensibility of the spectral traversal of RF energy among the generated harmonics. Furthermore, this study explores the utilization of multi-band non-reciprocal bandpass filtering to address the requirements of contemporary multifunctional systems. The investigation begins by examining a dual-band bandpass filter with single-band non-reciprocity, accompanied by its coupling matrix representation. Subsequently, a dual-band bandpass filter with simultaneous non-reciprocity in both bands is presented and analyzed. The findings of this research contribute to the advancement of magnetless non-reciprocal components, offering promising solutions for integrated transceiver systems and addressing the challenges associated with conventional approaches. The future scope includes formulating precise equations for in-band transmission zero placements in the response of the reverse direction, developing coupling matrix formulations for dual-band NR-BPFs with dual-band non-reciprocity, exploring tunability in center frequency and bandwidth, and designing compact MMIC NR-BPFs for 5G bands.

Contents

List of Figures

List of Tables

List of Acronyms

BPF	Bandpass Filter
BPP	Bandpass Prototype
BPR	Bandpass Resonator
BSR	Bandstop Resonator
DB-BPF	Dual-band Bandpass Filter
DMC	Distributedly Modulated Capacitor
IM	Intermodulation Products
LPF	Lowpass Filter
LPP	Lowpass Prototype
NR-BPF	Non-reciprocal Bandpass Filter
PSO	Particle Swarm Optimization
STM	Spatio-temporal Modulation
TVTL	Time-varying Transmission Line
TZ	Transmission Zero

Chapter 1

Introduction

Microwave filters play a crucial role in modern communication systems, enabling the selective transmission of signals within specific frequency ranges. These filters are traditionally designed as reciprocal devices, meaning that their transmission characteristics remain the same regardless of the direction of signal propagation. However, in certain applications, non-reciprocal behavior becomes essential to achieve advanced functionalities, such as isolators, circulators, and frequency-conversion devices. Non-reciprocal bandpass filters (NR-BPFs) have emerged as a significant area of research due to their ability to control signal flow in a unidirectional manner within a specific frequency band.

To date, significant advancements have been made in the development of non-reciprocal microwave components, including circulators, isolators, and gyrators. These components play a vital role in wireless systems by enabling unidirectional signal flow. Traditionally, these components have been constructed using ferrite-based magnetic materials. The unique property of these materials lies in their ability to break reciprocity due to the internal magnetic moment that is influenced by a strong external magnetic bias. However, the bulkiness and high cost of these components hinder their integration into modern systems. Active device-based solutions and magnetless nonreciprocal devices have been explored, but they come with limitations such as poor noise figure and limited power handling. Recently, magnetless nonreciprocal devices based on time-varying circuits have gained attention, utilizing spatiotemporal modulation (STM) to achieve nonreciprocity. STM provides design flexibility and has been demonstrated in various fields. Another approach involves angular-momentum biasing using ring or loop structures to mimic the Faraday effect. Both approaches show promise in achieving nonreciprocity at sub-wavelength scales and offer potential for miniaturization. Ultrawideband nonreciprocity can be achieved through sequential switching or commutated gyrators, which are compact and compatible with integrated circuit fabrication. However, challenges related to power consumption and clock leakage need to be addressed.

Achieving non-reciprocity in bandpass filters has been an active area of research in recent years. Various techniques have been explored, including the use of magnetic materials, non-linear components, and time-varying circuits. Among these approaches, spatio-temporal modulation has shown great promise in enabling non-reciprocity in bandpass filters. This technique involves the modulation of both spatial and temporal parameters of the filter, allowing for the creation of non-reciprocal behavior.

The concept of spatio-temporal modulation in microwave filters is rooted in the idea of breaking the spatial symmetry of the filter structure, combined with the dynamic modulation of its parameters over time. By carefully designing the spatial and temporal variations, it becomes possible to induce non-reciprocal effects and achieve desired signal routing functionalities.

The research objectives are formulated based on a comprehensive review of the existing literature on the design and analysis of spatio-temporal NR-BPFs. These objectives are centered around enhancing the filtering isolation response, developing unconventional spectral modeling techniques for NR-BPFs, and exploring the capabilities of multi-band functionality. The specific objectives can be summarized as follows:

1. Deployment of evolutionary algorithms to obtain circuit parameters that would achieve enhanced non-reciprocity without degradation in Insertion Loss (IL) and Return Loss (RL).
2. Construction of 3D coupling matrix for non-reciprocal bandpass filters along with the formulation of non-reciprocal S-parameter equations.
3. Development of dual-band non-reciprocal bandpass filters with single-band non-reciprocity.
4. Development of dual-band bandpass filters with dual-band non-reciprocal response.
5. Coupling matrix representation of dual-band non-reciprocal filters.

The research objectives outlined in this thesis are successfully implemented, leading to significant advancements in the field of non-reciprocal bandpass filters. The following discussions highlight the successful implementation of each objective and the contributions they make to the overall body of knowledge in this area.

The first objective aimed to delve deeper into the origin of non-reciprocity by proposing numerical analysis based on non-conventional filter polynomials. Through extensive research and analysis, novel filter polynomials were developed, allowing for a deeper understanding of non-reciprocal behavior in bandpass filters. Furthermore, optimization strategies and algorithms were devised to enhance the filtering isolation characteristics without the need for manual tuning of circuit parameters. This approach eliminates the trial and error method, making the design process more efficient and effective.

Building upon the insights gained from the origin of non-reciprocity, the second objective focused on improving the comprehensibility of spectral resonator generation at harmonic frequencies. To achieve this, the concept of a 3D coupling matrix was proposed. This coupling matrix not only facilitates the coupling of resonators at the fundamental tone but also pictorially represents the associated couplings between the fundamental and harmonically generated resonators. Additionally, non-conventional S-parameter equations were synthesized to accurately model non-reciprocal bandpass filters. These advancements in modeling and analysis techniques provide a more comprehensive understanding of the behavior of non-reciprocal filters.

Continuing the research, the next objective aimed to generate spatio-temporally modulated dual-band non-reciprocity. This involved proposing a dual-band distributed response that manifests a single-band non-reciprocity while also allowing for band tunability. Through the use of a dual-band coupling matrix approach and even-odd mode analysis, the holistic circuit was analyzed, and simulation results demonstrated a strong correlation with the proposed model. This achievement represents a significant milestone in the realization of dual-band non-reciprocal bandpass filters using distributed elements.

Lastly, the final objective focused on the design of a dual-band bandpass filter using lumped elements with simultaneous non-reciprocity in both bands. This novel approach involved coupling bandpass resonators and bandstop resonators, resulting in a circuit that achieves simultaneous non-reciprocity in both bands using only three time-modulating elements. The proposed circuit was simulated and measured, demonstrating its effectiveness and establishing it as the first of its kind in the dual-band regime for achieving simultaneous non-reciprocity.

The first objective aims to delve deeper into the origin of non-reciprocity by proposing numerical analysis based on non-conventional filter polynomials. Through extensive research and analysis, novel filter polynomials are developed, allowing for a deeper understanding of non-reciprocal behavior in bandpass filters. Furthermore, optimization strategies and algorithms are devised to enhance the filtering isolation characteristics without the need for manual tuning of circuit parameters. This approach eliminates the trial and error method, making the design process more efficient and effective.

Building upon the insights gained from the origin of non-reciprocity, the second objective focuses on improving the comprehensibility of spectral resonator generation at harmonic frequencies. To achieve this, the concept of a 3D coupling matrix is proposed. This coupling matrix not only facilitates the coupling of resonators at the fundamental tone but also pictorially represents the associated couplings between the fundamental and harmonically generated resonators. Additionally, non-conventional S-parameter equations are synthesized to accurately model non-reciprocal bandpass filters. These advancements in modeling and analysis techniques provide a more comprehensive understanding of the behavior of non-reciprocal filters.

Continuing the research, the next objective aims to generate spatio-temporally modulated dual-band non-reciprocity. This involves proposing a dual-band distributed response that manifests a single-band non-reciprocity while also allowing for band tunability. Through the use of a dual-band coupling matrix approach and even-odd mode analysis, the holistic circuit is analyzed, and simulation results demonstrate a strong correlation with the proposed model. This achievement represents a significant milestone in the realization of dual-band non-reciprocal bandpass filters using distributed elements.

Lastly, the final objective focuses on the design of a dual-band bandpass filter using lumped elements with simultaneous non-reciprocity in both bands. This novel approach involves coupling bandpass resonators and bandstop resonators, resulting in a circuit that achieves simultaneous non-reciprocity in both bands using only three time-modulating elements. The proposed circuit is simulated and measured, demonstrating its effectiveness and establishing it as the first of its kind in the dual-band regime for achieving simultaneous non-reciprocity.

In conclusion, the successful implementation of the research objectives outlined in this thesis has significantly advanced the field of non-reciprocal bandpass filters. The development of non-conventional filter polynomials, optimization strategies, and modeling techniques has enhanced our understanding of non-reciprocity and improved the design process. Furthermore, the realization of dual-band non-reciprocity using both distributed and lumped elements opens up new possibilities for the design of advanced microwave systems. These achievements contribute to the overall body of knowledge in the field and pave the way for future innovations in non-reciprocal bandpass filters and related applications.

Chapter 2

Literature Survey

2.1 Introduction

Non-reciprocal components are of paramount importance in many electronic systems. Traditionally, reliance on magnetic materials, such as ferrites, has been the basis of the functionality of such components. The internal magnetic moment under the influence of a strong external magnetic bias breaks the reciprocity of the materials [14]. However, today's state-of-the-art systems demand cost-effective, miniaturized, and integrated solutions. This can be achieved with magnetless non-reciprocal devices that are capable of breaking the Lorentz reciprocity principle [15]. In the past decade, passive metastructures have also been devised to achieve Faraday rotation without magnetic bias. Spatio-temporal biasing of the metasurfaces initiates frequency translation and harmonic mixing properties which, in turn, generate non-reciprocity [16, 17]. Recently, with the advent of magnetless non-reciprocal devices, time-varying circuits have been viewed as a remarkable breakthrough. This has, in fact, paved the path for researchers to develop non-reciprocal devices such as circulators [18, 19, 20, 21, 22, 23, 24, 25, 26, 27], isolators [28, 2, 29, 30], gyrators [31], and even leaky-wave antennas [32, 33]. Still, there remain some areas in the field of non-reciprocity which can be explored with the aid of magnetless time-varying circuits. One such area is the implementation of non-reciprocity in bandpass filters.

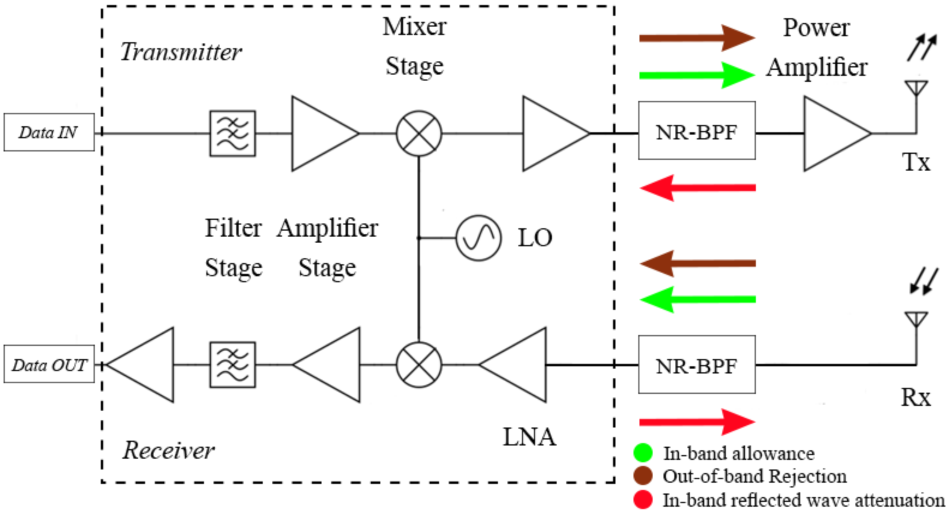

Figure 2.1: Block diagram of a transceiver deployed with NR-BPF.

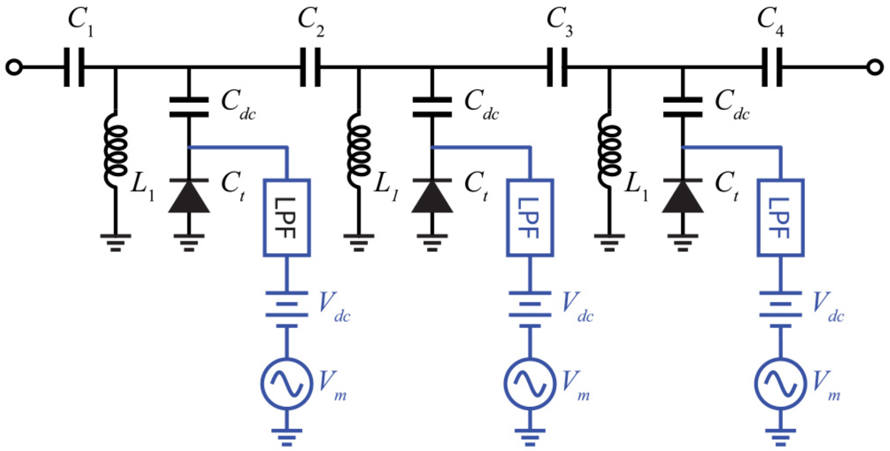

Figure 2.2: Block diagram of a 3^{rd} order NR-BPF using varactor diodes [1].

Non-reciprocal bandpass filters (NR-BPF) find a broad spectrum of applications in the domain of communication systems. One such application-specific deployment is in the wireless transceiver system shown in Fig. 2.1. The NR-BPF in the transmitter section allows only the in-band frequency components (indicated by green arrows) and prevents any out-of-band frequency components (indicated by brown arrows) to pass to the power amplifier stage in the forward direction, while at the same time preventing any in-band frequency components (indicated by red arrows) to pass back to the mixer stage as a result of reflection from the power amplifier and the antenna. Similarly, in the receiver section, the NR-BPF not only acts as a filter (indicated by green and brown arrows), but also acts as an isolator by attenuating any reflected wave that might pass to the antenna. The advantage of using a single NR-BPF to serve this dual purpose lies in the reduction of losses that would have been incurred by deploying both the filter and the isolator together to manifest the same phenomenon.

Although non-reciprocity in bandpass filters has been implemented using various techniques [34, 35, 36], implementation using time-modulated resonators is still nascent. Wu *et.al.* proposed a novel concept of an isolating bandpass filter with low forward transmission loss and high reverse isolation at the center frequency [1]. The basic block diagram of a 3^{rd} order NR-BPF is given in Fig. 2.2. The circuit consists of space-separated time-varying resonators in addition to the capacitors that are generated by virtue of admittance inverters (to be dealt with shortly). Owing to the non-linear capacitance property of a varactor diode under reverse bias, the modulation of the varactors within the resonators generates intermodulation (IM) products. The significant difference between the RF power distribution among the IM products in the forward and reverse paths generates non-reciprocity in the circuit characteristics. The essence of the time-varying capacitance lies in the generation of IM products, which, unlike time-invariant products, do not generate a reciprocal bandpass response. Interestingly, with only the DC bias applied, the varactor would behave as a normal capacitor and hence would not produce any non-reciprocity. It will be further explained in section II B that the amplitude, frequency, and phase of the AC signal applied to the time-varying capacitance determines the position of the IM products with respect to the RF signal in the frequency domain. Hence, the RF signal is translated to the higher and lower harmonic frequencies owing to the position of the IM products as it travels from source to load or vice versa. The frequency translation also leads to the distribution of RF power among these harmonics, but a wise choice of the parameters of the AC signal results in the constructive interference of the signals translated to harmonics with the signal at the fundamental frequency, thus reinforcing the RF signal reaching the load in the forward direction. Conversely, destructive interference between the signals in the reverse direction results in an attenuation of RF power reaching the source in the backward direction. This phenomenon causes the bandpass filtering response in the forward direction while triggering an isolation within the passband of the filter in the reverse direction.

The concept of time-varying transmission lines (TVTL) has already proved its usefulness in application-specific domains such as circulators, isolators, and other non-reciprocal communication systems. Non-reciprocal filters with the aid of TVTL, although in the nascent stage, may prove superior to circuits involving conventional bulky and expensive ferrite components.

The objective of this paper is to develop basic concepts for the design of time-modulated filters and to survey the current state of practical implementation of these filters. Specifically, the prerequisites for the concept which are historically significant are elaborated to set the foundation for a discussion of non-reciprocal filters. Secondly, the theory of non-reciprocity in filters at the fundamental frequency using spatio-temporal modulation (STM) is presented. Finally, a survey of practical implementation of the filters in lumped and distributed components is discussed. This review aims to contribute to the understanding of non-reciprocal filters and to open doors for researchers to accelerate the burgeoning development of the field of magnetless non-reciprocal filter design.

2.2 Prerequisites to the concept of Non-reciprocity

Before moving on to decipher the cause of non-reciprocity, it's helpful to understand the concepts that serve as milestones in the development of non-reciprocity and that still underpin modern day technological advances in this domain.

2.2.1 The Parametric Amplifier

Any amplifier can be considered to be a modulator in which the energy of the input wave is transformed to the load impedance by harnessing the energy from the amplifier's energy source. The amplifier's energy source can be either a DC or an AC supply. For a DC source, the amplified output waveform is an exact replica of the input waveform with the amplifier's energy source providing the useful gain. However, for an AC source, the output is not an exact replica of the input. In fact, the frequency of the output waveform is transformed owing to the generation of new frequencies due to the interaction of two waves of different frequencies. The spectral content of the output waveform contains an infinite number of transformed frequencies. These frequencies, denoted as $f_{y,z}$, where y and z are positive, negative, or zero integers, are harmonically related to the input wave frequency (f_0) and the frequency of the modulator's energy source (f_m) - also termed the local oscillator ($f_{y,z} = yf_0 + zf_m$). This energy conversion from one frequency component to another is governed by general power relations first described by J. M. Manley and H. E. Rowe [37] which are popularly known as the Manley-Rowe relations. These relations consist of two independent equations which govern nonlinear reactance modulators provided the nonlinear characteristic of the element (capacitor or inductor) is single-valued. These equations relate the power at different frequencies obtained after harmonic mixing of the input signal frequency and the local oscillator or modulation frequency. By expanding the charge q and flux linkage ψ for the capacitor and inductor respectively in terms of a Fourier series, the Manley-Rowe equations relating the average power flowing into the nonlinear element, $W_{y,z}$, at the harmonic frequencies $f_{y,z}$ with the individual components f_0 and f_m can be expressed as shown in (2.1).

$$\begin{aligned}\sum_{y=0}^{\infty}\sum_{z=-\infty}^{\infty}\frac{yW_{y,z}}{yf_0+zf_m}&=0\\ \sum_{y=-\infty}^{\infty}\sum_{z=0}^{\infty}\frac{yW_{y,z}}{yf_0+zf_m}&=0\end{aligned}\tag{2.1}$$

For a linear capacitor or inductor, without mixing terms, only two frequency components will be present, that is, either f_0 or f_m and $W_{y,z} = 0$ for all y and z, proving that (2.1) is satisfied. The Manley-Rowe relations, expressed in Equation (2.1), govern the power relations in nonlinear reactance modulators. These equations ensure good gain and stability in circuit analysis involving nonlinear reactance.

$$\begin{aligned}\frac{W_m}{f_m}+\frac{W_s}{f_s}&=0\\ \frac{W_0}{f_0}+\frac{W_s}{f_s}&=0\end{aligned}\tag{2.2}$$

Notably, if the circuit allows only the current of the sum frequency (f_s), equation (2.2) shows a gain at the sum frequency compared to the signal frequency. This type of amplifier is called a parametric up-converter.

$$\frac{W_m}{f_m}+\frac{W_d}{f_d}=0\tag{2.3a}$$

$$\frac{W_0}{f_0}-\frac{W_d}{f_d}=0\tag{2.3b}$$

Additionally, if the circuit permits the flow of the difference frequency (f_d), equation (2.3) reveals that the nonlinear reactance offers a negative resistance to the RF signal source. This negative resistance can result in free oscillations and is known as a negative resistance parametric amplifier. Magnetic and variable capacitor circuits exhibit similar behavior. These results can be applied to various nonlinear reactance elements, such as diodes, and have been studied in different contexts, including semiconductor diode-based parametric amplifiers and time-varying distributed reactance in propagating structures. The detailed analysis of parametric amplifier is given in Chapter 3.

A magnetic modulator has been demonstrated in [38]. It is shown that for the simplest modulation containing only a single magnetic modulator, the sum frequency introduces a positive resistance while the difference frequency introduces a negative resistance in the signal path. In the carrier or the local oscillator path, both of the frequencies introduce positive resistance. The same phenomenon occurs in case of a variable capacitor circuit [39, 40]. Thus, for any nonlinear reactance, the flow of current comprising the difference frequency causes abstraction of energy from the carrier (f_m) that is delivered to the signal (f_0) while that of the sum frequency results in abstraction of energy from both the carrier and the signal.

A parametric amplifier using semiconductor diodes has been illustrated in [41]. The application of parametric amplification has also been investigated in time-varying distributed reactance in propagating structures [42]. Depending on the phase and group velocity of the propagating wave, which in turn depends on the series reactance and the shunt susceptance of the transmission line, four cases have been studied; each case complies with the Manley-Rowe equations. If the phase and the group velocity are in the same direction, it leads to frequency conversion; that is, the power from one frequency is transferred to the other frequency with the additional power being supplied by the time-variant reactance (capacitor or inductor). If two waves of different group velocities but with the same phase velocities flow, it can be utilized as a filter or a frequency channel selector which has been further studied in [2].

2.2.2 Spatio-temporally modulated (STM) transmission line

From parametric amplifier theory, it is clear that nonlinear or time-varying reactance leads to mixing of harmonic frequencies, resulting in generation of intermodulation (IM) products. The IM products strictly follow the Manley-Rowe equations, provided the reactance is single-valued. One of the application-specific domains of this frequency-mixing behavior is the separation of spatio-temporally overlapping signals traveling in opposite directions without using bulky ferrite components as has been demonstrated in [43] and [44]. The concept of distributed modulated capacitors (DMC) which can serve as a time-varying transmission line in which varactor diodes are loaded along the length of the transmission line has been proposed in [2] and is shown in Fig. 2.3((a)).

The modified telegrapher's equation [45] for TVTL using time-varying capacitance is given by

$$
\begin{aligned}
\frac{\partial v(z,t)}{\partial z} &= -L\frac{\partial i(z,t)}{\partial t} \\
\frac{\partial i(z,t)}{\partial z} &= -\frac{\partial [C(z,t)v(z,t)]}{\partial t}
\end{aligned}
\tag{2.4}
$$

where L is the inductance per unit length and $C(z,t)$ denotes the time-varying capacitance per unit length. The time-varying capacitance $C(z,t)$ is usually implemented using a varactor diode, which is nothing but a voltage controlled capacitor where the reverse bias applied across the varactor changes the capacitance. In fact, the capacitance decreases with the applied reverse bias. So, an AC voltage applied across the varactor results in a corresponding variation in the

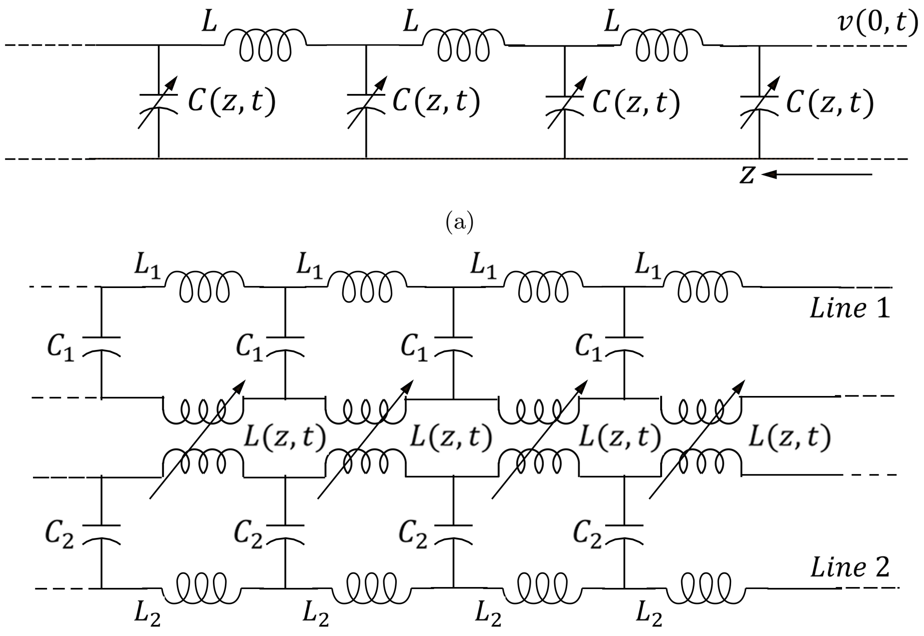

(a)

(b)

Figure 2.3: Time-varying transmission line integrated with spatio-temporally modulated transmission line (a) capacitance per unit length [2], (b) inductance per unit length [3].

capacitance which can be expressed by

$$C(z,t) = C_0 + \Delta C cos(\omega_m t - \beta_m z + \phi) \tag{2.5}$$

where C_0 denotes the mean capacitance per unit length and the second part of (2.5) corresponds to the capacitance due to the applied reverse bias ac voltage across the varactor where ΔC is the amplitude variation per unit length of the capacitance due to the reverse bias, ω_m is the angular frequency, and β_m is the phase constant. In a similar manner, a transmission line embedded in a ferromagnetic medium is demonstrated in [3] as shown in Fig. 2.3((b)). Here, the ferromagnetic medium is driven by a local oscillator which actually leads to the time variation in the transmission line. This time-varying ferromagnetic medium, in fact, provides a mutual coupling between the two transmission lines.

Just as in the case of transmission lines loaded with time-varying capacitance per unit length, the modified telegrapher's equation for Fig. 2.3((b)) is given in [3]. The characteristic impedance and phase constant of the lines are given as $Z_{0i} = \sqrt{\frac{L_i}{C_i}}$ and $\beta_i = \omega_i \sqrt{L_i C_i}$ where $i = 1, 2$. The ferromagnetic medium is energized by a traveling wave with a phase constant β and angular frequency ω. Similar to the time-varying capacitance, the time-varying inductance $L(z,t)$ takes the form given in [3]. If the frequency of the waves traveling in lines 1 and 2 are such that $\omega_1 + \omega_2 = \omega$, then, as in the case of parametric amplifiers, the energy of the local oscillator is coupled to the traveling waves in lines 1 and 2 and this leads to exponentially growing waves along the length of the transmission line, leading to exponential amplification. But the drawback of this circuit is that two separate transmission lines are needed for the coupling to occur and for the transfer of energy. So, a time-varying transmission line utilizing a spatio-temporal variation of the capacitance is a better choice.

Time-varying transmission line finds wide application not only in the generation of non-reciprocal components like isolators and circulators, but its unique feature of allowing propagation only in the direction of the carrier signal can be well utilized in the design of non-reciprocal filters, as was demonstrated for the first time in [1]. Let us suppose the angular frequency of the signal and the carrier wave traveling in the transmission line shown in Fig. 2.4 are ω_0 and ω_c, respectively.

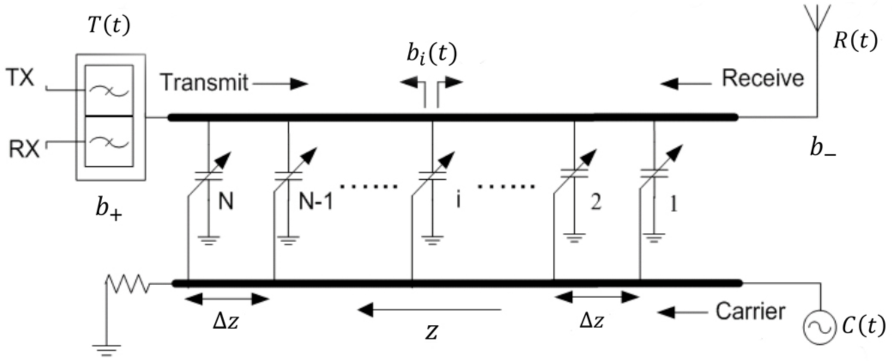

Figure 2.4: Concept of DMC as circulator, where $T(t) = e^{j\omega_0(t+\frac{z}{v_p})}$, $R(t) = e^{j\omega_0(t-\frac{z}{v_p})}$ and $C(t) = e^{j\omega_c(t-\frac{z}{v_p})}$ [4].

The signal arriving from the antenna is modulated by the varactors, and currents at the intermodulation products are generated. These currents travel both right and left along the upper transmission line. If the parametric conversion is considered at only the upper sideband ($\omega_0 + \omega_c$), the received signals at the left (b_+) and right (b_-) are given in [4]. Analysis of the received signal at either end reveals that, moving toward the receiver end in Fig. 2.4, the signal amplitude gradually increases; whereas, moving toward the transmitter end, the signal amplitude gradually decreases and reaches zero after some wavelengths. As the number of varactors increases, the faster the decay. This analysis proves to be the basis for further application-specific STM transmission lines with distributedly modulated capacitors.

2.3 Non-reciprocal filters

In the previous sections, parametric amplification, frequency mixing, and non-reciprocal behavior in time-varying transmission lines using STM were explained. Based on these properties of a TVTL, a filter in the forward direction with isolation in the backward direction has been demonstrated in [1]. Prior to digging deeper into the underlying cause of non-reciprocity in filter characteristics, we first discuss the foundations of the insertion loss method in the design of conventional filters.

2.3.1 Analysis of the Insertion Loss Method

The basis for the analysis of any filter function using the insertion loss method is the construction of a characteristic polynomial for the desired insertion loss (IL) and the return loss (RL) level in the lowpass prototype (LPP) domain [45]. Once the characteristic polynomial has been defined in the Laplace (s) domain, the next step is the extraction of the elemental values so as to design a circuit comprising the corresponding reactive elements. The LPP domain can be converted to the bandpass prototype (BPP) domain based on classical lowpass-bandpass transformations. Based on the synthesized parameters, the circuit can then be represented in a coupling matrix form.

The concept of a coupling matrix was first introduced in 1970 by Atia and Williams for the bandpass prototype model [46, 47]. Once the g values, frequency independent (FIR) elements, and coupling inverter values are extracted, the total coupled network can be represented in the form of a two-port network. This two-port network, using Kirchhoff's nodal laws, can be represented in a matrix form also known as a coupling matrix. It is an integration of the source and load impedances (R_S and R_L), the frequency dependent elements (capacitors and inductors), and the FIR elements, which leads to the mainline and cross-couplings represented by the matrix $\mathbf{M}$. Further details on the synthesis and scaling of the coupling matrix can be found in [13, 48, 49]. Modeling the elements in matrix form simplifies operations such as scaling, transformation, and inversion. The extracted network from the synthesized polynomials is pictorially shown in [5].

2.3.2 Analysis of Spatio-Temporal Transmission Lines

The linear time-varying (LTV) transmission line in Fig. 2.5((a)) consists of a shunt capacitor $C(t)$ modulated by a sinusoidal signal, which causes non-reciprocity. When multiple time-varying elements modulated with progressive phase shifts are added along the transmission line, as shown in Fig. 2.5((b)), the phenomenon is called spatio-temporal modulation. The time harmonic capacitance variation is given in (2.5). For our analysis, the spatial part ($\beta_m z$) is ignored and a new term ζ is introduced which is given by $\zeta = \frac{\Delta C}{C_0}$. Kirchhoff's law applied to the network in Fig. 2.5((a)) gives

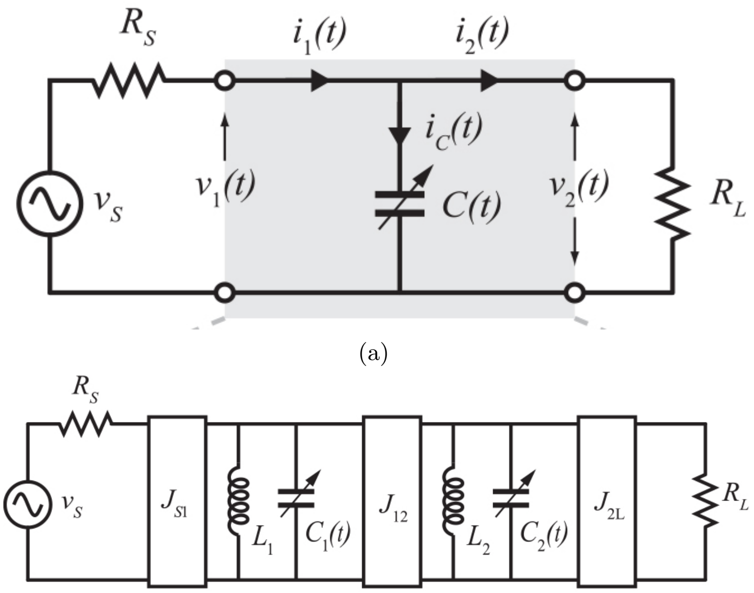

(a)

(b)

Figure 2.5: (a) Simple linear time-varying circuit with a single shunt capacitor modulated by a sinusoidal signal. (b) Generalized circuit topology of a 2^{nd}-order spatio-temporally modulated filter [1].

$$v_1(t) = v_2(t) \tag{2.6a}$$

$$i_1(t) = j\omega C(t) v_2(t) + i_2(t) \tag{2.6b}$$

Fourier analysis is used to transform the time domain equations (2.6) to the frequency domain equations (2.7).

$$V_1(\omega) = V_2(\omega) \tag{2.7a}$$

$$I_1(\omega) = j\omega C_0 V_2(\omega) + j\omega \frac{\Delta C}{2}[V_2(\omega - \omega_m)e^{j\phi} + V_2(\omega + \omega_m)e^{-j\phi}] + I_2(\omega) \tag{2.7b}$$

$$\mathbf{Y}_r^{(p)} = \begin{bmatrix} Y_q^{(-2)} + jB_p & jP^{(p)}(\omega - 2\omega_m) & 0 & 0 & 0 \\ jQ^{(p)}(\omega - \omega_m) & Y_q^{(-1)} + jB_p & jP^{(p)}(\omega - \omega_m) & 0 & 0 \\ 0 & jQ^{(p)}\omega & Y_q^{(0)} + jB_p & jP^{(p)}\omega & 0 \\ 0 & 0 & jQ^{(p)}(\omega + \omega_m) & Y_q^{(+1)} + jB_p & jP^{(p)}(\omega + \omega_m) \\ 0 & 0 & 0 & jQ^{(p)}(\omega + 2\omega_m) & Y_q^{(+2)} + jB_p \end{bmatrix} \tag{2.8}$$

The spectral admittance matrix (2.8) represents the resonators formed due to the generated intermodulation (IM) products. The matrix is not symmetric, indicating non-reciprocity. The couplings between different harmonic resonators are related by non-reciprocal admittance inverters (2.9), causing non-reciprocity in the system. The coupling topology in Fig. 2.6 further

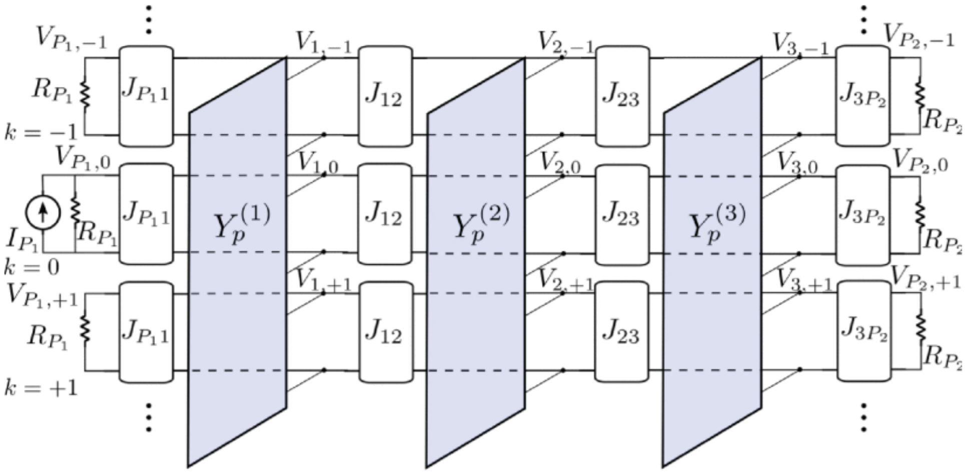

Figure 2.6: Equivalent circuit transformed from the basic coupled resonator circuit showing the generated nonlinear harmonics [5].

illustrates the cause of non-reciprocity, where the mainline inverters couple resonators within the same harmonics, and the inverters of equation (2.9) couple adjacent harmonic components of the same resonator. The detailed analysis and implication of each term is further explained in Chapter 3.

$$J_p^{(n,n-1)} = Q^{(p)}[\omega + n\omega_m] \tag{2.9a}$$

$$J_p^{(n-1,n)} = P^{(p)}[\omega + (n-1)\omega_m] \tag{2.9b}$$

In Fig. 2.7(a) and (c), electromagnetic waves travel between port 1 and port 2 solely through the resonators and mainline couplings. These waves exhibit no phase differences, as indicated by the absence of phase terms in the diagonal elements of the admittance matrix (2.8). Hence, without modulation, there is no non-reciprocity. However, Fig. 2.7(b) and (d) depict the travel of electromagnetic waves through nonlinear harmonic resonators resulting from capacitor modulation. Assuming a phase difference $\Delta\phi$ between the resonators and $\phi_1 = 0°$ for the first resonator, the total phase difference encountered by the wave in the forward direction is $+\phi_1 + \phi_2 - 2\phi_3 = -135°$, while in the backward direction it is $-\phi_1 - \phi_2 + 2\phi_3 = 135°$. The phase difference between the forward and backward waves amounts to 90°, providing an explanation for non-reciprocity.

Fig. 2.8((a)) shows the underlying phenomena encountered by the EM wave when it traverses from port 1 to port 2 (forward direction). The direction of the orange arrows indicate the probable paths taken by the EM wave in the forward journey through the mainline resonators as well as the resonators generated at the first harmonic frequency. Although the resonators at only the first harmonics are shown, the same holds for the higher order harmonics. The thickness of the arrows indicates the approximate energy content in the EM wave at the particular position. The blue arrows indicate the reflected wave at port 1, their direction and thickness conveying

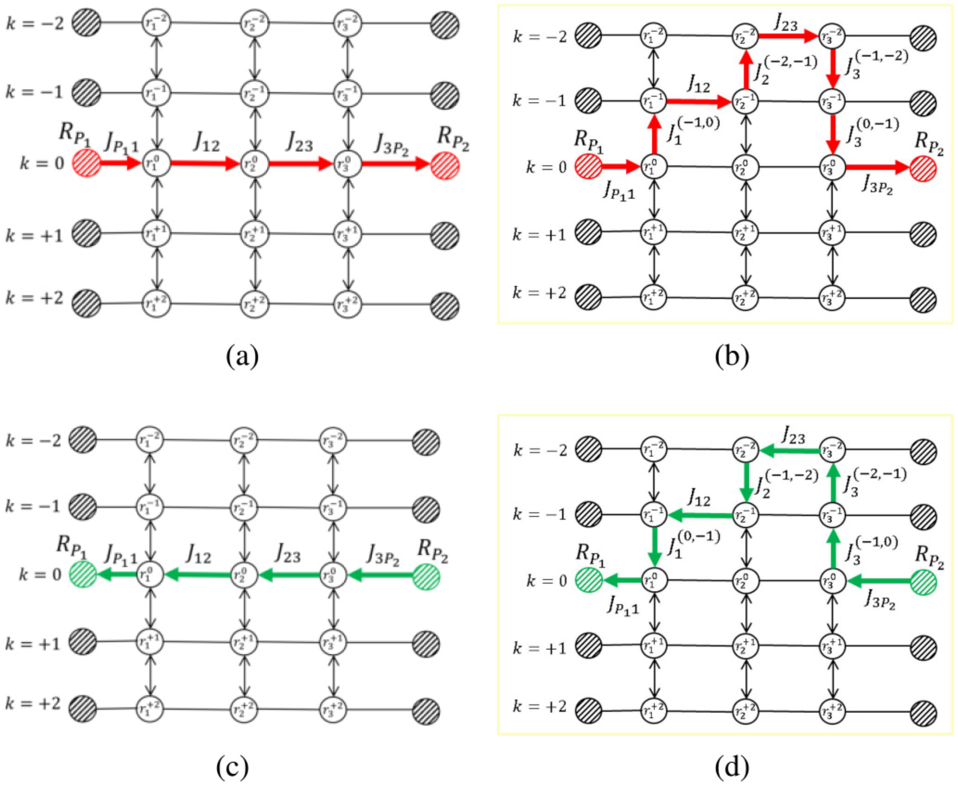

Figure 2.7: Different paths for the EM waves to traverse from (a) and (b) port 1 to 2 and (c) and (d) port 2 to 1 shown in the coupling topology in [5].

the same information as the orange ones. The energy of the EM wave is distributed among the fundamental and the harmonics, thereby incurring a loss just after encountering the first resonator. The remainder of the energy is further distributed in the corresponding mainline resonators as well as being redistributed among other higher order harmonics as it advances. By proper choice of circuit parameters, the energy of all the harmonics can be made to converge again at the fundamental frequency, thereby nullifying the IL. If the energy from the various harmonics does not upconvert and then downconvert back to the fundamental frequency, a considerable IL is encountered at the fundamental frequency, even if the circuit is lossless. Another important parameter that needs to be considered in the forward direction is the energy at port 1 that is reflected from the various harmonics back to the fundamental frequency. As the energy is up and downconverted to the higher order harmonics, reflected waves from various harmonics are in turn upconverted and downconverted back to the fundamental frequency, as indicated by vertical blue arrows in the vicinity of port 1. This phenomenon is responsible for additional energy being reflected back to port 1, thereby incurring an additional return loss (RL) apart from the RL due to the fundamental frequency alone. As the RL increases, the energy of the wave at the fundamental frequency reduces, thereby degrading the IL in the passband of the filter. So, in the forward direction, proper engineering of the circuit as well as the parameters is essential to reject higher order harmonics at both port 1 and port 2.

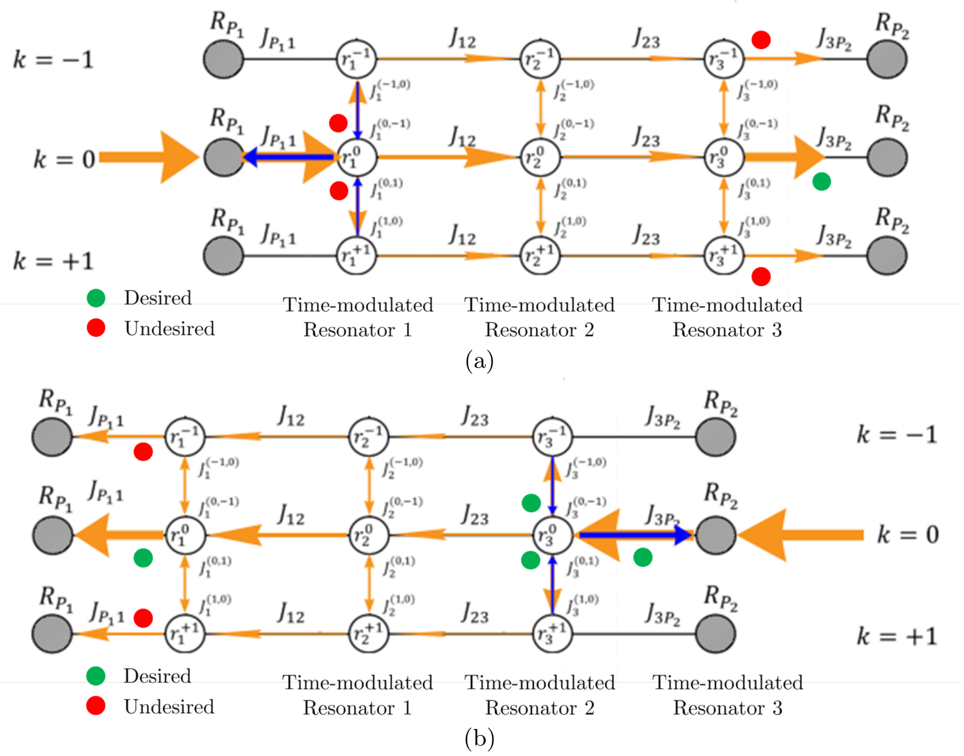

Figure 2.8: A pictorial representation of the transmission and reflection paths taken by the EM waves within the fundamental frequency and the first harmonics in the (a) forward direction and (b) backward direction.

Fig. 2.8((b)) shows the traversal of the EM wave from port 2 to port 1 (backward direction). Non-reciprocity demands isolation in the backward direction; the backward traveling EM wave must incur an IL in this path. As has already been discussed in the case of a forward traveling wave, nullification of harmonics at both the ports would promote low IL. Under this constraint, significant isolation can be achieved only if port 2 can be engineered in such a way that much of the energy is reflected by the higher order harmonics back to the fundamental frequency, in addition to the reflected wave at the fundamental frequency. Since the first constraint precludes the coupling of energy to the higher order harmonics in port 1, the only port that can be manipulated is port 2.

Additionally, the progressive phase difference ($\Delta\phi$) between the resonators should be chosen so that the total phase encountered by the EM wave while traversing the fundamental and IM products does not result in a destructive interference of the signal power at the load end in the forward direction. On the other hand, for the EM wave traveling in the backward direction, the total phase encountered must destructively interfere with the signal power, thereby increasing the backward IL considerably. Furthermore, it should be noted that the increase in the number of time-varying resonators results in an increase in the degrees of freedom for the EM energy traveling in the forward direction to converge back to the fundamental frequency from the harmonics, thereby enhancing the IL. A similar phenomenon occurs in the backward direction.

The increase in the number of resonators results in an enhancement of the conversion of EM energy from the fundamental to the harmonics in addition to the reflection incurred at port 2.

2.3.3 Implemented Filters and Discussion

It has been observed that with only one time-varying resonator, the circuit does not exhibit non-reciprocity at the center frequency, because the available power from the carrier frequency is distributed among both the carrier and the IM frequencies, and the latter exhibits loss only at the center frequency. Conversely, with more than one time-varying resonator, the power from the transmitted and reflected harmonic products is up-converted and down-converted back to the carrier frequency. Since the frequency translation is non-reciprocal as has been shown in preceeding equations, S_{21} at the center frequency becomes non-reciprocal as well.

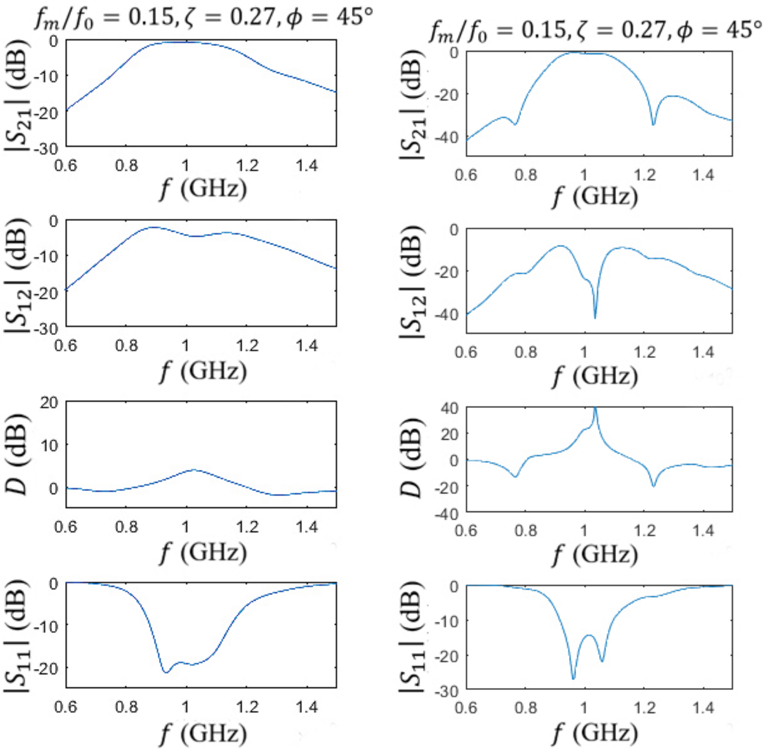

(a) (b)

Figure 2.9: S parameters along with Directivity (D (dB)) for (a) 2 resonators, (b) 3 resonators [1].

From Fig. 2.9, one can see that the performance is enhanced when the number of resonators is increased. Comparison of the results of a 3-pole filter with different numbers of harmonics has been elaborated in [1]. The results of that study show that convergence issues arise in the numerical results when the dimension of the spectral matrix increases from 3 to 7. This leads to variation in the transmission and the reflection curves. Good convergence as well as stable results are obtained when the dimension of the spectral matrix is 7, which indicates that the signal power is mostly contained within the range $\omega - 3\omega_m$ to $\omega + 3\omega_m$ for a three-pole filter.

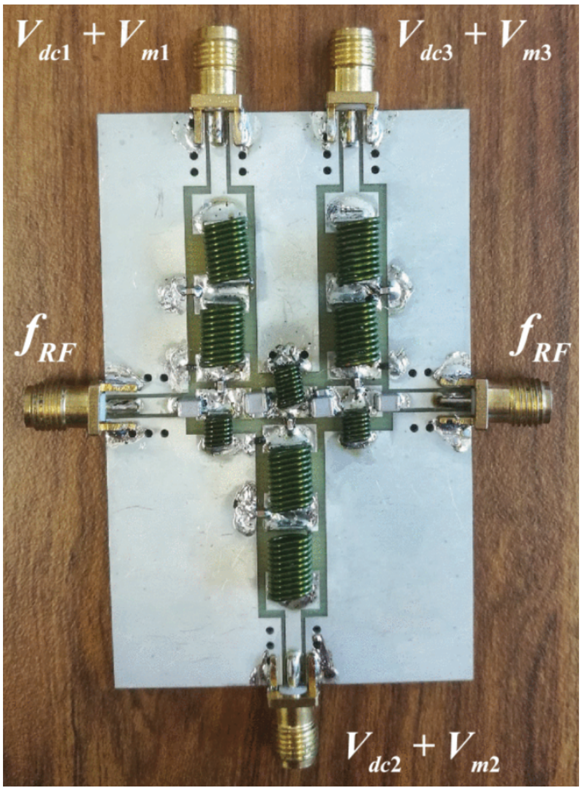

Figure 2.10: Fabricated prototype of the circuit schematic shown in Fig. 2.2 [1].

Further, a 0.043 dB equiripple filter exhibiting non-reciprocity with the circuit configuration shown in Fig. 2.2 has been built using lumped components with a center frequency (f_0) at 200 MHz and a bandwidth (BW) of 30 MHz [1]. The schematic has been substantiated with a fabricated prototype, as shown in Fig. 2.10. First, the LPP (g) values were obtained corresponding to an IL of 0.043 dB using the procedures listed in Section II A. The mean value of the capacitor (C_r) in the resonator was set to a feasible value of 13.2 pF. Correspondingly, $L_r = \frac{1}{\omega^2.C_r}$, where $\omega_0 = 2\pi f_0$. Based on the extracted values of the admittance inverters and replacing them with physical inverters with capacitors arranged in a π configuration, a filter using lumped components was built. The DC signal applied to the varactor (SMV1236) fixes the nominal capacitance value, whereas the superimposition of the AC signal results in a swing of the capacitance value from its nominal position, as has been theoretically shown in (2.5). The magnitude of the AC voltage swing depends on the magnitude of the chosen modulation index (ζ). The modulation signal is applied to the varactor through an LPF with a cutoff frequency much less than f_0 to prevent its interference with the modulation signal (f_m). The DC blocking capacitors (C_{ds}) isolate the shunt inductor from the DC path. The response of the circuit is shown in Fig. 2.11 and clearly reveals a directivity D of more than 20 dB in the passband. As has already been elaborated, the energy of the EM wave in the backward direction is distributed among the IM frequencies and, hence, the value of ω_m was set at 30 MHz, which ensures that the reflected energy at port 2 falls within the stopband of the filter.

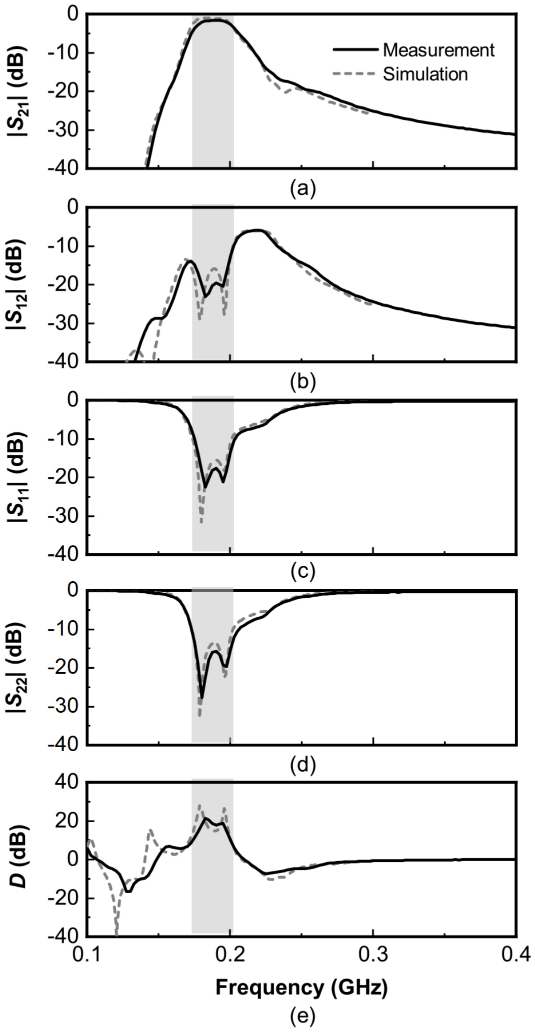

(e)

Figure 2.11: Comparison of the measured and simulated modulated responses for the circuit of Fig. 2.2. (a) Insertion loss $|S_{21}|$. (b) Reverse isolation $|S_{12}|$. (c) Reflection $|S_{11}|$. (d) Reflection $|S_{22}|$. (e) Directivity D [1].

Another implementation of a non-reciprocal BPF using lumped components was carried out in [6]. The varactor configuration for the resonator is shown in Fig. 2.12. The first step in the design of the desired un-modulated BPF is to choose the appropriate capacitor for the resonator. Once the capacitor value is fixed, the required DC biasing of the varactor is chosen to achieve the required capacitance value. This is followed by the optimization of the AC parameter values such as frequency, voltage, and the progressive phase shifts of the modulating signals so as to achieve a minimum IL in the passband in the forward direction and high reverse isolation. The analysis and the parameter extraction procedures followed here are based on the analysis in [1]. Further, a parametric study was used to obtain the optimized values of the circuit parameters

ζ, ω_m, and ϕ corresponding to the best response of the filter.

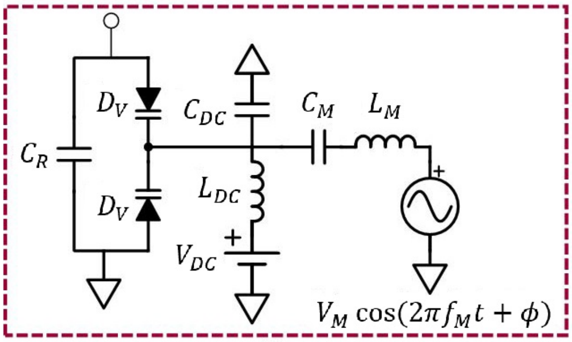

Figure 2.12: The capacitor network configuration to harness the resonant frequency modulation [6].

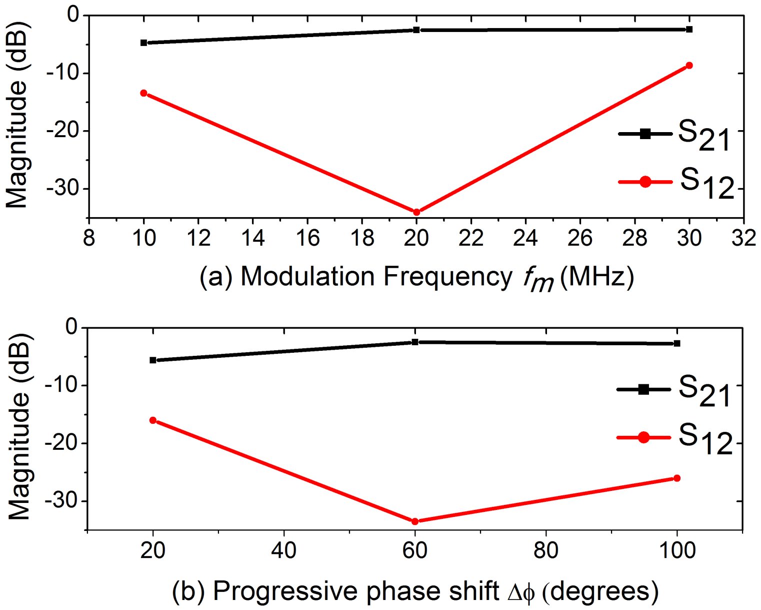

Figure 2.13: (a) The variation of IL and isolation with variation of f_m. (b) The variation of IL and isolation with variation of $\Delta\phi$.

Fig. 2.13(a) shows that the best response is obtained when the modulation frequency f_m is less than the bandwidth of the filter. This result is consistent with the fact that the reflected energy from port 2 does not fall in the passband. Too low of a modulation frequency results in a higher return loss from the harmonics at port 2 within the passband, while too high of a modulation frequency results in more energy coupling to the higher order harmonics, resulting in an increase in the IL in the passband. Fig. 2.13(b) shows that enhanced performance in terms of IL as well as directivity is obtained when $\Delta\phi = 60°$. It also shows that the variation in the modulation signal amplitude, which in turn is related to the parameter ζ, has an effect on the bandwidth and directivity of the filter. Lower ζ values result in wider bandwidth at the cost of degraded directivity while higher ζ values degrade the bandwidth, but the return loss as well as the directivity are enhanced.

The optimized filter characteristics corresponding to the circuit in Fig. 2.12 are shown in Fig. 2.14. The measured bandwidth is 27.5 MHz (19.2%) with the center frequency at 143 MHz. The measured minimum IL in the passband of the forward transmission response ($|S_{21}|$) and the maximum isolation in the reverse direction ($|S_{12}|$) were found to be 3.7 dB and 52.8 dB, respectively. This circuit also possesses the potential to have a tunable center frequency from 136 MHz to 163 MHz, simultaneously achieving non-reciprocity as shown in Fig. 2.15. This is done by uniformly altering the DC bias voltage on the three resonators. Although the IL is degraded in this case compared to [1], this is still the first ever reported non-reciprocal BPF with tunable center frequency.

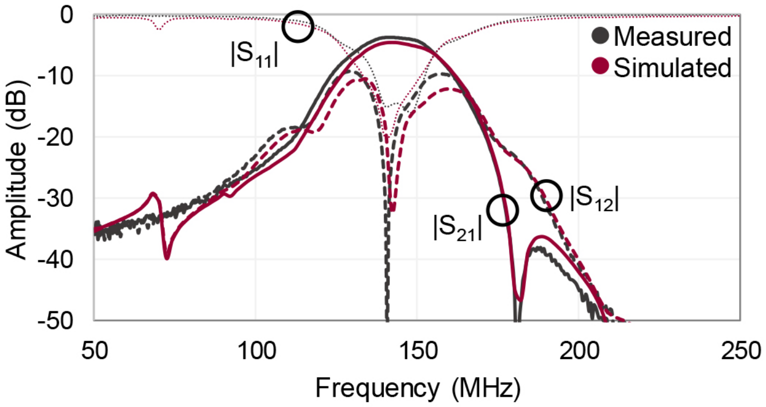

Figure 2.14: Contrast between the simulated and measured responses of power transmission and reflection for the fabricated prototype in Fig. 2.12 [6].

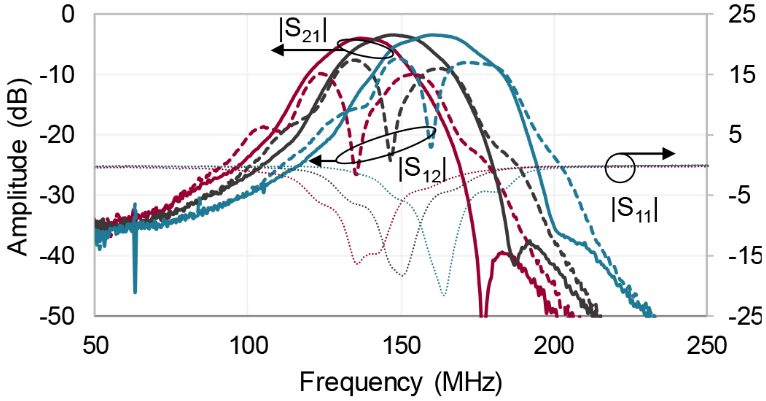

Figure 2.15: RF measured variation of the center frequency of the fabricated prototype in Fig 2.12 by modifying the DC bias to the varactors [6].

The filters in [1] and [6] used lumped components, which can be difficult to work with in the high frequency domain. So, the foundations laid in [1] were extended into a coupling matrix for the first time in [5], in which a 3-pole filter and a 4-pole filter were analytically formulated, simulated, and implemented using microstrip line showing non-reciprocity at the center frequency. The modulation signal parameters are optimized to maximize the energy that is coupled to the nonlinear harmonics, thus ensuring that most of the energy is transferred to the operating frequency. A coupling matrix is used to obtain the values of the circuit elements and obtain the desired response, followed by the optimization of the AC parameters, as explained above, in the analysis of the IL method for filter design.

A pictorial representation of the energy flow in the forward and reverse direction is shown in Fig. 3.7. Numerical analysis shows that decreasing the modulating signal frequency enhances directivity at the cost of narrower bandwidth. For the built filter, quarter wave microstrip lines terminated with a via hole on one side and connected to varactors on the other side were used. Both 3^{rd} and 4^{th} order filters were fabricated and compared with the simulation results. The geometry of the 3^{rd} order filter is shown in Fig. 2.16 and the corresponding S-parameters are shown in Fig. 2.17.

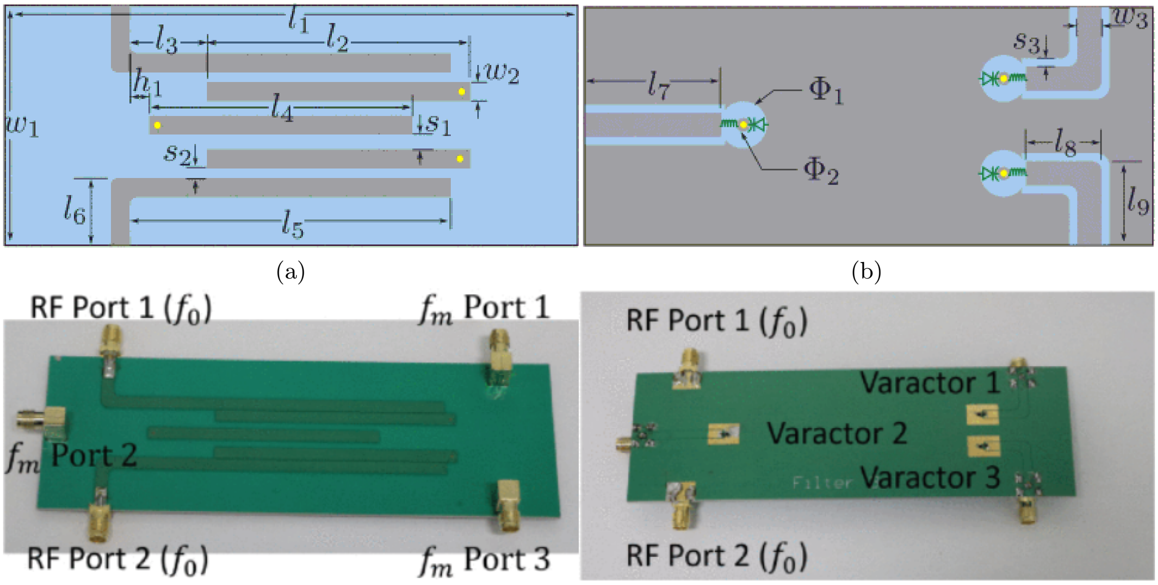

(a) (b)

(c) (d)

Figure 2.16: Distributed implementation of the 3^{rd} order non-reciprocal filter using microstrip technology. (a) and (b) Layout design of the top and bottom metalization layer, respectively. (c) and (d) Fabricated top and bottom metalization layers, respectively [5].

As in the case of lumped circuits, the RF and the modulating signals are isolated using choked inductors. Moreover, to increase the isolation further, the two signals are supported on two different planes of the substrate. Measured results exhibit slightly more IL in the passband owing to parasitic cross-coupling between non-adjacent resonators. After a resistor was connected in parallel to the resonators to model the losses incurred in the measured results good correspondance was achieved between the simulated and measured results. The directivity for

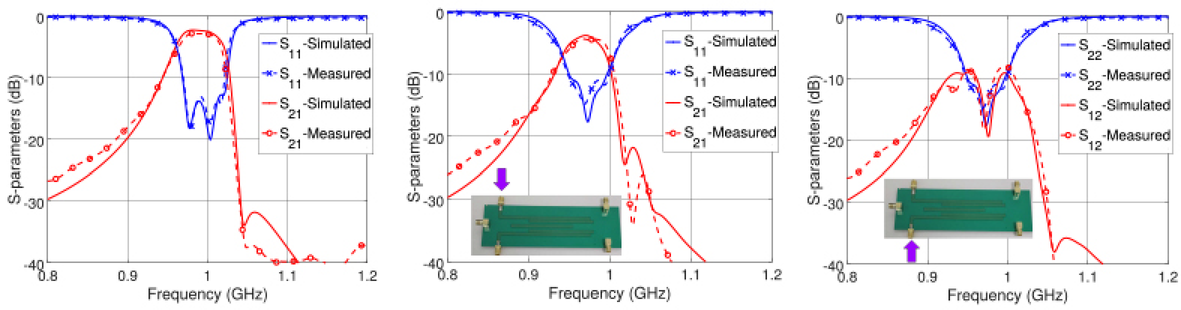

(a) (b) (c)

Figure 2.17: (a) 2-pole unmodulated response of the filter in Fig. 2.16, (b) and (c) Modulated response of the fabricated filter upon excitation by the modulating signal at the ports specified by the arrows [5].

the fourth order filter is 13.8 dB as compared to the 13.6 dB for the third order filter. Although the simulation and the measured results show good correlation, the complicated biasing design somewhat degrades the response.

Another distributed realization of a non-reciprocal filter using microstrip lines is shown in [7]. Initially, a parametric study was carried out to optimize the modulation frequency, followed by implementation of a 2-pole filter using microstrip lines. The parametric study provides neat and useful results which can be utilized to choose the values of the parameters.

	S_{21}	S_{11}	D	BW
$f_m \uparrow$	$\uparrow$	$\uparrow$	$\downarrow$	$!\downarrow$
$\zeta \downarrow$	$\uparrow$	$\uparrow$	$\downarrow$	$!\uparrow$
$\Delta\phi \uparrow$	$\uparrow\downarrow$	$\downarrow$	$\uparrow\downarrow$	$\uparrow$

Table 2.1: The variation of filter characteristics corresponding to parametric variations.

Table 2.1 represents the variation in filter characteristics with changes in parameters ζ, f_m, and $\Delta\phi$. Here, an ↑ beside the parameter name represents that the parameter value is increasing. For example, $f_m \uparrow$ means the effect of increasing f_m on the filter characteristics. Similarly, for the filter characteristics, an ↑ indicates an enhanced result is obtained, a ↓ indicates degradation of that particular characteristic, a ! mark before the ↑ or ↓ indicates a slight increase or decrease respectively and ↑↓ indicates that the characteristic first enhances and then degrades. It can be concluded that among the other parameters, $\Delta\phi$ plays a dominant role in determining the bandwidth of the response. It is also evident that increasing $\Delta\phi$ beyond 90° results in degradation of the response. This can be explained using the coupling topology given in [5]. If the EM wave traverses a path $J_{P_1 1} \rightarrow J_1^{(-1,0)} \rightarrow J_{12} \rightarrow J_{23} \rightarrow J_3^{(0,-1)} \rightarrow J_{3P_2}$ in the forward direction, then the total phase encountered by the wave is $\phi_1 - \phi_3 = -2\Delta\phi$. Conversely, in the backward direction, the total phase encountered is $2\Delta\phi$. Thus, the total phase difference incurred by the wave in the forward and backward direction is $4\Delta\phi$. So, as $\Delta\phi$ increases from

0° to 90°, the phase difference increases until it reaches its maximum, that is $360° = 0°$, hence a phase cancellation occurs at this point. Further increase in the $\Delta\phi$ results in the repetition of the same cycle starting from the minimum, thereby degrading the performance. If f_m increases to a large value, the IM products fall outside the bandwidth of the filter. As a result, the conversion of energy to the harmonics reduces, thereby increasing the bandwidth at the cost of reducing the non-reciprocity at the center frequency. On the other hand, reduction of f_m to a very small value results in the reduction of the number of reflection zeroes within the passband with a simultaneous generation of transmission zeroes outside the band. This phenomenon not only increases the selectivity of the filter, but also degrades the bandwidth. This compels the proper choice of the f_m value to obtain optimum results in terms of bandwidth and isolation. Works addressing the enhancement of bandwidth in non-reciprocal filters are still, to the authors' knowledge, unavailable and demand further research in this domain. With higher numbers of harmonics and more paths available for traversal, the phase cancellation of all the waves happens at no particular point, thus preserving the non-reciprocity at every instance.

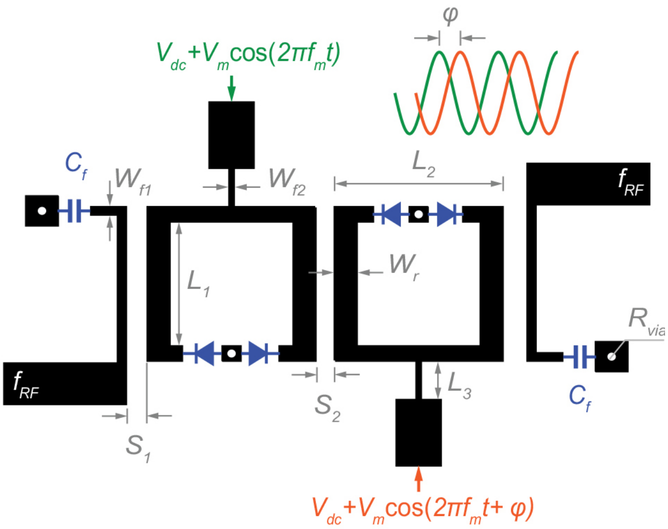

Figure 2.18: Layout design of the microstrip implementation of the proposed non-reciprocal filter [7].

The fabricated filter is fed with the modulating sources at the center of the half-wavelength resonators. This configuration nullifies the first odd-resonance voltage at the center, thus precluding any biasing components to separate the RF frequency f_{RF} from the modulation frequency f_m as was the case for [5] where a choke lumped inductor was used to separate the RF and the modulation path. This novel design reduces circuit complexity. The layout design of the distributed implementation is shown in Fig. 2.18.

The fabricated filter along with its response is shown in Fig. 2.19. While the lumped component representation shown above had better directivity, the distributed response is worse,

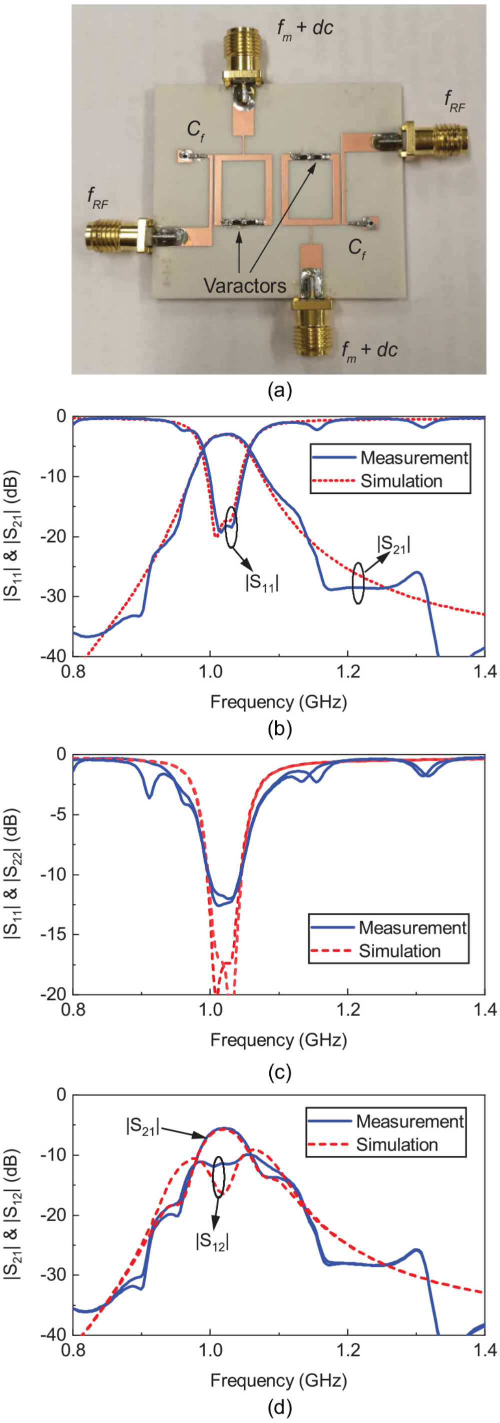

Figure 2.19: (a) A picture of the fabricated 2-pole non-reciprocal filter. (b) Simulated and measured results of the filter without modulation. (c) Simulated and measured S_{11} and S_{22} of the filter with modulation. (d) Simulated and measured S_{21} and S_{12} of the filter with modulation [7].

showing a directivity $D = 6.2$ dB for the fabricated circuit compared to $D = 12$ dB for the simulated response. The presence of lengthy cables at the modulating signal ports excites even order resonant modes and introduces loading effect on the resonator, which is likely the cause of this discrepancy.

Similarly, a 2^{nd} order non-reciprocal BPF using a microstrip structure has also been simulated

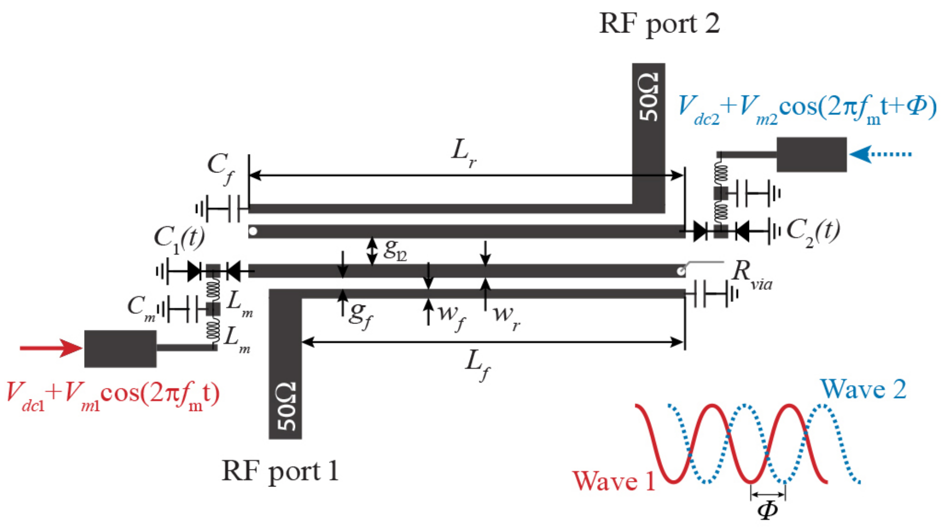

Figure 2.20: Layout design of the microstrip implementation of 2^{nd} order spatio-temporally modulated non-reciprocal filter using time modulated quarter wavelength resonators in [8].

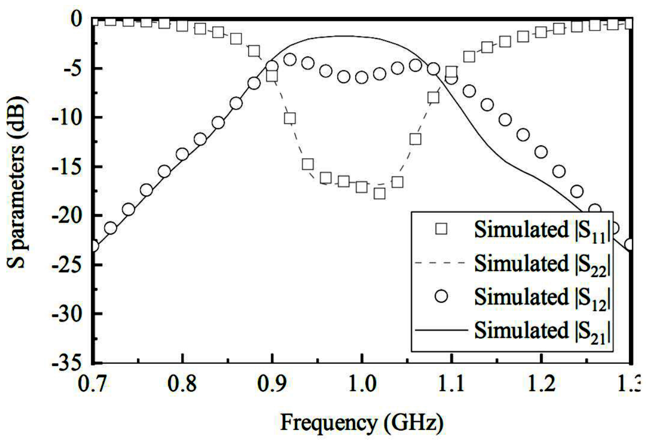

Figure 2.21: Simulated result showing clear non-reciprocity for the circuit in Fig. 2.20 [8].

in [8]. Parametric studies have been carried out which show an increase in the non-reciprocity with an increase in the modulation voltage, but the increased non-reciprocity degrades the insertion loss in the forward path. The circuit model is similar to the other works and the microstrip layout is shown in Fig. 2.20 and the corresponding S-parameters in Fig. 2.21. Simulation results show a clear non-reciprocity at the center frequency with a directivity of 4.7 dB.

The 2^{nd} order configuration of [8] has been extended to a 3^{rd} order $\lambda_g/2$ open-loop resonator (OLR) configuration in [9]. The main contribution of this literature is the achievement of STM in $\lambda_g/2$ resonators by loading them with time-modulated capacitors. The use of a modulation voltage source at the resonator center, along with a single inductor for enhanced biasing isolation, enables wideband tuning of the devices. The proposed resonator structure provides more than 30 dB RF to modulation isolation, ensuring low insertion loss and eliminating RF signal leakage

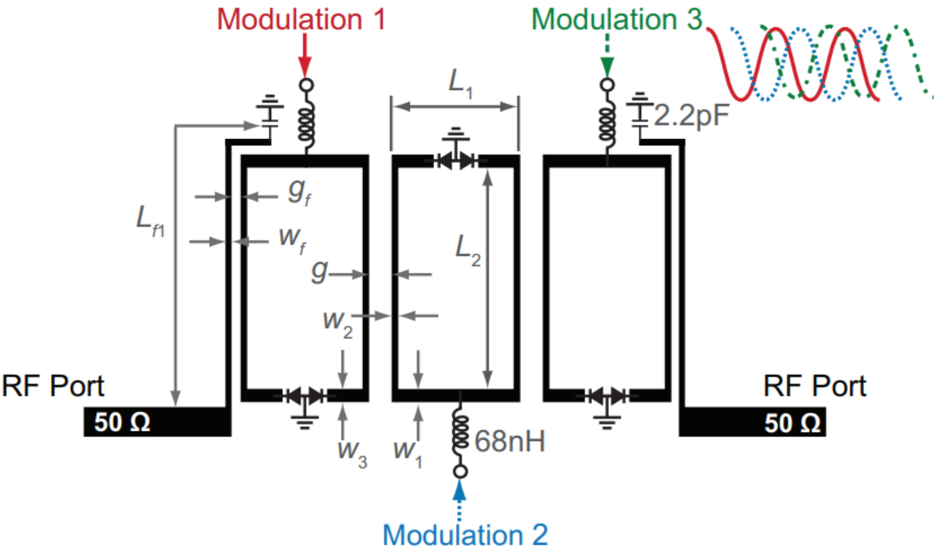

Figure 2.22: Schematic of the $\lambda_g/2$ OLR achiveing spatio-temporal non-reciprocity [9].

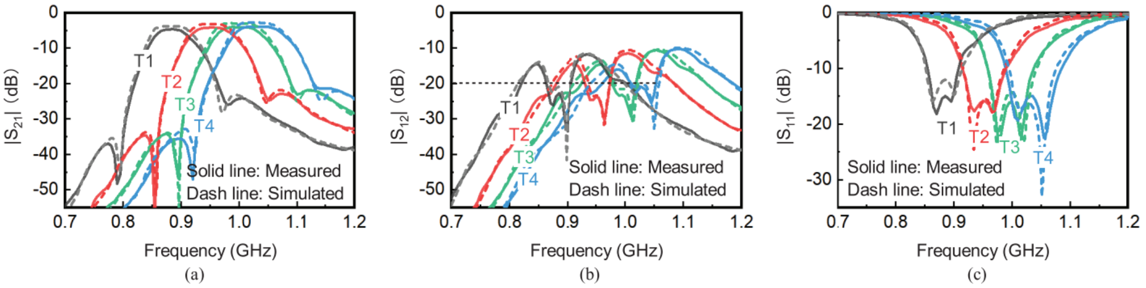

(a) (b) (c)

Figure 2.23: The tunable response of the schematic shown in Fig. 2.22 [9].

to the modulation ports. The research includes a simulated and measured 3-pole bandpass filter example, demonstrating minimal insertion loss of 3.9dB, a 20-dB isolation bandwidth of 42MHz at 1.0GHz, and a frequency tuning range of 885–1031MHz. The layout of the fabricated prototype is shown in Fig. 2.22 and the corresonding tunable response is shown in Fig. 2.23

A quasi-elliptic NR-BPF with fully reconfigurable response has been reported in [10]. By varying the resonant frequency of the BPF's resonators, the transfer function in the forward direction can be tuned in terms of frequency and bandwidth. For practical demonstration purposes, a lumped-element prototype centered at 300 MHz has been designed, manufactured, and measured as shown in Fig. 2.24. The prototype has demonstrated a center frequency tuning range of 1.15:1 and a bandwidth tuning range of 2.77:1 while maintaining non-reciprocal behavior. For all tuning states, the minimum in-band insertion loss in the forward direction has been measured between 1.7 and 4.3 dB, whereas the isolation in the reverse direction has been measured up to 30.9 dB, as shown in Fig. 2.25.

Recently, an innovative approach to magnet-less non-reciprocal bandpass filters (BPFs) has been presented in [11]. This approach involves the use of coupled static and time-modulated

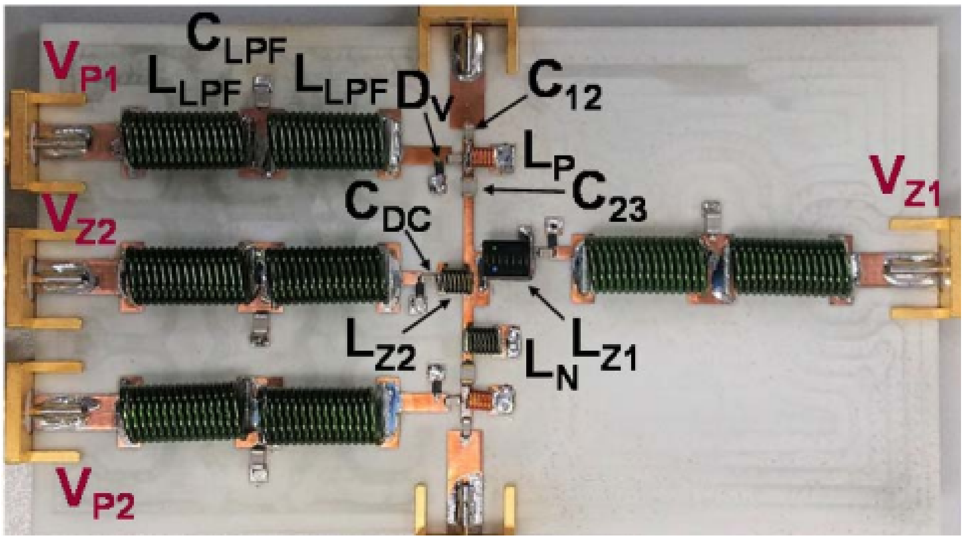

Figure 2.24: The fabricated lumped element prototype of [10].

resonators, enabling the BPF to achieve minimum forward insertion loss (IL) and two-pole isolation within the passband while maintaining wideband coverage and high isolation. In this design, the modulation signal is directly applied to the varactor through the transmission line, resulting in a simple yet effective implementation with an excellent non-reciprocal response. To validate the concept, a comprehensive study has been conducted, including design, simulation, and experimental analysis of a microstrip line non-reciprocal BPF operating at 1.46 GHz. The experimental results align closely with the simulation data, showcasing a forward IL of 3.10 dB and a reverse isolation of 20 dB over a bandwidth of 50 MHz. The coupling-routing diagram (CRD) for the proposed structure is shown in Fig. 2.26a, the corresponding layout and the fabricated prototype in Fig. 2.26b, and the measurement results of the circuit in Fig. 2.26c.

The research presented in [50] has extended the concept of a frequency tunable magnetless non-reciprocal bandpass filter (BPF) that has been implemented using time-modulated quarter-wave microstrip line resonators. This innovative design has allowed for the transformation of various termination impedances, including real-to-real, real-to-complex, and complex-to-complex. To achieve non-reciprocity, a modulation signal has been directly applied to the varactor through the transmission line. The modulation scheme employed in the proposed non-reciprocal BPF, though simple, has achieved an excellent non-reciprocal response. The center frequency (f_0) and the non-reciprocal behavior of the proposed BPF can be tuned by varying the dc bias voltage of the varactor. Experimental validation has been conducted using four prototypes of the non-reciprocal BPF: filter A (50-to-50 Ω), filter B (20-to-50 Ω), filter C (25+j10-to-50 Ω), and filter D (25+j10-to-55+j10 Ω). The measured results confirm that the center frequency of the non-reciprocal BPF can be tuned from 1.64 to 1.97 GHz (330 MHz), with a corresponding variation in forward insertion loss from 4.96 to 3.94 dB. Furthermore, the BPF has exhibited a

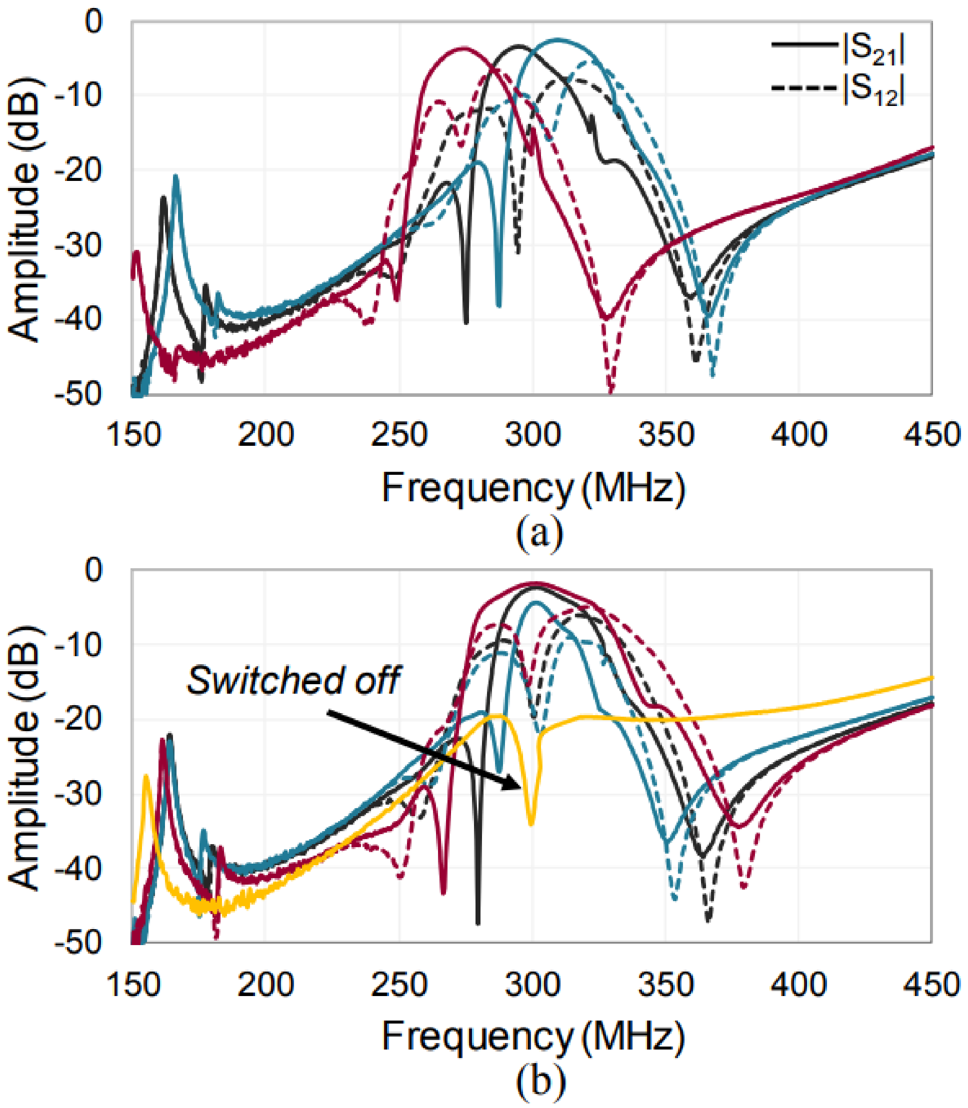

Figure 2.25: (a) The frequency tunability of the circuit shown in Fig. 2.24, and (b) the bandwidth tunability of the same circuit [10].

backward isolation of 20 dB over a bandwidth of 50 MHz.

The non-reciprocity in both the lumped and the distributed circuits discussed thus far depends solely on the incremental phase difference of the applied modulation signal to the varactors. Hence the power handling capabilities of the designed circuits depend largely on the varactor used and its breakdown voltage. Moreover, the theoretical foundations and design methodologies discussed so far, are based on single-band non-reciprocity. However, increasing demands of space sophistication, integration, and demand for multi-functional capabilities have provoked researchers to delve into dual-band non-reciprocal designs.

The first-ever multi-band non-reciprocity has been reported in [51], where parallel loaded lumped element resonators are spatio-temporally modulated to achieve non-reciprocal response in dual-band. The work has been extended to achieve simultaneous non-reciprocity in dual and triple band BPFs in [12]. The works discussed in these publications explore the imple-

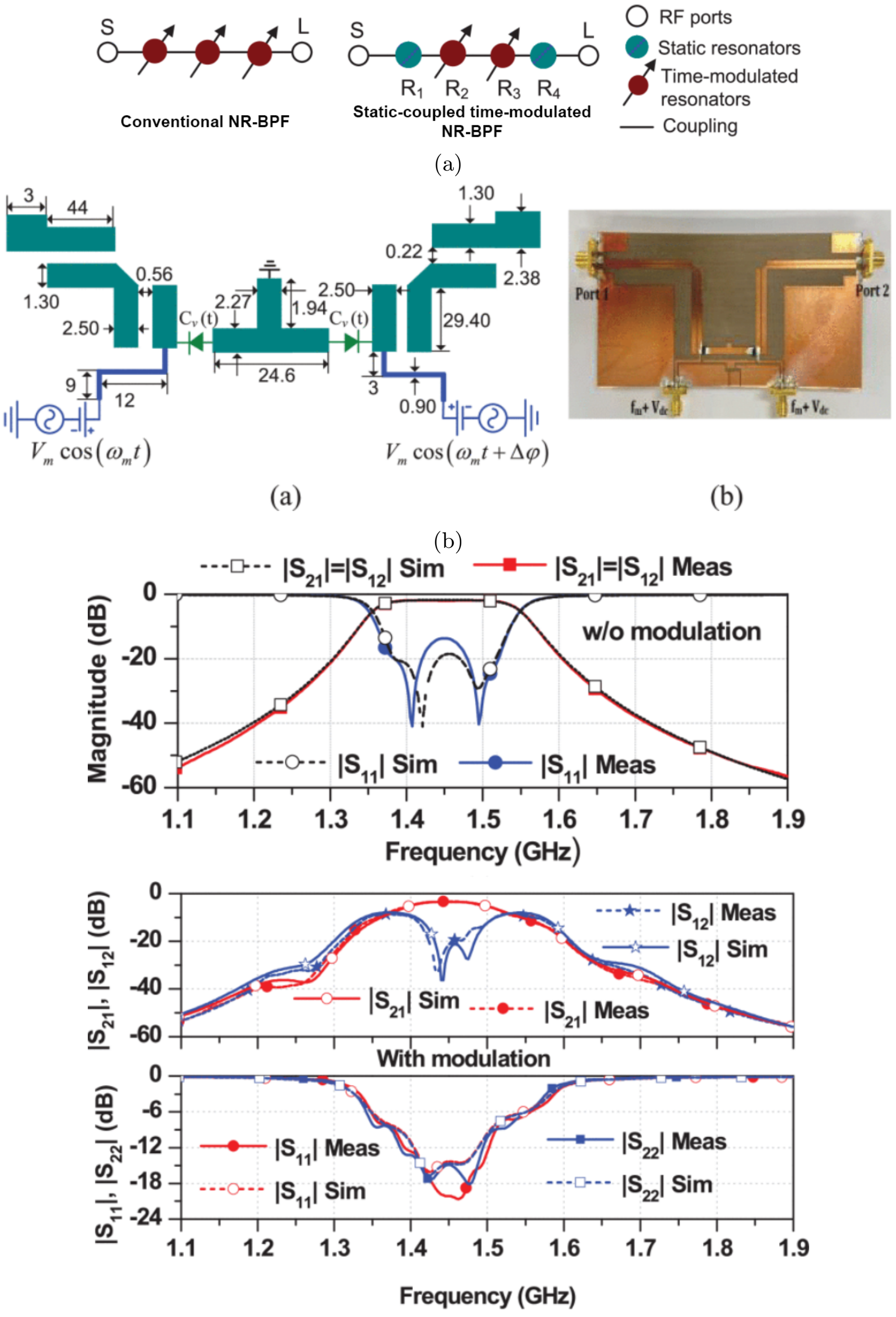

(a)

(b)

(c)

Figure 2.26: (a) The CR diagram of the proposed static and time-modulated coupled NR-BPF circuit, (b) schematic of the proposed circuit, (c) layout design and the fabricated prototype, and (d) the non-reciprocal response [11].

mentation of multi-band magnetless non-reciprocity using transversal frequency-selective signal paths formed by frequency-tunable and spatiotemporally modulated resonators. Each signal path enables the creation of an independent passband, offering control over both the frequency and direction of propagation. Consequently, the overall network can exhibit multiple frequency-reconfigurable non-reciprocal passbands (1-to-K configuration) as shown pictorially in Fig. 2.27.

The initial step involves demonstrating the operating principles and schematic of the mag-

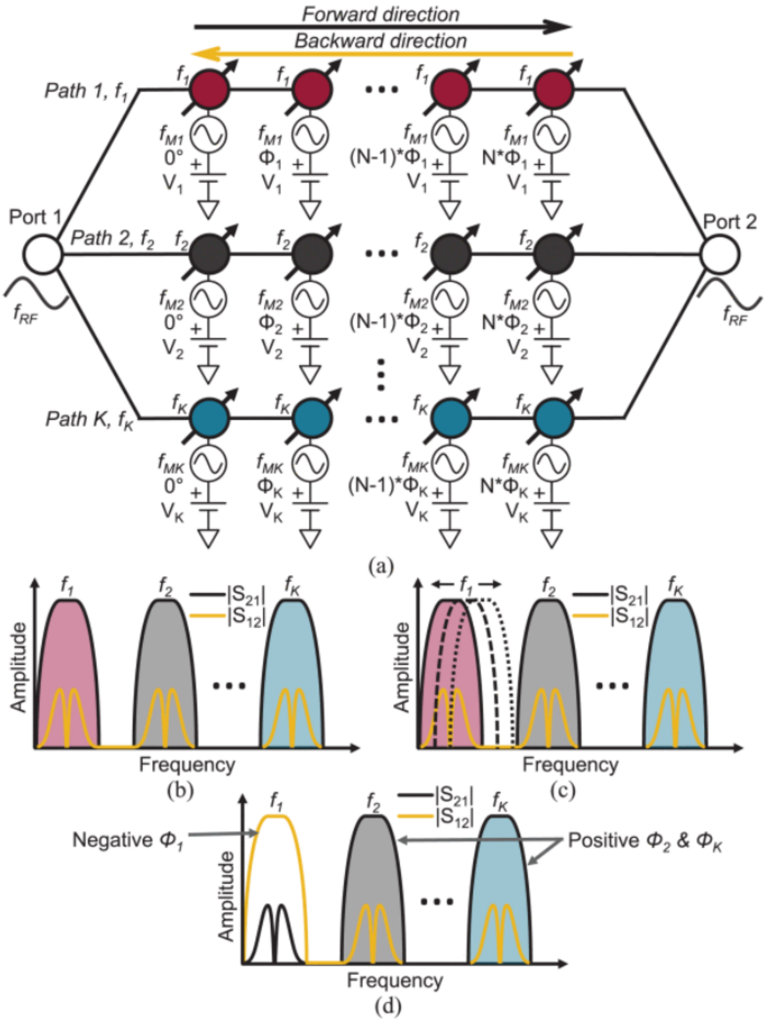

Figure 2.27: Multi-frequency selective paths and associated non-reciprocity phenomenon of [12].

netless and reconfigurable filtering isolator concept through circuit-based simulations of two- and three-path transversal filtering networks (referred to as two- and three-band networks). Detailed parametric analyses enable the determination of the independent modulation parameters for each band. Subsequently, the concept is extended to the design of magnetless, multiband filtering circulators. The operating and design principles of the circulator are elucidated through a circuit schematic and an ideally simulated dual-band example.

To validate the practical viability, three lumped-element (LE) prototypes consisting of two isolators and one circulator, shaped by two or three RF signal paths (corresponding to two and three passbands), have been implemented at the very high-frequency (VHF) band. These prototypes have exhibited an impressive maximum in-band isolation (IS) of up to 50 dB. Additionally, a frequency tuning range of up to 1.22:1 and the ability to change directionality have been achieved, showcasing the versatility and effectiveness of the proposed approach. The schematic of the dual-band NR-BPF using two 3^{rd} order lumped resonators is shown in Fig. 2.28a, and the corresponding reconfigurable responses are shown in Fig. 2.28b.

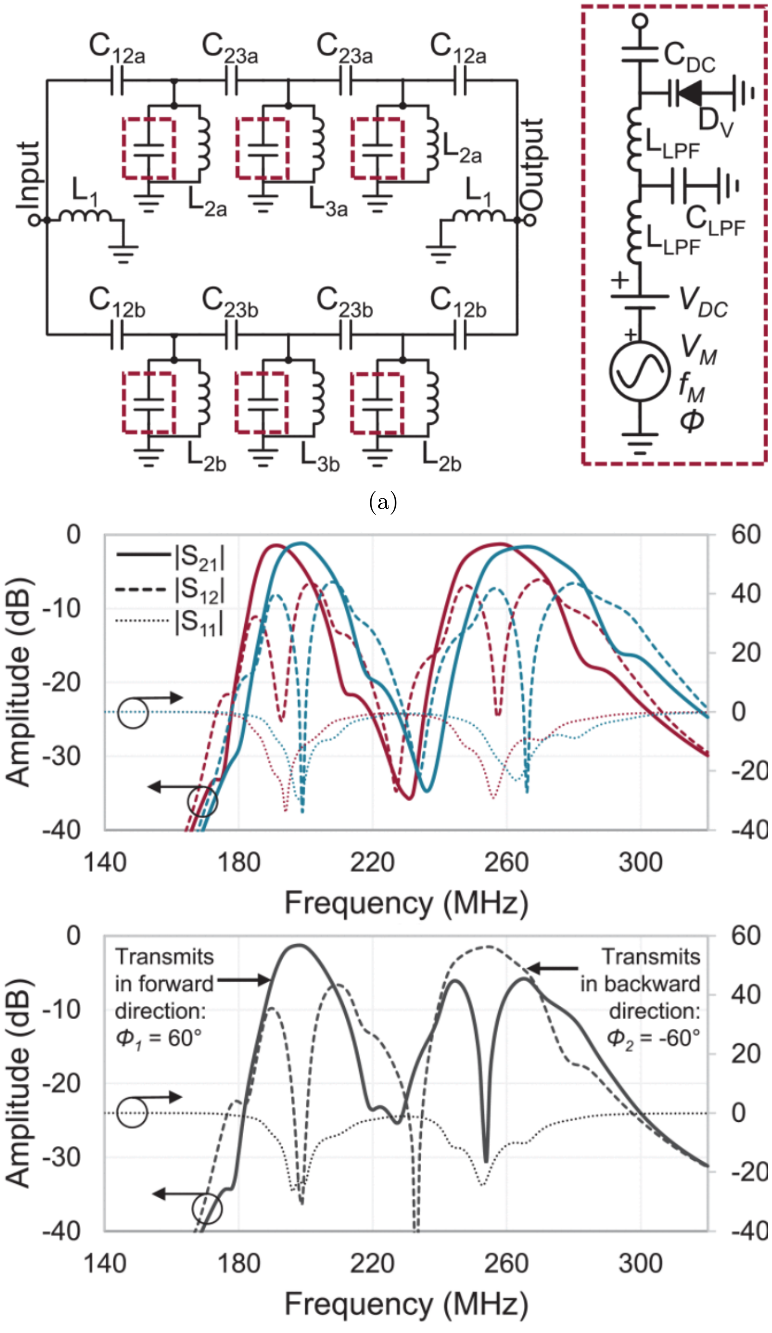

(a)

(b)

Figure 2.28: (a) Schematic of the proposed dual-band NR-BPF and (b) the corresponding response [12].

In sum, the recent literature, simulated comparisons, and mathematical analysis all corroborate the genesis of non-reciprocity in time-varying resonators owing to the incremental phase difference of the applied modulation signal. In addition to the incremental phase difference ($\Delta\phi$) and the effects of its variation, the other parameters that are equally important are the modulation index (ζ) and the modulation frequency (ω_m). With an increase in ζ from a nominal value, more energy is coupled to the higher order harmonics. As a result, the RL from the harmonics back to the fundamental frequency increases in both the ports, which in turn results in the degradation of IL in the forward direction while the isolation enhances in the reverse direction. Thus, a proper choice of $\Delta\phi$ is required to optimize the bandwidth and isolation of the filter, whereas that for the ζ results in optimization between the isolation and IL within the passband. The modulation frequency ω_m translates the reflected and transmitted wave to frequencies away from the fundamental frequency. A good response is obtained when the value of f_m is chosen such that $BW/2 < f_m < BW$. This indicates that the reflected energy from the first harmonics back to the fundamental frequency falls within the stopband of the filter. It is worthwhile to mention that the generated frequencies and their associated powers strictly adhere to the Manley-Rowe equations (eq. (2.1)). This implies that the power associated with the upconverted and downconverted signals depends on the frequency ω_m. Thus, the ω_m value needs to be properly optimized, not only in order to keep the reflected energy in the stopband, but also to maintain the power at the sum and difference frequencies, so as to obtain the IL within a reasonable limit.

2.4 Conclusion

Spatio-temporal non-reciprocal filters were reviewed and discussed in this paper. An extensive study was carried out starting from the parametric amplifier which serves as the key to understanding the spatio-temporal modulation followed by an analysis of time-varying transmission. These concepts serve as the prerequisites for the study of non-reciprocity in microwave filters. The role of synthesis and extraction of lumped components in the fabrication of filters was also discussed. The primary concept and the underlying cause of non-reciprocity was deciphered, followed by the responses of the filter networks and the recent technological advances in this field. Most of the notable work accomplished thus far in this field is on narrowband filters, leaving scope for broadband implementation in the near future. This domain, still relatively unexplored, leaves plenty of room for further research and development in the realization of cost-effective solutions with higher directivity and lower insertion loss which meet state-of-the-art technological demands.

2.5 Publications

1. **Prantik Dutta**, Gande Arun Kumar, Gopi Ram, ”Spatiotemporal Nonreciprocal Filters: Theoretical Concepts and Literature Review”, *IEEE Microwave Magazine* vol. 23, no. 6, pp. 85-101, June 2022, doi: 10.1109/MMM.2022.3157970.

Chapter 3

Theoretical Foundations of STM NR-BPFs

3.1 Introduction

This chapter provides a comprehensive exploration of the theoretical foundations underlying spatio-temporal modulated non-reciprocal bandpass filters (NR-BPFs). These filters play a crucial role in modern communication systems and signal processing, enabling efficient signal transmission and processing. The chapter begins by discussing the synthesis steps of reciprocal bandpass filters, starting with the formulation of the lowpass prototype (LPP) or g values and the generation of coupling matrix elements. It then delves into the theoretical origins of non-reciprocity, focusing on the underlying principles that govern the behavior of NR-BPFs. Finally, the chapter presents a numerical synthesis approach for designing direct-coupled NR-BPFs, combining theoretical insights with practical methods. By understanding the theoretical foundations and synthesis techniques, readers will gain the knowledge necessary to design and analyze NR-BPFs effectively.

3.2 Synthesis of LPP polynomials

Filter network synthesis starts from generating the elemental values of the lowpass prototype (LPP) model. The LPP model is then normalized in terms of frequency and impedance and terminated in equal-value resistors. By scaling the frequency and amplitude, filter networks can be derived for any desired frequency range and impedance levels. This simplifies the design of practical filters, regardless of their frequency range or physical realization.

The lowpass prototype filter used in this approach is normalized to a cutoff frequency of 1 rad/s and terminated in 1Ω resistors. The passband of this filter extends from $\omega = 0$ to $\omega = 1$, where ω represents angular frequency in rad/sec. For an ideal filter, achieving zero loss over the entire passband violates the causality condition. However, it is possible to have zero loss at certain frequencies called reflection zeros, where no power is reflected and the signal incurs no loss. These reflection zeros are confined to the passband of the filter function. The magnitude of the maximum reflected power over the passband is a design parameter for the filter prototype networks.

The use of lossless elements simplifies the synthesis process. Dissipation can be incorporated after the synthesis with minimal loss of accuracy, as long as the dissipation is small. Designing filters based on lossless prototype networks is suitable for various applications. This chapter focuses on the circuit theory approximation for designing lossless lowpass prototype filter functions. Fig. 3.1 shows a passive lossless 2 port network, in which the power transmitted to port 2 (P_T) can only be less than equal to the maximum power incident at port 1 (P_I) and the ratio of the two is given by $|T(s)|^2$ as given in (3.1), where $T(s)$ is termed as the transmission coefficient.

$$|T(s)|^2 = \frac{P_T}{P_1} = \frac{1}{1 + |K(s)|^2} \tag{3.1}$$

where $s = j\omega$ and $K(s)$ is the filter characteristic polynomial. Similarly, for lossless networks, the total reflected power and transmitted power sums up to unity. Thus, the reflected wave can

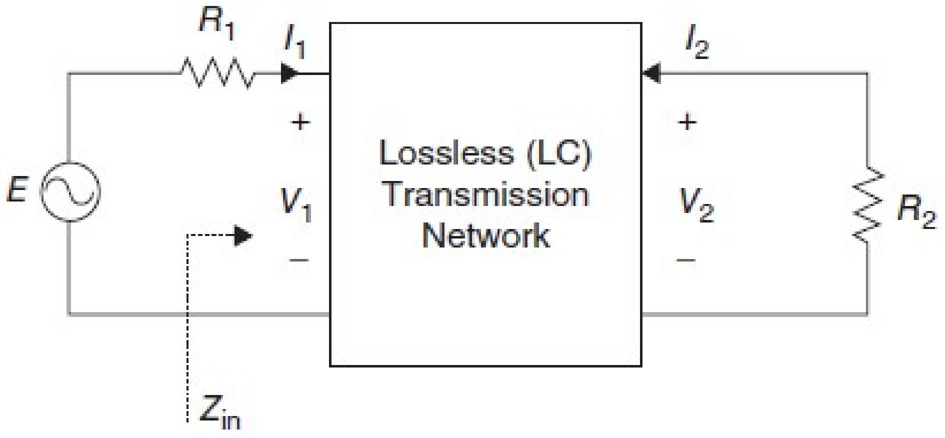

Figure 3.1: Block diagram of a conventional 2 port network [13].

be expressed in terms of reflection coefficient $R(s)$ and is given by (3.2).

$$|R(s)|^2 = \frac{|K(s)|^2}{1 + |K(s)|^2} \tag{3.2}$$

In the ω plane, the characteristic parameters insertion loss (IL) and return loss (RL) can be obtained from equations (3.1) and (3.2) and is given by

$$\begin{aligned} IL &= -20\log(T(j\omega)) \\ RL &= -20\log(R(j\omega)) \end{aligned} \tag{3.3}$$

As per the basic transmission line theory, the reflection coefficient $R(s)$ can be expressed in terms of the input impedance Z_{in} of the lossless network and the source impedance R_1, given in figure 3.1, and is given by (3.4).

$$R(s) = \frac{Z_{in}(s) - R_1}{Z_{in}(s) + R_1} = \frac{z_{in}(s) - 1}{z_{in}(s) + 1} = \frac{\frac{n(s)}{d(s)} - 1}{\frac{n(s)}{d(s)} + 1} \tag{3.4}$$

Therefore, the reflection coefficient can now be expressed in terms of numerator polynomial $F(s)$, also termed as the reflection polynomial, and denominator polynomials $E(s)$. Since, $s = j\omega$, the conjugate of these polynomials $F^*(s)$ and $E^*(s)$ are equivalent to $F(-s)$ and $E(-s)$, respectively. Thus, the reflected wave can be written as

$$|R(s)|^2 = \frac{F(s)F(-s)}{E(s)E(-s)} \tag{3.5}$$

Similarly, for lossless networks, the transmitted wave $T(s)$ can be represented as

$$|T(s)|^2 = \frac{E(s)E(-s) - F(s)F(-s)}{E(s)E(-s)} = \frac{P(s)P(-s)}{E(s)E(-s)} \tag{3.6}$$

The polynomials $F(s)$, $P(s)$, and $E(s)$ are the fundamental filter polynomials and can be synthesized according to the desired filter response. The roots of $F(s)$ form the reflection zeroes, while those of P(s) generate the transmission zeroes (TZs). From (3.1), the filter characteristic polynomial $K(s)$ can be written as

$$K(s) = \frac{P_I - P_T}{P_T} = \frac{P_R}{P_T} \tag{3.7}$$

where P_R stands for the reflected power and is equal to the difference between the incident and transmitted power for lossless networks. Again, from (3.1), a ripple factor (ϵ) is introduced to restrict the maximum amplitude to a specified value within a permissible bandwidth (conventionally unity) in the LPP model, also termed as the equiripple bandwidth. Thus (3.1) can be modified to (3.8) by substituting $\omega = 1$ in $s = j\omega$.

$$|T(j)|^2 = \frac{1}{1 + \epsilon^2 |K(j)|^2} \tag{3.8}$$

Thus, the ripple factor ϵ can be formulated as given in (3.9).

$$\epsilon = \sqrt{\frac{10^{IL_{s=j}/10} - 1}{|K(j)|^2}} \tag{3.9}$$

where $|T(j\omega)|^2 = 10^{-IL/10}$ can be obtained from (3.3). Thus, the characteristic polynomial $K(s)$ can now be written as

$$K(s) = \frac{\epsilon F(s)}{P(s)} \tag{3.10}$$

From (3.5), (3.6), and (3.9), the polynomial $E(s)$ can be written as

$$E(s)E(-s) = \frac{P(s)P(-s)}{\epsilon^2} - F(s)F(-s) \tag{3.11}$$

Since the polynomials $P(s)$ and $F(s)$ have their highest degree coefficients as unity, the highest degree coefficient of the polynomial $E(s)$ can also be made unity by introducing an extra term ϵ_R such that (3.12) is satisfied.

$$\frac{1}{\epsilon^2} + \frac{1}{\epsilon_R^2} = 1 \tag{3.12}$$

However, the concept of this extra parameter ϵ_R comes into the picture in canonical systems where the order of $P(s)$ is equal to that of $F(s)$; in most conventional filter designs, the degree of $P(s)$ is always less than the order of the filter. From (3.1), and by substituting (3.10) in place of $K(s)$, different types of filters can be synthesized. One class of filter prototype is the all-pole filter, where there are no transmission zeroes, that is $P(s) = 1$, and the response depends entirely on the $F(s)$ polynomial. One of the several forms of filter responses is termed the Butterworth response where $F(s) = s^n$, also termed as the maximally flat response, and has all the reflection zeroes at the origin position. Another widely used response shape is the Chebyshev response, where the polynomial $F(s)$ takes the form as given in (3.13).

$$F(s) = s^m(s^2 + p^2)(s^2 + q^2)... \tag{3.13}$$

where the values of p and q are determined by the Chebyshev polynomial and m is generally chosen to be unity, that is, there is a single TZ at the origin. For this case, the characteristic polynomial $K(j\omega)$ takes the Chebyshev polynomial form and is given by (3.14).

$$|K(j\omega)|^2 = \epsilon^2 T_n^2\left(\frac{\omega}{\omega_c}\right) \tag{3.14}$$

where $T_n(x) = \cos(n\cos^{-1}x)$ is the Chebyshev polynomial and can be constructed by a recursive method given by (3.15) starting from $T_0(x) = 1$ and $T_1(x) = x$. It is worthwhile mentioning that a conversion from $(x \rightarrow \frac{s}{j})$ needs to be implemented to get the characteristic polynomials in the complex frequency domain.

$$T_{n+1}(x) = 2xT_n(x) - T_{n-1}(x). \tag{3.15}$$

3.2.1 Chebyshev polynomial synthesis

For enhancing the comprehensibility of the polynomial synthesis, the domain of analysis is shifted to the ω plane. For a two-port lossless non-canonical network ($\epsilon_r = 0$), the transfer function S_{21}, reflection function S_{11}, and the ripple factor ϵ can be expressed as

$$\begin{aligned} S_{11}(\omega) &= \frac{F(\omega)}{E(\omega)} \\ S_{21}(\omega) &= \frac{P(\omega)}{\epsilon E(\omega)} \\ \epsilon &= \frac{1}{\sqrt{10^{RL/10}-1}}\left|\frac{P(\omega}{F(\omega)}\right|_{\omega=\pm 1} \end{aligned} \tag{3.16}$$

From (3.16), it can be deduced that

$$S_{21}(\omega)S_{21}^*(\omega) = \frac{P(\omega)P^*(\omega)}{\epsilon^2 E(\omega)E^*(\omega)} \tag{3.17}$$

Again, from the point of lossless networks ($S_{11}^2 + S_{21}^2 = 1$), $\epsilon^2 E(\omega)E^*(\omega)$ can be written as

$$\epsilon^2 E(\omega)E^*(\omega) = epsilon^2 F(\omega)F^*(\omega) + P(\omega)P^*(\omega) \tag{3.18}$$

Substituting (3.18) into (3.17), we get

$$S_{21}(\omega)S_{21}^*(\omega) = \frac{1}{[1 - j\epsilon C_N(\omega)]\left[1 + j\epsilon C_N^*(\omega)\right]} \tag{3.19}$$

where $C_N(\omega)$ is termed as the filtering polynomial of degree N and is the ratio of the reflection and transmission polynomial given by (3.20). Interestingly, its poles are the roots of the transmission polynomial $P(\omega)$, while its zeroes are those of the reflection polynomial $F(\omega)$.

$$C_N(\omega) = \frac{F(\omega)}{P(\omega)} \tag{3.20}$$

3.2.2 Recursive technique for polynomial synthesis

The generalized Chebyshev filtering polynomial $C_N(\omega)$ can be expressed as

$$\begin{aligned} C_N(\omega) &= \cosh\left[\sum_{n=1}^{N}\cosh^{-1}(x_n(\omega))\right] \text{ for } |\omega| \geq 1 \\ C_N(\omega) &= \cos\left[\sum_{n=1}^{N}\cos^{-1}(x_n(\omega))\right] \text{ for } |\omega| \leq 1 \end{aligned} \tag{3.21}$$

where $x_n(\omega)$ can be expressed in terms of the desired transmission zeroes, as given in (3.22).

$$x_n(\omega) = \frac{\omega - 1/\omega_{TZn}}{1 - \omega/\omega_{TZn}} \tag{3.22}$$

The recursive technique efficiently computes the numerator coefficients of $C_N(\omega)$, where the n^{th} degree polynomials are built from the preceding $(n-1)^{th}$ degree polynomial. The sequential steps for the recursive technique is given below.

Step 1: The order of the filter (N), desired return loss (RL), and m number of normalized transmission zeroes (TZs) are taken as inputs, where m is less than the order of the filter (N).

Step 2: The TZs are arranged in ascending order in an array M and the remaining $N - m$ positions are filled with ∞ values. Interestingly, if no TZs are specified, then an N^{th} dimensional array is filled with ∞.

Step 3: The variables are initialized:

- X is set to $1/M(1)$.
- Y is calculated as the square root of $1 - X^2$.
- $U(1)$ is set to $-X$.
- $U(2)$ is set to 1.
- $V(1)$ is set to Y.
- $V(2)$ is set to 0.

Step 4: A loop is run from $K = 3$ to $N + 1$:

- X is set to $(1/M(K-1))$.
- Y is calculated as the square root of $(1 - X^2)$.
- $U_2(K)$ and $V_2(K)$ are initialized to 0.
- A nested loop is performed from $J = 1$ to $K - 1$:

  - $U_2(J)$ is set to $-U(J) \times (X - Y) \times V(J)$.
  - $V_2(J)$ is set to $-V(J) \times (X + Y) \times U(J)$.
- Another nested loop is performed from $J = 2$ to K:
  - $U(J - 1)$ is added to $U_2(J)$.
  - $V(J - 1)$ is added to $V_2(J)$.
- Another loop is performed from $J = 3$ to K:
  - Add $Y \times V(J - 2)$ to $U_2(J)$.
- A loop is run from $J = 1$ to K:
  - $U(J)$ is set to $U_2(J)$.
  - $V(J)$ is set to $V_2(J)$.

Step 5: The above steps are repeated until the loop finishes for $K = N + 1$.

After successfully running the algorithm, the roots of $U_N(\omega)$ yields the N in-band reflection zeroes of the reflection polynomial $F(\omega)$, while the roots of $V_N(\omega)$ generate the $N - 1$ in-band reflection maxima. Additionally, from $P(\omega)$, the polynomial $E(\omega)$ and ϵ can also be calculated.

While the recursive technique directly computes the polynomials for any ordered filter even with transmission zeroes, its sometimes beneficial to calculate the g or LPP values directly from the Chebyshev polynomials to construct all-pole filter responses.

3.2.3 Calculation of g values of all-pole Chebyshev prototype

The g values corresponding to m^{th} degree filter with an equiripple level of ERL is given by

$$\begin{aligned}
g_0 &= 1 \\
\beta &= \ln\left(\coth\left(\frac{ERL}{17.37}\right)\right) \\
\gamma &= \sinh(\frac{\beta}{2m}) \\
a_i &= \sin\left[\frac{(2k-1)\pi}{2m}\right], \quad i = 1, 2, \ldots, n \\
b_i &= \gamma^2 + \sin^2\left(\frac{i\pi}{m}\right), \quad i = 1, 2, \ldots, n \\
g_1 &= \frac{2a_1}{\gamma} \\
g_i &= \frac{4a_{i-1}a_i}{b_{i-1}g_{i-1}} \quad i = 1, 2, \ldots, n \\
g_{n+1} &= \begin{cases} 1 & \text{if } n \text{ is odd} \\ \coth^2\left(\frac{\beta}{4}\right) & \text{if } n \text{ is even} \end{cases}
\end{aligned} \tag{3.23}$$

While these g values can directly be used to calculate the LPP circuit elements as well as direct-coupled filter networks with admittance inverters, they can also be used to form the coupling matrix elemental values.

3.2.4 Construction of direct-coupled bandpass filters from g values

Each section of resonators in the filter system is characterized by its own impedance, denoted as Z_R. The value of Z_R is typically determined by the selected inductor and can span a wide range of values. It is common for each resonator to exhibit a unique characteristic impedance.

The filter is connected to a source and load impedance, represented as Z_S and Z_L, respectively. While the standard value for these impedances is 50 Ω, they can be customized to suit specific requirements. Matching networks are employed to transform the resonator impedances to the source and load impedance. These networks often take the form of simple two-element L circuits, akin to designs made on a Smith Chart for achieving impedance transformation. For instance, they can facilitate a transition from 150 Ω to 50 Ω.

Between the resonator sections, inverters are employed, as shown in Fig. 3.2. The fundamental concept is to select a circuit that provides a 90° phase shift, which can be achieved through various circuit designs. The component values are then chosen to establish the impedance as $\sqrt{Z_1 \cdot Z_2}$. One of the simplest examples of an inverter is a 90° transmission line with a characteristic impedance equal to $\sqrt{Z_1 \cdot Z_2}$. To start with, either a suitable inductor or capacitor value is chosen for the k^{th} resonator (say L_k or C_k). Next, the impedance Z_k is calculated and is given by

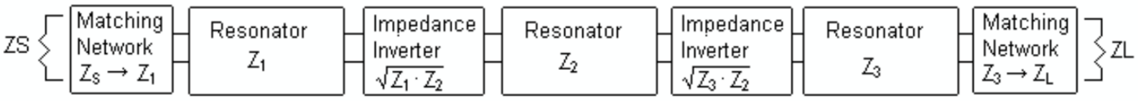

Figure 3.2: Topology of a three-pole direct-coupled BPF

$$Z_k = \frac{f_0 \cdot g_k \cdot \omega \cdot L_k}{BW} = \frac{f_0 \cdot g_k}{\omega \cdot C_k \cdot BW} \tag{3.24}$$

where f_0 is the center frequency, BW is the bandwidth, and g_k is the k^{th} elemental value. Now, the inter-resonator capacitor values coupling k^{th} and $k+1^{th}$ can be obtained by

$$C_{k,k+1} = \frac{1}{\sqrt{Z_k Z_{k+1}}\omega} \tag{3.25}$$

Similarly, the values of the series capacitors (C_{series}) and shunt capacitors (C_{shunt}) at the source and load ends are given by

$$C_{series} = \frac{1}{R_s\omega\sqrt{\frac{Z_1}{R_S}-1}} \tag{3.26}$$

$$C_{shunt} = \frac{\sqrt{\frac{Z_1}{R_S}-1}}{\omega Z_1} \tag{3.27}$$

Thus, the overall capacitances of the resonators are reduced from their original values to take into consideration the additional negative capacitances generated by these coupling capacitors as shown in Fig. 3.3.

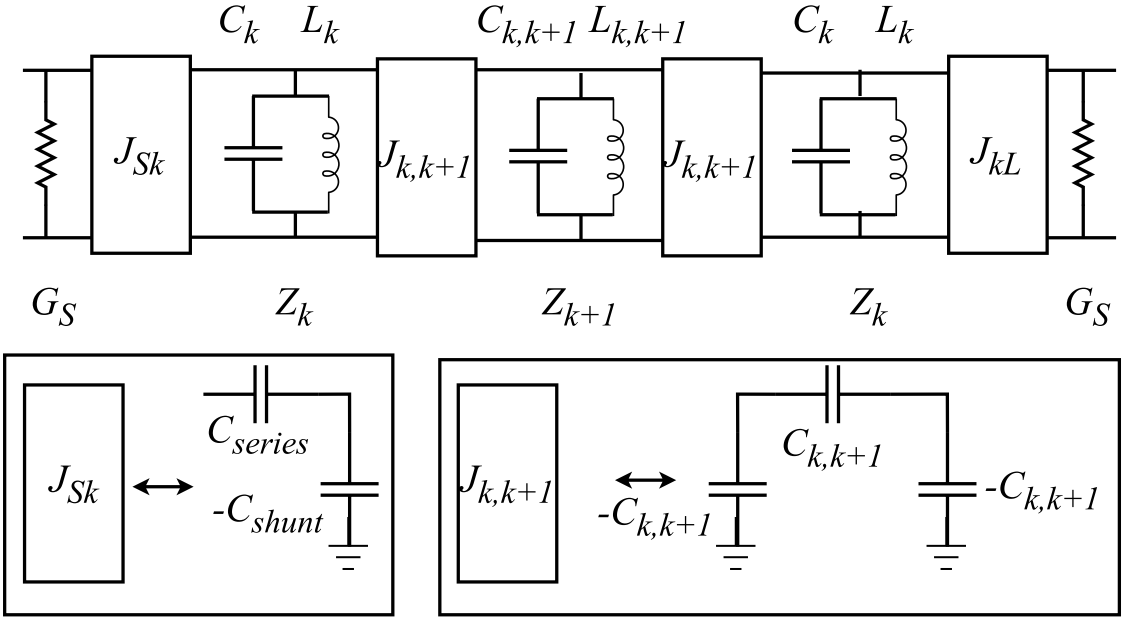

Figure 3.3: Schematic of Direct-coupled bandpass resonators coupled with admittance inverters.

Additionally, the admittance inverter values can be extracted from the circuit parameters to further delve into numerical analysis, as given by (??).

$$\begin{aligned} J_{sk} &= \sqrt{\frac{C_k Gs}{g_k}} \\ J_{12} &= \sqrt{\frac{C_k C_{k+1}}{g_k g_{k+1}}} \end{aligned} \tag{3.28}$$

It is worthwhile mentioning that for numerical analysis purpose, the ABCD parameters of the admittance inverters are given by (3.29).

$$J_{ABCD} = \begin{bmatrix} 0 & \pm\dfrac{1}{jJ} \\ \mp jJ & 0 \end{bmatrix} \tag{3.29}$$

3.2.5 g values to coupling matrix representation

On a similar note, for an $N \times N$ coupling matrix, the coupling coefficients can directly be formulated from the g values as shown below.

$$M_{i,i+1} = \frac{1}{\sqrt{g_j g_{j+1}}}, \quad i = 1, 2, \ldots, N-1 \tag{3.30}$$

$$R_1 = \frac{1}{g_0 \cdot g_1}, \quad R_N = \frac{1}{g_N \cdot g_{N+1}} \tag{3.31}$$

3.3 Prerequisites to the concept of Non-reciprocity

To ensure a comprehensive understanding of the theory, the prerequisites, already covered in Chapter 2, are presented here to provide illustrations and explanations of the underlying concepts that serve as milestones in the development of non-reciprocity.

3.3.1 The Parametric Amplifier

Any amplifier can be considered to be a modulator in which the energy of the input wave is transformed to the load impedance by harnessing the energy from the amplifier's energy source. The amplifier's energy source can be either a DC or an AC supply. For a DC source, the amplified output waveform is an exact replica of the input waveform with the amplifier's energy source providing the useful gain. However, for an AC source, the output is not an exact replica of the input. In fact, the frequency of the output waveform is transformed owing to the generation of new frequencies due to the interaction of two waves of different frequencies. The spectral content of the output waveform contains an infinite number of transformed frequencies. These frequencies, denoted as $f_{y,z}$, where y and z are positive, negative, or zero integers, are harmonically related to the input wave frequency (f_0) and the frequency of the modulator's energy source (f_m) - also termed the local oscillator ($f_{y,z} = yf_0 + zf_m$). This energy conversion from one frequency component to another is governed by general power relations first described by J. M. Manley and H. E. Rowe [37] which are popularly known as the Manley-Rowe relations. These relations consist of two independent equations which govern nonlinear reactance modulators provided the nonlinear characteristic of the element (capacitor or inductor) is single-valued. These equations relate the power at different frequencies obtained after harmonic mixing of the input signal frequency and the local oscillator or modulation frequency. By expanding the charge q and flux linkage ψ for the capacitor and inductor respectively in terms of a Fourier series, the Manley-Rowe equations relating the average power flowing into the nonlinear element, $W_{y,z}$, at the harmonic frequencies $f_{y,z}$ with the individual components f_0 and f_m can be expressed as shown in (3.32).

$$\begin{aligned}\sum_{y=0}^{\infty}\sum_{z=-\infty}^{\infty}\frac{yW_{y,z}}{yf_0+zf_m}&=0\\ \sum_{y=-\infty}^{\infty}\sum_{z=0}^{\infty}\frac{yW_{y,z}}{yf_0+zf_m}&=0\end{aligned}\tag{3.32}$$

For a linear capacitor or inductor, without mixing terms, only two frequency components will be present, that is, either f_0 or f_m and $W_{y,z}=0$ for all y and z, proving that (3.32) is satisfied. Any circuit analysis that includes nonlinear reactance should be checked with (3.32) to ensure good gain and stability.

Remarkable results can be obtained from (3.32). If the circuit is designed to allow only the current of harmonic frequency f_0+f_m, denoted as sum frequency f_s with associated power, then W_s is allowed to be present in addition to the individual frequencies f_0 and f_m, and equation (3.32) gives

$$\begin{aligned}\frac{W_m}{f_m}+\frac{W_s}{f_s}&=0\\ \frac{W_0}{f_0}+\frac{W_s}{f_s}&=0\end{aligned}\tag{3.33}$$

where W_0 is the power of the signal source and W_m is that of the power entering the nonlinear element from the local oscillator. Since power is supplied by the currents of frequencies f_0 and f_m, therefore W_0 and W_m are positive whereas W_s is negative, since power is being delivered at the frequency f_0+f_m. Therefore, (3.33) can be rearranged as

$$-\frac{W_s}{W_0}=1+\frac{f_m}{f_0}\tag{3.34}$$

Thus, a gain at the sum frequency ($f_s=yf_0+zf_m$) with respect to the signal frequency is obtained, and this type of amplifier is known as a parametric up-converter. The order of the modulation product is the sum of the integer values y and z [52]. An even more interesting result is obtained if, instead of the sum frequency, a difference frequency $f_d=f_m-f_0$ is allowed to flow. If the power delivered to the frequency component is W_d, then the Manley-Rowe equations for such a circuit turn out to be

$$\frac{W_m}{f_m}+\frac{W_d}{f_d}=0\tag{3.35a}$$

$$\frac{W_0}{f_0}-\frac{W_d}{f_d}=0\tag{3.35b}$$

From (3.35a), it can be seen that the local oscillator supplies energy to the nonlinear reactance; therefore, the power at the difference frequency is negative. This is because power is being delivered by the nonlinear reactance at the difference frequency. Consequently, from (3.35b), the power at the RF frequency W_0 should be negative. Thus, for this case, the nonlinear reactance offers a negative resistance to the RF signal source. This results in the abstraction of power from the local oscillator and this power is delivered to both the signal source and the signal generated with the difference frequency. This negative resistance creates an instability. The magnitude of the gain in this case is equivalent to that obtained in (3.34). If the external resistance to the difference frequency is now reduced from a large value, the total signal circuit resistance could approach zero. Under this condition, the external signal source can be removed and the three components, comprising the signal, the modulation, and the difference frequency (f_d), will continue to flow, resulting in free oscillations. This has been experimentally demonstrated in [53], where, the reduction in external resistance facilitated the production of sustained oscillations. The circuit operating under this condition is called a negative resistance parametric amplifier.

A magnetic modulator has been demonstrated in [38]. It is shown that for the simplest modulation containing only a single magnetic modulator, the sum frequency introduces a positive resistance while the difference frequency introduces a negative resistance in the signal path. In the carrier or the local oscillator path, both of the frequencies introduce positive resistance. The same phenomenon occurs in case of a variable capacitor circuit [39, 40]. Thus, for any nonlinear reactance, the flow of current comprising the difference frequency causes abstraction of energy from the carrier (f_m) that is delivered to the signal (f_0) while that of the sum frequency results in abstraction of energy from both the carrier and the signal.

3.3.2 Spatio-temporally modulated (STM) transmission line

From parametric amplifier theory, it is clear that nonlinear or time-varying reactance leads to mixing of harmonic frequencies, resulting in the generation of intermodulation (IM) products. The IM products strictly follow the Manley-Rowe equations, provided the reactance is single-valued. One of the application-specific domains of this frequency-mixing behavior is the manifestation of spatio-temporally modulated (STM) non-reciprocal bandpass filters without using bulky ferrite components. The concept relies on time-varying transmission line in which varactor diodes are loaded along the length of the transmission line has been proposed in [2] and is shown in Fig. 3.4.

The modified telegrapher's equation [45] for TVTL using time-varying capacitance is given by

$$\begin{aligned}\frac{\partial v(z,t)}{\partial z} &= -L\frac{\partial i(z,t)}{\partial t}\\ \frac{\partial i(z,t)}{\partial z} &= -\frac{\partial[C(z,t)v(z,t)]}{\partial t}\end{aligned} \tag{3.36}$$

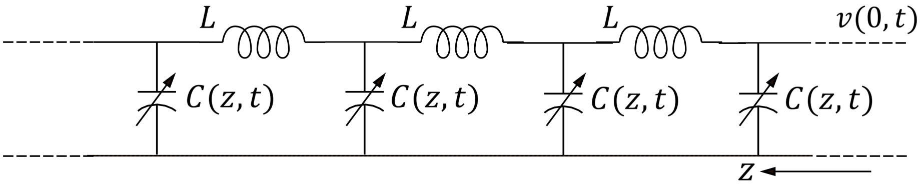

Figure 3.4: Time-varying transmission line integrated with spatio-temporally modulated capacitance per unit length [2].

where L is the inductance per unit length and $C(z, t)$ denotes the time-varying capacitance per unit length. The time-varying capacitance $C(z, t)$ is usually implemented using a varactor diode, which is nothing but a voltage controlled capacitor where the reverse bias applied across the varactor changes the capacitance. In fact, the capacitance decreases with the applied reverse bias. So, an AC voltage applied across the varactor results in a corresponding variation in the capacitance which can be expressed by

$$C(z, t) = C_0 + \Delta C cos(\omega_m t - \beta_m z + \phi) \tag{3.37}$$

where C_0 denotes the mean capacitance per unit length and the second part of (3.37) corresponds to the capacitance due to the applied reverse bias ac voltage across the varactor where ΔC is the amplitude variation per unit length of the capacitance due to the reverse bias, ω_m is the angular frequency, and β_m is the phase constant.

Time-varying transmission line finds wide application not only in the generation of non-reciprocal components like isolators and circulators but its unique feature of allowing propagation only in the direction of the carrier signal, can be well utilized in the design of non-reciprocal filters, as was demonstrated for the first time in [1].

3.4 Analysis of Spatio-Temporal Transmission Lines

In the previous sections, parametric amplification, frequency mixing, and non-reciprocal behavior in time-varying transmission lines using STM were explained. Based on these properties of a TVTL, a filter in the forward direction with isolation in the backward direction has been demonstrated in [1].

A linear time-varying (LTV) transmission line is shown in Fig. 3.5((a)). The time-varying shunt capacitor $C(t)$, which can be implemented using the varactor diode, happens to be the primary underlying cause of non-reciprocity (which will be explored in due course). If, in place of a single time-varying element, multiple time-varying elements are added along the transmission line, as shown in Fig. 3.5((b)), with each modulated by sinusoidal signals with progressive phase shifts, then the phenomenon is termed spatio-temporal modulation since the time-varying elements are separated in space as well as being time modulated with different phase angles.

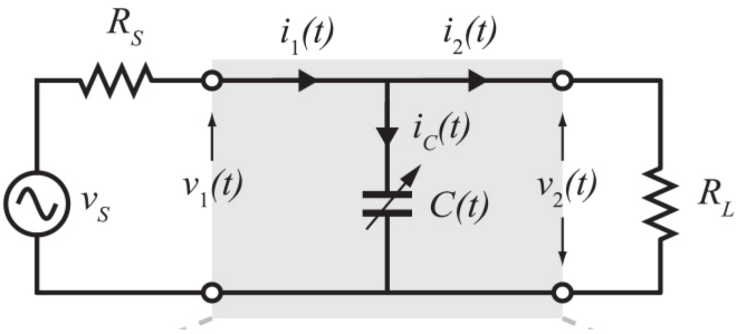

(a) a

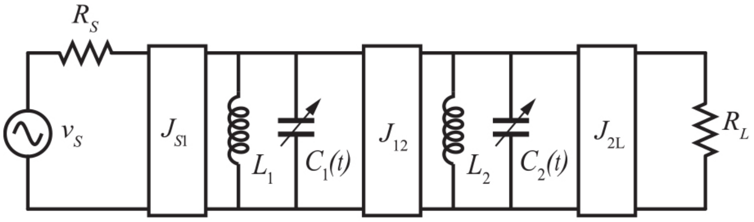

(b) b

Figure 3.5: (a) Simple linear time-varying circuit with a single shunt capacitor modulated by a sinusoidal signal. (b) Generalized circuit topology of a 2^{nd}-order spatio-temporally modulated filter [1].

Since the STM transmission line deals with the harmonics of the signal frequency ω and the modulation frequency ω_m, the analysis should be transformed from the time domain to the frequency domain using Fourier analysis [54]. The time harmonic capacitance variation is given in (3.37). For our analysis, the spatial part ($\beta_m z$) is ignored and a new term ζ is introduced which is given by $\zeta = \frac{\Delta C}{C_0}$. Kirchhoff's law applied to the network in Fig. 3.5((a)) gives

$$v_1(t) = v_2(t) \tag{3.38a}$$

$$i_1(t) = j\omega C(t) v_2(t) + i_2(t) \tag{3.38b}$$

Substituting only the time-varying portion of $C(t)$ from (3.37) and applying a Fourier transform to the equation set (3.38), it can be shown that

$$V_1(\omega) = V_2(\omega) \tag{3.39a}$$

$$I_1(\omega) = j\omega C_0 V_2(\omega) + j\omega \frac{\Delta C}{2} [V_2(\omega - \omega_m) e^{j\phi} + V_2(\omega + \omega_m) e^{-j\phi}] + I_2(\omega) \tag{3.39b}$$

Likewise, multiplying $e^{\pm j\omega_m t}$ to both sides of eq. (3.38) and then applying fourier transform in a similar manner, the other harmonic products, also known as intermodulation (IM) products, are obtained shown below.

$$V_1(\omega \pm \omega_m) = V_2(\omega \pm \omega_m) \tag{3.40a}$$

$$\begin{aligned} I_1(\omega+\omega_m) = {} & j(\omega+\omega_m)C_0V_2(\omega+\omega_m) \\ & + j(\omega+\omega_m)\frac{\Delta C}{2}[V_2(\omega)e^{j\phi} + V_2(\omega+2\omega_m)e^{-j\phi}] \\ & + I_2(\omega+\omega_m) \end{aligned} \tag{3.40b}$$

$$\begin{aligned} I_1(\omega-\omega_m) = {} & j(\omega-\omega_m)C_0V_2(\omega-\omega_m) \\ & + j(\omega-\omega_m)\frac{\Delta C}{2}[V_2(\omega-2\omega_m)e^{j\phi} + V_2(\omega)e^{-j\phi}] \\ & + I_2(\omega-\omega_m) \end{aligned} \tag{3.40c}$$

Similar expressions can be obtained at even higher order harmonics from equation (3.39) and can be integrated into a spectral admittance matrix [55] as given in [1]. When an LC resonator with an FIR element is used in place of the time variant capacitor alone, extra $1/j\omega L$ and jB terms are added to the admittance matrix. For the bandpass prototype, the admittance of a resonator comprising the unmodulated capacitance of the varactor C_0, the inductor L, and a FIR element B at the n^{th} IM product is denoted in (3.41)

$$Y_q^{(n)} = jC_0(\omega+n\omega_m) + \frac{1}{jL(\omega+n\omega_m)} + jB \tag{3.41}$$

If additionally two terms $P^{(p)}$ and $Q^{(p)}$ corresponding to the p^{th} resonator are defined as

$$P^{(p)} = \frac{\zeta}{2}e^{-j\phi_p} \tag{3.42a}$$

$$Q^{(p)} = \frac{\zeta}{2}e^{j\phi_p} \tag{3.42b}$$

the spectral admittance matrix of the p^{th} resonator is given by (3.43). In terms of Fourier series representation, the modulation of the varactor generates an infinite number of IM products $(\omega \pm n\omega_m)$, but only a limited range of IM products will suffice.

$$\mathbf{Y}_r^{(p)} = \begin{bmatrix} Y_q^{(-2)}+jB_p & jP^{(p)}(\omega-2\omega_m) & 0 & 0 & 0 \\ jQ^{(p)}(\omega-\omega_m) & Y_q^{(-1)}+jB_p & jP^{(p)}(\omega-\omega_m) & 0 & 0 \\ 0 & jQ^{(p)}\omega & Y_q^{(0)}+jB_p & jP^{(p)}\omega & 0 \\ 0 & 0 & jQ^{(p)}(\omega+\omega_m) & Y_q^{(+1)}+jB_p & jP^{(p)}(\omega+\omega_m) \\ 0 & 0 & 0 & jQ^{(p)}(\omega+2\omega_m) & Y_q^{(+2)}+jB_p \end{bmatrix} \tag{3.43}$$

In the matrix shown in (3.43), IM products only up to $n = \pm 2$ are considered for analysis. Apart from the center element of the matrix, the other diagonal elements depict the new resonators formed due to the generated IM products, while the off-diagonal elements represent the couplings between the different harmonic components of the same resonator [5]. A closer

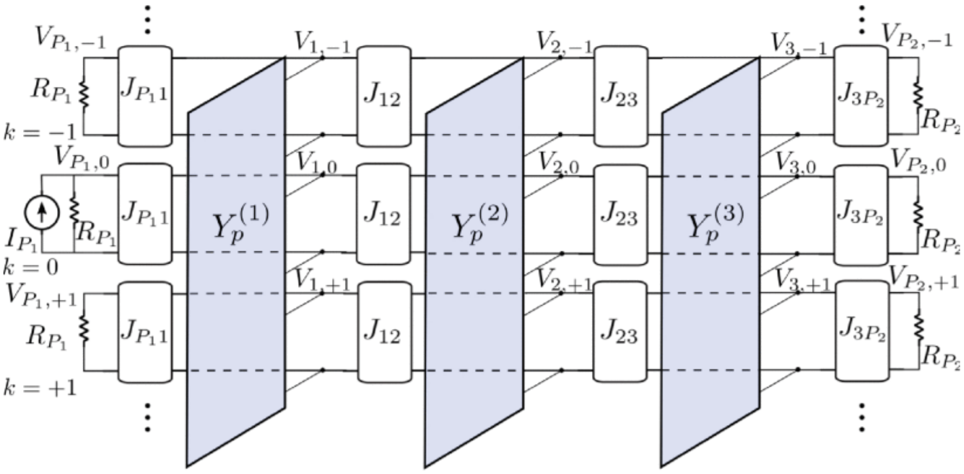

Figure 3.6: Equivalent circuit transformed from the basic coupled resonator circuit showing the generated nonlinear harmonics [5].

look into the matrix in (3.43) shows that the matrix is not symmetric. This implies that apart from the mainline couplings (the J inverters), the couplings between the harmonic resonators are related by a non-reciprocal admittance inverter which, for a coupling between two different harmonics $(n-1)$ and n for a resonator p, is given by

$$J_p^{(n,n-1)} = Q^{(p)}[\omega + n\omega_m] \tag{3.44a}$$

$$J_p^{(n-1,n)} = P^{(p)}[\omega + (n-1)\omega_m] \tag{3.44b}$$

The first equation of (3.44) represents an up-conversion from the $(n-1)^{th}$ to the n^{th} harmonic while the second one represents the down-conversion. The equivalent circuit of the spectral admittance matrix is shown in Fig. 3.6.

On the basis of equations (3.43) and (3.44), a coupling topology has been framed in [5], which delves deeper into the underlying cause of non-reciprocity. In the coupling topology, the mainline $J_{i,i+1}$ inverters couple the different resonators within the same harmonics (ω or $\omega \pm k\omega_m$), but the inverters of equation (3.44) show the coupling between contiguous harmonic components of the same resonator. Since these couplings between the adjacent nonlinear harmonics are non-reciprocal, the response of the system is also non-reciprocal [56]. It is clear that the phase terms associated with these couplings between adjacent nonlinear harmonics (eq. (3.44)) are the underlying cause of non-reciprocity.

Fig. 3.7(a) and (c) represent the traveling of electromagnetic waves to and from port 1 and port 2 only through the resonators and the mainline couplings. This traveling wave does not encounter any phase differences as is evident from the fact that there are no phase terms linked with the diagonal elements in the admittance matrix shown in (3.43). This indicates that, without modulation, there is no non-reciprocity. Now, if Fig. 3.7(b) and (d) are observed, they show the traveling of electromagnetic waves through the nonlinear harmonic resonators

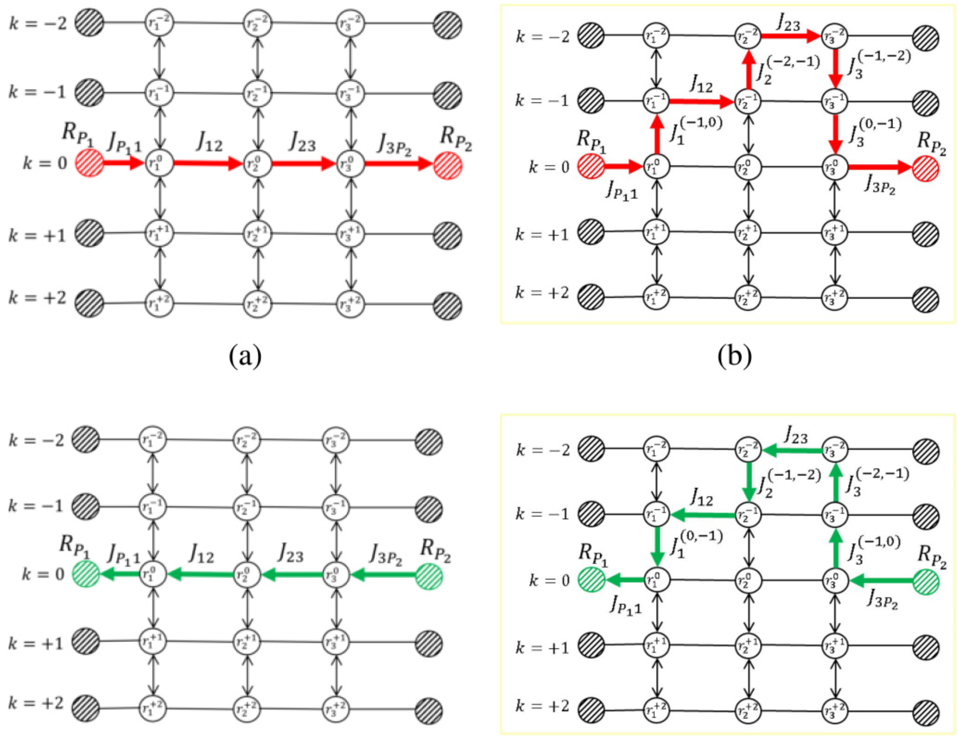

(a) (b)

(c) (d)

Figure 3.7: Different paths for the EM waves to traverse from (a) and (b) port 1 to 2 and (c) and (d) port 2 to 1 shown in the coupling topology in [5].

generated due to the modulation of the capacitor. If the phase difference between the resonators is considered as $\Delta\phi$ and the phase of the first resonator as $\phi_1 = 0°$, then the total phase difference encountered by the wave in the forward direction is $+\phi_1 + \phi_2 - 2\phi_3 = -135°$ and that in the backward direction is $-\phi_1 - \phi_2 + 2\phi_3 = 135°$. The phase difference between the forward and backward traveling wave is 90°, thus explaining the concept of non-reciprocity. Alternately, if the $ABCD$ parameters of the 2-pole filter shown in [1] are found to be

$$AD - BC = \frac{{C_0}^2\,{\omega_1}^2 - {J_{12}}^2 + \frac{{C_0}^2\,\zeta^2\,(\omega-\omega_m)\,\omega\,\mathrm{e}^{-j\Delta\phi}}{4} + \frac{{C_0}^2\,\zeta^2\,(\omega+\omega_m)\,w\,\mathrm{e}^{j\Delta\phi}}{4}}{{J_{12}}^2} + j\,\frac{{C_0}^2\,\mathrm{J}_{S1}\,{\omega_1}^2}{J_{12}}$$
$$+\,j\,\frac{{C_0}^2\,\mathrm{J}_{S1}\,\zeta^2\,(\omega-\omega_m)\,\omega\,\mathrm{e}^{-j\Delta\phi}}{4\,J_{12}} + j\,\frac{{C_0}^2\,\mathrm{J}_{S1}\,\zeta^2\,(\omega+\omega_m)\,\omega\,\mathrm{e}^{j\Delta\phi}}{4\,J_{12}} \tag{3.45}$$

where $\omega_1 = \omega - \frac{1}{\omega L C_0}$. When there is no modulation, $\zeta = 0$ and at the center frequency, $\omega_0 = \frac{1}{\sqrt{LC_0}}$ and thus ω_1 turns out to be zero. Then the $AD - BC$ of (3.45) becomes

$$AD - BC = 1 \tag{3.46}$$

Thus, mathematical analysis proves that the modulation frequency ω_m and modulation index ζ, along with the phase difference between the resonators $\Delta\phi$, generate the non-reciprocity in these spatio-temporal circuits. Although this analysis relies on the manifestation of non-reciprocity by the time-varying circuits, the underlying cause of the phenomenon remains somewhat unclear.

3.4.1 Initialization of Circuit Parameters

The initial values of the circuit parameters ζ, f_m, and $\Delta\phi$ are chosen so as to maintain a tradeoff between the insertion loss (IL) and isolation at the center frequency. It has been observed from the parametric studies of the non-reciprocal response that the strongest isolation is achieved when the modulation frequency (f_m) is approximately equal to the equiripple bandwidth of the filter. A stronger isolation at the center frequency can be achieved by increasing f_m, but at the cost of degraded IL. As far as the modulation index is concerned, the lower the value of ζ, the better the IL. This is quite obvious as a lower ζ indicates a low capacitance deviation, which tends more to the static response generation. From parametric study, as will be visible later, the degradation in IL is proportional to the ζ value. Additionally, the isolation at center frequency reaches almost maximum when ζ is almost equal to 0.3. This can be explained by closely observing the resonant frequency variation pattern $f = 1/\sqrt{(L(C_0 \pm \Delta C))}$ with respect to the deviation of the capacitance ΔC from the nominal value C_0, which happens to be falling at the band edges of the passband for $\zeta = 0.3$. An increment of ζ value beyond a certain level would result in a RF signal power scattering significantly away from the passband, thereby leading to a considerably higher IL. Thus, the AC amplitude and the DC offset of the sinusoidal signal applied to the varactor diode to manifest the deviation in capacitance and the nominal capacitance, respectively, must comply with the desired ζ value to obtain the non-reciprocal response. Owing to the odd symmetry of S_{21} and S_{12} with respect to $\phi = 180^\circ$ as is evident from (3.42) and (3.43), a progressive phase shift of either 0° or 180° would result in a static response. However, a range of values between them would result in the nonuniform RF energy scattering among the harmonics in opposite directions and, in turn, generate an isolating filter response. A decent value of 40° to 60° maintains a good tradeoff between the IL and isolation bandwidth.

3.5 Direct-coupled NR-BPF numerical simulation algorithm

The numerical simulation of a n^{th} order (over here 3^{rd} order is chosen for ease of comprehension) direct-coupled NR-BPFs starts from choosing the elemental values L or C_0 and obtaining the admittance inverter values for the desired specifications in terms of the center frequency (f_0), return loss (RL), and the fractional bandwidth of the filter structure. The spectral ABCD parameters for the 3^{rd} order filter is given by (3.47), which is obtained by cascaded multiplication of the ABCD parameters of the constituent admittance inverters, given by (3.29) multiplied by a unitary matrix of the order equal to the number of harmonic generators considered, and the spectral admittance matrices of the individual LC resonators, given by (3.43).

$$
\begin{aligned}
A &= \frac{J_{3L} \cdot J_{12}^2 \cdot \mathbf{U} + J_{3L} \cdot Y_{LC_1} \cdot Y_{LC_2}}{J_{S1} \cdot J_{12} \cdot J_{23}} \\
B &= \frac{J_{23}^2 \cdot Y_{LC_1} + J_{12}^2 \cdot Y_{LC_3} + Y_{LC_1} \cdot Y_{LC_2} \cdot Y_{LC_3}}{J_{S1} \cdot J_{12} \cdot J_{23} \cdot J_{3L}} \\
C &= \frac{J_{S1} \cdot J_{3L} \cdot Y_{LC_2}}{J_{12} \cdot J_{23}} \\
D &= \frac{J_{S1} \cdot J_{23}^2 \cdot \mathbf{U} + J_{S1} \cdot Y_{LC_2} \cdot Y_{LC_3}}{J_{12} \cdot J_{23} \cdot J_{3L}}
\end{aligned}
\tag{3.47}
$$

The compact algorithm, starting from the elemental values is given in .

```
Input  : Parameters: $f_0$, $\omega_0$, $L$, $C_0$, $n$, $\zeta$, $f_m$, $w_m$, $\Delta\phi$, $\phi_1$, $\phi_2$, $\phi_3$, $w$, $J_{S1}$, $J_{12}$, $J_{23}$, $J_{3L}$
Output: Plots of $S$-parameters
Set the value of the fundamental frequency $f_0$ and calculate the angular frequency $\omega_0$;
Define the values of the inductors $L$;
Calculate the corresponding capacitor values $C_0$ using the formula $\left(\frac{1}{\omega_0{}^2 L}\right)$;
Set the number of harmonics $n$, the value of the modulation index $\zeta$, the modulation
  frequency $f_m$, and the progressive phase shift between the sinusoidal signals applied to
  the resonators $\Delta\phi$;
Calculate the angular frequency $\omega_m$ using the formula $2\pi f_m$;
Set the value of the phase of the first resonator to $\phi_1 = 0°$, and the subsequent
  resonators to $\phi_2 = \Delta\phi$ and $\phi_3 = 2\Delta\phi$;
Define the angular frequency range $\omega$;
Set the values of $J_{S1}$, $J_{12}$, $J_{23}$, and $J_{3L}$ as admittance inverters;
for each frequency point in $\omega$ do
    Calculate the spectral admittance matrix $Y_{LC_1}$, $Y_{LC_2}$, and $Y_{LC_3}$ using the spectral
      admittance matrix defined for each resonator;
    Calculate the spectral ABCD parameters $A$, $B$, $C$, and $D$ based on $YLC1$, $YLC2$,
      and $YLC3$;
    Calculate the spectral $S$-parameters $S_{21}$, $S_{12}$, $S_{11}$, and $S_{22}$ at each frequency point;
end
Plot the $S$-parameters $S_{21}$, $S_{12}$, $S_{11}$, and $S_{22}$ as a function of frequency by taking the
  magnitude in dB of the center element of the spectral matrices which denotes the
  fundamental frequency;
```

Algorithm 1: Algorithm for calculating and plotting S-parameters

3.6 Measurement Setup

On the basis of the design foundations laid by reciprocal BPFs, the measurement setup for a typical 3^{rd} order lumped element NR-BPF, shown in Fig. 3.8, consists of space-separated

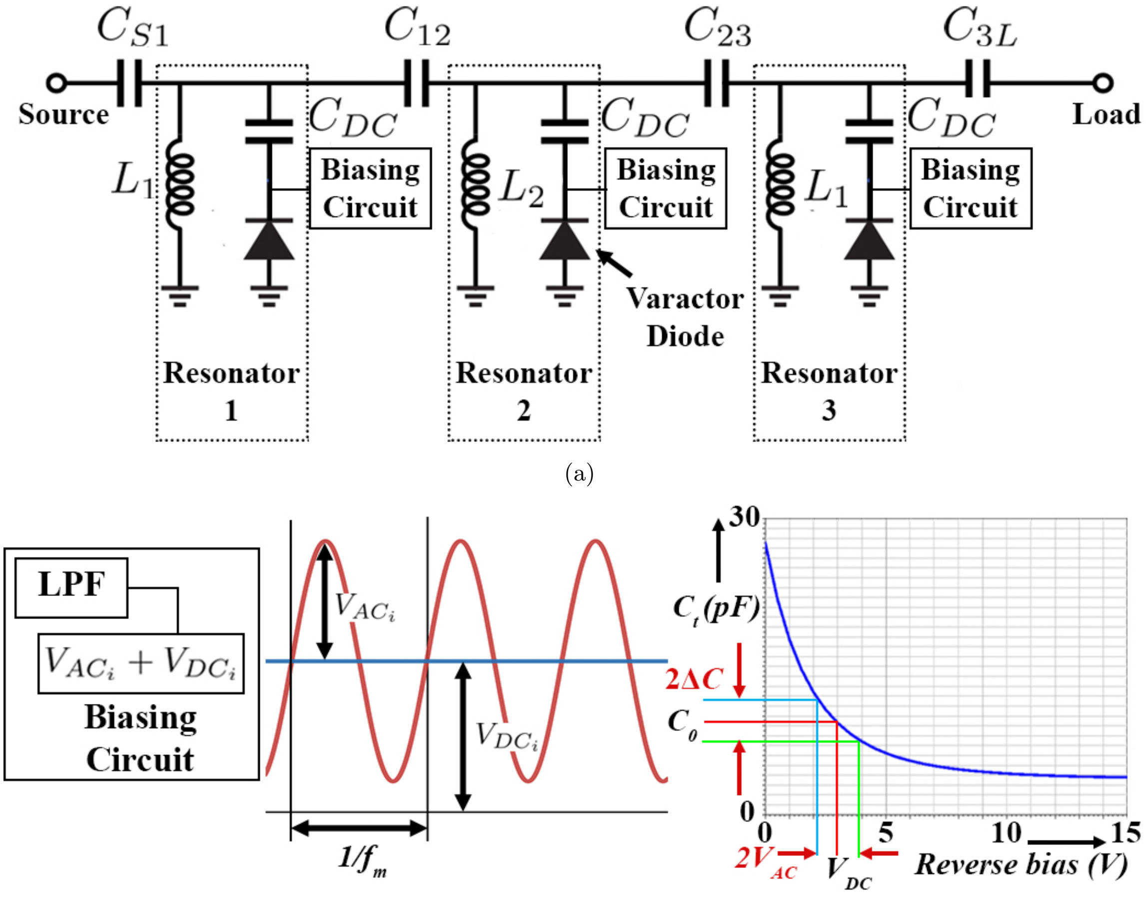

(a)

(b)

Figure 3.8: (a) The biasing circuit to the varactors and (b) the corresponding generation of time-varying capacitance with the aid of a modulation signal having a fixed DC offset.

varactor-loaded resonators 1-3 in Fig. 3.8(a)) coupled by capacitors C_{S1}, C_{12}, C_{23}, and C_{3L}. The source and load should be connected to VNA while the modulation signals are applied from arbitrary function generators. The sinusoidal signals applied to the time-varying capacitors (varactor diodes) in each of the resonators have (a) a DC offset bias to fix the nominal capacitance value (C_0) and (b) an AC bias, characterized by a constant frequency (f_m) for all the resonators to manifest the deviation in the capacitance value (ΔC) along with an incremental phase angle between the resonators ($\Delta\phi$). The DC blocking capacitor blocks the DC from getting shorted through the low impedance inductive path, and the biasing network comprises lumped element lowpass filters or choke inductors to isolate the RF from the low-frequency modulation signal. From a logical point of view, a V_{DC} value should be chosen in the piecewise linear region of the varactor characteristic curve shown in Fig. 3.8 (b), which results in an approximately uniform capacitance deviation (ΔC) from the nominal capacitance (C_0). It is worth mentioning that the same measurement procedure applies to distributed configurations as well.

3.7 Conclusion

In conclusion, this chapter has provided a comprehensive exploration of the theoretical foundations of spatio-temporal modulated non-reciprocal bandpass filters (NR-BPFs). We began by delving into the synthesis steps of reciprocal bandpass filters, starting with the formulation of lowpass prototype (LPP) or g values and the generation of coupling matrix elements. Building upon this understanding, we then ventured into the origin of non-reciprocity and examined the theoretical underpinnings of spatio-temporal modulation in NR-BPFs.

3.8 Publications

1. **Prantik Dutta**, Gande Arun Kumar, Gopi Ram, ”Spatiotemporal Nonreciprocal Filters: Theoretical Concepts and Literature Review”, *IEEE Microwave Magazine* vol. 23, no. 6, pp. 85-101, June 2022, doi: 10.1109/MMM.2022.3157970.

Chapter 4

Numerical Insight into the Origin of Non-reciprocity and Performance Enhancement in Non-reciprocal Bandpass Filters using Evolutionary Algorithm

4.1 Introduction

Non-reciprocity, using time-varying transmission lines (TVTL), has recently emerged as a potential alternative to the bulky and expensive ferrite components for their operations [14, 57]. This embryonic concept has witnessed the development of magnet-less circulators [58, 59, 60, 18, 22, 24], gyrators [61] and leaky wave antennas [62]. Lately, the concept of TVTL has documented its proficiency in the design of non-reciprocal bandpass filters (NR-BPF). These filters, apart from filtering, act as isolators in the reverse direction, thereby aiding in miniaturization by reducing the number of components in transceiver systems. When placed in between the power amplifier and the antenna in a transmitter section, the losses that would have been incurred by installing separate filter and isolator structures could be significantly reduced. Similarly, in the receiver section, the placement of an NR-BPF reduces the noise figure and alleviates the leakage from the LO through the antenna.

The first fabricated lumped realization of NR-BPF [1] using spatio-temporal modulation (STM) achieves non-reciprocity at 200 MHz with the aid of manual optimization to choose the parameter values that manifest non-reciprocity. Further, manual optimization has been carried out in the lumped realization of NR-BPF with tunable center frequency [6]. Although the circuit proves its efficacy in achieving non-reciprocity in three distinct center frequencies, it suffers from a degraded IL in the passband. The concept of coupling matrix has been used to analytically formulate the non-reciprocal phenomenon followed by a distributed realization with microstrip technology in [5]. Although this work reports the first distributed realization, manual optimization results in a degraded insertion loss (IL) and return loss (RL) within the passbands. Frequency tunable NR-BPFs using distributed realizations have been reported in [7, 9]. A considerable enhancement in results has been obtained in these works, but the parametric values have been chosen using a trial-and-error method. An NR-BPF using mixed static and time-modulated resonators has been reported for the first time in [11] followed by parametric variation of the circuit attributes. Similar sort of parametric optimization has been reported in [50] with a frequency tunable NR-BPF capable of transforming real and complex termination impedances. Subsequent NR-BPF realizations [8, 63], using similar trends of manual optimization and parametric variation, have further upgraded the design and methodologies to create a trade-off between the non-reciprocity and other parameters like IL and RL in the passband.

In this chapter, the engrossing idea of NR-BPF with the aid of STM is conceptualized numerically using a capacitive coupled lumped network. The onset of admittance inverters and the successive parametric engineering to incorporate the desired resonator values is detailed. The resonators are eventually spatio-temporally modulated with a specific combination of modulation frequency (f_m), modulation index (ζ) and the progressive phase shift between the sinusoidal signals applied to each resonator ($\Delta\phi$) to generate a nominal non-reciprocal response. A parametric study of these competitors to a successful non-reciprocal response generation is carried out to obtain an enhanced response. The problems associated with the parametric simulation is addressed which is eventually resolved by using optimization alorithms. The onset of this optimization technique commences with the understanding of the underlying phenomenon behind the non-uniform distribution of RF signal power among the harmonics in opposite directions and is substantiated with the aid of filtering polynomials. These polynomials provide a clear insight into the origin of at least one transmission zero within the passband in the reverse direction, thereby promoting the non-reciprocal response. Further, the aforementioned non-uniform spectral dispersion of power among the harmonics, generated due to the modulation of the time-varying resonators, is tabularly illustrated to comprehend the phenomenon by considering all the spectral components holistically. Consequently, the need for an optimization algorithm is judiciously explained, followed by PSO algorithm to obtain the parameter values to achieve the best possible isolation between the forward and reverse paths while preserving the IL and RL in the passband. The numerical model, designed at 150 MHz, has been simulated and fabricated using lumped components and the measured results comply well with the modeling and the simulated results.

4.2 The non-reciprocal phenomenon using spatio-temporal modulation and the parametric analysis

Conventional reciprocal bandpass filters in the microwave frequency domain comprise of LC resonators which are constructed from the lowpass prototype (LPP) models. The LPP model is used to obtain the LPP or g values corresponding to the desired filter characteristics. Once the LPP model is constructed, frequency and impedance scaling needs to be incorporated to generate the resonators' reactance values. In addition to the resonators, there are immittance inverters to couple between the adjacent resonators as well as between the resonators, the source, and the load. Immitance inverters are also used to convert series resonators to parallel and vice versa as shown in Fig 4.1.

The sequential steps to generate the admittance inverter values from the g values for a 3^{rd} order bandpass filter centered around 200 MHz with a 0.043 dB ripple factor and 30 MHz bandwidth, are given below. These steps build the foundation of the design of bandpass filters which can eventually be integrated with time-varying capacitors to implement non-reciprocity.

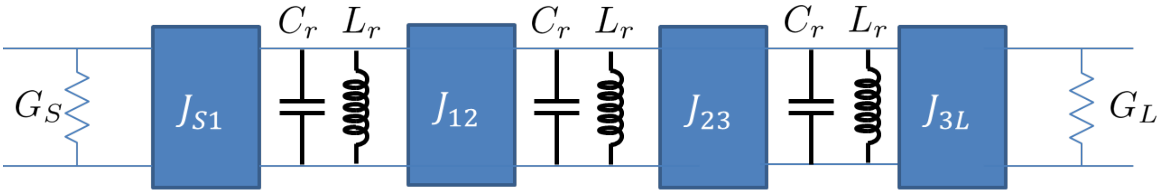

Figure 4.1: Schematic of a conventional capacitive-coupled reciprocal BPF.

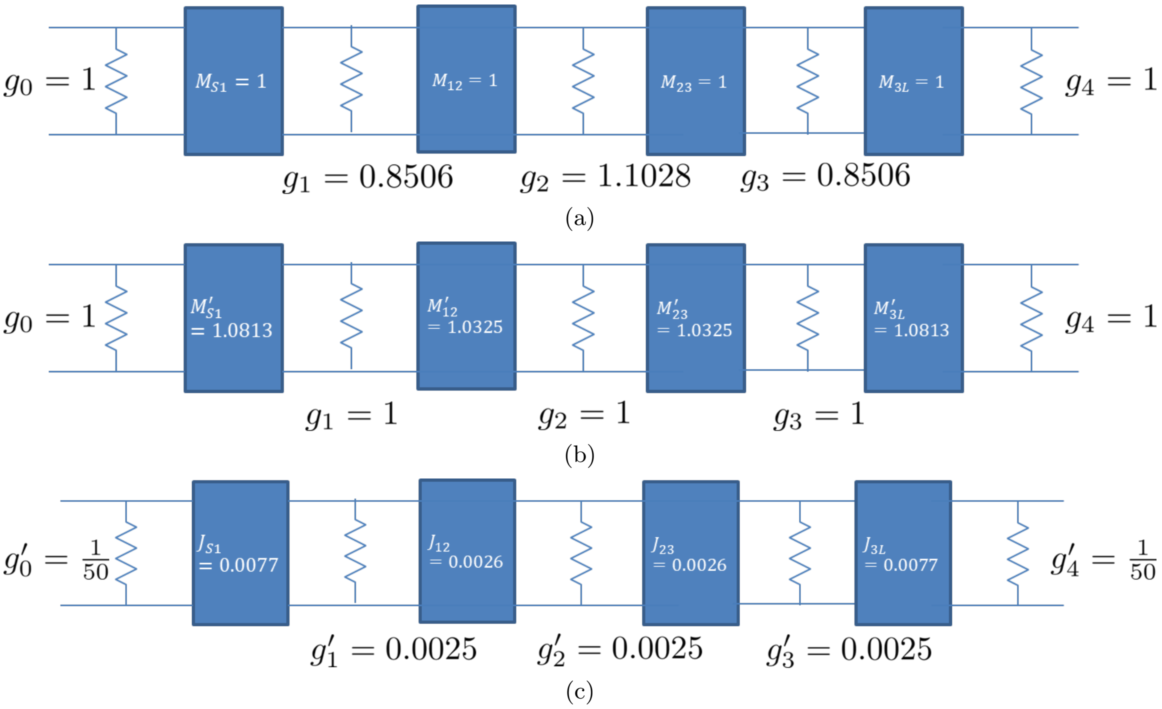

Figure 4.2: (a) Schematic of a conventional 3^{rd} order BPF with unity inverters, (b) the schematic with g values normalized to unity, and (c) the modified schematic with impedance scaled admittance inverters.

Step 1: The LPP or g values are obtained for the design specifications based on the center frequency, bandwidth, and ripple factor. The schematic is constructed with unity admittance inverters as shown in Fig. 4.2(a).

Step 2: The g values are normalized to 1; correspondingly, the admittance inverter values are normalized according to the formula $M'_{xy} = \frac{M_{xy}}{g_x g_y}$ as shown in Fig. 4.2(b).

Step 3: From the conventional LPP to BPP extraction, the g values can be converted to the resonator values by the formula $C_r = \frac{g}{\omega_0 FB}$ and $L_r = \frac{1}{\omega_0^2 C_r}$. Contrarily, for a given capacitance value C_r, we can reconstruct the corresponding g and L_r. So, if the desired C_r is 13.2 pF for all the resonators, the corresponding modified g value will be $g' = 0.0025$.

Step 4: The admittance scaling is done on the source and load g values, that is, $g'_{0,4} = \frac{g_{0,4}}{50}$. Now, based on the g' values, the admittance inverter values are transformed by the formula $J'_{xy} = M'_{xy}\sqrt{g'_x g'_y}$ as shown in Fig. 4.2(c).

To generate the S-parameter response using numerical simulation, the ABCD matrices of the overall schematic can be obtained by multiplication of the ABCD matrices of the individual elements. The ABCD submatrices of the resonators (T_{rx}), the admittance inverters ($T_{J_{xy}}$), and the total ABCD matrix (T_t) are given by eq. (4.1).

$$T_{rx} = \begin{bmatrix} 1 & 0 \\ j\omega C_{rx} + \frac{1}{j\omega L_{rx}} & 1 \end{bmatrix} \tag{4.1a}$$

$$T_{J_{xy}} = \begin{bmatrix} 0 & \frac{-1}{jJ_{xy}} \\ jJ_{xy} & 0 \end{bmatrix} \tag{4.1b}$$

$$T_t = T_{J_{S1}} T_{r1} T_{J_{12}} T_{r2} T_{J_{23}} T_{r3} T_{J_{3L}} \tag{4.1c}$$

Once the total ABCD matrix (T_t) is obtained, the conventional ABCD to S parameter matrix conversion is applied, considering equal source and load impedance, as given in eq. (4.2).

$$S_{11} = \frac{A + \frac{B}{R_L} - \frac{C}{R_S} - D}{A + \frac{B}{R_L} + \frac{C}{R_S} + D} \tag{4.2a}$$

$$S_{12} = \frac{2(AD - BC)}{A + \frac{B}{R_S} + CR_L + D} \tag{4.2b}$$

$$S_{21} = \frac{2}{A + \frac{B}{R_L} + \frac{C}{R_S} + D} \tag{4.2c}$$

$$S_{22} = \frac{-A + \frac{B}{R_L} - \frac{C}{R_S} + D}{A + \frac{B}{R_S} + CR_L + D} \tag{4.2d}$$

Based on the specifications of the schematic shown in Fig. 4.2, the numerical response of the circuit is shown in Fig. 4.3.

On the basis of the design foundations laid by reciprocal BPFs, a typical 3^{rd} order NR-BPF, shown in Fig. 4.4, consists of space-separated time-varying resonators (depicted as $C_{rk}(t)$ in Fig. 4.4(a) and the corresponding lumped representation of the varactor-loaded resonators 1-3 in Fig. 4.4(b)) coupled by immittance inverters (indicated by J_{S1}, J_{12}, J_{23}, and J_{3L} in Fig. 4.4(a) and the corresponding lumped representation using the capacitors C_{S1}, C_{12}, C_{23}, and C_{3L} in the Fig. 4.4(b)). The sinusoidal signals applied to the time-varying capacitors (varactor diodes) in each of the resonators have (a) a DC offset bias to fix the nominal capacitance value (C_0) and (b) an AC bias, characterized by a constant frequency (f_m) for all the resonators to manifest the deviation in the capacitance value (ΔC) along with an incremental phase angle between the resonators ($\Delta\phi$). The parameters f_m together with $\Delta\phi$ and the modulation index ($\zeta = \Delta C/C_0$) hold the key to the manifestation of non-reciprocity at the center frequency (f_0) [64]. The characteristic equation governing the k^{th} time-varying capacitor within the space-separated resonators is given by

$$C_{r_k}(t) = C_{0_k} + \Delta C_k \cos(\omega_m t + k\Delta\phi) \tag{4.3}$$

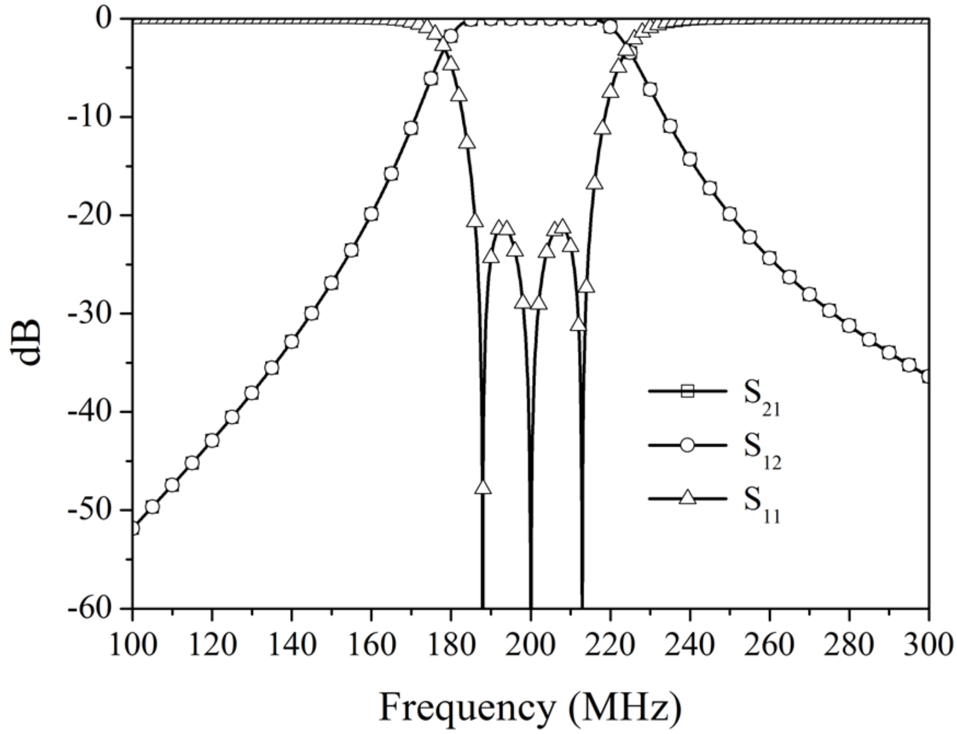

Figure 4.3: Analytical response of the schematic shown in Fig. 4.2(c).

The evolution of non-reciprocity lies in the non-uniform distribution of RF power among the generated intermodulation (IM) products in the forward and reverse directions, illustrated in [65]. The generation of IM products in addition to the signal at the RF frequency is a direct manifestation of the deployment of time-varying capacitors in the resonators. In circuital point of view, this time-varying capacitance is generated due to the modulation of the varactor diodes with time-harmonic signals. In the frequency domain, the mixing of the RF signal with the carrier signal generates an infinite number of IM products and can be represented by a spectral ABCD matrix. Temporal modulation of space-separated resonators with sinusoidal signals having the same frequency but different phase angles results in the non-uniformity in the RF power distribution in opposite directions. From the mathematical point of view, the spectral ABCD matrices can be generated starting from the $Y_{LC} = j\omega C_{rx} + \frac{1}{j\omega L_{rx}}$ term in eq. (4.1) which can be modified to integrate all the spectral intermodulation products, as given in eq. (4.4), where $X = (\omega - \omega_m)$ and $X = (\omega + \omega_m)$.

$$Y'_{LC} = jC_0 \begin{bmatrix} X\frac{\zeta}{2}e^{j\phi} & X - \frac{1}{XLC_0} & X\frac{\zeta}{2}e^{-j\phi} & 0 & 0 \\ 0 & \omega\frac{\zeta}{2}e^{j\phi} & \omega - \frac{1}{\omega LC_0} & \omega\frac{\zeta}{2}e^{-j\phi} & \\ 0 & 0 & Y\frac{\zeta}{2}e^{j\phi} & Y - \frac{1}{YLC_0} & Y\frac{\zeta}{2}e^{-j\phi} \end{bmatrix} \tag{4.4}$$

Correspondingly, eq. (4.1)(a) can be written as

$$T'_{rx} = \begin{bmatrix} 1 & 0 \\ Y'_{LC} & 1 \end{bmatrix} \tag{4.5}$$

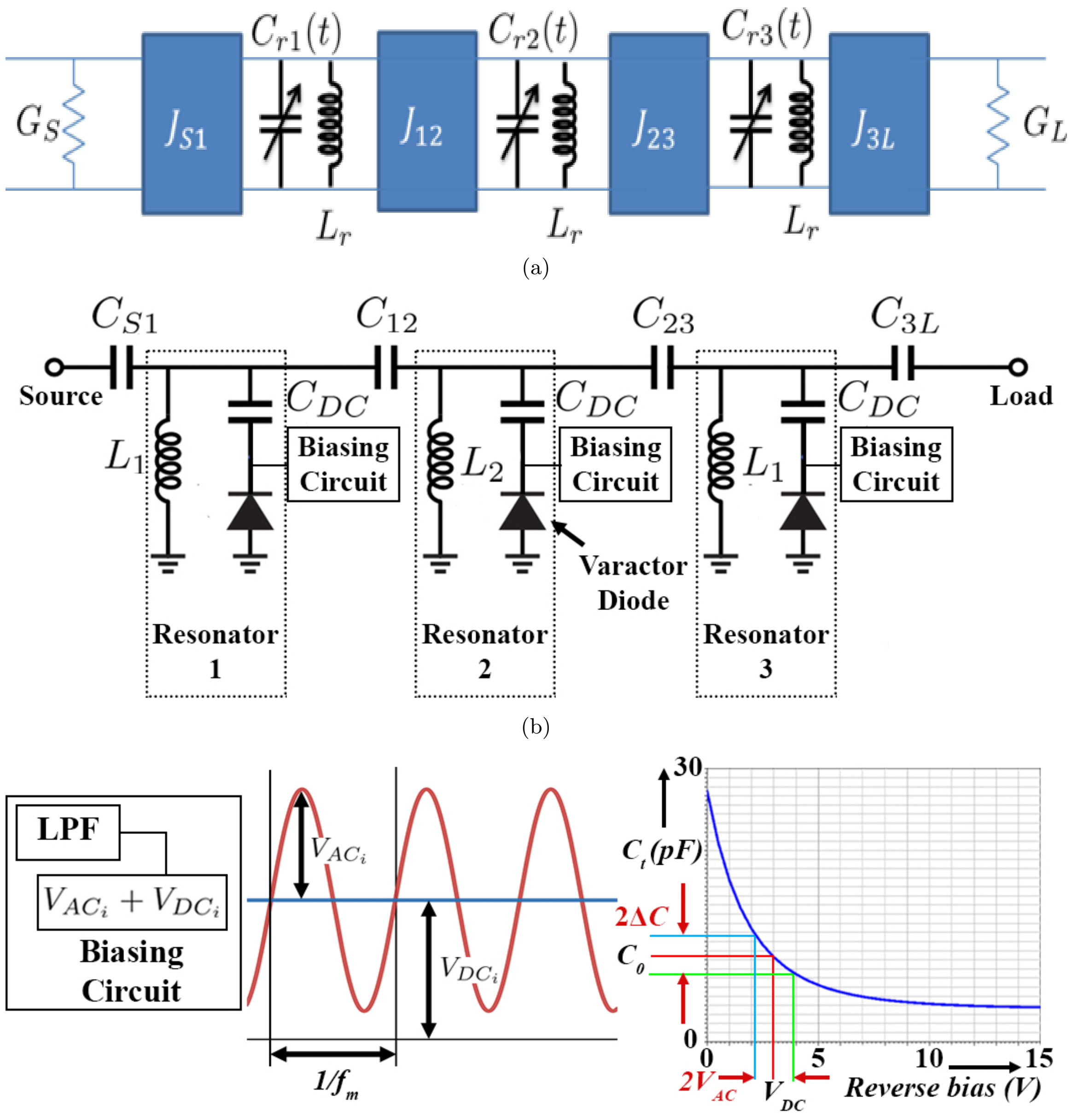

(a)

(b)

(c)

Figure 4.4: (a) Schematic of a 3^{rd} order NR-BPF; (b) the biasing circuit to the varactors and the corresponding generation of time-varying capacitance with the aid of modulation signal having a fixed DC offset.

Similarly, the rest of the equations of eq. (4.1) and (4.2) can be modified by taking into consideration the spectral admittance matrix instead of the fundamental tone alone. The competitors participating in achieving nonreciprocity are the modulation index ζ and frequency f_m applied to each resonator along with an incremental phase difference $\Delta\phi$ between each resonator starting with 0° for the first resonator. Mathematical analysis reveals that the results turn out to be reciprocal when $\zeta = 0$. Notably, each of the parameters has a different effect on the filter characteristics. For instance, the value of ζ, although it has a direct influence on the isolation at the center frequency, indirectly influences the insertion loss (IL) at the passband. Thus, a judicious choice of parameters is a necessity in the manifestation of non-reciprocity at the center

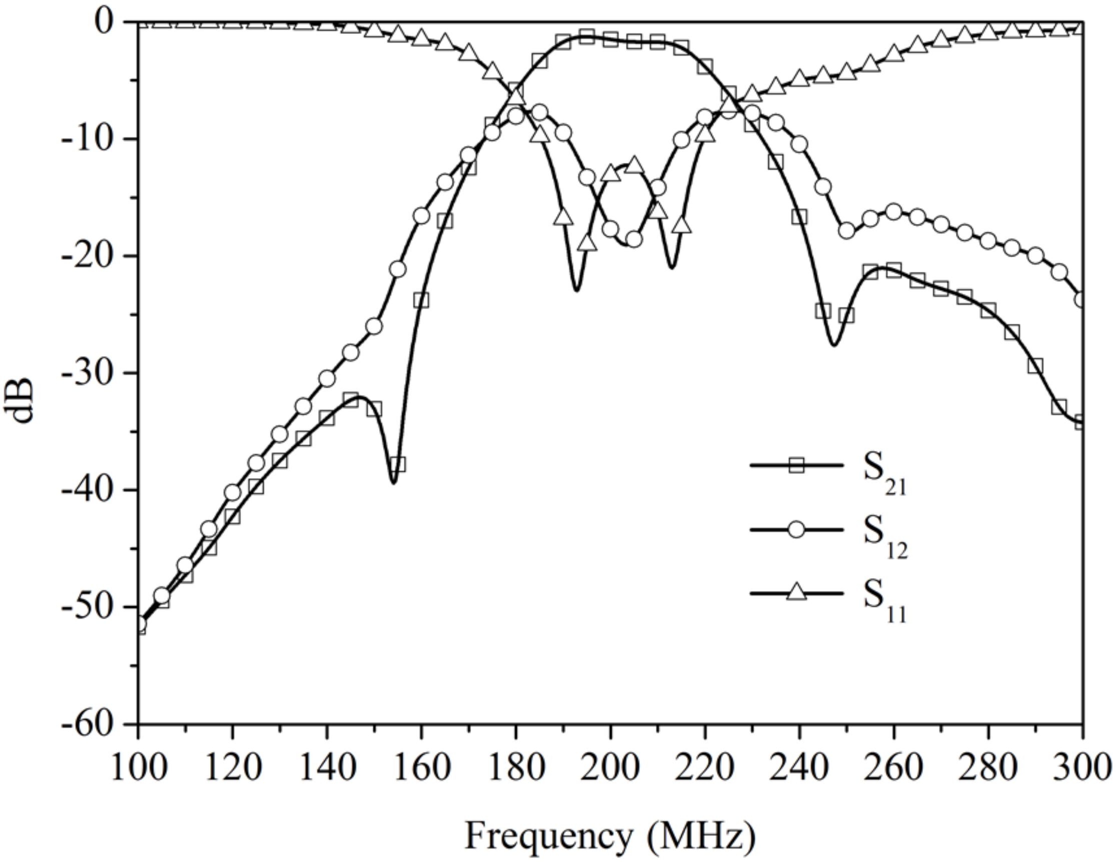

Figure 4.5: Nominal non-reciprocal response of the third-order bandpass filter.

frequency. There lies the efficacy of a parametric analysis for advancing research in this field in a more systematic way.

The following section deals with the nominal numerical response of a non-reciprocal bandpass filter by integrating time-varying resonators in the schematic shown in Fig. 4.1, followed by the parametric analysis of the individual parameters, and finally the resultant numerical response obtained from the best parametric values.

4.2.1 Nominal NR-BPF response

The nominal non-reciprocal filter response is shown in Fig. 4.5. This is based on a random set of values that gives the best response with the imposition of certain constraints as available in the literature in this domain. The values of the parameters are chosen such that the apparent result seems to be the best in terms of IL, RL, and isolation at the center frequency. The response shown in Fig. 4.5 clearly exhibits nonreciprocity at the center frequency. Although the insertion loss and the return loss (S_{11}) degrade from that of the reciprocal response; still, the return loss is almost 11 dB at the center frequency. In fact, the cost of obtaining enhanced non-reciprocity is the degradation of the IL and the RL as compared to the reciprocal response of Fig. 4.3. The difference in dB between the forward transmission and the reverse isolation of the response is termed as the directivity (D) and is one of the important parameters to assess the quality of non-reciprocity.

4.2.2 Parametric variation of ζ

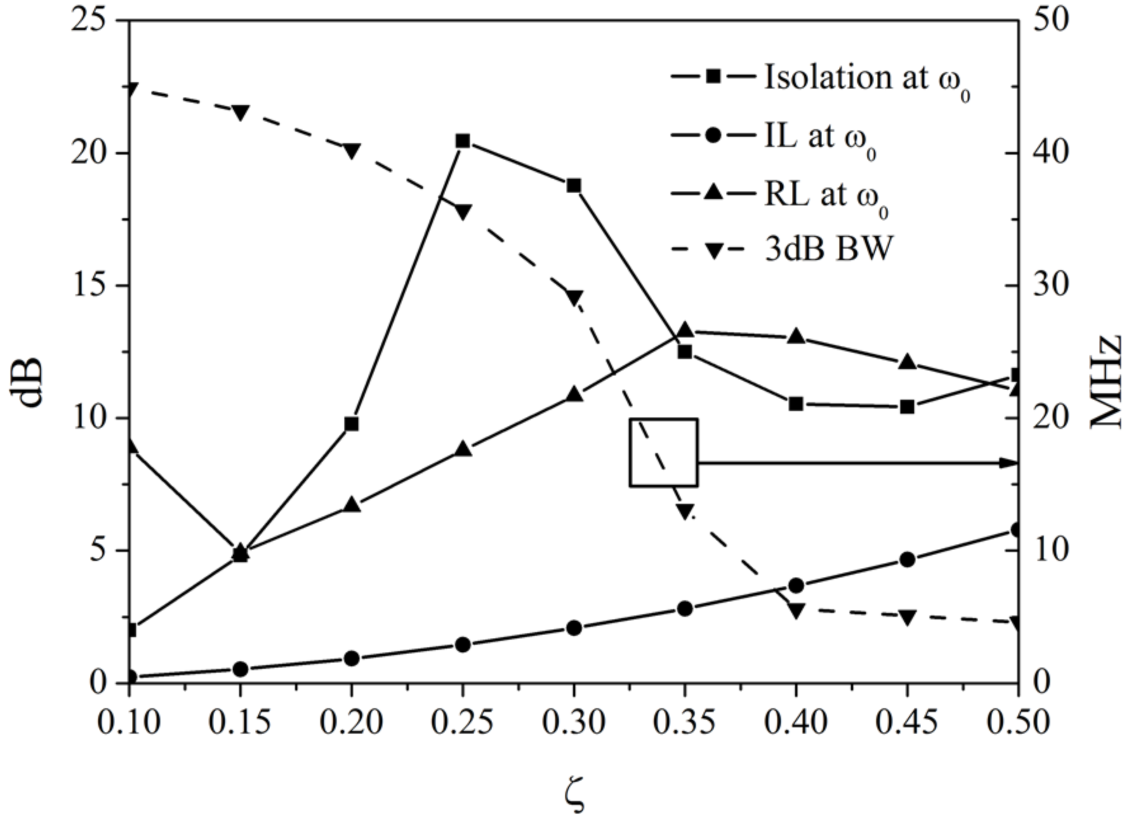

Figure 4.6: Parametric variation of the modulation index (ζ).

The parameter ζ has a direct influence on the amount of energy translated from the fundamental frequency to the harmonics. As is evident from the spectral admittance matrix given in eq. (4.4), the energy converted to the IM products is directly proportional to ζ in any frequency of interest within the evaluation range. A ζ value of zero indicates zero deviation of capacitance from the nominal value, and hence no mixing products are generated, thereby resulting in the static response. With the increase of ζ, the nonuniform conversion of RF energy from the center frequency f_0 to the harmonics at $f_0 \pm f_m$ in opposite directions increases, thereby generating the non-reciprocal response. A ζ value of approximately 0.3 results in the modification of resonant frequency roughly equal to the bandwidth of the response, thereby leading to the maximum isolation within the passband, as explained in Chapter 3. Increasing ζ further results in a degradation of IL in the forward direction. The variation of the filter characteristics with the variation of the modulation index is shown in Fig. 4.6.

4.2.3 Parametric variation of f_m

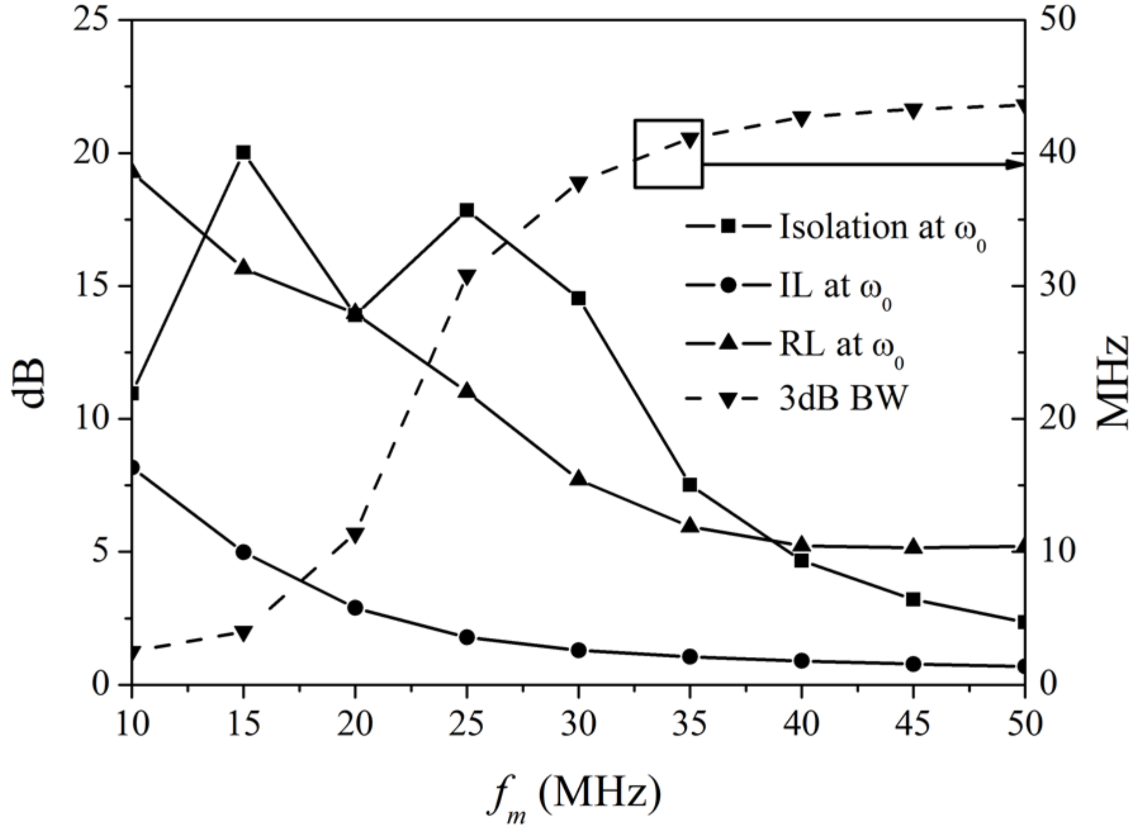

Figure 4.7: Parametric variation of the modulation index (f_m).

The value of f_m should be selected close to the equi-ripple bandwidth of the filter. This ensures that the RF energy converted from the center frequency to the harmonics falls well within the passband, thereby incurring a reduced IL in the forward direction. The main influence of f_m is on the bandwidth of the filter. As is evident from the spectral matrix, the higher the f_m, the harmonic components sharing the energy of the RF source get shifted away from the center frequency, thereby widening the bandwidth at the cost of a degraded IL within the passband. The parametric variation of the modulation or the pump frequency is shown in Fig. 4.7. As is evident, the 3 dB bandwidth increases when the value of f_m increases, owing to the separation of the harmonics from the center frequency. Contrarily, the other parameters degrade if there is a large divergence of the modulation frequency from an optimum value.

4.2.4 Parametric variation of $\Delta\phi$

Variation of $\Delta\phi$ has a direct influence on the sideband lobes of the S_{12} curve. The lower the value of this parameter, the lower is the sideband lobes of S_{12}. At the cost of degrading the isolation at the center frequency. Secondly, a minimal value of $\Delta\phi$ results in a minimum amount

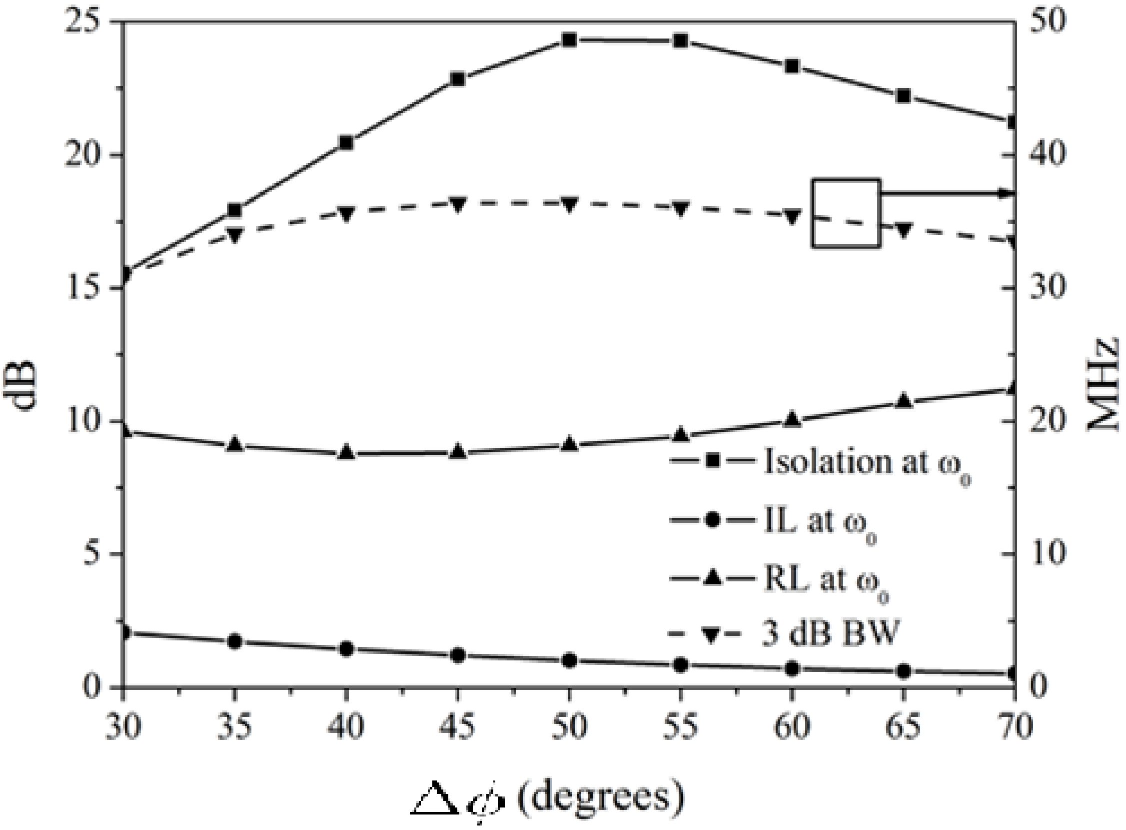

Figure 4.8: Parametric variation of the modulation index ($\Delta\phi$).

of isolation as the curves tend towards the reciprocal responses. The parametric variation of this parameter is shown in Fig. 4.8. As is evident, although this parameter doesn't have much of an impact on the variation of the characteristics like the former ones, yet, it is the most important factor for the phenomenon of STM, and indeed, it has the optimum value for the maximum manifestation of non-reciprocity.

4.2.5 Overall variation of the parameters

Summing up, each of the parameters possesses competitive qualities, and they unanimously strive for the best possible result in terms of IL, RL as well as directivity within the passband. Therefore, based on the parametric studies done so far, the parameters should be chosen judiciously to perform the task in whatever the application demands. Based on the parametric simulations, the parameters are wisely chosen to get an enhanced result in terms of IL, RL, and directivity together with the 3 dB BW of the non-reciprocal bandpass filter, and a comparison of the result before and after the parametric simulation is shown in Fig. 4.9. To be more precise, the 3 dB bandwidth of the non-reciprocal filter covers a frequency range of 36.4 MHz as compared to 40 MHz in the case of the non-modulated reciprocal response.

The dashed gray lines and black lines in Fig. 4.9 represent the characteristics before and

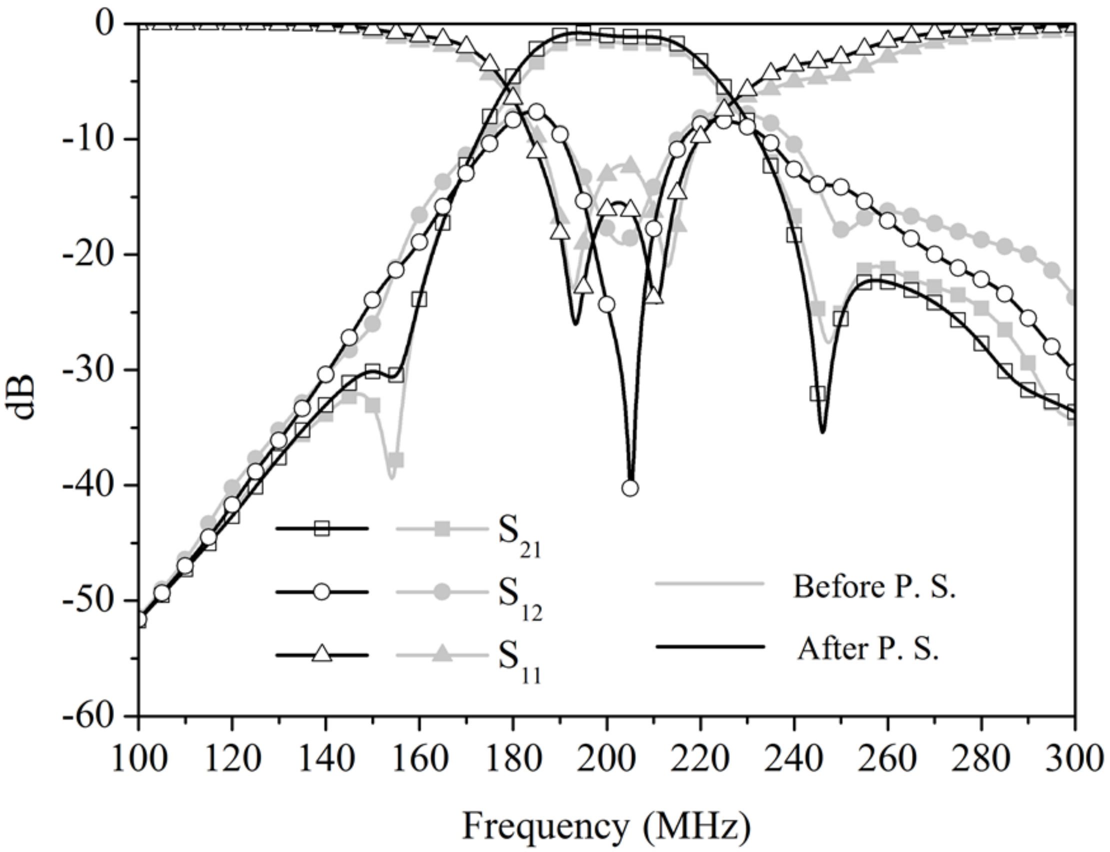

Figure 4.9: Comparison of the result before and after parametric simulation.

after parametric simulation, respectively (P. S. in the figure stands for parametric simulation). The minimum passband IL and the IL at f_0 is enhanced to 0.8 dB and 1 dB respectively after parametric simulations as compared to 1.3 dB and 1.5 dB in the nominal response before the parametric simulations. The minimum RL within the passband is 9 dB at the band edges, while the maximum RL goes up to 26 dB as compared to almost 10 dB in the former one (Fig. 4.3) while it is approximately 22 dB in the latter one (Fig. 4.9). More than 15 dB RL is incurred for a bandwidth of more than 28 MHz in the case of modulated response after parametric simulation, while a very narrow bandwidth at the points of reflection zeroes has an RL better than 15 dB. The directivity at the center frequency is more than 30 dB, while the minimum isolation at the band edges is approximately 8 dB. This is greatly enhanced as compared to the nominal response, which gives a directivity of approximately 18 dB at the center frequency.

4.3 Deeper insight into the non-reciprocal phenomenon and the scope of optimization

To meet the demand of enhancing the EM energy reaching the load end in the forward direction, meticulous restriction of energy conversion to higher order harmonics at the load end should be taken care of. Secondly, a considerable reduction in the reflected energy from the harmonics

Table 4.1: Fractional Power Conversion among the Fundamental and IM Products.

$\|S_{11}\|^2$	$f_0 - f_m$	f_0	$f_0 + f_m$
$f_0 - f_m$	0.338	✗ 0.067	0.067
f_0	0.235	0.024	0.31
$f_0 + f_m$	0.049	✗ 0.034	0.147

(a)

$\|S_{21}\|^2$	$f_0 - f_m$	f_0	$f_0 + f_m$
$f_0 - f_m$	0.224	0.021	0.009
f_0	✗ 0.036	✓ 0.821	✗ 0.052
$f_0 + f_m$	0.006	0.029	0.303

(b)

$\|S_{22}\|^2$	$f_0 - f_m$	f_0	$f_0 + f_m$
$f_0 - f_m$	0.398	✓ 0.257	0.058
f_0	0.038	✓ 0.018	0.028
$f_0 + f_m$	0.042	✓ 0.253	0.209

(c)

$\|S_{12}\|^2$	$f_0 - f_m$	f_0	$f_0 + f_m$
$f_0 - f_m$	0.116	0.159	0.177
f_0	✗ 0.121	0.008	✗ 0.185
$f_0 + f_m$	0.125	0.182	0.169

(d)

to the fundamental at the source end promotes an increase in the energy reaching the load. Contrarily, in the backward direction, the reflection of energy from the higher order harmonics to the fundamental fosters an isolation by ensuring adequate energy reflected to the load end. This complex internal phenomenon entails proper engineering of the circuit parameters to direct the energy flow in the requisite direction to obtain the best possible result both in terms of isolation as well as IL and RL in the passband.

Table 4.1 illustrates the numerical simulation results of fractional power conversion among the fundamental and the harmonics of an NR-BPF. The tabular data is obtained after converting the spectral admittance matrix in [1] into an effective spectral S-parameter matrix for a NR-BPF operating at 150 MHz with a 30 MHz bandwidth. The modified spectral S-parameter equations that are extended versions of eq. (4.2) are obtained by considering spectral ABCD parameters as given below.

$$A = \frac{J_{3L}J_{12}^2\mathbf{U} + J_{3L}Y'_{LC1}Y'_{LC2}}{J_{S1}J_{12}J_{23}} \tag{4.6a}$$

$$B = \frac{J_{23}^2Y'_{LC1} + J_{12}^2Y'_{LC3} + Y'_{LC1}Y'_{LC2}Y'_{LC3}}{J_{S1}J_{12}J_{23}J_{3L}} \tag{4.6b}$$

$$C = \frac{J_{S1}J_{3L}Y'_{LC2}}{J_{12}J_{23}} \tag{4.6c}$$

$$D = \frac{J_{S1}J_{23}^2\mathbf{U} + J_{3L}Y'_{LC1}Y'_{LC2}}{J_{S1}J_{12}J_{23}} \tag{4.6d}$$

The **U** in equations (4.6) refers to an unitary matrix whose order is equal to the maximum number of harmonics or intermodulation (IM) products considered and is at par with the order of the spectral admittance matrices Y'_{LCx} of the individual resonators. These equations when fed to the equations of (4.2) frame the spectral S-parameter equations that give a clear picture of the spectral harmonic contents at the frequency band of interest.

The time-modulated resonators of Fig. 4.4 (a) lead to the generation of additional energy traversal paths wherein the same coupling structure characterizes each path, i.e., each additional traversal path generated due to the harmonics differs in the spectral component as is evident from the spectral admittance matrix in [1, 5] but the values of the time-invariant coupling capacitors remain unaltered. This phenomenon can be modeled using the spectral ABCD matrix shown in eq. (4.7), where $\mathbf{Y_{Rk}}$ represents the k^{th} time-varying resonator from the source end. Additionally, each time-invariant coupling capacitor is modeled with an additional identity matrix $\mathbf{U}$ of the order equal to the highest order of the harmonic contents considered in the analysis.

$$\mathbf{T} = \begin{bmatrix} \mathbf{U} & \frac{1}{j\omega C_{S1}}\mathbf{U} \\ 0 & \mathbf{U} \end{bmatrix} \begin{bmatrix} \mathbf{U} & 0 \\ \mathbf{Y_{R1}} & \mathbf{U} \end{bmatrix} \begin{bmatrix} \mathbf{U} & \frac{1}{j\omega C_{12}}\mathbf{U} \\ 0 & \mathbf{U} \end{bmatrix} \begin{bmatrix} \mathbf{U} & 0 \\ \mathbf{Y_{R2}} & \mathbf{U} \end{bmatrix} \begin{bmatrix} \mathbf{U} & \frac{1}{j\omega C_{23}}\mathbf{U} \\ 0 & \mathbf{U} \end{bmatrix} \begin{bmatrix} \mathbf{U} & 0 \\ \mathbf{Y_{R1}} & \mathbf{U} \end{bmatrix} \begin{bmatrix} \mathbf{U} & \frac{1}{j\omega C_{3L}}\mathbf{U} \\ 0 & \mathbf{U} \end{bmatrix} \tag{4.7}$$

The next step lies in converting the spectral ABCD matrix of (4.7) into the spectral S-parameters by the conventional conversion equations [13]. The spectral S-parameters thus obtained in Table 4.1 fosters an easy understanding of the power distributed in the fundamental as well as in the harmonics. By the same token of interest, ignoring the higher order terms and considering $C_{S1} = C_{3L}$ and $C_{12} = C_{23}$, the transmission polynomials $P_{21}\omega$ and P_{12_ω} in the forward and backward directions respectively can be obtained and is given in (4.8).

$$\mathbf{P_{21}}(\omega) = -2C_{12}^2 C_{S1}^2 Z_0 \omega^4 \mathbf{U} \tag{4.8a}$$

$$\begin{aligned} \mathbf{P_{12}}(\omega) = & -4j\omega \mathbf{Y_{R1}}(C_{12} + C_{12}\mathbf{Y_{R2}} \\ & + C_{S1}\mathbf{Y_{R2}} + C_{S1}\mathbf{Y_{R1}}\mathbf{Y_{R2}}Z_0) \end{aligned} \tag{4.8b}$$

where $\mathbf{Y_{R1}}$ and $\mathbf{Y_{R2}}$ are the spectral admittance matrices and are functions of ω. Finding the zeroes of the equations in (4.8) gives the transmission zeroes within the frequency range of interest. These two contradictory equations reveal that there is no transmission zero in the forward direction in the fundamental mode of traversal owing to the absence of $\mathbf{Y_{Rk}}$ terms and the presence of only real terms in (4.8a), whereas solving (4.8b) provides at least one distinct transmission zero at the center frequency in the fundamental mode of traversal in the backward direction thereby promoting isolation.

Although the analysis carried out above fosters the contradictory response and the origin of transmission zero in the backward direction, the overall analysis and the corresponding deployment of an optimization algorithm should be carried out holistically by considering all the harmonic contents in the spectral scattering parameters. Tables 4.1(a) and 4.1(b) represent the reflected and transmitted power conversion among the harmonics in the forward direction, respectively, while tables 4.1(c) and 4.1(d) represent the reflected and transmitted power conversion among the harmonics in the backward direction, respectively. For instance, the second column of the first row in table 4.1(a) (marked by ✗) represents the fraction of power reflected from the first harmonic at the lower side ($f_0 - f_m$) to the center frequency (f_0). Similarly, the second column of the second row in table 4.1(b) (marked by ✓) represents the transmission at the center frequency. The symbols (✓) and (✗) denote the desired and undesired components, respectively. Thus, this table enhances the comprehension of the dispersion of the spectral energy both in the forward and reverse direction, which in turn manifests the non-reciprocal phenomenon.

Enhancing the IL in the passband would require increasing the power transmission at the center frequency (cell marked by ✓) in table 4.1(b) by simultaneously reducing the power converted from the center frequency to the harmonics at the load end (cells marked by ✗) in table 4.1(b) and substantially minimizing the RL at the center frequency (marked by gray cell) by reducing the reflected power from the harmonics back to the center frequency at the source end (cells marked by ✗) in table 4.1(a). On the other hand, to achieve non-reciprocity at the center frequency, in addition to the fractional reflected power at the fundamental alone, the fractional power reflected from the harmonics to the center frequency (cells marked by ✓) in table 4.1(c) should also be enhanced, thereby increasing the total IL in the passband (marked by gray cell) in table 4.1(d); herein lies the scope of optimization. Manual optimization arrives at a crude approximation of the relation between the circuit parameters and the filter characteristics, which concludes that increasing ω_m and decreasing ζ enhances the IL and RL in the passband but degrades the isolation, whereas, decreasing $\Delta\phi$ enhances RL, but increasing it gradually, first enhances and then degrades the IL and directivity after a certain value is reached. Another drawback lies in wisely initializing the circuit parameters (ζ, f_m, and $\Delta\phi$) with some arbitrary values followed by sweeping one parameter at a time by keeping two of the remaining parameters fixed. Any erroneous prediction of the initial values would end up in a choice of parameter values far from the global convergence point. Apart from the dubiety in the veracity of this parametric study to search for the best possible result, the technique is arduous and its inefficiency in handling constrained optimization problems happens to be major setback. Contrarily, the deployment of an optimization algorithm would consider all the circuit parameters simultaneously, which collectively would strive to obtain the best isolation, apart from maintaining an optimum IL and RL within the passband. The tables serve as an aid to the optimization algorithm; wherein the main objective is to reduce the center element of table 4.1(d) (related to reverse isolation) and maximize the center element of table 4.1(b) (related to forward transmission), thereby maximizing the non-reciprocity. In this work, PSO based evolutionary algorithm has been proposed to obtain the best choice of circuit parameters.

4.4 PSO algorithm

Particle Swarm Optimization (PSO) is one of the metaheuristic algorithms to optimize non-linear continuous functions. The concept of this algorithm has been inspired by swarm intelligence often observed in the social behaviour of a flock of birds or a school of fishes [66]. The population of solutions is termed a swarm composed of several agents known as particles. The particles are initialized with a random set of solutions which then collectively hover over the problem space, the speed of which depends on a velocity parameter assigned to each particle. The best positions of each particle, denoted by p_{best}, are tracked in each iteration. Based on these memories, the individual velocities and hence their positions are updated at each iteration. Eventually, the algorithm converges to the global best result, denoted by g_{best}, by the collective participation of the individual particles in the population and fetches the values of the best combination of the parameters.

In this work, PSO algorithm is utilized to extract the optimizing parameter values to obtain the optimal non-reciprocal result in a 3^{rd} order 150 MHz BPF having a bandwidth of 15 MHz. The first step requires the parameters ζ, f_m, and $\Delta\phi$ with random values within a given range. The next crucial step lies in exercising a constraint on IL and RL at the center frequency (f_0), considering n harmonics above and below f_0, and is given in equation (4.9) as the cost function (CF) shown below

$$CF = \begin{cases} FR_{sum} + BT_{sum} + FT_{sum} + BR_{sum}, & \text{if IL } \leq \text{ 1 dB \& RL } \geq \text{ 15 dB} \\ FR_{sum} + BT_{sum} + FT_{sum} + BR_{sum} + a, & \text{otherwise} \end{cases} \tag{4.9}$$

where, the acronyms FR, FT, BR and BT denote reflection in the forward direction (table 4.1(a)), transmission in the forward direction (table 4.1(b)), reflection in the backward direction (table 4.1(c)) and transmission in the backward direction (table 4.1(d)), respectively. The variables (FR_{sum}, BT_{sum}, FT_{sum} and BR_{sum}) are responsible for summing up the energy contents in the respective harmonics and are given by

$$FR_{sum} = FR_{sum} + w * FR(m, 0) \tag{4.10a}$$

$$BT_{sum} = BT_{sum} + w * BT(0, m) \tag{4.10b}$$

$$FT_{sum} = FT_{sum} + w * FT(0, m) + 1/FT(0, 0) \tag{4.10c}$$

$$BR_{sum} = BR_{sum} + w * BR(m, 0) + BR(0, 0) \tag{4.10d}$$

The appearance of the letter 'a' in equation (4.9) is a bit intriguing; it is an arbitrary number chosen to have a value much greater than the minimum value of CF that can be obtained. If the conditions are not satisfied, then there is a sudden surge in the deterioration of the value of CF owing to the large value of 'a', and hence, the position and global best of the algorithm are maintained at the last best values and the algorithm continues its search for the optimal minimum in the right direction. The variable 'm' in equation (4.10) varies in the range of $m \leq |n|$ excluding $n = 0$ and the variable 'w', denoting the associated weight, is given by $w = 1/m$. In this algorithm, according to the rule given in [67], the value of n is set to 2. The numbers within the brackets (i, j) represent the energy translation from the i^{th} harmonic to the j^{th} harmonic. For instance, $FT(0, -1)$ represents the energy translation from f_0 to $f_0 - f_m$ (marked by ✗) in the first column of table 4.1(b). The weight (w) is designed in such a way to commensurate the energy content with the degree of the harmonics. This deliberately promotes the algorithm to emphasize more on the harmonics nearer to the center frequency possessing more spectral energy. For the specified band of harmonic content denoted by 'n', the algorithm calculates the weighted sum of the desired and undesired components in one single loop. It is worthwhile mentioning that the undesired components are specified as reciprocals to facilitate the algorithm to converge to an optimal minimum. On an interesting note, numerical simulations reveal that the algorithm converges to a better result if different modulation indices are applied on each varactor. The algorithm successfully converges after 128 iterations with a population size of 100. The cognitive and social parameter constants in the velocity and position equations are judiciously chosen as 1.5 [68]. Holistically, the steps toward a successful convergence of the algorithm for the desired specification of a filter can be summarized in the following steps.

Step 1: An appropriate capacitance value is chosen based on feasibility; the inductor values are calculated based on the chosen capacitance values for each resonator depending on the order and the specifications of the filter.

Step 2: The admittance inverter values are calculated based on the conventional filter design approach. These values might be the values of the coupling matrix defined for the specification.

Step 3: The cost function CF defined above based on the k^{th} order spectral power $(k = 2n + 1)$ calculated from the spectral S-parameter analysis in [64], the lower and upper bounds of the parameters ζ, f_m and $\Delta\phi$, and the conditions of IL, RL and isolation are fed as input to the algorithm.

Step 4: The algorithm is run for the maximum number of iterations specified with the defined population size, the velocity, and the social parameters.

4.5 Experimental Validation and discussion

The parameter values extracted using the PSO algorithm ($\zeta = 0.134$, $f_m = 11.6$ MHz and $\Delta\phi = 63°$) are used to modulate the time-varying capacitors (realized using SMV1236 varactors) in each of the resonators. A plot of convergence of the algorithm to the minimum value of cost function is shown in Fig. 4.10.

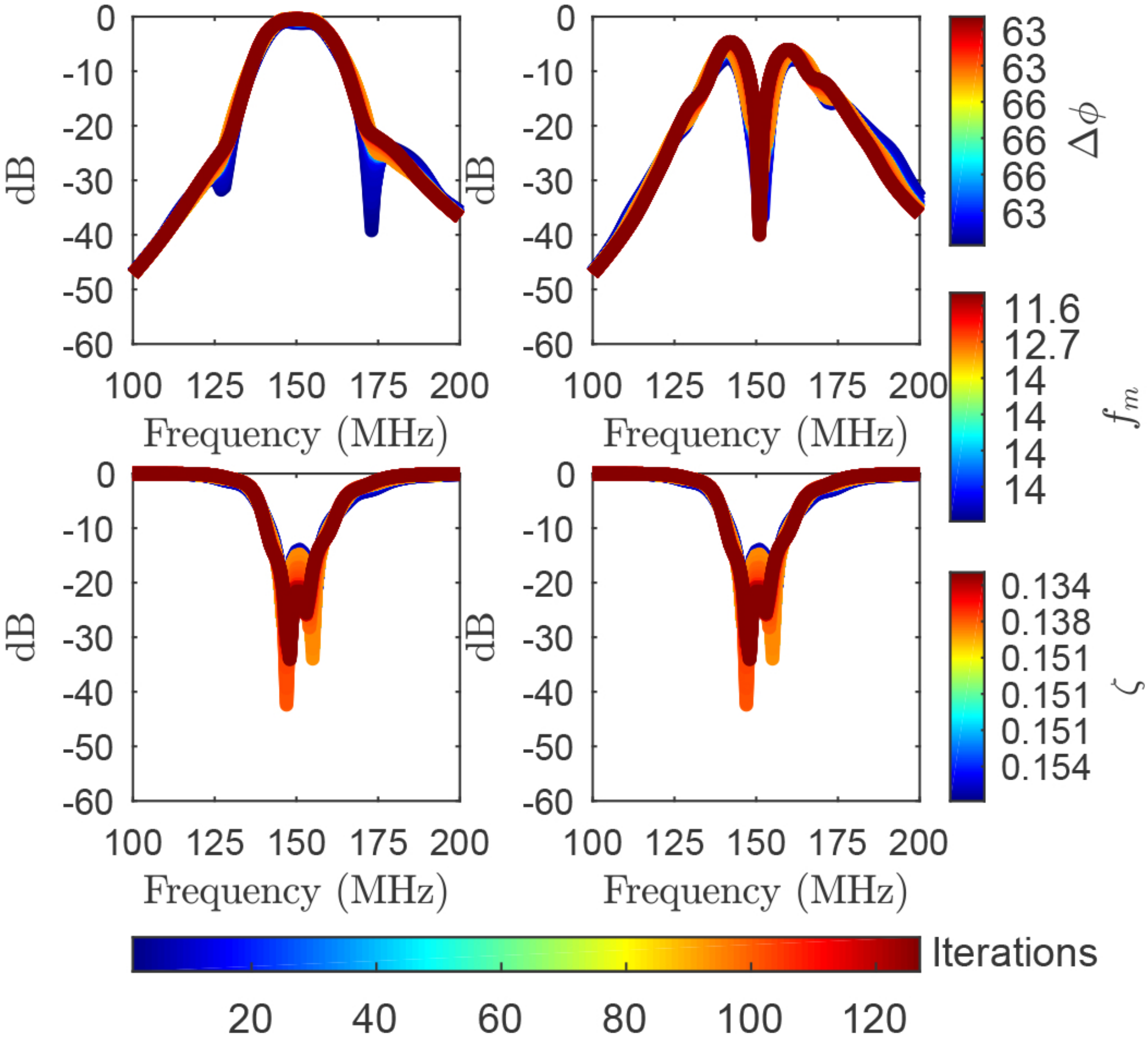

Figure 4.10: Variation of parameters as the algorithm converges to the global minimum.

The ζ values determine the deviation ΔC from the nominal capacitance value C_0 of the varactor diode. To transform the domain of ζ from determining the ΔC to the estimation of the deviation in the biasing voltage from the DC value so as to obtain the corresponding ΔC, a piecewise linear region in the varactor characteristics is judiciously chosen to approximate the variation of ΔV_{AC}. In short, V_{DC} determines the nominal value C_0 while V_{AC} determines the deviation in capacitance ΔC so as to incorporate the parameter ζ. The circuit parameter values of Fig. 4.4 are $C_{S1} = C_{3L} = 6.2$ pF, $C_{12} = C_{23} = 1.8$ pF, $L_1 = L_3 = 82$ nH, $L_2 = 100$ nH and $C_{DC} = 82$ pF. The AC and DC biasing values ($V_{DC_1} = V_{DC_3} = 2.73$ V, $V_{DC_2} = 2.04$ V,

$V_{AC_1} = 0.28$ V, $V_{AC_2} = 0.25$ V and $V_{AC_3} = 0.5$ V) extracted using the ζ values, are applied through a LPF circuit. The circuit is simulated using Cadence AWR software and fabricated on a FR4 substrate, shown in the inset of Fig. 4.11.

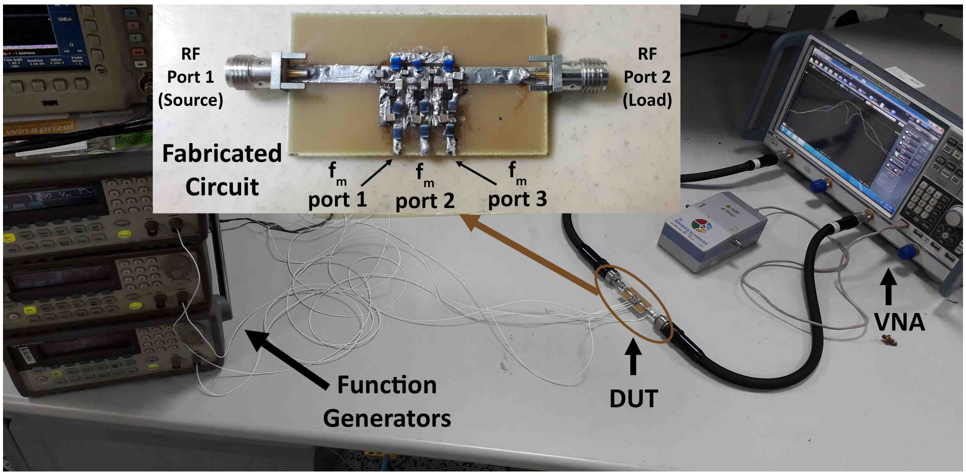

Figure 4.11: Experimental setup of the 3^{rd} order NR-BPF and the fabricated circuit (inset).

Fig. 4.12(a)-(d) compares the simulated and measured results with the numerical modeling. An almost comparable correlation of the results vouches for the accuracy of the model. The results show a promising non-reciprocal response centered around 150 MHz. A slight reduction in bandwidth is observed in the simulation and measurement owing to the usage of standard values of the lumped components and the piecewise linear approximation in the varactor characteristics, which results in a slight deviation of ΔC values and hence, the ζ values. The IL at the center frequency has slightly degraded in the case of circuit simulation (0.96 dB) and measurement (1.1 dB) as compared to the numerical result (0.85 dB) owing to the resistive losses in the varactor.

The detailed specifications of the simulated and measured parameters of the NR-BPF prototype is given in Table 4.2.

Table 4.2: Filter Specifications

Sl. No.	Parameter	Simulation	Experiment
1.	Center Frequency	150 MHz	150 MHz
2.	Bandwidth	15 MHz	15 MHz
3.	Insertion Loss	0.96 dB	1.1 dB
4.	Return Loss	16.8 dB	16.2 dB
5.	Isolation	32.8 dB	28.6 dB

A comparison table with other works in the lumped domain is shown in Table 4.3. The minimum passband IL is 1.1 dB, which is, by far, the best IL achieved so far. The measured RL of the prototype NR-BPF is greater than 16 dB, thereby ensuring good matching with the source/load. A directivity of 28.6 dB is achieved in the measured results. Even though the

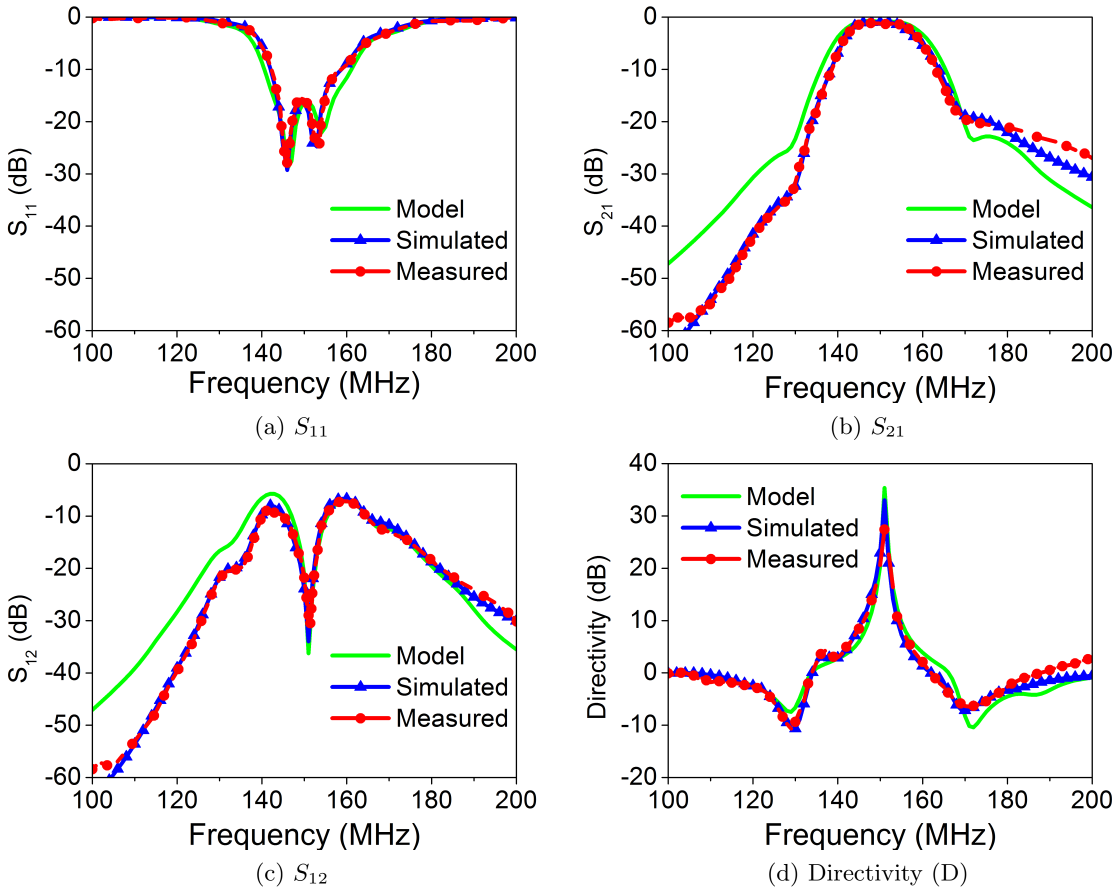

(a) S_{11} (b) S_{21} (c) S_{12} (d) Directivity (D)

Figure 4.12: Comparison of the numerical, simulation and experimental results for (a) input reflection (S_{11}), (b) forward transmission (S_{21}), (c) reverse isolation (S_{12}) and (d) directivity.

directivity is 52.8 dB in [6], it suffers an IL of 3.7 dB, which not only nullifies the competency of the power amplifier in the transmitter section, it also degrades the noise figure if implemented in the receiver section. As an experimentation purpose, the algorithm in (4.9) has been carried out with the maximum IL constraint of 3 dB. The results show a promising isolation of 63 dB with an IL of 3.2 dB and a RL of 12 dB; the extracted parameters corresponding to this result are $\zeta = 0.2$, $f_m = 8$ MHz and $\Delta\phi = 55°$. This experimentation comes to a logical conclusion that the trade-off associated with a high isolation is a degraded IL and RL. It is also observed in the simulation and measurement results that constraining the minimum value of the RL to 20 dB results in further lowering of the bandwidth and a significant drop in the directivity. The algorithm has been run on an Intel Xeon Bronze 1.70 GHz system configuration comprising of 64 GB RAM and it successfully converges after 128 iterations in 458 seconds.

4.6 Conclusion

This chapter commences with the numerical explanation of the onset of non-reciprocity in spatio-temporally modulated bandpass filters. The modelling of spectral ABCD matrices to deal with the harmonics associated with time-modulation of sequentintial resonators embarks with a brief

Table 4.3: Comparison with other works in the literature

	Technology	f_0 **(GHz)**	**IL**	**RL**	**D**
[1]	Lumped	0.19	1.5	15	20.2
[6]	Lumped	0.14	3.7	>14	52.8
[5]	Distributed	0.96	4.5	N/A	13.8
[9]	Distributed	1	3.9	16.1	23.2
[11]	Distributed	1.46	3.1	15.2	20.2
[50]	Distributed	1.97	3.98	>16.13	20.1
This work	Lumped	0.15	1.1	16.2	28.6
This work*	Lumped	0.15	3.2	14	63.2

IL, RL, and Directivity (D) are in dB scale.
* indicates the experimentation done with IL = 3 dB.

explanation of admittance inverters in a capacitive-coupled bandpass filter. The modelling of non-reciprocal bandpass filter is substantiated with a parametric analysis of the underlying parameters competing together to achieve the filtering isolation in the passband. Subsequently, the non-uniform spectral distribution of RF power in opposite directions in non-reciprocal bandpass filters is illustrated and corroborated with the aid of filtering polynomials. Further, PSO based evolutionary algorithm is deployed for the first time to extract the circuit parameters of a 150 MHz NR-BPF using lumped components. Contrary to the manual parametric optimization, which relies on parametric simulations, the PSO algorithm searches for the best possible combination of the parameters to obtain the most satisfactory result in terms of isolation between the forward and reverse paths, without degrading the IL and RL in the passband; thereby expounding its efficacy in this domain. The results reveal a tradeoff between IL and isolation in the filter characteristics. The model and the parameters extracted using the algorithm have been experimentally validated and a satisfactory correlation between the model, simulation, and experimental results justifies the analysis. The algorithm possesses the potential to be exploited to obtain the best possible parametric values for any desired non-reciprocal filter configurations.

4.7 Publications

1. **Prantik Dutta**, Gande Arun Kumar, Gopi Ram, D. Suneel Varma "Magnetless 3-pole Non-reciprocal Bandpass Filter: Numerical Analysis with MATLAB Simulation", *2021 International Conference on Computing, Communication, and Intelligent Systems (ICCCIS)*, doi:10.1109/ICCCIS51004.2021.9397139.

2. **Prantik Dutta**, Gande Arun Kumar, Gopi Ram, "Non-reciprocal Bandpass Filters: Para-

metric Simulation", *2022 IEEE Wireless Antenna and Microwave Symposium (WAMS)*, doi:10.1109/WAMS54719.2022.9848139.

3. **Prantik Dutta**, Gande Arun Kumar, Gopi Ram, "Numerical Insight into the Origin of Non-reciprocity and Performance Enhancement in Non-reciprocal Bandpass Filters using Evolutionary Algorithm", *IIEEE Transactions on Computer-Aided Design of Integrated Circuits and Systems*, doi:10.1109/TCAD.2022.3216757.

Chapter 5

Numerical Design of non-reciprocal bandpass filters with the aid of 3D Coupling Matrix for 5G bands

5.1 Introduction

The coupling matrix is a fundamental tool in the design of microwave filters. It characterizes the interconnection between resonators in a filter structure and determines their coupling strengths [45, 69, 13]. By manipulating the coupling matrix, designers can achieve specific filter responses, such as bandpass, bandstop, or multiband characteristics. The proper design of the coupling matrix is crucial for achieving desired filter performance in terms of bandwidth, selectivity, and insertion loss. Various techniques and algorithms have been developed to optimize the coupling matrix and enhance filter design efficiency. However, the conventional coupling matrix synthesis and representation deals with reciprocal filters; to deal with spectrally generated resonators, as is the case for non-reciprocal bandpass filters, the entire analysis needs to be modified to suit the scenario. This nonconventional coupling matrix analysis approach is still in the infant stage of development in the context of spatio-temporally modulated non-reciprocal bandpass filters.

This chapter commences with a basic apprehension of the essence of coupling matrix in the design of bandpass filters. The general coupling matrix theory and the subsequent synthesis of the same are elaborately explained. The synthesis of traversal coupling matrix and its conversion to practically realizable folded coupling matrix is followed by the S-parameter equations governing the $N \times N$ and $N+2$ coupling matrices. The conceptualization is carried forward gradually to the domain of NR-BPFs. First, the underlying phenomenon behind the manifestation of non-reciprocity is illustrated briefly to enhance the comprehension of the subsequent descriptions. Modulation of the time-varying resonators using sinusoids results in the generation of harmonics; consequently, the power from the RF signal gets distributed among these harmonics. The entire process is clubbed together peerlessly into a 3D coupling matrix representation. This representation provides a comprehensive explanation of the phenomenon and is also utilized to obtain flagship equations for a 3^{rd} order NR-BPF. The subsequent section focuses on the evolution of the 3D coupling matrix followed by the corresponding equations that can fully model the phenomenon. These equations reveal the origin of differences in the RF signal in opposite directions. The equations can be modified easily to design higher-order filters and implement cross-couplings. The analysis is extended to numerically simulate non-reciprocity in BPFs in four different frequency bands of the 5G spectrum; it also highlights the sequential design steps and provides parametric values for the design configurations. Eventually, the parametric variations with the variation in the frequency bands is studied, which lessens the total dependency on the trial-and-error method to obtain the parameter values, followed by an EM simulation of a cross-coupled NR-BPF using combline configuration and experimental validation with an NR-BPF designed using lumped components which confirms the accuracy of the model.

5.2 The general Coupling Matrix Synthesis and application

This section deals with the significance of coupling matrix and the classical synthesis of the same. A typical coupling matrix (CM) deals with the overall couplings associated with the adjacent and the non-adjacent resonators. In short, it defines all the immitance as well as cross-coupled inverters in a matrix form. Before we move on the generic synthesis techniques of Coupling Matrix, the foundations of the Insertion Loss method in the design of conventional filters seek attention.

5.2.1 General Polynomial Synthesis and Extraction Procedure

For any lumped, linear and time-invariant circuits, the IL is given by

$$IL(dB) = 20 \log |H(j\omega)| \tag{5.1}$$

Where $H(s)$ is the transducer function defined as the ratio of maximum power from the ideal voltage source to the power delivered to the load [70]. The transducer function is related to the characteristic function $K(s)$ by

$$|H(s)|^2_{s=j\omega} = 1 + |K(s)|^2_{s=j\omega} \tag{5.2}$$

The characteristic function is, in fact, the ratio of the reflection polynomial $F(s)$ to the transmission polynomial $P(s)$. Based on the order of the polynomials, the passband ripples as well as some design contraints, the filter characteristics are categorised into Butterworth, Chebyshev and Elliptic Filters [71, 72]. The general polynomial synthesis methods for Chebysheb filters is given in [73] and a faster technique that works for both symmetrical and asymmetrical transmission zeros positions is demonstrated in [74]. The polynomials $F(s)$ and $P(s)$ are nothing but the S-parameters of the network and are given by

$$\begin{aligned} S_{11} &= F(s) \\ S_{21} &= P(s)/\varepsilon \end{aligned} \tag{5.3}$$

where ϵ is the ripple factor and defines the amount of ripples in the passband. The constraints for the order of the polynomials as well as the formula for deriving the elemental values for the Chebyshev and Butterworth filters are derived in [71] and that for the elliptic filters is given in [72].

The general polynomial synthesis methods for Chebysheb filters is given in [73] and faster technique that works for both symmetrical and asymmetrical transmission zeros positions is demonstrated in [74]. To simplify the synthesis procedure, the polynomial functions are dealt with in the ω plane rather than the s-plane.

The ripple factor is given by the relation

$$\varepsilon = \frac{1}{\sqrt{10^{RL/10} - 1}} \left| \frac{P(\omega)}{F(\omega)} \right|_{\omega=\pm 1} \tag{5.4}$$

where RL is the return loss in the passband. The S_{21} parameter can also be written in terms of alternating pole formula [13] given by

$$\begin{aligned} S_{21}(\omega)S_{21}(\omega)^* &= \frac{P(\omega)P(\omega)^*}{\varepsilon^2 E(\omega)E(\omega)^*} \\ &= \frac{1}{[1-j\epsilon C_N(\omega)][1+j\epsilon C_N(\omega)]} \end{aligned} \tag{5.5}$$

Having done with the polynomial synthesis, the next step is to design a realizable filter circuit using lumped components from the synthesized polynomials so as to obtain the desired filter response. Detailed theories about these have been already prescribed in [75, 76, 77, 78, 79, 80]. The number of these lumped elements determine the order of the filter. Often, a parameter is encountered which can neither be defined as the capacitor or inductor; in fact it is simply a frequency-independent reactive elements known as FIR elements which was first discovered by Baum [81]. In addition, frequency-independent immitance inverters (admitance or impedence inverters) [82, 83, 84] which are nothing but quarter-wave impedence matching devices and coupling inverters which act as coupling elements between the resonantors are also encountered.

The extraction of lumped component values for the LPP filter (LPP) better known as g values are also facilitated by the use of $ABCD$ polynomials [69]. The $ABCD$ parameters give a better understanding of the synthesis of mainline and cross couplings, the latter being used for asynchronously tuned filters or filters having finite transmission zeros. Further details for the synthesis and extraction of the lumped component values (more specifically g values) are given in [85, 86, 87, 88, 89, 90].

For instance, for a Chebysheb polynomial, the filter function of degree N can be expressed as

$$C_N(\omega) = \cosh\left[\sum_{n=1}^{n=N} \cosh^{-1}(x_n(\omega))\right] \tag{5.6}$$

where $x_n(\omega)$ is the function of the frequency variable ω and the transmission zeroes ω_n given by the relation

$$x_N(\omega) = \frac{\omega - \frac{1}{\omega_n}}{1 - \frac{1}{\omega_n}} \tag{5.7}$$

The solution of (5.6) gives the characteristic of the desired filter.

5.2.2 General Coupling Matrix Representaton

Once the g values as well as the coupling and FIR elements are extracted, they can now be represented in a matrix form better known as coupling matrix. Modeling the elements in matrix form simplifies the operations such as scaling, transformation and inversion. The concept

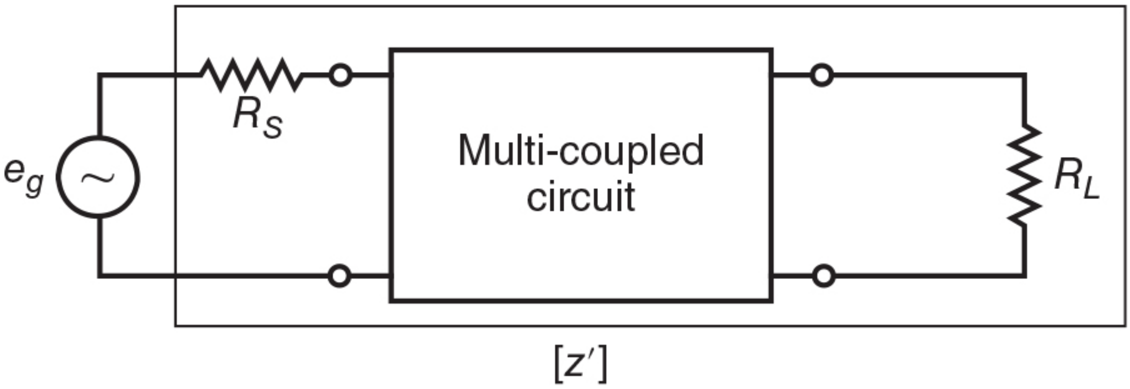

Figure 5.1: Overall impedence matrix [z'] of the coupled resonator circuit operating between source impedence R_S and R_L [13].

of coupling matrix was first introduced in 1970 by Atia and Williams for the bandpass prototype model [47, 91, 92, 46]. Once the g values, FIR elements and coupling inverter values are extracted, the total coupled network can be represented in a two port form shown in Fig. 5.1. Kirchoff's nodal law may be applied to the network to obtain the equations which may be represented now in the matrix form given as

$$\left[e_g\right] = \left[z'\right]\left[i\right] \tag{5.8}$$

The $[z']$ in eq. (5.8) is termed as the $N+2$ coupling matrix and is an integration of the source and load impedences (R_S and R_L), the frequency dependent elements ($s\mathbf{I}$) where $\mathbf{I}$ represents the capacitors or inductors and the frequency independent elements that is FIR elements which leads to the mainline and cross-couplings represented by the matrix $\mathbf{M}$ and is given by

$$\left[z'\right] = \mathbf{R} + \left[s\mathbf{I} + j\mathbf{M}\right] = \mathbf{R} + \left[z\right] \tag{5.9}$$

where the impedence matrix z is now purely reactive. Further details on the synthesis and scaling of the coupling matrix can be found in [93, 48, 94, 49]. The extracted network from the synthesized polynomials is shown in Fig. 5.2. It may be seen that the impedance matrix $[z']$ is itself the sum of three N ×N matrices:

1. The main coupling matrix jM given in eq. (5.10) is a $N \times N$ matrix containing the values of the mutual couplings between the nodes of the network and equal in value to the immittance inverters in the LPP domain. The elements are either referred to as mainline couplings if they couple the adjacent resonators ($M_{i,i+1}$), cross couplings if they represent couplings between non-adjancent resonators ($M_{i,j}$ where $i \neq j \pm 1$), and self-resonant

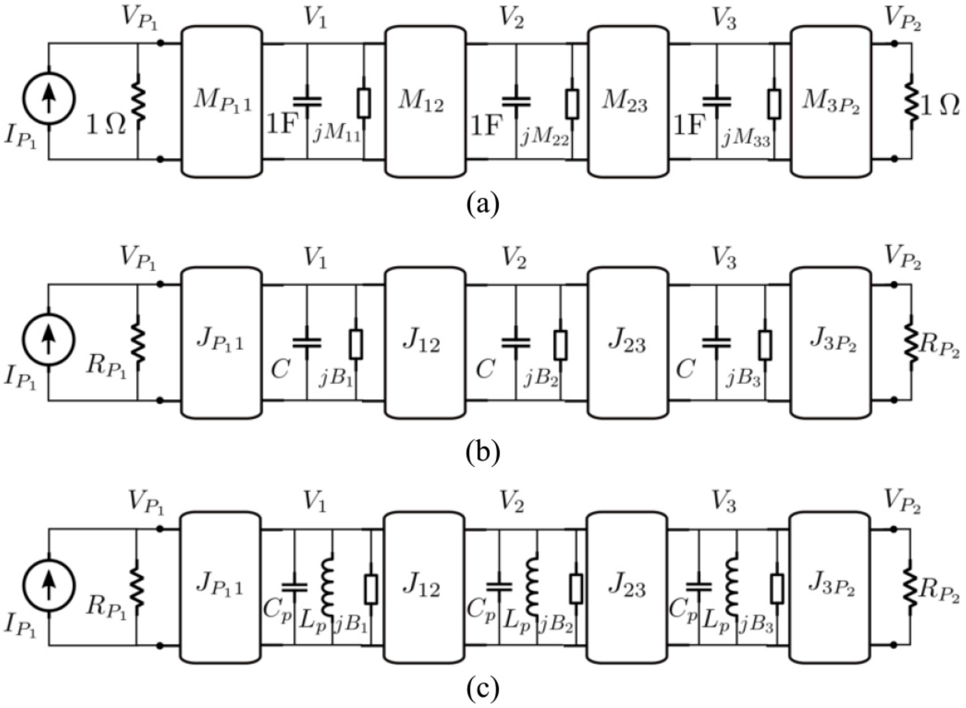

Figure 5.2: Equivalent circuit of an ideal lossless filter based on lumped elements and admittance inverters. (a) Normalized low-pass prototype with all elements having unitary values. (b) Low-pass prototype scaled to arbitrary capacitance values C and port impedances R_{P_1} and R_{P_2}. (c) Bandpass network resultingfrom a standard low-pass to bandpass transformation [5].

couplings ($M_{i,i}$) associated with frequency invariant reactance (FIR) elements.

$$j\mathbf{M} = \begin{bmatrix} M_{11} & M_{12} & M_{13} & \cdots & M_{1N} \\ M_{21} & M_{22} & M_{23} & \cdots & M_{2N} \\ M_{31} & & \ddots & & \vdots \\ \vdots & & & \ddots & M_{N-1,N} \\ M_{N1} & \cdots & & M_{N-1,N} & M_{NN} \end{bmatrix} \tag{5.10}$$

2. The frequency variable matrix $s\mathbf{I}$ contains the frequency-variable impedance portion in each loop either in the LPP or BPP domain. It comprises of an N ×N matrix with all entries zero except for the diagonal filled with $s = j\omega$ and is given in eq. (5.11).

$$j\mathbf{I} = \begin{bmatrix} s & 0 & 0 & \cdots & 0 \\ 0 & s & 0 & \cdots & 0 \\ 0 & & \ddots & & \vdots \\ \vdots & & & \ddots & 0 \\ 0 & \cdots & & 0 & s \end{bmatrix} \tag{5.11}$$

3. The termination impedance matrix $\mathbf{R}$ is an $N \times N$ matrix containing the termination impedances at the top left and bottom right corners of the matrix with all other elements

as zero as given in eq. (5.12)

$$\mathbf{R} = \begin{bmatrix} R_S & 0 & 0 & \cdots & 0 \\ 0 & s & 0 & \cdots & 0 \\ 0 & & \ddots & & \vdots \\ \vdots & & & \ddots & 0 \\ 0 & \cdots & & 0 & R_L \end{bmatrix} \tag{5.12}$$

5.2.3 The evolution of $N+2$ coupling matrix from $N \times N$ coupling matrix

The conventional $N \times N$ coupling matrix possesses the capability to handle mainline couplings as well as non-adjacent resonator couplings, better known as cross-couplings, but fails to support source-load coupled structures as the matrix doesn't provide separate rows and columns for the same. This difficulty can be addressed by constructing the $N+2$ coupling matrix.

The impedance matrix $[z]$ in eq. (5.9) represents a purely reactive network driven by the voltage source with an internal impedance of R_s and terminated by a load R_L as shown in Fig. 5.3 (a). The source and load terminations may well be normalized to unity by the insertion of impedance inverters M_{S1} and M_{NL} having impedance values of $\sqrt{R_S}$ and $\sqrt{R_L}$, respectively, as shown in Fig. 5.3 (b). Consequently, the terminating impedances become admittances and the $[z]$ matrix surrounded by the two inverters may be represented as the dual admittance matrix $[y]$. The input/output inverters can eventually be absorbed in the admittance matrix by adding an extra row on top and bottom and an extra column to the left and right of the $N \times N$ matrix thereby generating the $N+2$ coupling matrix.

5.2.4 $N+2$ Coupling Matrix synthesis: Sequential Steps

The overall theory behind the synthesis technique has been detailed in the last section. A better comprehension of the same demands jotting down the sequential steps given below for ease of perusal.

Step 1: The order (n), center frequency (f_c), bandwidth (BW), the desired return loss (RL), the quality factor (Q_u) of the resonators to be incorporated, and the number of TZs on either side of f_c are taken as input. The number of TZs should not be greater than $n/2$.

Step 2: The lower and upper cutoff frequencies (f_L and f_u), and the fractional bandwidth (FBW) are calculated based on the desired f_c and BW of the filter.

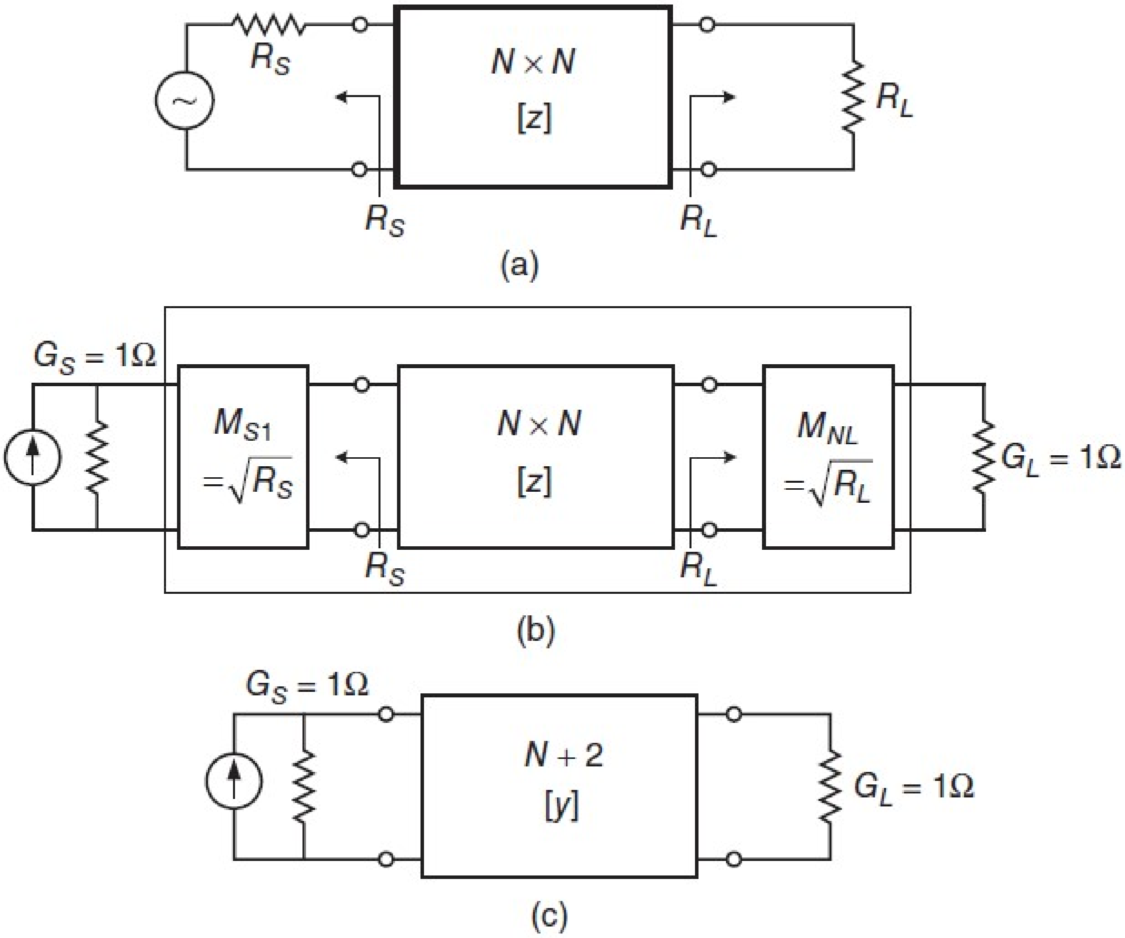

Figure 5.3: Evolution of $N+2$ coupling matrix from $N \times N$ coupling matrix. (a) The series resonator circuit representing the impeance matrix $[z]$. (b) Impedance inverters added to normalize the source/load terminations to unity. (c) $N+2$ matrix representing the parallel resonator circuit.

Step 3: The LPP domain normalized TZ positions (ω'_{TZ}) in ω domain are obtained by

$$\omega'_{TZ} = \frac{1}{FBW}\left(\frac{\omega_{TZ}}{\omega_c} - \frac{\omega_c}{\omega_{TZ}}\right) \tag{5.13}$$

where $\omega_c = 2\pi f_c$. The denominator polynomial of the filter characteristic polynomial is eventually obtained from ω'_{TZ}.

Step 4: The recursive technique for filter generation requires a 1-D array of length equal to the order of the filter containing the normalized TZs (ω'_{TZ}). For non-cross-coupled circuits, where the number of finite transmission zeroes (FTZ) is zero, all the elements of the array need to be filled by ∞; otherwise, the remaining elements in the array after placing the normalized TZs should be filled with ∞. Subsequently, the array should be sorted in ascending order, and the conventional recursive technique is applied on the same to generate the polynomials U and V

Step 5: The roots of the numerator polynomial $F(s)$, also termed as the reflection polynomial, are obtained by finding the roots of the polynomial U and the polynomial $F(s)$ is constructed by multiplying the roots by the imaginary term j and arranging them in ascending order.

Step 6: The denominator polynomial $P(s)$, also termed as the transmission polynomial, is obtained by constructing the polynomial from the sorted 1-D array as given in Step 4. Additionally, for non-cross-coupled circuits, an imaginary term j needs to be multiplied if the filter order is even, while for cross-coupled circuits, j must be multiplied if the difference between the filter order and the number of FTZs is even.

Step 7: To obtain the polynomial $E(s)$, first the ripple factor ϵ and ϵ_r needs to be calculated. The essence of ϵ_r comes into the picture only while dealing with fully canonical networks where the total number of FTZs is equal to the order of the filter, in other cases the value of ϵ_r is equal to one. If the number of FTZ is less than the order of the filter, ϵ is given by

$$\epsilon = \frac{1}{\sqrt{(10^{RL/10}-1)}} \left|\frac{P(s)}{F(s)}\right|_{s=\pm j} \tag{5.14}$$

Additionally, for fully canonical networks, ϵ_r has a value greater than unity and is obtained from ϵ as given below.

$$\epsilon_r = \frac{\epsilon}{\sqrt{\epsilon^2-1}} \tag{5.15}$$

Step 8: Finally, the polynomial $E(s)$ is obtained by convolution of $F(s)''$ and $P(s)''$ as shown below.

$$E(s) = \frac{F(s)''}{\epsilon_r^2} + \frac{P(s)''}{\epsilon^2} \tag{5.16}$$

where $F(s)''$ and $P(s)''$ are obtained by convolution of $F(s)$ and $P(s)$ polynomial with $F(s)'$ and $P(s)'$, respectively, where $F(s)'$ and $P(s)'$ polynomials are the conjugates of $F(s)$ and $P(s)$ whose k^{th} coefficient is multiplied by the factor $(-1)^k$ ($k = 0$ to n). It is worth mentioning that in the case of $P(s)'$, to be at par in symmetry with $F(s)'$, the polynomial length should be adjusted by filling the vacant positions with zero. Subsequently, the positive roots of $E(s)$ are considered to construct the final polynomial.

Step 9: From the generated polynomials $F(s)$, $P(s)$, and $E(s)$, the admittance parameters (y) of the network needs to be calculated. These admittance parameters can directly be converted to ABCD or S-parameters using conventional $y \longleftrightarrow$ ABCD or $y \longleftrightarrow$ S conversions. In this case, the focus is mainly on generating coupling matrix, which has a multitude of benefits in the context of filter designs. The y matrix can be written as

$$Y_(s) = \frac{1}{y_d(s)} \begin{bmatrix} y_{11n}(s) & y_{12n}(s) \\ y_{21n}(s) & y_{22n}(s) \end{bmatrix} \tag{5.17}$$

Owing to the symmetry of the network, $y_{22n}(s)$, $y_{21n}(s)$, and $y_d(s)$ are sufficient for the analysis where

$$\begin{aligned} y_{21n}(s) &= P(s)/\epsilon \\ y_{22n}(s) &= l(s) \\ y_d(s) &= k(s) \\ y'_{21n}(s) &= y_{21n} - j\frac{\epsilon(\epsilon_r - 1)y_d(s)}{\epsilon_r} \end{aligned} \tag{5.18}$$

$$\begin{aligned} m(s) &= \Re(e_0 + f_0) + j\Im(e_1 + f_1)s + \Re(e_2 + f_2)s^2 + ... \\ n(s) &= j\Im(e_0 + f_0) + \Re(e_1 + f_1)s + j\Im(e_2 + f_2)s^2 + ... \end{aligned} \tag{5.19}$$

where $k(s) = m(s)$ and $l(s) = n(s)$ if the filter order is even; otherwise $k(s) = n(s)$ and $l(s) = m(s)$. The term y'_{21n} comes into the picture only in the fully canonical case as will be seen in the next step.

Step 10: Once the elements are individually obtained, $Y(s)$ can be represented as

$$Y(s) = \sum_{k=1}^{n} \frac{1}{s - j\lambda_k} \begin{bmatrix} r_{11k} & r_{12k} \\ r_{21k} & r_{22k} \end{bmatrix} \tag{5.20}$$

where r_{ijk} obtained by calculating the residues of y_{ijk} and y_d polynomials considering y_d has purely imaginary roots. Thus, each ratio can be written as

$$\frac{y_{ijk}}{y_d} = \frac{r_{ij1}}{s - j\lambda_1} + \frac{r_{ij2}}{s - j\lambda_2} + \frac{r_{ij3}}{s - j\lambda_3} + ... \tag{5.21}$$

It is worth mentioning that this can only be obtained if the degree of the numerator polynomial is less than that of the denominator polynomial. In the case of canonical filters, where the number of FTZs is equal to the filter order, the order of y_{21n} has to be reduced by one and this reduction is reflected in y'_{21n} expression given in (5.18). Consequently, the residues can be obtained by taking the numerator as y'_{21n} in place of y_{21n} for fully canonical filter synthesis. Finally, λ_k values are obtained by taking the imaginary part of the poles obtained from the residue calculations arranged in ascending order, while the residues r_{21k} and r_{22k} are obtained by taking the real parts of the residues obtained and arranged in the order of λ_k.

Step 11: The penultimate step lies in generating the traversal coupling matrix (TCM) from the poles and residues obtained. The crude form of TCM is given below

$$TCM = \begin{bmatrix} 0 & \frac{r_{211}}{\sqrt{r_{221}}} & \frac{r_{212}}{\sqrt{r_{222}}} & \frac{r_{213}}{\sqrt{r_{223}}} & \frac{\epsilon(\epsilon_r - 1)}{\epsilon_r} \\ \frac{r_{211}}{\sqrt{r_{221}}} & -\lambda_1 & 0 & 0 & \sqrt{r_{221}} \\ \frac{r_{212}}{\sqrt{r_{222}}} & 0 & -\lambda_2 & 0 & \sqrt{r_{222}} \\ \frac{r_{213}}{\sqrt{r_{223}}} & 0 & 0 & -\lambda_3 & \sqrt{r_{223}} \\ \frac{\epsilon(\epsilon_r - 1)}{\epsilon_r} & \sqrt{r_{221}} & \sqrt{r_{222}} & \sqrt{r_{223}} & 0 \end{bmatrix} \tag{5.22}$$

From the steps mentioned above, if we want to design a filter circuit at 900 MHz center frequency with a 0.043 dB equiripple bandwidth of 60 MHz and having a FTZ at 1 GHz, the TCM obtained is

$$TCM = \begin{bmatrix} 0 & -0.6085 & 0.7655 & -0.4644 & 0 \\ -0.6085 & 1.4952 & 0 & 0 & 0.6085 \\ 0.7655 & 0 & -0.2580 & 0 & 0.7655 \\ -0.4644 & 0 & 0 & -1.3992 & 0.4644 \\ 0 & 0.6085 & 0.7655 & 0.4644 & 0 \end{bmatrix} \tag{5.23}$$

Step 12: The final step lies in converting the TCM to folded coupling matrix (FCM) by a series of rotations about the pivot positions. The FCM clearly indicates the inter-resonator couplings and the same can be used to design the desired filter configurations. It can be shown that the eigen values of the TCM remains same if it is pre and post-multiplied with a rotation matrix R and R^t, respectively, as shown below.

$$TCM_R = R \times TCM \times R^t \tag{5.24}$$

where TCM_R is the modified matrix and R^t is the transpose of R. To illustrate the rotation of the matrix, the TCM given in (5.23) will be used over here. To annihilate a particular column element having an index k in a given row with an index i, the pivot element needs to be chosen with an index is $(k-1,k)$. Similarly, if a particular row element with an index l in a given column j needs to be annihilated, a pivot index $(l, l+1)$. Thus, in the case of the TCM in (5.23), the first element to be annihilated is the M_{S3} element having the value of -0.4644 which is in the 4^{th} position of the 1^{st} row, that is $i = 1$ and $k = 4$. Therefore, the pivot element index is chosen as $(3, 4)$. Now, the R matrix needs to be constructed which is basically an identity matrix with its $(k-1, k-1)^t h$ and $(k, k)^t h$ terms replaced by $\cos(\theta_r)$ while its $(k, k-1)^t h$ and $(k-1, k)^t h$ terms are replaced by $\sin(\theta_r)$ and $-\sin(\theta_r)$, respectively in case of annihilating specific column elements in a particular row. This phenomenon continues until all the undesired column elements of the first row are eliminated.

The next step lies in annihilating specific undesired row elements starting from the last column. Accordingly, if the 3^{rd} row element of the 5^{th} column needs to be annihilated, then the pivot index should be chosen as $(3,4)$. Again, the R matrix needs to be constructed with its $(l,l)^th$ and $(l+1,l+1)^th$ terms replaced by $\cos(\theta_r)$ while its $(l+1,l)^th$ and $(l,l+1)^th$ terms are replaced by $\sin(\theta_r)$ and $-\sin(\theta_r)$, respectively, where

$$\theta_r = \tan^{-1}\left(\frac{-TCM(i,k)}{TCM(i,k-1)}\right) \tag{5.25}$$

$$\theta_r = \tan^{-1}\left(\frac{TCM(l,j)}{TCM(l+1,j)}\right) \tag{5.26}$$

where (5.25) and (5.26) are used for annihilating specific column elements in a particular row and specific row elements in a particular column, respectively.

After all the undesired coupling elements are annihilated using matrix rotations at each stage, the folded coupling matrix (FCM) is obtained. The FCM for the TCM considered in (5.23) is given below.

$$FCM = \begin{bmatrix} 0 & -1.0826 & 0 & 0 & 0 \\ -1.0826 & 0.0860 & 0.9870 & 0.3439 & 0 \\ 0 & 0.9870 & -0.3340 & 0.9870 & 0 \\ 0 & 0.3439 & 0.9870 & 0.0860 & 1.0826 \\ 0 & 0 & 0 & 1.0826 & 0 \end{bmatrix} \tag{5.27}$$

The $N \times N$ CM can be extracted from this FCM by drawing out only the middle elements and ruling out the first and the last row and column of the $N+2$ CM. Additionally, the source/load to first/last resonator couplings need to be incorporated into a separate $\mathbf{R}$ matrix whose all elements are zero except the position of $\mathbf{R}_{11}$ and $\mathbf{R}_{nn}$ which are equal to M_{S1}^2.

5.2.5 S-parameter representation of CM

The S-parameter equations to realize $N \times N$ CM ($\mathbf{M}$) are given by

$$S_{11(22)} = 1 + 2jM_{S1}^2 \begin{bmatrix} \lambda_1 - jM_{S1}^2 & M_{12} & M_{13} & \cdots & M_{1N} \\ M_{21} & \lambda_2 + M_{22} & M_{23} & \cdots & M_{2N} \\ M_{31} & & \ddots & & \vdots \\ \vdots & & & \ddots & M_{N-1,N} \\ M_{N1} & \cdots & & M_{N-1,N} & \lambda_3 + M_{NN} \end{bmatrix}^{-1}_{11(NN)} \tag{5.28}$$

$$S_{21(12)} = -2jM_{S1}^2 \begin{bmatrix} \lambda_1 - jM_{S1}^2 & M_{12} & M_{13} & \cdots & M_{1N} \\ M_{21} & \lambda_2 + M_{22} & M_{23} & \cdots & M_{2N} \\ M_{31} & & \ddots & & \vdots \\ \vdots & & & \ddots & M_{N-1,N} \\ M_{N1} & \cdots & & M_{N-1,N} & \lambda_3 + M_{NN} \end{bmatrix}^{-1}_{N1(1N)} \tag{5.29}$$

where λ_i takes incorporates the LPP-BPP domain transformation and is given by (5.30). It is worth mentioning that the values of λ_i are same for synchronous resonators (having the same resonant frequencies).

$$\lambda_i = \frac{1}{FB}\left(\frac{f_i}{f_c} - \frac{f_c}{f_i}\right) \tag{5.30}$$

Similarly, the S-parameter equations governing the $N+2$ CM (FCM) are given by

$$S_{11(22)} = 1 + 2j \left(\begin{bmatrix} -j & 0 & 0 & \cdots & 0 & 0 \\ 0 & \lambda_1 & 0 & \cdots & 0 & 0 \\ 0 & 0 & \lambda_2 & 0 & 0 & \vdots \\ \vdots & 0 & 0 & \ddots & \cdots & 0 \\ 0 & 0 & 0 & \cdots & \lambda_N & 0 \\ 0 & 0 & 0 & \cdots & 0 & -j \end{bmatrix} + FCM \right)^{-1}_{11(NN)} \tag{5.31}$$

$$S_{21(12)} = -2j \left(\begin{bmatrix} -j & 0 & 0 & \cdots & 0 & 0 \\ 0 & \lambda_1 & 0 & \cdots & 0 & 0 \\ 0 & 0 & \lambda_2 & 0 & 0 & \vdots \\ \vdots & 0 & 0 & \ddots & \cdots & 0 \\ 0 & 0 & 0 & \cdots & \lambda_N & 0 \\ 0 & 0 & 0 & \cdots & 0 & -j \end{bmatrix} + FCM \right)^{-1}_{N1(1N)} \tag{5.32}$$

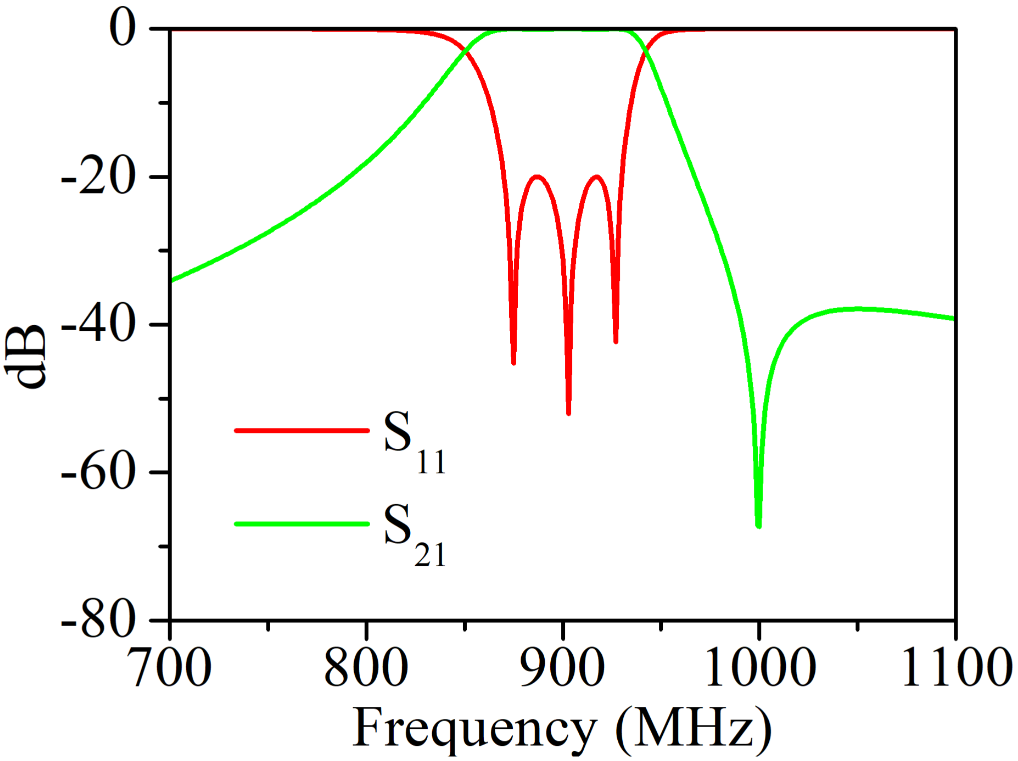

Figure 5.4: The response of the FCM given in eq. (5.23)

The $lambda_i$ values, as will be visible in the non-reciprocal case, themselves get dismantled at harmonic frequencies away from the center frequency; thus, they are no longer single-valued elements, instead, each represents a matrix to be incorporated into the holistic CM equations. The overall S-parameter response of the FCM is shown in Fig. 5.4.

5.3 The non-reciprocal phenomenon

A typical NR-BPF, shown in Fig. 5.5(a), consists of space-separated time-varying resonators apart from admittance inverters coupling the consecutive resonators and the resonators with source/load. The space-separated resonators are integrated with time-modulated capacitors (C_{r_i}), each of which is characterized by a nominal capacitance value (C_0) and a sinusoidal deviation from the nominal value (ΔC) with the aid of an AC bias. The characteristic equation and modulation index (ζ_k) governing the k^{th} time-varying capacitor ($k = 1, 2, .., n$) is given by

$$C_{r_k}(t) = C_{0_k} + \Delta C_k \cos\left(2\pi f_m t + k\Delta\phi\right) \tag{5.33}$$

$$\zeta_k = \frac{\Delta C_k}{C_{0_k}} \tag{5.34}$$

For an n^{th} order filter, the sinusoidal signals, modulating each of the time-varying capacitors, have (a) a DC offset bias to fix the nominal capacitance value (C_{0_k}) for the filter to resonate at the center frequency and (b) an AC bias, characterized by a constant frequency (f_m) for all

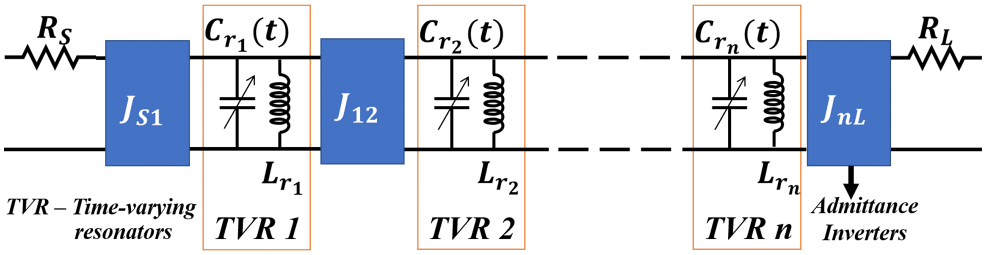

(a) Equivalent Circuit of NR-BPF

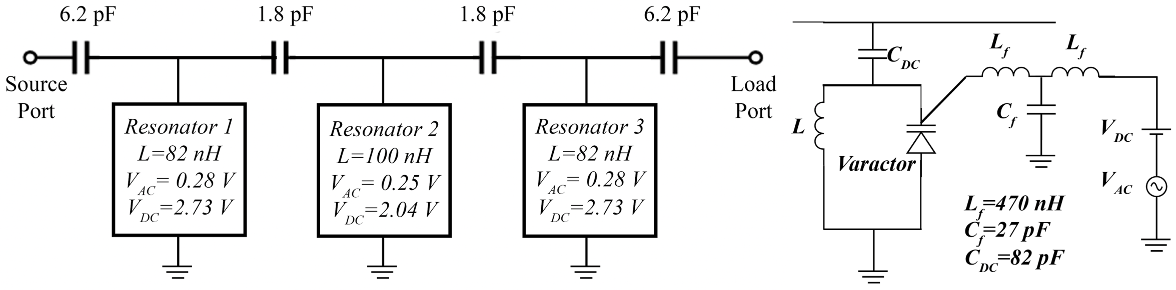

(b) Circuital components and bias values

(c) Resonator configuration

Figure 5.5: (a) Equivalent circuit of an NR-BPF. (b) and (c) Schematic of the designed filter structure.

the resonators to manifest the deviation in the capacitance value (ΔC_k) along with dissimilar phase angles (starting from 0 for the first resonator and $k\Delta\phi$ for the k^{th} resonator from the source end, where $k = 1, 2, .., n$ and $\Delta\phi$ is the progressive phase shift). As a matter of fact, the modulation index (ζ_k) for the k^{th} resonator depends upon the ratio of the AC and DC bias of the sinusoidal signal applied. The modulation frequency (f_m) together with the modulation index (ζ) and the progressive increment in the phase angles between the resonators ($\Delta\phi$), holds the key to the manifestation of non-reciprocity at the center frequency (f_0).

The evolution of non-reciprocity lies in the distribution of RF power among the harmonics generated due to the modulation of the non-linear capacitance by a modulating sinusoid [1]. Fig. 5.6 shows the traversal of EM wave through the NR-BPF in the forward and backward directions. The '0' in the bubbles represent the resonators at the center frequency, while '±1' represents the generated resonators at the first harmonics. The J values represent the admittance inverters between the source and 1^{st} resonator (J_{S1}) and between the n^{th} resonator and the load (J_{nL}). In the forward direction (fig. 5.6(a)), a substantial amount of EM energy reaching the load (marked by green arrow) demands diminution of the energy converted to the harmonics at the load end (marked by horizontal red arrows), thereby strengthening the energy reaching the load at the center frequency. By the same token of interest, the restriction of the reflected energy from the harmonics back to the center frequency at the source end (marked by vertical red arrows) results in the reduction in RL within the passband, thereby enhancing the IL in the forward direction.

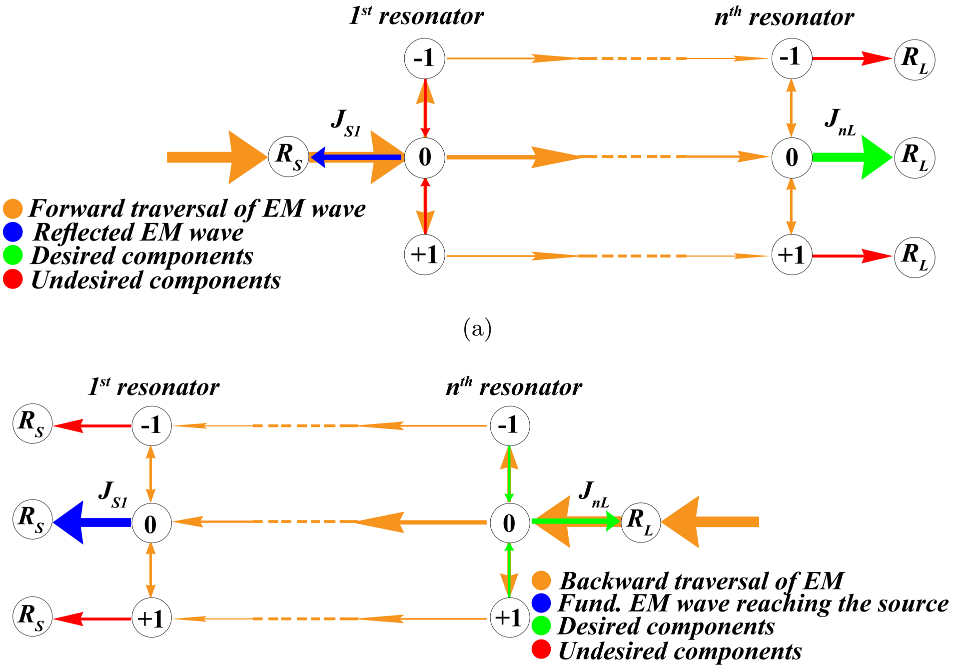

(a)

(b)

Figure 5.6: Traversal of EM wave in NR-BPF in (a) the forward direction (b) the reverse direction.

Analogously, in the backward direction (fig. 5.6(b)), deliberate reduction of EM energy reaching the source end at the center frequency (marked by the blue arrow) demands enhancing the energy reflected from the higher order harmonics back to the center frequency at the load end thereby increasing the energy reflected back to the load, ensuring adequate IL in the passband. This illustration gives an insight into the onset of the 3D coupling matrix explicitly explained in the next section. Further details about the dispersal of spectral energy have been illustrated in Chapter 2.

5.4 Evolution of 3D Coupling Matrix

A typical coupling matrix (CM) for a reciprocal filter network aids in understanding the resonator configurations as well as the inter-resonator couplings in the form of an admittance matrix between the source and the load. For a reciprocal network without any additional paths generated by the IM products, the EM wave travels from source to load, and the process can be represented by an $N+2$ reciprocal coupling matrix (RCM) [67] given by (5.35).

$$RCM = \begin{pmatrix} 0 & M_{S1} & 0 & 0 & 0 \\ M_{S1} & \lambda_1 & M_{12} & 0 & 0 \\ 0 & M_{12} & \lambda_2 & M_{23} & 0 \\ 0 & 0 & M_{23} & \lambda_3 & M_{3L} \\ 0 & 0 & 0 & M_{3L} & 0 \end{pmatrix} \tag{5.35}$$

where λ_i takes into consideration the i^{th} resonator starting from the source end and is given by

$$\lambda_i = fC_p(i) - \frac{1}{fL_p(i)} \tag{5.36}$$

$$\boldsymbol{\lambda_{n_i}} = \begin{pmatrix} AC_{p_i} - \frac{1}{AL_{p_i}} & A\frac{\zeta}{2}C_{p_i}e^{-j\phi} & 0 & 0 & 0 \\ B\frac{\zeta}{2}C_{p_i}e^{j\phi} & BC_{p_i} - \frac{1}{BL_{p_i}} & B\frac{\zeta}{2}C_{p_i}e^{-j\phi} & 0 & 0 \\ 0 & f\frac{\zeta}{2}C_{p_i}e^{j\phi} & fC_{p_i} - \frac{1}{fL_{p_i}} & f\frac{\zeta}{2}C_{p_i}e^{-j\phi} & 0 \\ 0 & 0 & \bar{B}\frac{\zeta}{2}C_{p_i}e^{j\phi} & \bar{B}C_{p_i} - \frac{1}{\bar{B}L_{p_i}} & \bar{B}\frac{\zeta}{2}C_{p_i}e^{-j\phi} \\ 0 & 0 & 0 & \bar{A}\frac{\zeta}{2}C_{p_i}e^{j\phi} & \bar{A}C_{p_i} - \frac{1}{\bar{A}L_{p_i}} \end{pmatrix} \tag{5.37}$$

$$A = f - 2f_m \quad \bar{A} = f + 2f_m \tag{5.37a, b}$$

$$B = f - f_m \quad \bar{B} = f + f_m \tag{5.37c, d}$$

where f is the frequency variable that sweeps through the band of interest, $C_p(i)$ and $L_p(i)$ represent the capacitance and inductance values that comprise the i^{th} resonator.

It is worthwhile mentioning that the coupling matrix values in (5.35) are normalized with respect to the lowpass prototype (LPP) values. The expression (5.36) has been intentionally expressed in the frequency domain to assist the numerical modeling; the additional 2π has been absorbed in the C_p and L_p values. λ_i is used to convert from LPP to bandpass prototype (BPP) domain. The L and C values obtained from this transformation may not be feasible for practical implementation; hence, the λ_i in (5.36) enables the choice of L_p and C_p values based on feasibility such that it matches the bandpass prototype values.

As the domain of analysis is shifted from reciprocal to non-reciprocal representation, the λ_i composed of time-invariant L and time-variant C splits up into harmonics owing to the generation of IM products as shown in Fig. 5.6. Hence, the same representation of RCM in (5.35) can now be represented in the form shown in Fig. 5.7 taking into consideration each additional horizontal line in Fig. 5.6 owing to the dispersion of spectral energy among the generated harmonics ($f \pm f_m$) due to spatio-temporal modulation. The form in Fig. 5.7 portrays a fascinating insight into the non-reciprocal phenomenon. The disbanding of individual resonators, represented by $\boldsymbol{\lambda_{n_i}}$ (given in (5.37)), into harmonic products, as explained in Chapter 3, results in the generation of separate layers of CM with each layer representing a particular harmonic product. On an interesting note, all the other coupling elements (M^x_{S1}, M^x_{12}, and so on) possess the same values. This denotes that the additional generation of resonators at harmonic frequencies generates separate RF paths apart from the fundamental alone, with the inter-resonator couplings or the source/load couplings having the same values in all the paths. Apart from the additional

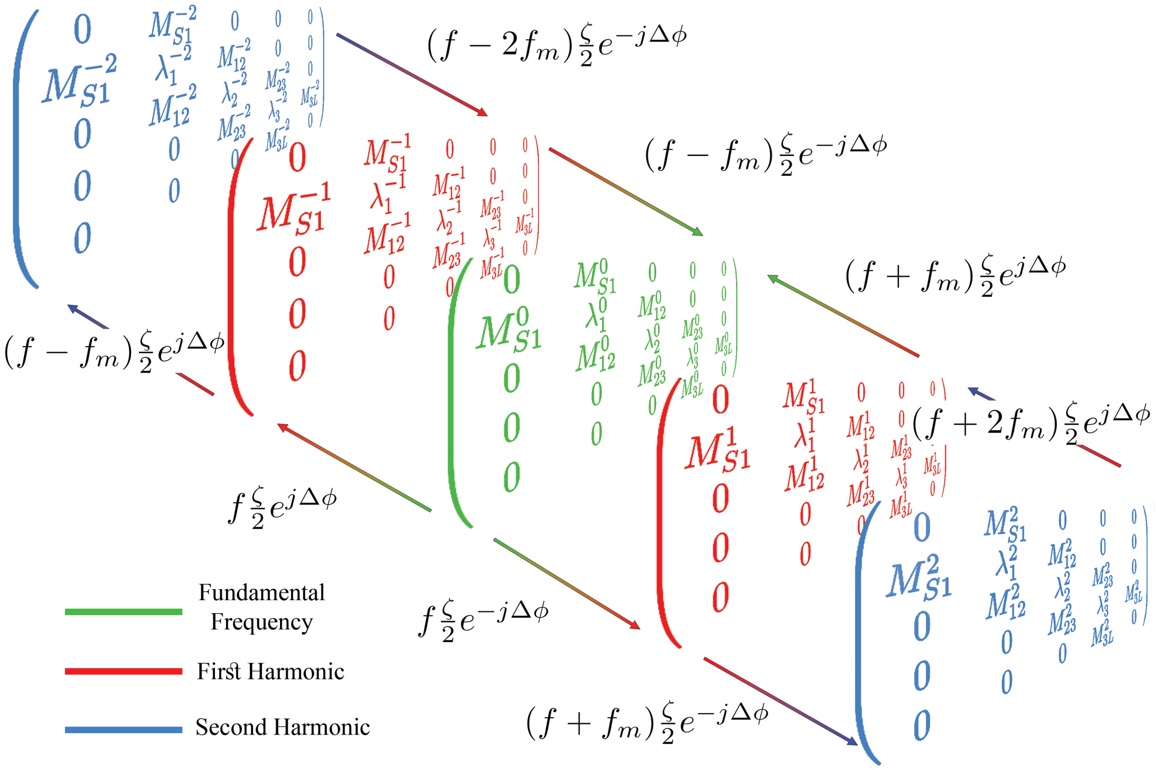

Figure 5.7: 3D non-reciprocal coupling matrix showing the additional couplings between each layer of spectral coupling matrices.

degrees of freedom for the RF signal, the link among the harmonically generated resonators is established with an additional inter-harmonic coupling. These two phenomena substantiate the generation of non-reciprocity in the filter characteristics.

Without loss of generality, the equations defining the S-parameters for a 3^{rd} order non-reciprocal circuit with the second resonator having a different combination than the first and the third resonator have been derived and are given in (5.38).

$$S_{11}=\frac{\mathbf{U}-2j\mathbf{R}(-j\mathbf{M}^2+\mathbf{R}\boldsymbol{\lambda}_{n_2}+j\boldsymbol{\lambda}_{n_1}\boldsymbol{\lambda}_{n_2})}{2\mathbf{M}^2\mathbf{R}+j\mathbf{M}^2\boldsymbol{\lambda}_{n_1}+j\mathbf{M}^2\boldsymbol{\lambda}_{n_3}+j\mathbf{R}^2\boldsymbol{\lambda}_{n_2}-\mathbf{R}\boldsymbol{\lambda}_{n_1}\boldsymbol{\lambda}_{n_2}-\mathbf{R}\boldsymbol{\lambda}_{n_2}\boldsymbol{\lambda}_{n_3}-j\boldsymbol{\lambda}_{n_1}\boldsymbol{\lambda}_{n_2}\boldsymbol{\lambda}_{n_3}} \tag{5.38a}$$

$$S_{21}=\frac{-2\mathbf{M}^2\mathbf{R}}{2\mathbf{M}^2\mathbf{R}+j\mathbf{M}^2\boldsymbol{\lambda}_{n_1}+j\mathbf{M}^2\boldsymbol{\lambda}_{n_3}+j\mathbf{R}^2\boldsymbol{\lambda}_{n_2}-\mathbf{R}\boldsymbol{\lambda}_{n_1}\boldsymbol{\lambda}_{n_2}-\mathbf{R}\boldsymbol{\lambda}_{n_2}\boldsymbol{\lambda}_{n_3}-j\boldsymbol{\lambda}_{n_1}\boldsymbol{\lambda}_{n_2}\boldsymbol{\lambda}_{n_3}} \tag{5.38b}$$

$$S_{22}=\frac{\mathbf{U}-2j\mathbf{R}(-j\mathbf{M}^2+\mathbf{R}\boldsymbol{\lambda}_{n_2}+j\boldsymbol{\lambda}_{n_3}\boldsymbol{\lambda}_{n_2})}{2\mathbf{M}^2\mathbf{R}+j\mathbf{M}^2\boldsymbol{\lambda}_{n_3}+j\mathbf{M}^2\boldsymbol{\lambda}_{n_1}+j\mathbf{R}^2\boldsymbol{\lambda}_{n_2}-\mathbf{R}\boldsymbol{\lambda}_{n_3}\boldsymbol{\lambda}_{n_2}-\mathbf{R}\boldsymbol{\lambda}_{n_2}\boldsymbol{\lambda}_{n_1}-j\boldsymbol{\lambda}_{n_3}\boldsymbol{\lambda}_{n_2}\boldsymbol{\lambda}_{n_1}} \tag{5.38c}$$

$$S_{12}=\frac{-2\mathbf{M}^2\mathbf{R}}{2\mathbf{M}^2\mathbf{R}+j\mathbf{M}^2\boldsymbol{\lambda}_{n_1}+j\mathbf{M}^2\boldsymbol{\lambda}_{n_3}+j\mathbf{R}^2\boldsymbol{\lambda}_{n_2}-\mathbf{R}\boldsymbol{\lambda}_{n_2}\boldsymbol{\lambda}_{n_1}-\mathbf{R}\boldsymbol{\lambda}_{n_2}\boldsymbol{\lambda}_{n_1}-j\boldsymbol{\lambda}_{n_3}\boldsymbol{\lambda}_{n_2}\boldsymbol{\lambda}_{n_1}} \tag{5.38d}$$

These equations have been framed after a series of spectral inverse operations collectively applied on all the layers of the 3D coupling matrix by considering matrix forms ($\boldsymbol{\lambda}_{n_i}$ given in (5.37)) instead of λ_i in (5.28) and (5.29) used in reciprocal cases. It should be noted that the coupling elements and the resonator configurations used in (5.38) no longer possess a single value; instead, each represents a spectral harmonic matrix at each frequency point of interest. The resonator configurations given by $\boldsymbol{\lambda_{n_i}}$ represent the spectral admittance matrix of the i^{th} resonator configuration. The frequency-independent couplings marked in bold vectorially represent the spectral scattering at the onset of spatio-temporal modulation, i.e., $\mathbf{M_{a,b}} = M_{a,b}\mathbf{U}$ where $\mathbf{U}$ represents the identity matrix having a dimension equivalent to the order of the spectral matrix taken into consideration. The equations in (5.38) deal solely with non-cross-coupled circuits and convert the domain of $N + 2$ coupling matrix into the domain of harmonic representation, where at each frequency point, a spectral matrix is generated having the order equal to the maximum order of the harmonic contents selected for achieving non-reciprocity. A clear indication of the origin of non-reciprocity sprouts from the difference in (5.38c) and (5.38d), which owes to the generation of IM products due to STM. It is to be noted that only the central element in the matrices presented in (5.38) represents the fractional power conversion at the fundamental; the other elements in the matrix represent the inter-harmonic spectral power conversion. In fact, all the elements collectively participate in generating non-reciprocity at the fundamental frequency. In the reciprocal scenario, the $\boldsymbol{\lambda_{n_i}}$ of all the resonators would be the same resulting in a perfect match between the S_{21} and S_{12}. These four equations, first of their kind in the literature, provide an analytical insight into the underlying phenomenon behind the manifestation of non-reciprocity.

On a similar note, the non-reciprocal S-parameter equations that can deal with cross-coupled networks demand cross-coupling elements in CM representations, as has been shown in the FCM of (5.23), are given in (5.39). In these cases, the additional cross-couplings and FIR elements need to be considered. In (5.39), $\mathbf{U}$ denotes the unitary matrix whose order is determined by the maximum number of spectral harmonics apart from the fundamental considered for analysis, λ_i represents the bandpass transformation values for the resonator at i^{th} position from the source end, $\mathbf{M_{ij}} = M_{ij}\mathbf{U}$ represents the coupling elements, $\mathbf{F_i} = F_i\mathbf{U}$ represents the FIR elements, and $\mathbf{R} = R\mathbf{U}$ represents the source/load transformed impedances, where $R = M_{S1}^2$ and the multiplication of the additional unitary matrix to each of the components account for the additional coupling matrix generated at the spectral harmonic frequencies.

5.5 Numerical Analysis Results and Discussions

The discussions on the 3D coupling matrix and the flagship equations laid down in the previous sections can be used to directly compute the non-reciprocal phenomena for different 3^{rd} order filter configurations. It must be noted that although the equations have been designed only for 3^{rd} order synchronously tuned filters having the same coupling index M between each resonator, the same can be modified for any ordered filters even with cross-couplings involved.

Numerical simulations have been carried out using the equations for varying frequency ranges, as shown in Fig. 6.3. The frequency bands shown in the figure are broadly used in the 5G spectrum of mobile communications. These bands are specifically chosen to minimize the efforts required to develop NR-BPF in these bands starting from scratch; the parametric values obtained in these graphs can be used to manifest non-reciprocity with very fine or minimal tuning. The sequential design steps of an NR-BPF are given below:

Step 1: Based on feasibility, an appropriate capacitance value (C_{p_i}) is chosen; this might be the unbiased capacitance value of the chosen varactor diode.

Step 2: Inductance values (L_{p_i}) are obtained for each resonator from the chosen capacitance values.

Step 3: Calculate λ_i using (5.36) for all the frequencies.

Step 4: Construct the CM to obtain the coupling coefficiencts using the λ_i values and the desired IL and RL [13].

Step 5: Initialize the parameters ζ, f_m, and $\Delta\phi$ and construct $\boldsymbol{\lambda_{n_i}}$ from (5.37).

Step 6: Parametrically modify the parameters iteratively to achieve a proper non-reciprocity in the passband using (5.37) and (5.38).

Fig. 6.3 shows that adequate directivity (S_{21}(dB)-S_{12}(dB)) is achieved in all the cases. All the plots have revealed an IL < 1 dB, RL > 15 dB and $S_{12} < -20$ dB within the passband. Further, the plots reveal the origin of two finite transmission zeroes (TZs) in the non-reciprocal response, although the reciprocal response is designed for an all-pole filter. This phenomenon

$$S_{11(22)} = \frac{\mathbf{U} - 2j\mathbf{R}(-\mathbf{M_{23}}^2 + \mathbf{F_1}\boldsymbol{\lambda_2} + \mathbf{F_2}\boldsymbol{\lambda_3}(\boldsymbol{\lambda_1}) - j\mathbf{R}\boldsymbol{\lambda_2} + \boldsymbol{\lambda_2}\boldsymbol{\lambda_3}(\boldsymbol{\lambda_1}) + \mathbf{F_1}\mathbf{F_2} - j\mathbf{F_2}\mathbf{R})}{\mathbf{F_1}\mathbf{A} - \mathbf{F_1^2}\mathbf{B} - j\mathbf{R_1}\mathbf{C} + \boldsymbol{\lambda_1}(\boldsymbol{\lambda_3})\boldsymbol{D} + \boldsymbol{\lambda_2}\boldsymbol{E} + \boldsymbol{\lambda_3}(\boldsymbol{\lambda_1})\boldsymbol{E} - 2\mathbf{M_{12}}\mathbf{M_{13}}\mathbf{M_{23}} - \boldsymbol{\lambda_1}(\boldsymbol{\lambda_3})\boldsymbol{\lambda_2}\boldsymbol{\lambda_3}(\boldsymbol{\lambda_1})} \tag{5.39a}$$

$$S_{21(12)} = \frac{-2j\mathbf{R}(-\mathbf{M_{13}}\boldsymbol{\lambda_2} + \mathbf{F_2}\mathbf{M_{13}} - \mathbf{M_{12}}\mathbf{M_{23}})}{\mathbf{F_1}\mathbf{A} - \mathbf{F_1^2}\mathbf{B} - j\mathbf{R_1}\mathbf{C} + \boldsymbol{\lambda_1}(\boldsymbol{\lambda_3})\boldsymbol{D} + \boldsymbol{\lambda_2}\boldsymbol{E} + \boldsymbol{\lambda_3}(\boldsymbol{\lambda_1})\boldsymbol{E} - 2\mathbf{M_{12}}\mathbf{M_{13}}\mathbf{M_{23}} - \boldsymbol{\lambda_1}(\boldsymbol{\lambda_3})\boldsymbol{\lambda_2}\boldsymbol{\lambda_3}(\boldsymbol{\lambda_1})} \tag{5.39b}$$

$$\mathbf{A} = \mathbf{M_{12}^2} + \mathbf{M_{23}^2} + 2j\boldsymbol{R_1}\boldsymbol{\lambda_2} - \boldsymbol{\lambda_1}\boldsymbol{\lambda_2} - \boldsymbol{\lambda_2}\boldsymbol{\lambda_3} \quad \mathbf{B} = \boldsymbol{F_2} + \boldsymbol{\lambda_2} \tag{5.39c,d}$$

$$\mathbf{C} = \mathbf{M_{13}^2} + \mathbf{R_1^2} + j\boldsymbol{\lambda_1}\boldsymbol{R} + \boldsymbol{R}\boldsymbol{\lambda_3} - \boldsymbol{\lambda_1}\boldsymbol{\lambda_3} \quad \mathbf{D} = \mathbf{M_{12}^2} + \mathbf{M_{23}^2} - 2\boldsymbol{F_1}\boldsymbol{F_2} - \boldsymbol{\lambda_1}\boldsymbol{\lambda_2} - \boldsymbol{\lambda_2}\boldsymbol{\lambda_3} \tag{5.39e,f}$$

$$\mathbf{E} = \mathbf{M_{23}^2} - \mathbf{F_1}\mathbf{F_2} \quad \mathbf{F} = \mathbf{M_{13}^2} + \mathbf{R^2} \quad \mathbf{G} = \mathbf{M_{12}^2} - \mathbf{F_1}\mathbf{F_2} \tag{5.39g,h,i}$$

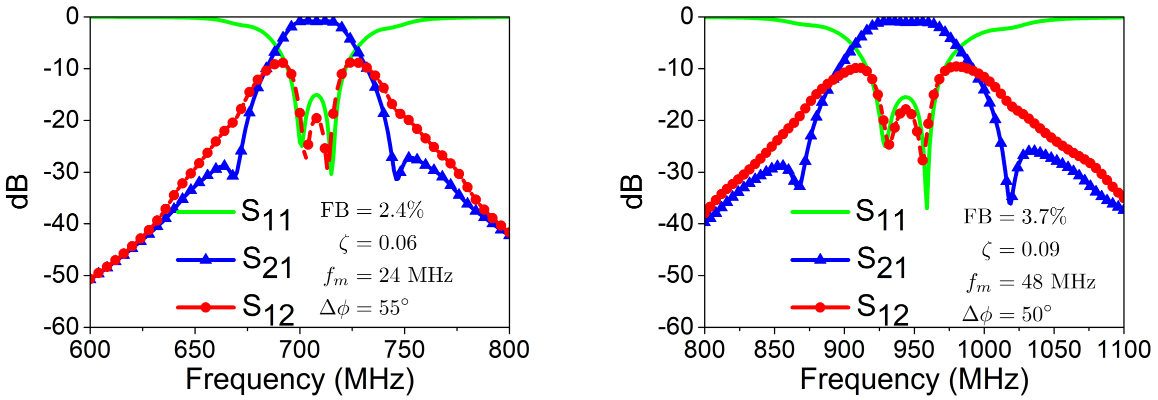

(a) n12 Uplink (b) n8 Downlink

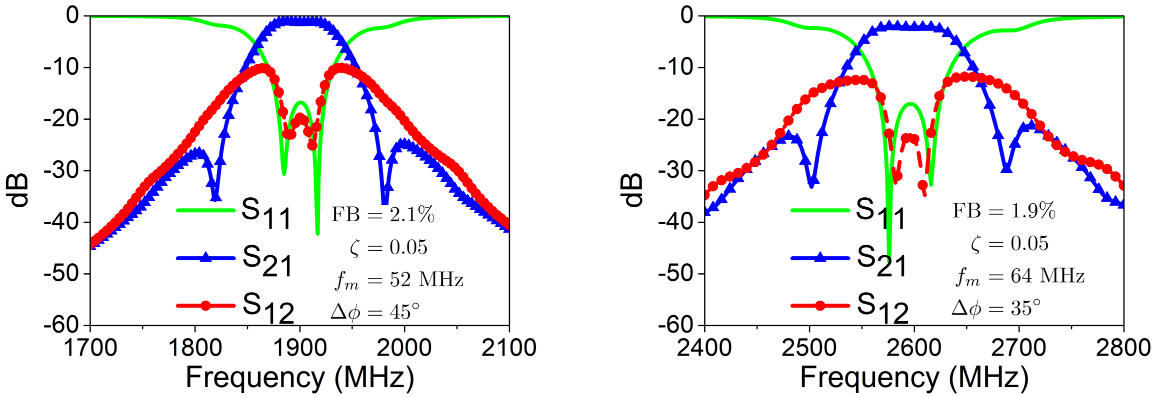

(c) n39 (d) n38

Figure 5.8: Numerical simulation results in the 5G NR operating bands in FR1 for (a) n12 Uplink (699 MHz - 716 MHz), (b) n8 Downlink (925 MHz - 960 MHz), (c) n39 (1880 MHz - 1920 MHz) and (d) n38 (2570 MHz - 2620 MHz).

confirms the generation of the 3D coupling matrix wherein the traversal of RF energy occurs not only through the adjacent resonators at the fundamental frequency (middle green coloured matrix in Fig. 5.7) which would only manifest an all-pole response, but also through the non-adjacent resonators and between the resonators and the load owing to the couplings generated at the harmonic frequencies (red and blue coloured matrices in Fig. 5.7). Apart from generating non-reciprocity, this phenomenon enhances the selectivity of the filter suitable for mobile communication applications.

Interesting results can be obtained from the study of parametric variations. The ζ values are directly proportional to the filter's fractional bandwidth (FB). Thus, the varactors to be implemented for a filter with a higher fractional bandwidth must have a steeper capacitance-voltage (CV) curve to narrow down the reverse voltage tuning range. The modulation frequency f_m should be slightly higher than the filter bandwidth, which promotes the RF energy in the backward direction to fall outside the passband. For a lower value of the f_m, the separation between the two TZs of the S_{12} curve converges to a single point with high isolation only at the center frequency. Similarly, the variation of $\Delta\phi$ indicates that it is indirectly proportional to the frequency range of the filter.

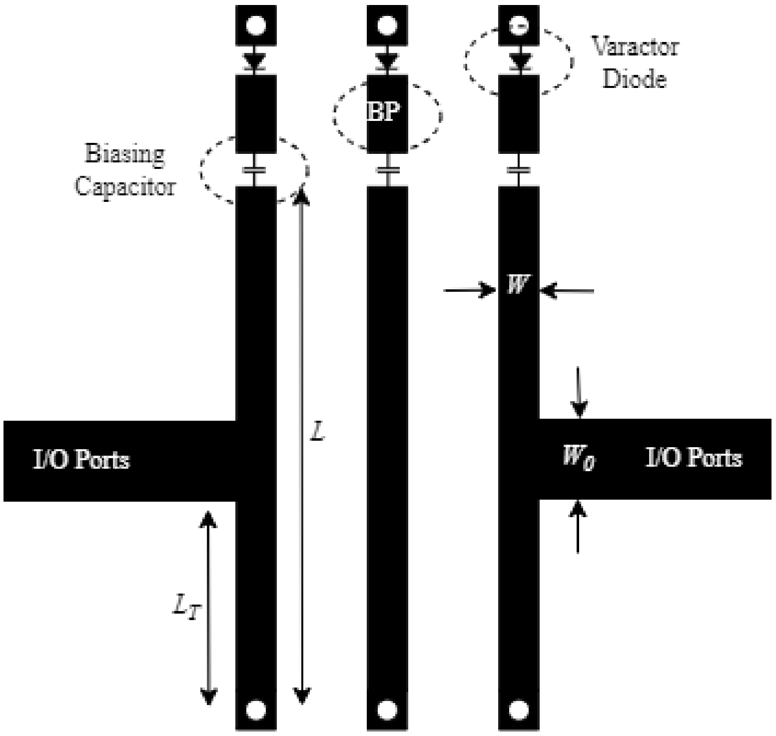

Figure 5.9: Schematic of the third-order combline architecture.

5.6 EM Simulated Results and Practical Implementations

The design steps enumerated above can be utilized to construct NR-BPFs in either lumped or distributed domains. As an example, a cross-coupled EM simulated 3rd order combline structure is shown in Fig. 5.9. It consists of an input-tapped varactor-loaded combline configuration. The $N+2$ cross-coupled reciprocal CM synthesized at a center frequency of 854 MHz with a bandwidth of 35 MHz is given below.

$$FCM_R = \begin{bmatrix} 0 & 1.2214 & 0 & 0 & 0 \\ 1.2214 & 0.0954 & 1.1834 & 0.3188 & 0 \\ 0 & 1.1834 & -0.308 & 1.1834 & 0 \\ 0 & 0.3488 & 1.1834 & 0.0954 & 1.2214 \\ 0 & 0 & 0 & 1.2214 & 0 \end{bmatrix} \tag{5.40}$$

The resonator lengths, the adjacent resonator gaps, and the tapped positions are tuned to match the coupling matrix values and the external quality factors. Specifically, the resonator widths are set to be 70 Ω, and the lengths are a little less than $\lambda_g/4$ and are accounted by the series combination of capacitor and varactor which increases the length of the resonator. The tapped position is adjusted to account for the source and load couplings with the first and last resonator, respectively. The dimensions of the architecture given in Fig. 5.9 are $L = 3.64$ cm, $W = 2.9$ mm, $L_T = 1$ mm, and $W_0 = 2.378$ mm. The acronym BP represents the biasing points where the external bias is applied through a choke inductor. The varactor diode used is SMV1237 and the capacitor used is 3.3 pF. The capacitors are used to prevent the grounding of the DC signals. The combline configuration features a compact and tunable bandpass filter as compared to interdigitated or open-loop resonator configuration. The non-adjacent resonator couplings in this configuration add a transmission zero at the upper passband edge, thereby enhancing the skirt frequency response without any additional source-load coupling circuitry.

The EM simulated reciprocal response is shown in Fig. 5.10a. The results show a clear tunable response varying from 858 MHz to 937 MHz having a bandwidth of almost 35 MHz for the first band to about 30 MHz for the last band. The varactor diode used is SMV1237 from Skyworks. The response shows clear tunability varying from 854 MHz to 935 MHz with a bandwidth of almost 30-35 MHz. The insertion loss variation throughout the tunability range is almost 2.3 dB to 2.6 dB with a return loss of more than 20 dB throughout the range. The results reveal a TZ placed at the upper passband edge owing to the generation of FIR elements due to asynchronous tuning and non-adjacent resonator coupling in the combline architecture.

The corresponding non-reciprocal responses throughout the tunability range are given in Fig. 5.10b. The insertion loss (IL) for the non-reciprocal response is varying from 3.7 dB to 4.1 dB and is fairly comparable to the other tunable non-reciprocal circuits. The return loss (RL) is more than 20 dB for the entire tunability range and the isolation is also more than 20 dB for all the bands except the last one at the frequency of 935 MHz where it is almost 18 dB, nevertheless, it's a fair rejection as for the backward wave is concerned. It is to be noted that the tuning range of this reciprocal circuit is far more than is portrayed in the results. The limited tuning range is to account for the tradeoffs associated with increased IL and reduction of bandwidth in the non-reciprocal case. A fair bandwidth is considered which is apt for the usage in any 5G bands.

In the lumped domain, an NR-BPF has been implemented with lumped elements at 150 MHz with a fractional bandwidth of 10% to enhance comprehensibility. The schematic, component values, and the resonator configuration is shown in Fig. 5.5(b) and (c). The varactor used is SMV1236 and the coupling coefficients for the desired f_0 and bandwidth are calculated and are given by $R^2 = M_{S1} = M_{3L} = 1.8664$ and $M = M_{12} = M_{23} = 1.4549$. These values are then applied to the spectral S-parameter equations using $\zeta = 0.16$, $f_m = 13$ MHz and $\Delta\phi = 50^\circ$ to manifest the non-reciprocal phenomenon. The fabricated prototype and the corresponding S-parameters comply well with the numerical model and are shown in Fig. 5.11. The AC and DC biasing are set to achieve the desired capacitance variations based on the ζ values. Reverse isolation of approximately 18 dB is incurred with a minimum IL of 1.5 dB and a forward RL better than 17 dB in the measured results, and the detailed filter specifications are shown

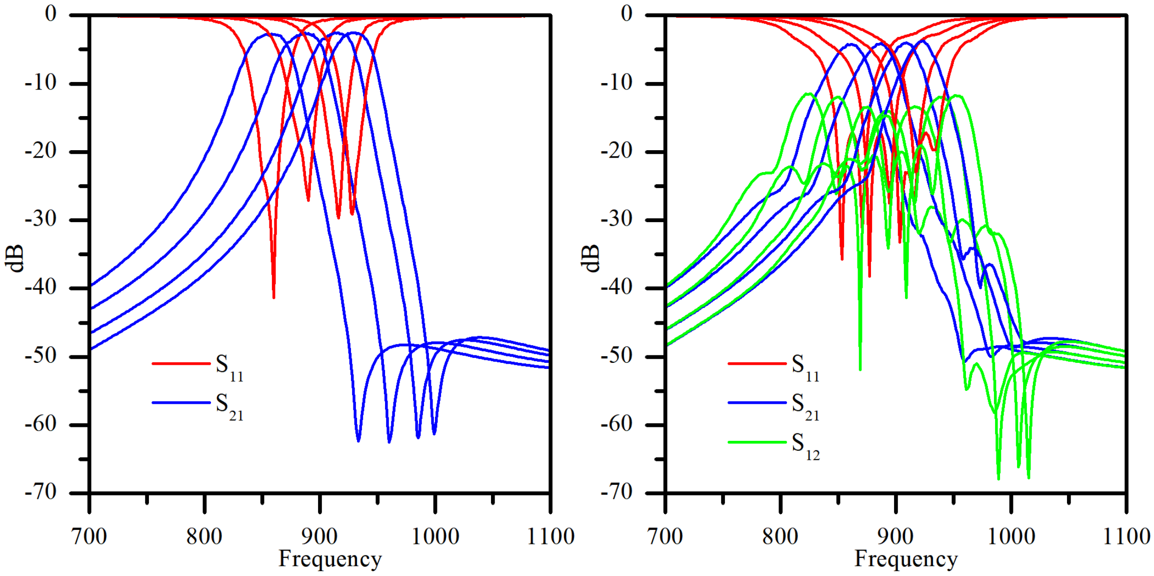

(a) Reciprocal response (b) Non-reciprocal response

Figure 5.10: The EM simulated response of the combline architecture.

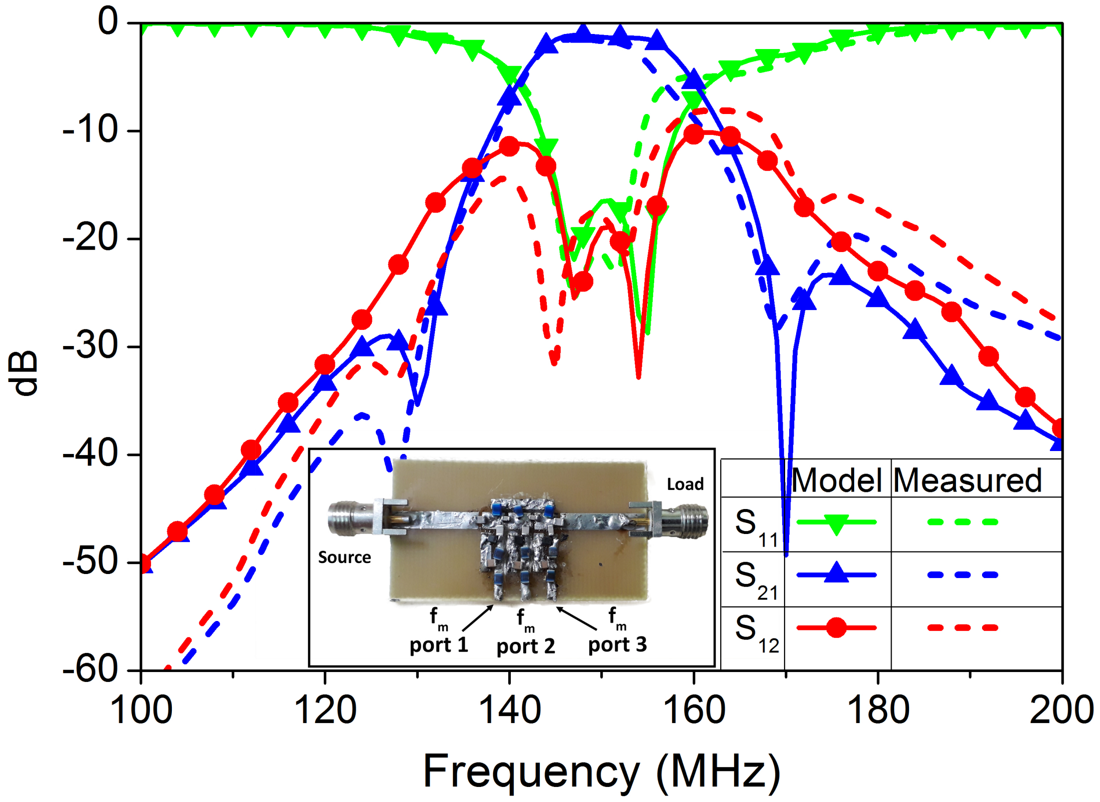

Figure 5.11: The experimental validation of the model. The fabricated circuit (inset)

in Table 5.1. The results clearly reveal the onset of two distinct transmission zeroes at the passband edges owing to the additional couplings between non-adjacent resonators and between the resonators and the load generated due to the non-reciprocal phenomenon as is evident from the 3D coupling matrix.

Table 5.1: Filter Specifications

Sl. No.	Parameter	Model	Experiment
1.	Center Frequency	150 MHz	149.3 MHz
2.	Bandwidth	15 MHz	14.6 MHz
3.	Insertion Loss	1.38 dB	1.5 dB
4.	Return Loss	17 dB	17 dB
5.	Isolation	$\approx$ 20 dB	$\approx$ 18 dB

5.7 Conclusion

In this chapter, the concept of a 3D coupling matrix has been demonstrated for the first time to deal with spatio-temporal non-reciprocal bandpass filters. The conversion from 2D to 3D coupling matrix has been supplemented with the derivation of flagship equations capable of directly computing the S-parameters for direct-coupled as well as cross-coupled structures without delving into spectral admittance conversions. These equations have been used to numerically design non-reciprocal bandpass filters in four 5G mobile communication bands. The parameters extracted can be directly used in hardware implementations, and the process has been demonstrated with the implementation of non-reciprocity in both distributed and lumped filter designs. The equations, first of their kind, can be improved to incorporate complex cross-couplings that can be used to design more selective filters with enhanced skirt frequency characteristics.

5.8 Publications

1. **Prantik Dutta**, Gande Arun Kumar, Gopi Ram, ”Numerical Design of Non-Reciprocal Bandpass Filters With the Aid of 3D Coupling Matrix for 5G Bands”, *IEEE Transactions on Circuits and Systems II: Express Briefs*, vol. 69, no. 7, pp. 3334-3338, July 2022, doi: 10.1109/TCSII.2022.3157644.

2. **P. Dutta**, G. A. Kumar, G. Ram and D. S. Varma, ”Compact Tunable Non-Reciprocal Bandpass Filter with the aid of Combline Architecture,” 2022 IEEE Microwaves, Antennas, and Propagation Conference (MAPCON), Bangalore, India, 2022, pp. 1003-1006, doi: 10.1109/MAPCON56011.2022.10047764.

Chapter 6

Coupling Matrix Representation of Dual-band Bandpass Filter with a Single-band Non-reciprocity

6.1 Introduction

The evolving approach of designing non-reciprocal bandpass filters (NR-BPF) utilizing the concept of spatio-temporal modulation (STM) has recently grabbed significant attention. The target application of these NR-BPFs in modern transceiver systems allows filtering in one direction with simultaneous isolation in the opposite direction. The present-day miniaturization and integration scenario demands multi-band filters to cater to the overwhelming magnitude of space sophistications. A breakthrough in integrability can be attained if compact multi-band isolating filters are instrumental in replacing separate entities of filter and isolator; therein lies the impetus behind the inception of a cost-effective and miniaturized dual-band NR-BPF to be equipped in monolithic integrations. Recently, dual-band and triple-band NR-BPFs using lumped realizations have been put forth in [51] and [12], respectively, which present the design and validation of multiband isolators and circulators with reconfigurable bandpass filtering capabilities. These devices utilize frequency-tunable and spatiotemporally modulated resonators to shape transversal frequency-selective signal paths. Each path creates an independently controllable passband in terms of frequency and direction of propagation. This allows the overall network to have multiple non-reciprocal passbands that can be reconfigured. Three lumped-element prototypes were implemented at the VHF band, achieving high in-band isolation and frequency tuning with directional changes.

In this chapter, a novel coupling matrix (CM) synthesis technique of dual-band BPF with a single-band non-reciprocity is proposed. The holistic synthesis technique combines the characteristic polynomials of the individual bands scaled and shifted to their individual lower or upper bands. This method has the advantage of having independent access to the CM elements framing the individual bands, thereby allowing the spatio-temporal modulation (STM) of the desired band to achieve non-reciprocity with the aid of harmonic or intermodulation (IM) products. The CM combines a 3^{rd} order BPF configuration for the first band with a sharp transmission zero (TZ) at the upper edge with a 2^{nd} order dual-mode configuration for the second band. STM is then applied to the first band to obtain an isolating filter response without interference on the second band. The veracity of the synthesized CM is substantiated by the design of compact, closely-spaced dual-band BPF that integrates a 3^{rd} order varactor-loaded combline configuration exhibiting the first non-reciprocal band and a dual-mode varactor integrated U-shaped structure loaded with a short-circuited stub resulting in the second band. The varactor-integrated second band is also modeled with the aid of even-odd mode analysis which gives a clear indication of the dual-mode behaviour. The chapter commences with a brief introduction to the concept of STM, along with its unconventional non-reciprocal CM representation. This is followed by an elaborative approach to the theoretical foundation behind the synthesis of the dual-band CM. The subsequent section deals with the generation of non-reciprocal response in the first band owing to the time-modulation of the first band with suitable circuit parameters, and is eventually followed by the experimental validation. The proposed CM synthesis approach, the first of its kind in the dual-band regime of non-reciprocal bandpass filters, finds a versatile domain of application in modern NR-BPF designs.

6.2 Spatio-temporal modulation and the corresponding coupling matrix representation

This section buttresses the foundations behind the onset of non-reciprocity in spatio-temporally modulated NR-BPFs starting with a single time-modulated resonator. Further, for a smooth transition into the holistic synthesis of dual-band non-reciprocal coupling matrix, a general theory of unconventional non-reciprocal coupling matrix is provided to enhance the comprehensibility of the phenomenon.

6.2.1 Temporally modulated resonator and the onset of non-reciprocity

This section deals with a single time-modulated resonator loaded at either end with a capacitor having a capacitance of C_B and a varactor diode with a nominal capacitance value of C_V as shown in Fig. 6.1. The varactor diode is modulated with a time-varying sinusoidal signal via a choke inductor, and the overall time-varying capacitance $C_T(t) = C_V(t) + C_B$ obtained by the parallel configuration follows the time-modulated equation given by eq. (6.1).

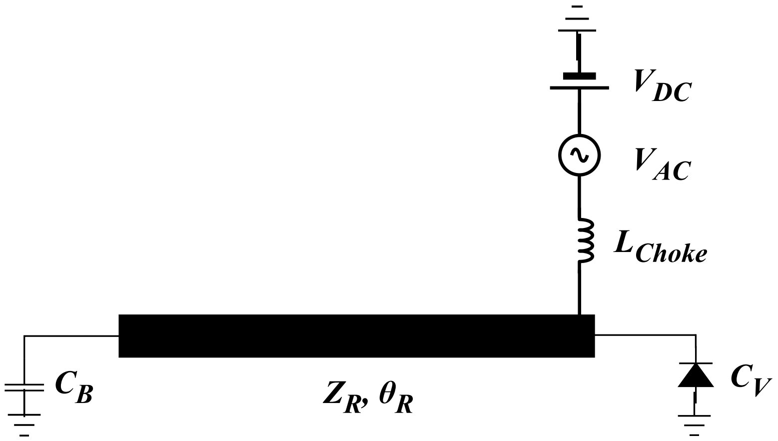

Figure 6.1: Time-modulated resonator configuration.

$$C_T(t) = C_{T0} + \Delta C_T \cos(2\pi f_m t + \phi) \tag{6.1}$$

where C_{T0} is the DC or the nominal capacitance directly linked with the DC biasing (V_{DC}) applied while the sinusoidal variation of the capacitance, owing to the AC biasing (V_{AC}), is given by ΔC_T, and the ratio of the two is termed as the modulation index (ζ), where $\zeta = \Delta C_T / C_{T0}$. The modulation frequency is given by f_m while the phase of the sinusoidal signal applied to the resonator is given by ϕ. The term spatio-temporally modulated resonator refers to the temporal modulation of space-separated resonators with a finite modulation frequency (f_m), modulation index (ζ), and an incremental phase difference ($\Delta\phi$) between the signals applied to the successive resonators starting with 0° for the first resonator to $n\Delta\phi$ for the n^{th} resonator. Spatio-temporal modulation engenders a non-uniform distribution of RF power among the generated IM products in the opposite directions, and a judicious choice of the circuit parameters (ζ, f_m, and $\Delta\phi$) manifests non-reciprocal filtering isolator response [1].

6.2.2 The General non-reciprocal CM representation

The conventional CM in reciprocal filter design represents the relationships between the input and output ports of the filter. It characterizes the transfer of energy and signals between different ports and provides important information about the filter's performance. The reciprocal CM (shown in Fig. 5.35) with its corresponding synthesis and application has already been detailed in Chapter 5. The general non-reciprocal coupling matrix representation deals with the dismantling of sequential resonators at harmonic positions apart from the center frequency. A typical 3^{rd} order non-reciprocal CM can be represented in the form given in eq. (6.2).

$$\bar{M} = \begin{pmatrix} 0 & M_{S1} & M_{S2} & M_{S3} & M_{SL} \\ M_{S1} & \bar{\lambda_1} & M_{12} & M_{13} & M_{1L} \\ M_{S2} & M_{21} & \bar{\lambda_2} & M_{23} & M_{2L} \\ M_{S3} & M_{31} & M_{32} & \bar{\lambda_3} & M_{3L} \\ M_{SL} & M_{1L} & M_{2L} & M_{3L} & 0 \end{pmatrix} \tag{6.2}$$

where $\bar{\lambda_i}$ represents not only the LPP to BPP transformation of the i^{th} resonator but also considers the harmonic products generated by time-modulation of the corresponding varactor diode at that node as given in eq. (6.3).

$$\bar{\lambda_1} = j\bar{\omega_0}C_0 + \frac{j}{\bar{\omega_0}L_0} \tag{6.3}$$

where $\bar{\omega_0}$ takes into account all the IM products generated by the temporally modulated resonator and differs from ω_0 in the conventional CM formulation as shown in [95]. The primary advantage of CM is the enhancement in the degrees of freedom in the filter design, which enables the incorporation of a variety of cross-couplings between non-adjacent resonators.

6.3 Analytical formulation of Dual-band BPF

The coupling matrix analysis of dual-band BPFs begins with the construction of an efficient filter polynomial capable of characterizing the dual-band response. Apart from possessing the characteristics of the individual bands, the resultant filtering polynomial and eventually the generated CM should have dedicated control over the respective bands. This phenomenon can be achieved by a reciprocal summation of the individual filtering polynomials in the following manner

$$C_{N_R}(\omega) = \frac{1}{\frac{1}{C_{N_1}(\omega)} + \frac{1}{C_{N_2}(\omega)}} \tag{6.4}$$

where, $C_{N_R}(\omega)$ is the resultant characteristic filter polynomial after combining the two filters having characteristic polynomials $C_{N_1}(\omega)$ and $C_{N_2}(\omega)$. However, the polynomials $C_{N_k}(\omega)$ ($k = 1$ ... no. of passbands) are originally in the lowpass prototype domain, and the mere merging of multiple polynomials would result in a superposition in the same frequency range. Therefore, each of the polynomials should be shifted to the desired frequency determined by the conversion from the bandpass to lowpass domain. Additionally, the lowpass prototype to bandpass prototype conversion takes a form given below.

$$\omega_{LPP} = \frac{1}{FBW_T}\left(\frac{\omega_{BPP}}{\omega_{BP_T}} - \frac{\omega_{BP_T}}{\omega_{BPP}}\right) \tag{6.5}$$

where ω_{LPP} and ω_{BPP} denotes the angular frequency in the lowpass prototype (LPP) and bandpass prototype (BPP) domain, respectively. BP_T and FBW_T denote the overall center frequency and fractional bandwidth, respectively. The overall center frequency is obtained by averaging the lowest band-edge frequency of the lowest band with the highest band-edge frequency of the upper band. Similarly, the overall bandwidth is the difference between the highest band-edge frequency of the upper band and the lowest band-edge frequency of the lowest band.

The proposed analytical methodology combines the design strategies of a 3^{rd} order conventional bandpass filter with a 2^{nd} order dual-mode configuration coupled through a common source/load structure. The notion behind such a combination is to have a non-reciprocal band manifested by the 3^{rd} order configuration with a reciprocal second band at any arbitrary frequency. It is worthwhile mentioning that a distinct TZ should be placed between the two bands to realize a sharp rejection. This can be accomplished by incorporating a TZ at the upper passband edge of the first band with a suitable cross-coupling scheme; the engineering of the second band happens to be quite complex as the degrees of freedom for cross-coupling schemes reduce owing to a lower order dual-mode configuration.

The comprehensive approach towards a successful dual-band coupling matrix configuration begins with the polynomial synthesis of the individual bands, followed by a systematic combination of the generated polynomials into a dual-band characteristic polynomial. The subsequent steps generate the overall traversal coupling matrix from the generated polynomial using the conventional residue method, as demonstrated in [96]. Before delving into the analysis of individual bands separately, the systematic approach toward the generation of the dual-band CM from the individual characteristics is enumerated below:

Step 1: The desired center frequency (CF), bandwidth, order, and position of TZs are chosen.

Step 2: The CF and the TZ positions are transformed from BPP to LPP domain.

Step 3: The obtained LPP domain CF and TZ values are then passed on to the conventional recursive technique to obtain the reflection polynomial $F(s)$.

Step 4: The roots of $F(s)$ and the TZ values are then transformed to the lower and upper end of the initial BPP spectrum for the lower and upper band, respectively.

Step 5: The transmission polynomial $P(s)$ is thereafter obtained from the modified TZ position while the value of the ripple factor (ϵ) is calculated from the magnitude of the modified polynomial ratio.

Step 6: Finally, the reciprocal of the overall characteristic polynomial $C(s)$ is obtained by the reciprocal addition of the individual characteristic polynomials.

Step 7: Pivoting and folding is done on the individual coupling matrices obtained for both bands, followed by the merging of the resultant folded coupling matrices into the final dual-band CM.

The comprehensive analysis can be segregated into a separate lower-band and upper-band analysis.

6.3.1 The Lower band

The characteristic polynomial of a 3^{rd} order BPF configuration with a TZ at the upper passband edge is modeled based on the center frequency, bandwidth, and the desired position of the TZ. In this case, the center frequency of the lower band is chosen to be around 550 MHz with a bandwidth of 35 MHz and having a distinct TZ zero placed at around 656 MHz. However, the center frequency can be translated to accomodate any 5G FR1 bands. The corresponding LPP domain position of the TZ for a return loss (RL) of 20 dB is obtained at 5.5676. Correspondingly, the recursive technique is applied on the LPP domain TZ to obtain the roots of the $F(s)$ polynomial. An interesting equation in dealing with the shifting and scaling of the TZ and the $F(s)$ roots is given in eq. (6.6).

$$x' = \frac{x \pm \frac{CF}{1-CF}}{\frac{1}{1-CF}} \tag{6.6}$$

where x refers to either the $F(s)$ roots or the original TZ position and x' represents the modified values, CF represents the LPP domain center frequency after BPP to LPP transformation, given by (6.5), for the upper and the lower band [96]. The corresponding $N+2$ coupling matrix $M1$ for the lower band after the conventional orthogonalization procedure is given by eq. (6.7).

$$M1 = \begin{pmatrix} 0 & -0.65 & 0 & 0 & 0 \\ -0.65 & 5.5 & 0.38 & 0.035 & 0 \\ 0 & 0.38 & 5.46 & 0.38 & 0 \\ 0 & 0.035 & 0.38 & 5.5 & 0.65 \\ 0 & 0 & 0 & 0.65 & 0 \end{pmatrix} \tag{6.7}$$

To realize a simplified circuit that can faithfully establish such a CM given by eq. (6.7), the varactor-loaded combline configuration is chosen as this structure is compact and promotes a TZ at the upper passband edge due to its default 1^{st} to 3^{rd} resonator cross-coupling. This self-engineered coupling configuration precludes the deployment of any additional cross-coupling circuitry. The filter configuration is shown in Fig. 6.2(a), in which the resonant frequency depends on the length (L_c) and width (W_c) of the resonators along with the overall capacitance of the varactor diodes (C_{v1} and C_{v2}) and the DC blocking capacitors (C_1) loaded at both ends of each resonator. In contrast, the bandwidth of the response depends on the input/output coupling gaps (S_1) and coupling gaps between the strips (S_2).

Fig. 6.3(a) compares the simulated response of the 3^{rd} order combline configuration with that obtained from the CM model. As explained, a TZ is observed at the upper out-of-band region, which, as will be dealt with in the overall response, promotes a sharp rejection between the bands, thereby enhancing the dual-band characteristics.

6.3.2 The Upper band

The proposed upper band synthesis is somewhat intriguing with the introduction of dual modes to manifest the 2^{nd} order response. The dual-mode response is segregated into two single-mode responses, each resonating at the individual reflection zeroes of the desired 2^{nd} order frequency response. The combination of the characteristics of the two single-mode responses into the dual-mode characteristic polynomial and the successive CM synthesis of the overall upper band response is the same as that of the lower band. The dual-mode CM of the second band operating at 980 MHz with a bandwidth of 70 MHz is given by (6.8). This can also be equipped to operate

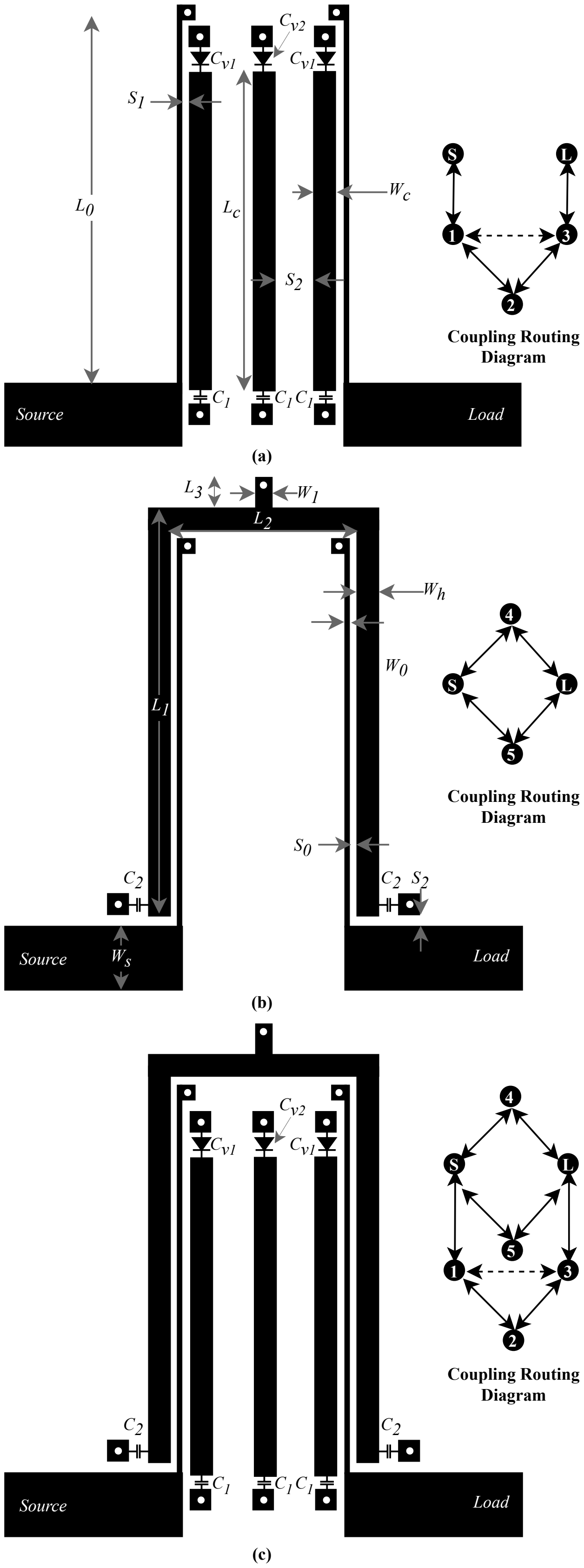

Figure 6.2: (a) The 3^{rd} order Combline portion of the circuit manifesting the lower band, (b) the dual-mode configuration, (c) the overall circuit.

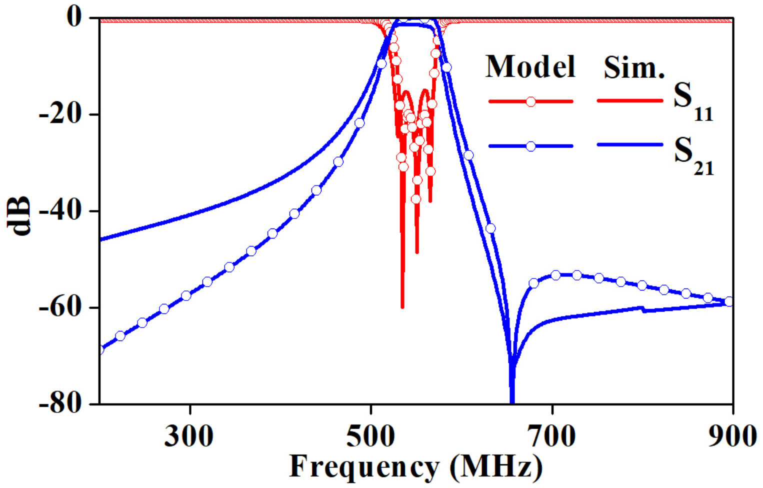

(a) The Lower band

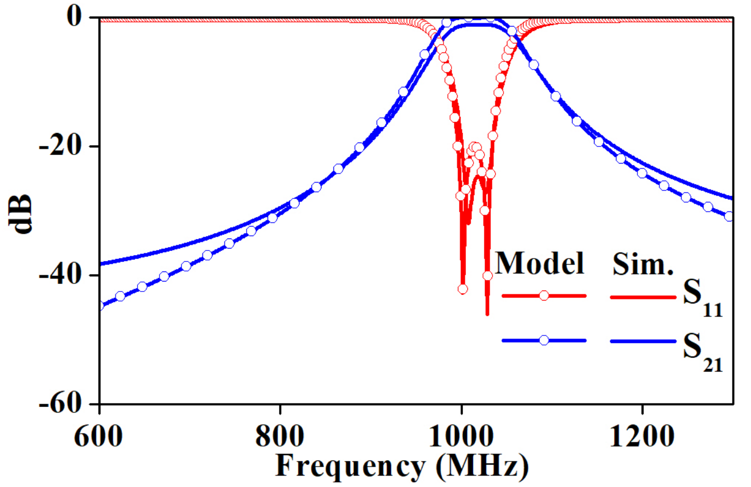

(b) The Upper band

Figure 6.3: Comparison of the numerical and simulation results for (a) the lower band and (b) the upper band.

in any of the NR operating bands in 5G FR1 spectrum.

$$M2 = \begin{pmatrix} 0 & -0.3 & 0.3 & 0 \\ -0.3 & -0.3 & 0 & 0.3 \\ 0.3 & 0 & -0.7 & 0.3 \\ 0 & 0.3 & 0.3 & 0 \end{pmatrix} \tag{6.8}$$

The matrix $M2$ is somewhat non-conventional, having the same source/load coupling with the first as well as the second resonator, but there lie no couplings between the individual resonators. A keen observation of the diagonal elements of the matrix reveals a difference between the self-resonant frequency in terms of magnitude but not in phase. This affirms the frequency shifting of the two poles from each other, but collectively they form the two reflection poles of the second band owing to the unipolar phase. A fair difference in polarity of the diagonal elements between matrices $M1$ and $M2$ reveals that $M1$ models the lower band while $M2$ deals only with the upper band.

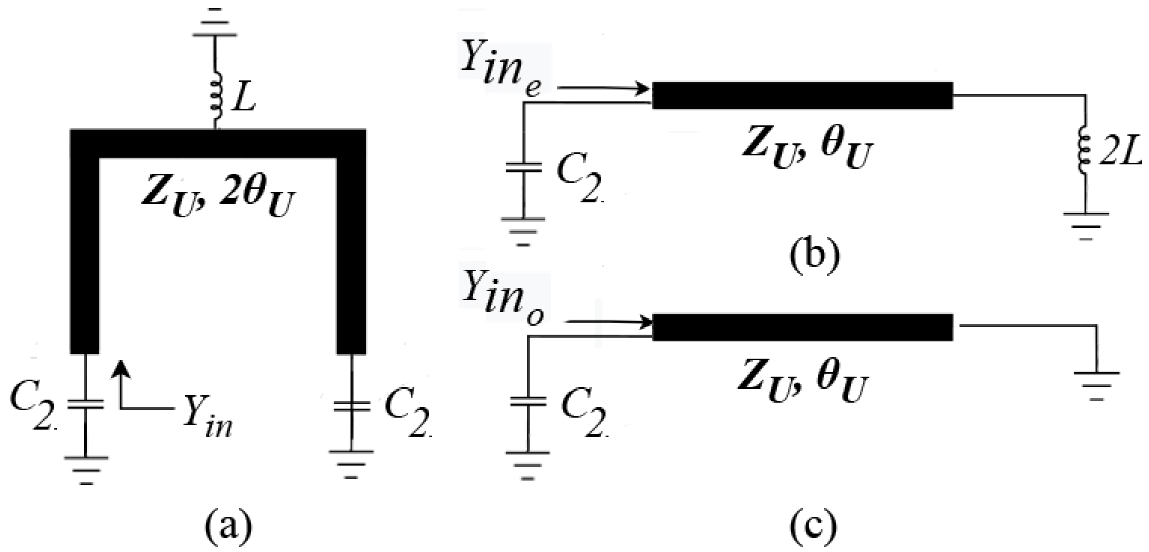

Figure 6.4: (a) The capacitor-integrated U-shaped resonator loaded with a short-circuited stub; the corresponding (b) the even-mode circuit and (c) the odd-mode circuit.

The upper band is realized using an U-shaped hairpin resonator loaded with a short-circuited stub, as shown in Fig. 6.2(b). The purpose of this stub, having a length L_3 and width W_1 and can be modeled as a shunt inductor, is to generate the dual-mode resonance condition, thereby accounting for the difference in resonant frequency in accordance with $M2$. The dual-mode resonance condition exhibited by this structure can be analyzed using even and odd mode structures on account of the symmetry in the circuit, as shown in Fig. 6.4. The comparison of the CM result with that of the simulated structure is shown in Fig. 6.3(b).

Additionally, the tunability feature can be achieved in the second band with the aid of an additional varactor diode combined with the static capacitor C_1, as shown in Fig 6.5(a). Therefore, the upper band, manifested by the U-shaped hairpin resonator with a short-circuited stub with length L_2 and width W_1, can be modeled as a shunt inductor which promotes the dual-mode resonance condition as is evident from the coupling scheme shown in Fig. 6.2(b). The dual-mode resonance condition exhibited by this structure can be analyzed using even and odd mode structures on account of the symmetry in the circuit as shown in Fig 6.5. From Fig. 6.5(b), the even mode admittance Y_{in_e} can be written as

$$Y_{in_e} = j\left[\omega_e C_t - Y_U \frac{Z_U - 2\omega_e L \tan\theta_U}{2\omega_e L + Z_U \tan\theta_U}\right] \tag{6.9}$$

where, Z_U and Y_U are the characteristic impedance and admittance of the U-shaped resonator, $\theta_U = \beta(L_1 + L_2/2)$ denotes the electrical length of the symmetric half of the resonator, ω_e denotes the even-mode resonant frequency, and C_t represents the collective capacitance of the varactor C_{v1} and C_1 and is given by

$$C_t = \frac{C_{v2}C_2}{C_{v2} + C_2} \tag{6.10}$$

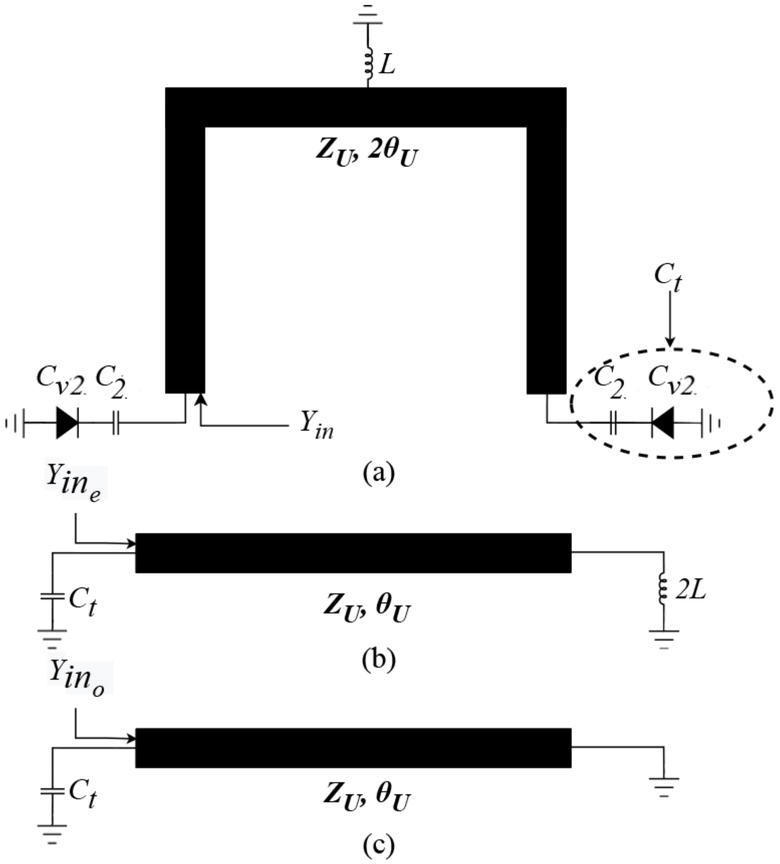

Figure 6.5: (a) The varactor-integrated U-shaped resonator loaded with a short circuit stub exhibiting tunability in the second band, (b) the even-mode circuit, and (c) the odd-mode circuit.

The even mode resonance frequency can be obtained by solving $Im(Y_{in_e}) = 0$ and is given by the quadratic equation

$$2\pi f_e \tan \frac{2\pi f_e \sqrt{\epsilon_{re}}(L_1 + L_2/2)}{c}(C_t Z_U + 2Y_U L) + 8\pi^2 f_e^2 C_t L = 1 \tag{6.11}$$

It is evident from eq. (6.11) that the even mode resonant frequency is determined by the electrical length (θ_U), which in turn is dependent on L_1 and L_2, the overall capacitance C_t which depends on the varactor biasing and the inductance (L) provided by the short-circuited stub. Fig. 6.6 shows the variation of the even mode resonant frequency with the variation of the stub length (L_3). The variation of the inductance shifts the even mode resonant frequency, thereby widening the bandwidth. Thus, the stub length can be adjusted to obtain the desired bandwidth at the specified center frequency.

Similarly, the odd mode admittance (Y_{in_o}) and the corresponding resonant frequency (f_o) can be obatined from Fig. 6.5(c) and is given by eq. (6.12) and eq. (6.13), respectively.

$$Y_{in_o} = j\left[\omega_o C_t - Y_U \cot\theta_U\right] \tag{6.12}$$

$$f_o \tan \frac{2\pi f_o \sqrt{\epsilon_{re}}(L_1 + L_2/2)}{c} = \frac{Y_U}{2\pi C_t} \tag{6.13}$$

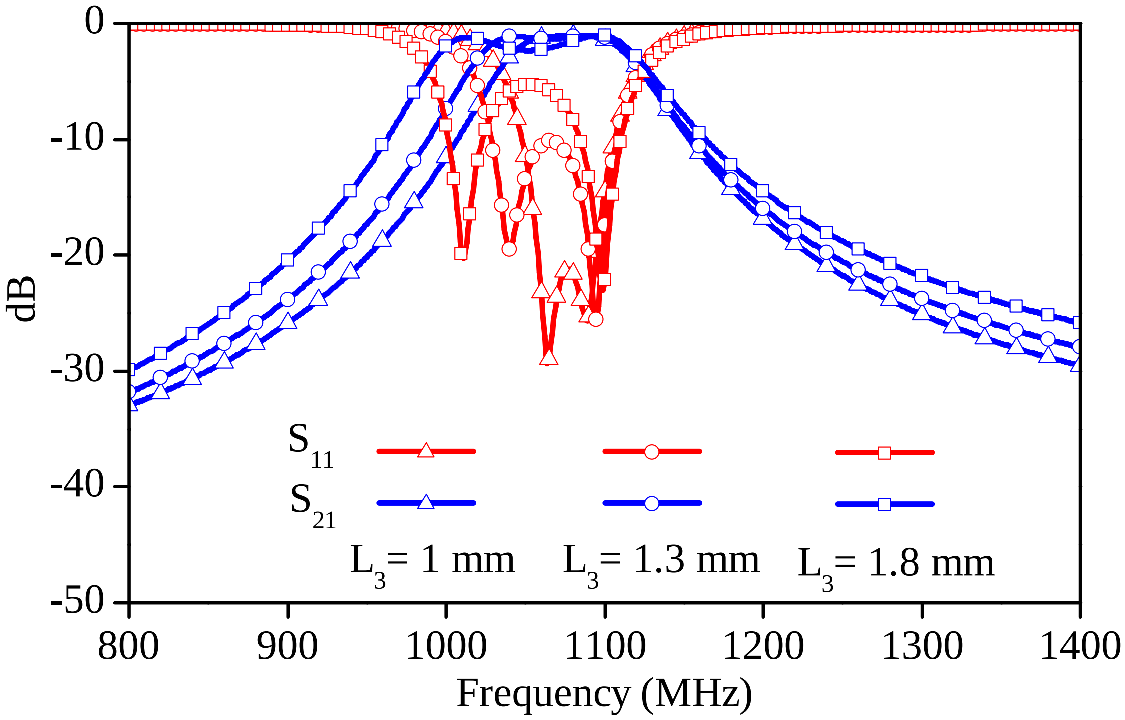

Figure 6.6: Deviation of the reflection poles with the increase in the stub length of the U-shaped resonator.

It is discernible from eq. (6.13) that the odd mode resonant frequency depends only on the electrical characteristics of the U-shaped resonator and the total capacitance (C_t), which in turn depends on the varactor biasing. Thus, the additional inductance provided by the short-circuited stub adds on to the difference between the even-mode and odd-mode resonance, thereby generating the dual pole response at the upper passband. Fig. 6.7 shows the dual-mode response of the U-shaped resonator and the variation of the center frequency with the variation in C_{v2}. Although two distinct transmission poles are visible at the even-mode and odd-mode resonant frequency points at the nominal capacitance values, the even-mode resonant frequency overlaps with the odd-mode frequency after a certain capacitance value resulting in a single transmission pole, as is evident for $C_{v2} = 9$ pF in Fig. 6.7. It is worth noting that the total capacitance (C_t) depends on the varactor diode biasing, which exhibits tunability of the second band.

6.3.3 The overall response

Once the individual coupling matrices for each of the bands are constructed, the same are combined to form the overall CM for the dual-band configuration given in eq. (6.14). The overall CM is realized using the schematic shown in Fig. 6.2(c). It is to be noted that the bandwidth is set to cover the entire range and not just the individual frequency bands. The quality factor is set to $Q = 150$ to correlate with the simulated results. The Q value is calculated based on the collective loaded Q or the varactor-loaded microstrip line. The model and the simulated

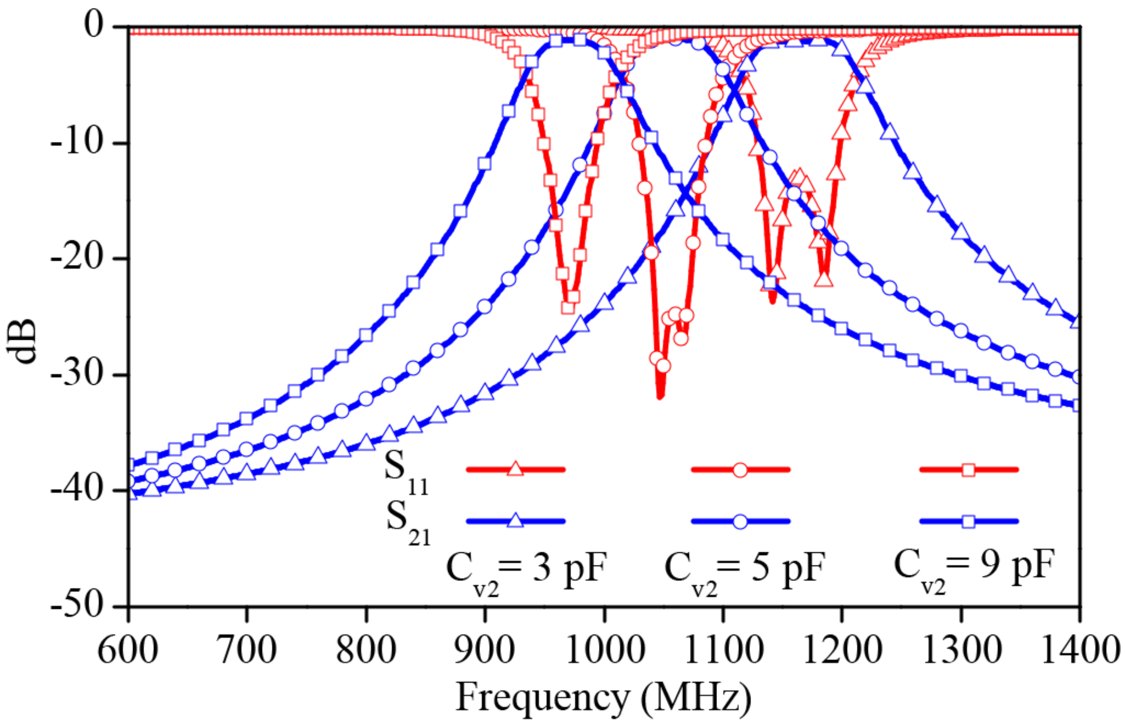

Figure 6.7: Variation of the resonant frequency with the variation of the varactor capacitance.

result are compared in Fig. 6.8. A sharp TZ is visible between the two bands owing to the 1^{st} to 3^{rd} resonator coupling of the combline structure. This adds to the novelty of sharp rejection between the bands without any additional coupling circuitry.

$$M = \begin{pmatrix} 0 & -0.65 & 0 & 0 & -0.30 & 0.30 & 0 \\ -0.65 & 5.5 & 0.38 & 0.022 & 0 & 0 & 0 \\ 0 & 0.38 & 5.46 & 0.38 & 0 & 0 & 0 \\ 0 & 0.022 & 0.38 & 5.5 & 0 & 0 & 0.65 \\ -0.3 & 0 & 0 & 0 & -0.3 & 0 & 0.3 \\ 0.3 & 0 & 0 & 0 & 0 & -0.7 & 0.3 \\ 0 & 0 & 0 & 0.65 & 0.3 & 0.3 & 0 \end{pmatrix} \tag{6.14}$$

6.4 The Non-Reciprocal Response

If the first three diagonal elements defining the 3^{rd} order first band is time-modulated with sinusoidal signals having the same frequency (f_m) and modulation index (ζ) but with a progressive phase shift ($\Delta\phi$) between the resonators, IM products are generated, and this leads to the formation of a 3D coupling matrix for the first band resulting in the generation of non-reciprocity. The non-reciprocal CM can be modeled by deploying the non-reciprocal design parameter ($\bar{\lambda}$) in the first three diagonal elements of eq. (6.14), which incorporates the modulation parameters

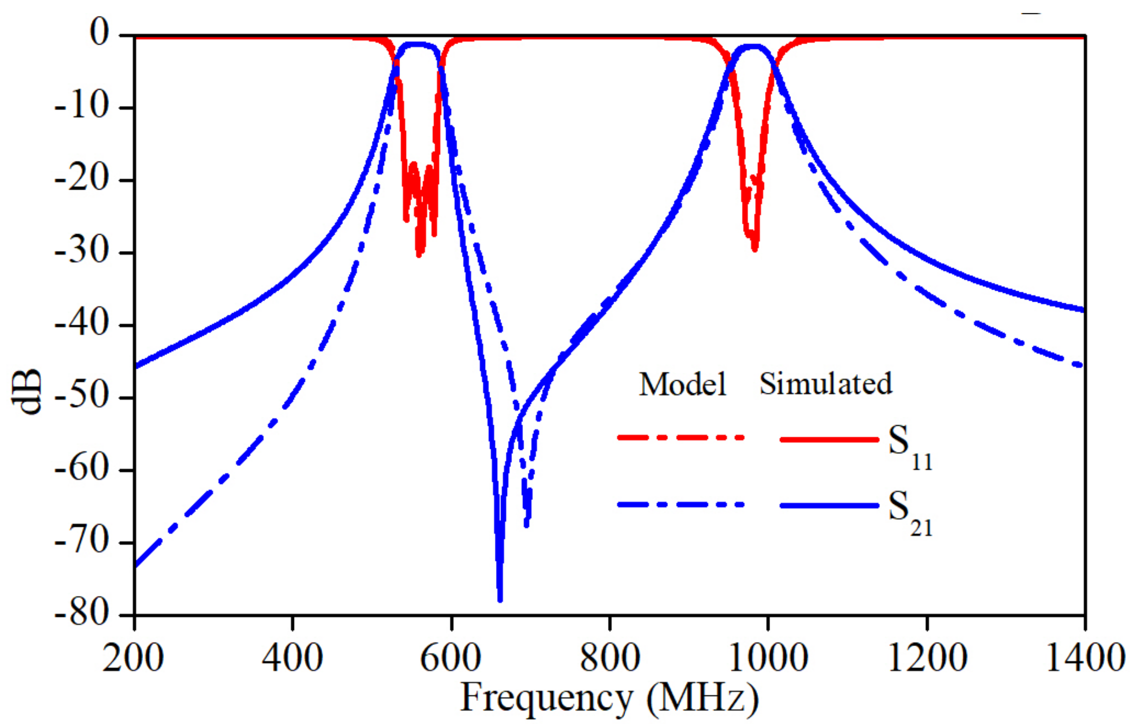

Figure 6.8: Comparison of the model and simulated dual-band reciprocal response of the overall circuit.

(ζ, f_m, and $\Delta\phi$) and takes into consideration the desired number of IM products (over here 5) to generate non-reciprocity, while for the reciprocal band, the conventional reciprocal λ is considered. ω'_{TZ} The modified non-reciprocal coupling matrix is given in eq. (6.15).

$$\bar{M} = \begin{pmatrix} 0 & -0.65 & 0 & 0 & -0.30 & 0.30 & 0 \\ -0.65 & \bar{\lambda}_1 + 5.5 & 0.38 & 0.022 & 0 & 0 & 0 \\ 0 & 0.38 & \bar{\lambda}_2 + 5.46 & 0.38 & 0 & 0 & 0 \\ 0 & 0.022 & 0.38 & \bar{\lambda}_3 + 5.5 & 0 & 0 & 0.65 \\ -0.3 & 0 & 0 & 0 & \lambda_4 - 0.3 & 0 & 0.3 \\ 0.3 & 0 & 0 & 0 & 0 & \lambda_5 - 0.7 & 0.3 \\ 0 & 0 & 0 & 0.65 & 0.3 & 0.3 & 0 \end{pmatrix} \tag{6.15}$$

It is worthwhile mentioning that all other coupling elements need to be multiplied by an identity matrix of the order equal to the order of $\bar{\lambda}_i$ to comply with the matrix operations. The subsequent step lies in the design of $N+2$ folded CM S-parameter equations for the total response using the procedure followed in [95]. The parametric values used to generate the non-reciprocal response are $\zeta = 0.2$, $f_m = 35$ MHz, and $\Delta\phi = 50°$, as explained in Chapter 3. Additionally, a Q value of 57 is calculated for the first band by taking the collective loading of the microstrip line with the varactor diode and the practical capacitor Q, in addition to the dielectric loss considered. The holistic non-reciprocal S-parameter equations are given in Appendix.

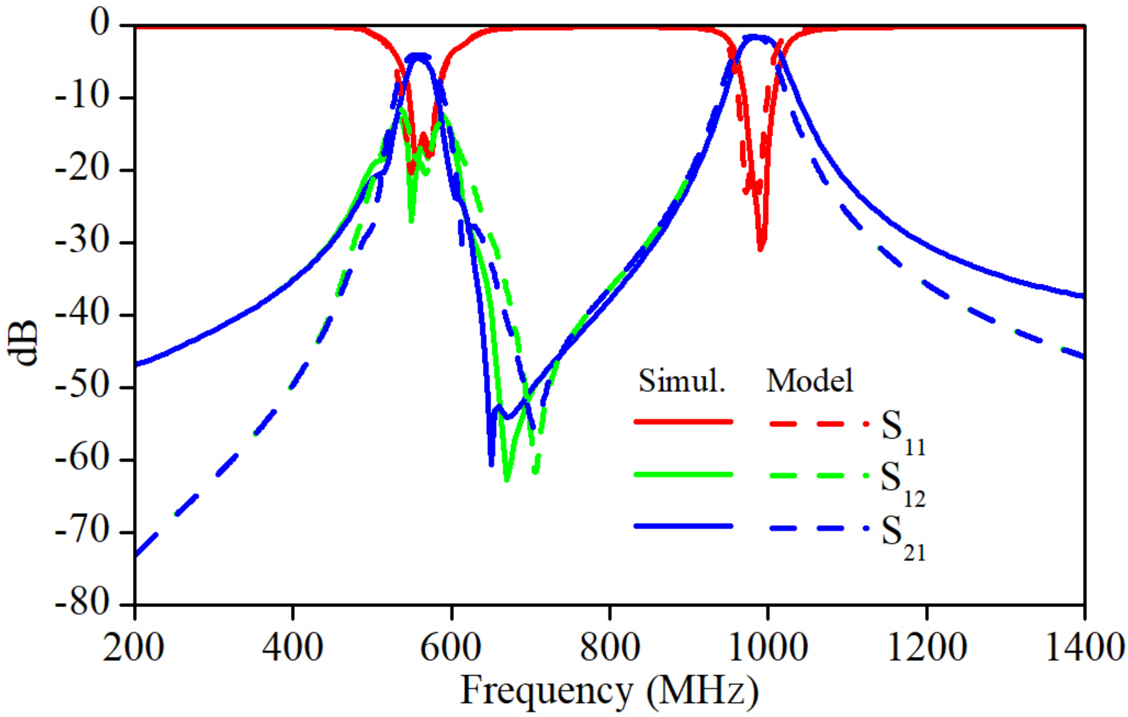

Figure 6.9: Comparison of the simulated and the analytical non-reciprocal dual-band response.

In the context of the design prototype, if the varactor diodes in the combline configuration of Fig. 6.2 are time-modulated with the circuit parameters obtained from the analytical modeling, the circuit behaves as an isolating filter, wherein the response provides a filtering phenomenon with deep isolation within the passband in opposite directions. In contrast, the non-reciprocal phenomenon is not observed in the dual-mode second band owing to the use of a time-invariant resonator both in the analysis and the design prototype. Thus, this overall response provides a dual-band response with a single-band non-reciprocity, as shown in Fig. 6.9.

6.5 Experimental Validation and discussion

The model has been validated by fabricating the circuit on an RT/Duroid 5880 substrate ($\epsilon = 2.2$, $\tan\delta = 0.0009$), and the fabricated prototype is shown in Fig. 6.10.

The varactor diodes (C_{v1}, C_{v2} and C_{v3}) used are Skyworks SMV1236-001LF; extra DC blocking capacitors (C_1 and C_2) are used in both the combline and the U-shaped resonator configuration to isolate the RF signal from the DC biasing. The varactors are biased using choke inductors (100 nH) connected in an external circuitry to isolate the RF and DC path further. The dimensions of the fabricated prototype as obtained from Fig. 6.2 are $W_s = 2.38$ mm, $W_0 = 0.18$ mm, $W_c = 0.85$ mm, $W_h = 0.7$ mm, $W_1 = 0.76$ mm, $L_0 = 18.6$ mm, $L_1 = 19$ mm, $L_2 = 7.88$ mm, $L_3 = 1$ mm, $L_c = 15$ mm, $S_0 = 0.22$ mm, $S_1 = 0.24$ mm, $S_2 = 2.1$ mm, $S_3 = 0.6$ mm, and the via hole diameters are 0.35 mm.

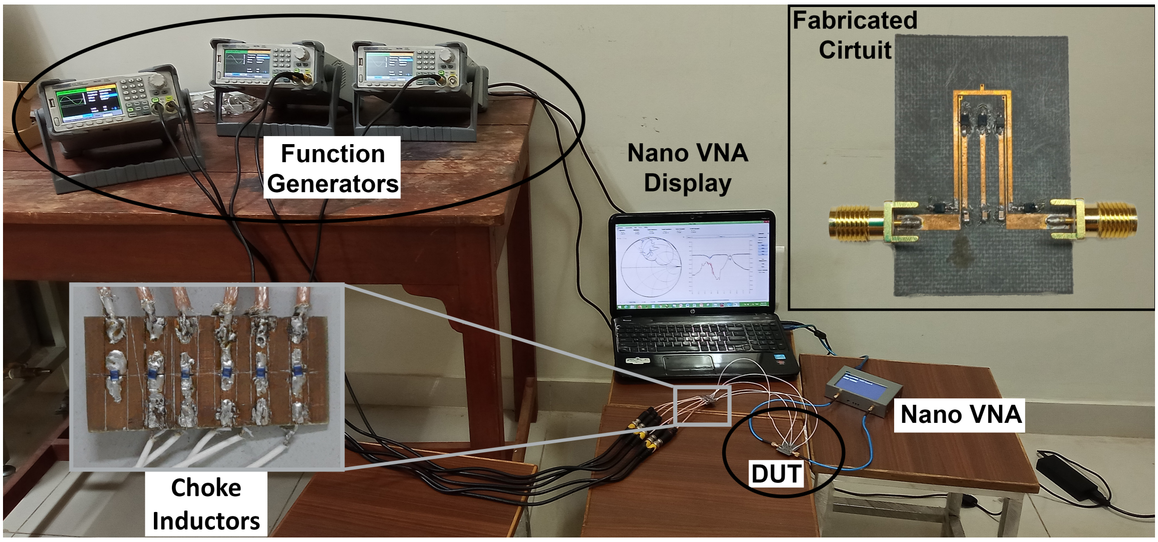

Figure 6.10: The experimental setup and the fabricated prototype of the dual-band bandpass filter with a single band non-reciprocity (inset).

To manifest the non-reciprocal response in the combline architecture, the DC biasing applied to the varactor diodes are 2.8 V, 3 V, and 2.8 V, respectively, from the first resonators while the AC biasings are 1.2V, 1.6V and 1.2V respectively. The modulation frequency applied is 38 MHz for all the resonators, and the incremental phase shifts between the sinusoidal signals is 50°. These values are chosen parametrically to manifest the desired isolation without degrading the insertion loss and return loss.

The U-shaped structure integrated with capacitors $C_1 = 3.3$ pF and the varactor diodes C_{v1} along with the short-circuited stub results in the tunable second band with the DC biasing applied at the conjunction of the capacitor and the varactor through an external choke inductor of 100 nH. The DC biasing applied to manifest the tunability is 2.7 V to 5 V.

Fig. 6.11 compares the simulation and measurement results of the fabricated prototype shown in the inset of Fig. 6.10. A sharp non-reciprocity covering the entire bandwidth of the first band is observed. In contrast, the second band is tunable with a reciprocal response. The non-reciprocal band is centered around 520 MHz with a bandwidth of 40 MHz. The measured insertion loss incurred for the non-reciprocal band is 4.8 dB compared to 4.7 dB for the simulated response; the measured and simulated return loss is more than 12 dB covering the entire passband, while the measured isolation is more than 18 dB. A slight bandwidth widening in the case of the non-reciprocal response is observed in the measured response due to the lumped capacitors used. The IL achieved in the non-reciprocal response is comparable with the recent works in the single-band domain; nevertheless, this circuit is the first of its kind in the dual-band regime. The reciprocal response can be tuned from 910 MHz to 980 MHz with a bandwidth in the range of around 40 MHz to 45 MHz, respectively. The variation of the measured insertion loss throughout the tunability range is about 3 dB to 3.1 dB. In comparison, the return loss

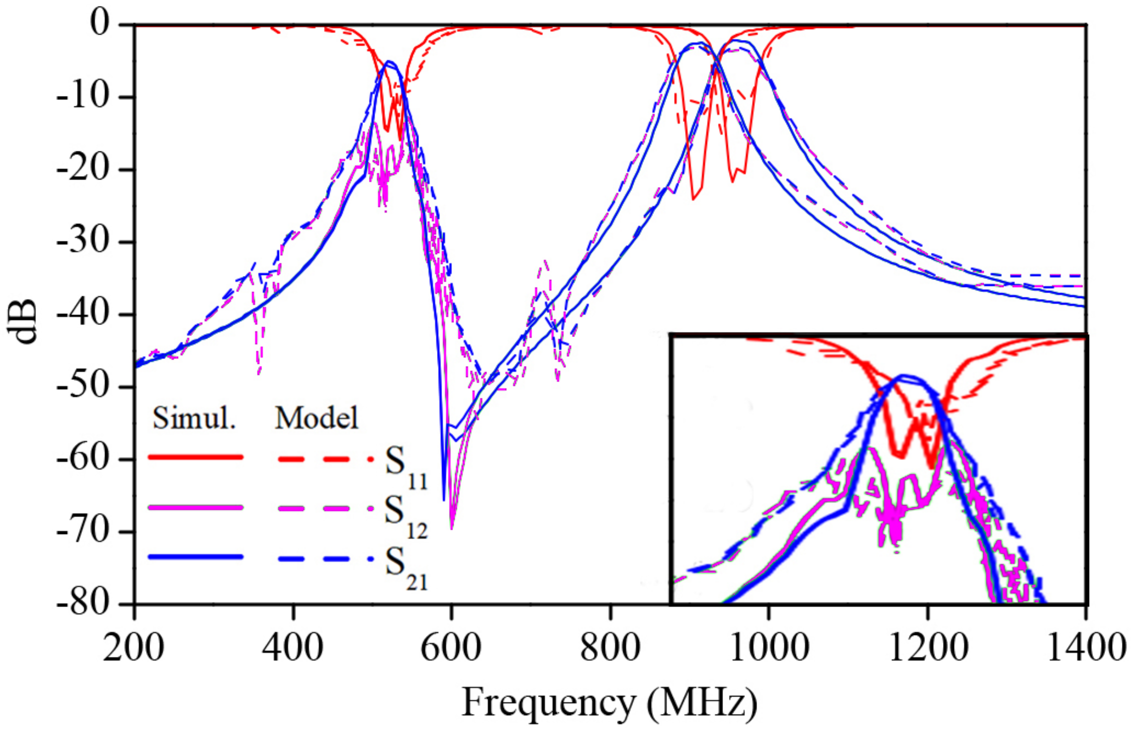

Figure 6.11: Comparison of the EM simulated and the measured results of the fabricated circuit.

is somewhat degraded owing to the lumped components used and is about 11 dB compared to around 20 dB in the simulated response. The complete design specifications for both the bands is given in Table 6.1. It is worthwhile mentioning that the actual tuning range is practically more than 70 MHz; however, IL and RL degrade with tuning. The results in Fig. 6.11 reveal that neither the non-reciprocity in the first band nor the tunability in the second band affects the other band, thereby elucidating the independence of the bands. The simulated and the measurement results comply well and vouch for the accuracy of the model.

Table 6.1: Filter Specifications

Sl. No.	Parameter	Simulation 1st band	Experiment 1st Band	Simulation 2nd band	Experiment 2nd Band
1.	Center Frequency	520 MHz	520 MHz	910-980 MHz	910-980 MHz
2.	Bandwidth	40 MHz	42 MHz	40-45 MHz	40-45 MHz
3.	Insertion Loss	4.8 dB	4.7 dB	2.8-2.9 dB	3-3.1 dB
4.	Return Loss	>12 dB	>12 dB	20 dB	11 dB
5.	Isolation	>18 dB	>18 dB	Reciprocal Band	

In Table 6.2, a comprehensive comparison between this work and state-of-the-art design methodologies is provided. From a design standpoint, this work stands out as the first distributed realization of a dual-band non-reciprocal bandpass filter (NR-BPF) with a single-band non-reciprocity. The non-reciprocal characteristics exhibited by this design are comparable to the best-performing works in this field. The IL achieved in the non-reciprocal response is on

Table 6.2: Comparison with other works in the literature

	Technology	f_0 **(MHz)**	**BW**	**IL**	**D**	**Size** $\lambda_g \times \lambda_g$	**Synthesis Approach**
[1]	Lumped/SB	190	33	1.5	20.2	NA	Direct Coupled
[97]	Lumped/SB	136-163	27.5	<4.1	>20	NA	Direct Coupled
[67]	Dist./SB	960	43.2	4.5	13.8	0.85×0.28	SB Coupling Matrix
[98]	Dist./SB	1020	65	5.5	≈ 11	0.2×0.2	Coupled Resonator
[50]	Dist./SB	1640-1970	50	4.96-3.94	20	NA	Coupled Resonator
[51]	Lumped/DB	198-224 249-291	23 21.8	2.9 2.6	8.4-44.8 8-44.3	NA	DB Direct Coupled
[12]	Lumped/TB	198-210 247-271 302-369	16.5 23 27.5	4 3.7 3.6	9.4-30.5 9-36.5 8.5-49.8	NA	TB Direct Coupled
This Work	Dist./DB	520 980	40 40-45	4.8 ≈ 3	20 (NRB) RB	0.15×0.09	DB Cross-Coupled Coupling Matrix

IL, RL, and Directivity (D) are in dB, BW is in MHz; SB = Single Band, DB = Dual Band, TB = Triple Band, RB = Reciprocal Band, and NRB = Non-reciprocal Band.

par with recent advancements in the single-band domain; nevertheless, this circuit is the first of its kind in the dual-band distributed regime. Moreover, this work presents the synthesis of an unconventional dual-band cross-coupled non-reciprocal coupling matrix (CM) for the first time, which provides the capability of realizing multi-band non-reciprocal filters while providing dedicated control over each individual band. This feature allows for enhanced flexibility and adaptability in filter design. Furthermore, the compactness of the circuit is worth highlighting. The incorporation of a capacitively loaded combline section contributes to its reduced size compared to previous works. This compact design makes it highly suitable for integration into modern transceiver systems, where space optimization is crucial.

6.6 Conclusion

In this paper, a novel coupling matrix design of dual-band BPF with a single-band non-reciprocity is presented, which discreetly combines the characteristics of the individual bands into the coupling matrix representation of the desired frequency-shifted lower and upper bands. These coupling matrices are then meticulously combined to form the overall coupling matrix. The predominant advantage of this method lies in having dedicated access to the individual matrix elements that frame the corresponding band. The final step incorporates spatio-temporal modulation (STM) to the desired band to effectuate a non-reciprocal filtering isolation with minimum interference on the other band. The model combines a 3^{rd} order cross-coupled conventional filter structure to manifest the non-reciprocal lower band with a dual-mode 2^{nd} order reciprocal upper band. The precision of the analytical formulation is substantiated with the aid of a compact dual-band fabricated prototype combining a common source/load coupled 3^{rd} order combline structure and a 2^{nd} order dual-mode configuration realized using stub-loaded U-shaped resonator. The non-reciprocal coupling matrix, the first of its kind in the regime of dual-band isolating filter, finds a versatile application in modern dual-band non-reciprocal filter designs.

6.7 Appendix: Dual-Band Non-reciprocal S-parameter equations

The holistic S-parameter equations for the dual-band configuration are given by eq. (6.16).

$$\begin{aligned} S_{11} &= \frac{A+iB}{C+iD} \\ S_{21} &= \frac{E}{C+iD} \end{aligned} \tag{6.16}$$

where A-E are given by eq. (6.17)-(6.21). These equations are derived by rigorous inverse operations on the $N+2$ folded CM to consider all the harmonic products in the analysis. A logical solution would require multiplying the individual components (including λ_4, which happens to generate a reciprocal response) with a unitary matrix of the order equal to the order of $\bar{\lambda}_i$ which denotes the number of harmonics, taken into consideration. It is worth mentioning that if the harmonics are not considered, then a simple multiplication of the nominal values of each component will fetch the reciprocal results. The final step to generate the non-reciprocal response is to interchange the values of λ_1 and λ_3 and feed into the same S_{11} and S_{21} equations of (6.16) to compute S_{22} and S_{12}. These equations can be directly used to generate a non-reciprocal response with the desired coupling element values and a judicious choice of non-reciprocal parameters (ζ, f_m, and $\Delta\phi$).

$$\begin{aligned} A = {} & M_{22}M_{S1}^2\lambda_4^2(\bar{\lambda}_3-\bar{\lambda}_1) - M_{S1}^2\bar{\lambda}_2\lambda_4^2(\bar{\lambda}_1-\bar{\lambda}_3) - M_{22}M_{44}M_{55}M_{S1}^2(\bar{\lambda}_1-\bar{\lambda}_3) \\ & - M_{22}M_{44}M_{S1}^2\lambda_4(\bar{\lambda}_1-\bar{\lambda}_3) - M_{22}M_{55}M_{S1}^2\lambda_4(\bar{\lambda}_1-\bar{\lambda}_3) \\ & - M_{44}M_{55}M_{S1}^2\bar{\lambda}_2(\bar{\lambda}_1-\bar{\lambda}_3) - M_{44}M_{S1}^2\bar{\lambda}_2\lambda_4(\bar{\lambda}_1-\bar{\lambda}_3) - M_{55}M_{S1}^2\bar{\lambda}_2\lambda_4(\bar{\lambda}_1-\bar{\lambda}_3) \end{aligned} \tag{6.17}$$

$$
\begin{aligned}
B = {} & 8M_{12}^2M_{S4}^4(M_{11} - M_{13}) - 4M_{22}M_{S4}^4(M_{11}^2 - M_{13}^2) \\
& - \lambda_4^2(M_{11} - M_{13})(-2M_{12}^2 + M_{11}M_{22} + M_{13}M_{22}) - 4M_{S4}^4\bar{\lambda}_2(M_{11}^2 + M_{13}^2) \\
& + 4M_{12}^2M_{S4}^4(\bar{\lambda}_1 + \bar{\lambda}_3) - \lambda_4^2(\bar{\lambda}_2M_{11}^2 + M_{22}M_{S1}^4) + \lambda_4^2(M_{12}^2\bar{\lambda}_1 + M_{12}^2\bar{\lambda}_3 + M_{13}^2\bar{\lambda}_2 - M_{S1}^4\bar{\lambda}_2) \\
& - \lambda_4(M_{11} - M_{13})(M_{44} + M_{55})(-2M_{12}^2 + M_{11}M_{22} + M_{13}M_{22}) \\
& + M_{44}M_{55}(M_{12}^2\bar{\lambda}_1 - M_{11}^2\bar{\lambda}_2 + M_{12}^2\bar{\lambda}_3 + M_{13}^2\bar{\lambda}_2) - 4M_{11}M_{22}M_{S4}^4(\bar{\lambda}_1 + \bar{\lambda}_3) \\
& - M_{22}M_{S1}^4\lambda_4(M_{44} + M_{55}) - M_{44}M_{55}M_{S1}^4\bar{\lambda}_2 - M_{11}M_{22}\lambda_4^2(\bar{\lambda}_1 + \bar{\lambda}_3) - M_{11}^2\bar{\lambda}_2\lambda_4(M_{44} + M_{55}) \\
& + M_{12}^2M_{44}\lambda_4(\bar{\lambda}_1 + \bar{\lambda}_3) + M_{13}^2\bar{\lambda}_2\lambda_4(M_{44} + M_{55}) + M_{12}^2M_{55}\lambda_4(\bar{\lambda}_1 + \bar{\lambda}_3) \\
& - 4M_{11}M_{S4}^4\bar{\lambda}_2(\bar{\lambda}_1 + \bar{\lambda}_3) - 4M_{S4}^4\bar{\lambda}_1\bar{\lambda}_3(M_{22} + \bar{\lambda}_2) - M_{S1}^4\bar{\lambda}_2\lambda_4(M_{44} + M_{55}) \\
& - M_{11}\bar{\lambda}_2\lambda_4^2(\bar{\lambda}_1 - \bar{\lambda}_3) - \bar{\lambda}_1\bar{\lambda}_3\lambda_4^2(M_{22} + \bar{\lambda}_2) + 4M_{12}^2M_{S1}^2M_{S4}^2(M_{55} + \lambda_4) \\
& + 2M_{12}^2M_{44}M_{55}(M_{11} - M_{13}) - M_{22}M_{44}M_{55}(M_{11}^2 - M_{13}^2 + M_{S1}^4) - M_{11}M_{22}M_{44}\lambda_4(\bar{\lambda}_1 + \bar{\lambda}_3) \\
& - M_{11}M_{22}M_{55}\lambda_4(\bar{\lambda}_1 + \bar{\lambda}_3) - M_{11}M_{44}M_{55}\bar{\lambda}_2(\bar{\lambda}_1 + \bar{\lambda}_3) - M_{44}M_{55}\bar{\lambda}_1\bar{\lambda}_3(M_{22} + \bar{\lambda}_2) \\
& - M_{11}\bar{\lambda}_1\bar{\lambda}_2\lambda_4(M_{44} + M_{55}) - M_{11}\bar{\lambda}_2\bar{\lambda}_3\lambda_4(M_{44} + M_{55}) - M_{22}\bar{\lambda}_1\bar{\lambda}_3\lambda_4(M_{44} + M_{55}) \\
& - \bar{\lambda}_1\bar{\lambda}_2\bar{\lambda}_3\lambda_4(M_{44} + M_{55}) - 2M_{22}M_{S1}^2M_{S4}^2(M_{11}M_{44} - M_{13}M_{44} + M_{11}M_{55} + M_{13}M_{55}) \\
& - 4M_{11}M_{S1}^2M_{S4}^2\lambda_4(M_{22} - \bar{\lambda}_2) - 2M_{11}M_{44}M_{S1}^2M_{S4}^2\bar{\lambda}_2(M_{11} - M_{13}) \\
& - M_{22}M_{44}M_{S1}^2M_{S4}^2(\bar{\lambda}_1 + \bar{\lambda}_3) - 2M_{11}M_{55}M_{S1}^2M_{S4}^2\bar{\lambda}_2(M_{11} + M_{13}) \\
& - M_{22}M_{55}M_{S1}^2M_{S4}^2(\bar{\lambda}_1 + \bar{\lambda}_3) - 2M_{22}M_{S1}^2M_{S4}^2\lambda_4(\bar{\lambda}_1 + \bar{\lambda}_3) - M_{44}M_{S1}^2M_{S4}^2\bar{\lambda}_2(\bar{\lambda}_1 + \bar{\lambda}_3) \\
& - M_{55}M_{S1}^2M_{S4}^2\bar{\lambda}_2(\bar{\lambda}_1 + \bar{\lambda}_3) - 2M_{S1}^2M_{S4}^2\bar{\lambda}_2\lambda_4(\bar{\lambda}_1 - \bar{\lambda}_3) - M_{11}M_{22}M_{44}M_{55}
\end{aligned}
\tag{6.18}
$$

$$
\begin{aligned}
C = {} & A - 4M_{12}^2M_{44}M_{S4}^2(M_{11} - M_{13}) + 2M_{22}M_{44}M_{S4}^2(M_{11}^2 - M_{13}^2) - 4M_{12}^2M_{55}M_{S4}^2(M_{11} - M_{13}) \\
& + 2M_{22}M_{55}M_{S4}^2(M_{11}^2 - M_{13}^2) - 8M_{12}^2M_{S4}^2\lambda_4(M_{11} - M_{13}) - 2M_{S1}^2\lambda_4^2(M_{12}^2 - M_{11}M_{22}) \\
& + 4M_{22}M_{S4}^2\lambda_4(M_{11}^2 - M_{13}^2) - 2M_{12}^2M_{44}M_{S4}^2(\bar{\lambda}_1 + \bar{\lambda}_3) + 2M_{44}M_{S4}^2\bar{\lambda}_2(M_{11}^2 - M_{13}^2) \\
& - 2M_{12}^2M_{S1}^2\lambda_4(M_{44} + M_{55}) + 2M_{55}M_{S4}^2\bar{\lambda}_2(M_{11}^2 - M_{13}^2) - 2M_{12}^2M_{55}M_{S4}^2(\bar{\lambda}_1 + \bar{\lambda}_3) \\
& + 4M_{S4}^2\bar{\lambda}_2\lambda_4(M_{11}^2 - M_{13}^2) + 2M_{11}M_{22}M_{44}M_{S1}^2(M_{55} + \lambda_4) + 2M_{S1}^2\lambda_4^2(M_{11}\bar{\lambda}_2 + M_{22}\bar{\lambda}_1) \\
& - 4M_{12}^2M_{S4}^2\lambda_4(\bar{\lambda}_1 + \bar{\lambda}_3) + 2M_{11}M_{22}M_{44}M_{S4}^2(\bar{\lambda}_1 + \bar{\lambda}_3) + 2M_{11}M_{22}M_{55}M_{S4}^2(\bar{\lambda}_1 + \bar{\lambda}_3) \\
& + 2M_{11}M_{44}M_{S4}^2\bar{\lambda}_2(\bar{\lambda}_1 + \bar{\lambda}_3) + 4M_{11}M_{22}M_{S4}^2\lambda_4(\bar{\lambda}_1 + \bar{\lambda}_3) + 2M_{11}M_{55}M_{S4}^2\bar{\lambda}_2(\bar{\lambda}_1 + \bar{\lambda}_3) \\
& + 4M_{11}M_{S4}^2\bar{\lambda}_2\lambda_4(\bar{\lambda}_1 + \bar{\lambda}_3) + 2M_{11}M_{22}M_{55}M_{S1}^2\lambda_4 + (2M_{S4}^2\bar{\lambda}_1\bar{\lambda}_2\bar{\lambda}_3 + 2M_{22}M_{S4}^2\bar{\lambda}_1\bar{\lambda}_3 \\
& \qquad + 2M_{22}M_{S1}^2\bar{\lambda}_1\lambda_4 + 2M_{11}M_{S1}^2\bar{\lambda}_2\lambda_4 + 2M_{S1}^2\bar{\lambda}_1\bar{\lambda}_2\lambda_4)(M_{44} + M_{55}) + 2M_{S1}^2\bar{\lambda}_1\bar{\lambda}_2\lambda_4^2 \\
& + 2M_{44}M_{55}M_{S1}^2(M_{11}\bar{\lambda}_2 + M_{22}\bar{\lambda}_1) + 4M_{S4}^2\bar{\lambda}_1\bar{\lambda}_3\lambda_4(M_{22} + \bar{\lambda}_2) + 2M_{44}M_{55}M_{S1}^2(-M_{12}^2 + \bar{\lambda}_1\bar{\lambda}_2)
\end{aligned}
\tag{6.19}
$$

$$
\begin{aligned}
D = {} & B + 2\lambda_4^2(M_{11} - M_{13})(-2M_{12}^2 + M_{11}M_{22} + M_{13}M_{22}) - 2\lambda_4^2(M_{12}^2\bar{\lambda}_1 - M_{11}^2\bar{\lambda}_2 + M_{12}^2\bar{\lambda}_3 + M_{13}^2\bar{\lambda}_2) \\
& - 2\lambda_4(M_{11} - M_{13})(M_{44} + M_{55})(-2M_{12}^2 + M_{11}M_{22} + M_{13}M_{22}) \\
& - 2M_{44}M_{55}(M_{12}^2\bar{\lambda}_1 - M_{11}^2\bar{\lambda}_2 + M_{12}^2\bar{\lambda}_3 + M_{13}^2\bar{\lambda}_2) + 2M_{11}M_{22}\lambda_4^2(\bar{\lambda}_1 + \bar{\lambda}_3) \\
& - 2\lambda_4(M_{44} + M_{55})(M_{12}^2\bar{\lambda}_1 - M_{11}^2\bar{\lambda}_2 + M_{12}^2\bar{\lambda}_3 + M_{13}^2\bar{\lambda}_2) \\
& + 2\lambda_4^2(M_{11}\bar{\lambda}_1\bar{\lambda}_2 + M_{11}\bar{\lambda}_2\bar{\lambda}_3 + M_{22}\bar{\lambda}_1\bar{\lambda}_3 + \bar{\lambda}_1\bar{\lambda}_2\bar{\lambda}_3) \\
& + 2M_{44}M_{55}(M_{11} - M_{13})(-2M_{12}^2 + M_{11}M_{22} + M_{13}M_{22}) \\
& + 2M_{11}M_{22}\lambda_4(\bar{\lambda}_1 + \bar{\lambda}_3)(M_{44} + M_{55}) + 2M_{11}M_{44}M_{55}\bar{\lambda}_2(\bar{\lambda}_1 + \bar{\lambda}_3) \\
& + 2M_{11}M_{22}M_{44}M_{55}(\bar{\lambda}_1 + \bar{\lambda}_3) + 2\bar{\lambda}_1\bar{\lambda}_2\bar{\lambda}_3\lambda_4(M_{44} + M_{55}) + 2M_{11}\bar{\lambda}_1\bar{\lambda}_2\lambda_4(M_{44} + M_{55}) \\
& + 2M_{22}\bar{\lambda}_1\bar{\lambda}_3\lambda_4(M_{44} + M_{55}) + 2M_{11}\bar{\lambda}_2\bar{\lambda}_3\lambda_4(M_{44} + M_{55}) + 2M_{44}M_{55}\bar{\lambda}_1\bar{\lambda}_3(M_{22} + \bar{\lambda}_2)
\end{aligned}
\tag{6.20}
$$

$$
\begin{aligned}
E = {} & 2M_{12}^2M_{S1}^2\lambda_4^2 - 2M_{S4}^2(M_{11} - M_{13})(M_{44} - M_{55})(-2M_{12}^2 + M_{11}M_{22} + M_{13}M_{22}) \\
& - 2M_{S4}^2\bar{\lambda}_1\bar{\lambda}_2\bar{\lambda}_3(M_{44} - M_{55}) + 2M_{11}M_{55}M_{S4}^2\bar{\lambda}_2(\bar{\lambda}_1 + \bar{\lambda}_3) - 2M_{44}M_{S4}^2\bar{\lambda}_2(M_{11}^2 - M_{13}^2) \\
& + 2M_{12}^2M_{S1}^2\lambda_4(M_{44} + M_{55}) + 2M_{12}^2M_{S4}^2\bar{\lambda}_1(M_{44} - M_{55}) + 2M_{12}^2M_{S4}^2\bar{\lambda}_3(M_{44} - M_{55}) \\
& + 2M_{55}M_{S4}^2\bar{\lambda}_2(M_{11}^2 - M_{13}^2) - 2M_{22}M_{S4}^2\bar{\lambda}_1\bar{\lambda}_3(M_{44} - M_{55}) - 2M_{13}M_{S1}^2\bar{\lambda}_2\lambda_4(M_{44} + M_{55}) \\
& + 2M_{44}M_{55}M_{S1}^2(M_{12}^2 - M_{13}M_{22}) - 2M_{13}M_{S1}^2\lambda_4^2(M_{22} + \bar{\lambda}_2) - 2M_{11}M_{22}M_{S4}^2\bar{\lambda}_1(M_{44} - M_{55}) \\
& - 2M_{11}M_{22}M_{S4}^2\bar{\lambda}_3(M_{44} - M_{55}) - 2M_{13}M_{22}M_{S1}^2\lambda_4(M_{44} + M_{55}) \\
& - 2M_{44}\bar{\lambda}_2(M_{13}M_{55}M_{S1}^2 + M_{11}\bar{\lambda}_1M_{S4}^2) - 2M_{11}M_{44}M_{S4}^2\bar{\lambda}_2\bar{\lambda}_3
\end{aligned}
\tag{6.21}
$$

6.8 Publications

1. **Prantik Dutta**, Gande Arun Kumar, Gopi Ram, "A Novel Compact Closely-spaced Dual-band Bandpass Filter with Non-reciprocal Lower Band and Tunable Reciprocal Upper Band", *IEEE Microwave and Wireless Technology Letters (Under Review).*

2. **Prantik Dutta**, Gande Arun Kumar, Gopi Ram, "Coupling Matrix Representation of Dual-band Bandpass Filter with a Single-band Non-reciprocity", *IEEE Transactions on Microwave Theory and Techniques (Under Review).*

Chapter 7

Dual-band bandpass filters with dual-band non-reciprocity

7.1 Introduction

The concept of spatio-temporal modulation (STM) has emerged as an evolving approach for designing non-reciprocal bandpass filters (NR-BPF) and has gained significant attention in recent times. These NR-BPFs are specifically designed for applications in modern transceiver systems where filtering is required in one direction while achieving isolation in the opposite direction.

With the ongoing trend of miniaturization and integration, there is a growing need for multi-band filters to address the increasing complexity within limited space.

To address this demand, there is a desire to replace separate filter and isolator components with compact multi-band isolating filters, thereby achieving breakthrough integrability. This motivates the development of a cost-effective and miniaturized dual-band NR-BPF that can be seamlessly integrated into monolithic systems. Still, the research in the domain of dual-band non-reciprocal filter designs and the corresponding developments are in the embryonic stage. Notably, recent research has introduced dual-band and triple-band NR-BPFs using lumped realization [51, 12] which focus on the design and validation of multiband isolators and circulators with reconfigurable bandpass filtering capabilities. The proposed devices in these works employ frequency-tunable and spatiotemporally modulated resonators to shape transversal frequency-selective signal paths. Each path is capable of independently controlling the passband in terms of frequency and direction of propagation. This enables the overall network to exhibit multiple non-reciprocal passbands that can be reconfigured according to the desired specifications. To demonstrate the practical implementation, three lumped-element prototypes were developed and tested at the VHF band. These prototypes achieved high in-band isolation and demonstrated the ability to tune the frequency and change the directionality of the signals. Nevertheless, these approaches suffer from drawbacks such as increased space complexity and the need for multiple signal sources to modulate each resonator in bandpass configurations. In order to overcome these challenges, researchers have explored different dual-band filter configurations to further enhance the generation of non-reciprocal responses.

Various dual-band bandpass filter (BPF) structures have emerged to meet the demands of miniaturization and integration in monolithic systems. Stepped impedance resonator (SIR)-based dual-band BPFs have been prominent [99, 100, 101, 102, 103, 104], providing steep selectivity and passband control. However, they suffer from reduced bandwidth, higher insertion loss (IL), and larger circuit size. Stub-loaded resonators [105, 106, 107] offer efficient control over center frequency but sacrifice selectivity. Substrate-integrated-waveguide (SIW) technology [108, 109] and complementary split ring resonators (CSRR) [110] have been utilized but fall short for closely spaced bands. Balanced differential mode (DM) filters [111, 112, 113] provide immunity to interference but introduce additional complexity. Designs incorporating transversal signal interaction [114] or reflectionless techniques [115] suffer from degraded passband IL. A compact dual-band BPF on a paper substrate [116] proves versatile but lacks competitiveness for closely spaced bands.

This chapter focuses on implementing dual-band bandpass filters with dual-band non-reciprocities. Various design strategies incorporating varactor diodes to implement tunability have been studied so as to find an effective solution to the objective of achieving simultaneous non-reciprocity in dual-band bandpass filters, which is still in the early stages of development. Two approaches have been explored, with the first approach failing to provide a non-reciprocal response. However, the second approach has successfully demonstrated the non-reciprocal phenomenon in both bands, marking a significant achievement.

The chapter is divided into two parts. In the first part, a novel dual-band bandpass filter configuration is proposed, utilizing a combination of combline architecture and a series configuration of LC resonator with a hairpin-like structure. This configuration results in closely spaced dual-band response, low-loss characteristics, and significant rejection between the two bands. Additionally, the series LC resonator introduces a distinct transmission zero between the bands without the need for additional circuitry. Numerical analysis and experimental results validate the proposed filter configuration, although the order of the filter structure inhibits the manifestation of non-reciprocity.

The second part of the chapter proposes a novel design methodology of lumped-element closely-spaced dual-band bandpass filter (BPF) with simultaneous dual-band non-reciprocity and a sharp transmission zero (TZ) in between by effectively combining spatio-temporal modulated (STM) bandpass resonators coupled with static bandstop resonators. Unlike previous approaches that use multiple direct-coupled STM resonator structures with common source/load terminations, this work achieves the dual-band non-reciprocal phenomenon by temporal modulation of only the 3rd order bandpass resonator structure, thereby promoting a simpler and cost-effective solution by reducing the number of time-modulating elements to half. The proposed circuit holds great potential for achieving dual-band filtering isolation in modern transceiver systems that rely on very closely spaced bands.

7.2 The proposed dual-band reciprocal filter

The proposed dual-band bandpass filter, shown in Fig. 7.1, combines the effect of a combline architecture consisting of the capacitors C_p along with the microstrip lines of length L_1 manifesting the upper band while the lower band is at the resonant frequency of the hairpin-like structure shorted using via holes along with a series configuration of LC resonator as indicated in the figure. The overall configuration of the lower band provides a short circuit at the upper band frequency approximately at the feed point, thereby stimulating the conventional second-order combline filter structure at the desired upper band. The lower band is substantiated by the lower structure comprising the series LC resonator, the transmission lines, and the via hole configuration which acts as a parallel LC network. The even and odd mode resonant frequencies

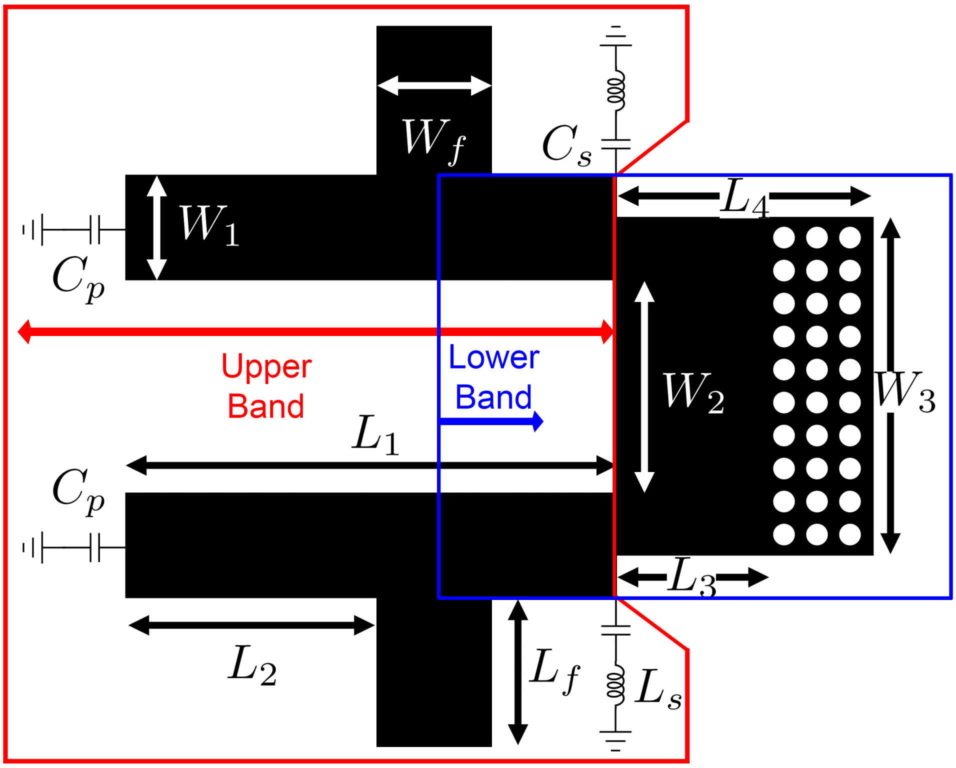

Figure 7.1: Configuration of the proposed DBPF.

generated by the overall lower band structure in Fig. 7.1 exhibit the second-order lower band. The numerical analysis of the filter structure is presented in the subsequent section 7.3 with experimental validation in section 7.4.

7.3 Numerical Analysis and Simulation

The circuit has been interpreted using even-odd mode analysis owing to the symmetry of the structure as shown in Fig. 7.2(a). The even-mode circuit is shown in Fig. 7.2(b) and the odd-mode circuit can be analyzed from the same circuit by bypassing the capacitor (C_v) and inductor (L_v) and directly terminating the transmission line with characteristics (Z_3 and θ_3) with a short circuit as shown in Fig. 7.2(c). Consequently, the analysis can be segregated into three separate scenarios - the lower band, the upper band, and the transmission zero. In each scenario, particular transmission lines along with lumped elements come into action, thereby manifesting a separate phenomenon.

7.3.1 The Lower band

The lower band is realized by the lower portion of the structure comprising the series resonator, the transmission lines along with the via hole configuration which can be modelled as a parallel LC resonator, wherein the inductance arises from the collective impact of the total inductance

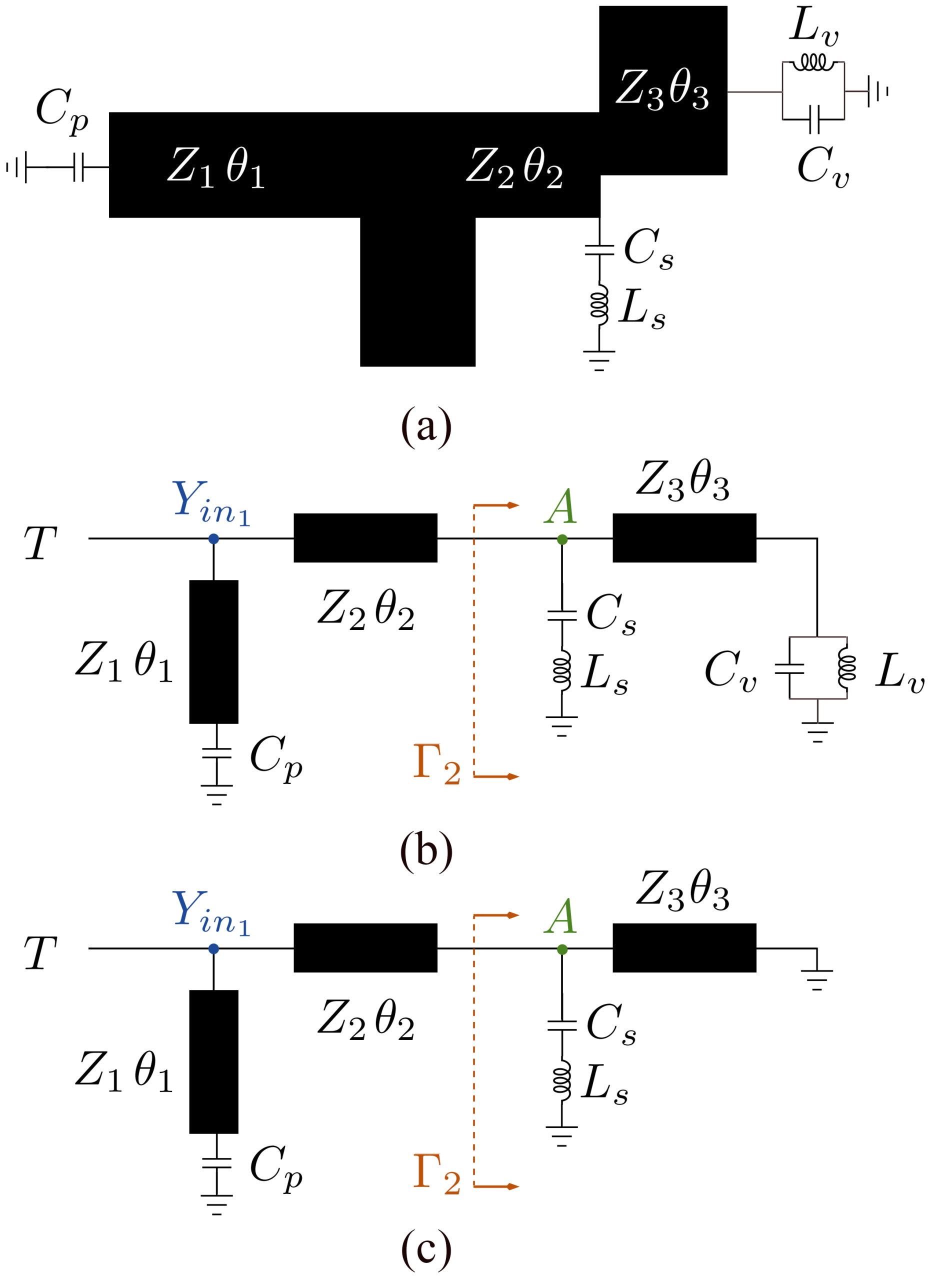

Figure 7.2: (a) The symmetric half of the circuit shown in Fig. 7.1, (b) The even-mode structure and (c) The odd-mode structure.

of all the via holes and the capacitance comes from the via pad area. The resonant frequencies of the lower half of the circuit responsible for the lower band can be obtained by solving for the zeroes of the reflection coefficient ($\Gamma_2 = 0$) of one half of the circuit, where Γ_2 is given by,

$$\Gamma_2 = -\frac{Z_3}{2}\left[\frac{Y_e}{Y_e Z_3 + 2} + \frac{Y_o}{Y_o Z_3 + 2}\right] \tag{7.1}$$

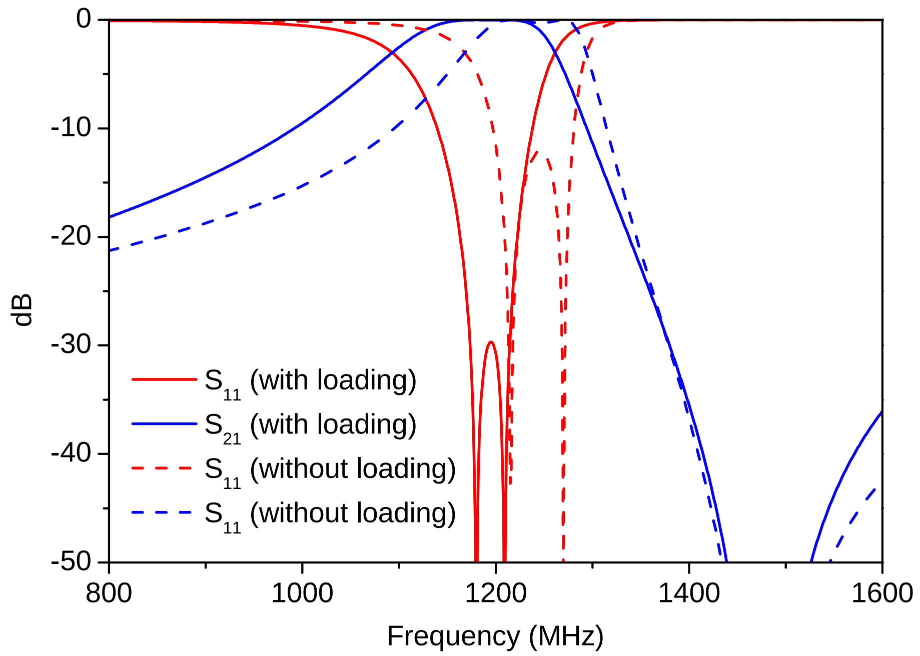

Figure 7.3: Deviation of the lower band resonant frequency due to loading effect

where

$$Y_e = \frac{j\omega C_s}{1-\omega^2 L_s C_s} + \frac{Z_3 + jZ_v \tan\theta_3}{Z_v + jZ_3 \tan\theta_3} \tag{7.2}$$

$$Y_o = \frac{j\omega C_s}{1-\omega^2 L_s C_s} - jY_3 \cot\theta_3 \tag{7.3}$$

where Y_e and Y_o represent the even and odd mode admittance of the circuit looking from point A in Fig. 7.2(b) and (c) respectively and Z_v represents the collective impedance of the via holes along with the pad. Additionally, there is a shift of resonant frequency owing to the loading effect of the upper portion of the circuit. Smith chart results of the upper portion of the circuit at the lower band resonant frequency reveal an additional shunt capacitance of approximately 3 pF. The deviation in resonant frequency is shown in Fig. 7.3. The reflection zeroes in this structure are directly impacted by the overall combination of the series and the shunt LC network along with the characteristics of the transmission line.

7.3.2 The Upper band

The combline configuration directly manifests the upper band at the vicinity of the resonant frequency of the series LC circuit. The key parameters responsible for this conventional dual-pole combline response are the lengths L_1 and L_2, the width W_1, and the spacing W_2 of the two lines along with the capacitor C_p. The $N+2$ coupling matrix for the combline configuration designed at 1.8 GHz and having a bandwidth of 100 MHz is given by (7.4).

$$M = \begin{pmatrix} 0 & 1.4312 & 0 & 0 \\ 1.4312 & 0 & 2.167 & 0 \\ 0 & 2.167 & 0 & 1.4312 \\ 0 & 0 & 1.4312 & 0 \end{pmatrix} \tag{7.4}$$

Additionally, the design of the lower half of the circuit comprising of the series resonator, the transmission lines along with the via hole configuration has been made in such a way that it provides approximately a short circuit at point A as indicated in the circuit at the center frequency of operation of the combline configuration. This ensures the minimal loading effect of the lower portion of the circuit on the combline configuration. The overall reflection coefficient Γ_T [13] is given by (7.5)

$$\Gamma_T = S_{11_1} + \frac{S_{11_1} S_{12_1} \Gamma_2}{1 - S_{22_1} \Gamma_2} \tag{7.5}$$

where the S parameters are obtained by solving the ABCD parameters (T) of the cascading configuration of the combline section from Fig. 7.2 given by

$$T = \begin{bmatrix} 1 & 0 \\ Y_{in_1} & 1 \end{bmatrix} \begin{bmatrix} \cos\theta_2 & jZ_2 \sin\theta_2 \\ jY_2 \sin\theta_2 & \cos\theta_2 \end{bmatrix} \tag{7.6}$$

where, Z_2, Y_2, and θ_2 represents the characteristic impedance, admittance, and the electric length of the series transmission line and Y_{in_1} represents the admittance of the shunt line terminated by the capacitor C_p and is given by

$$Y_{in_1} = Y_1 \frac{Z_1 + jZ_{C_p} \tan\theta_1}{Z_{C_p} + jZ_1 \tan\theta_1} \tag{7.7}$$

7.3.3 The transmission zero

The transmission zero is directly manifested at the resonant frequency of the series LC resonator with the series impedance given by (7.8) which behaves like a short circuit at the resonant frequency ($f = \frac{1}{2\pi\sqrt{(L_s C_s)}}$).

$$Z_s = \frac{1 - \omega^2 L_s C_s}{j\omega C_s} \tag{7.8}$$

The schematic simulation (performed in Cadence AWR) of the overall response of the circuit is given in Fig. 7.4. The results clearly reveal a dual-band response with distinct isolation in between the two bands. The first band, manifested by the lower portion of the circuit with an additional loading effect as illustrated in Fig. 7.3, is centered around 1.17 GHz with a bandwidth of 180 MHz. In contrast, the second band, owing to the combline configuration, is centered around 1.9 GHz and has a bandwidth of 290 MHz.

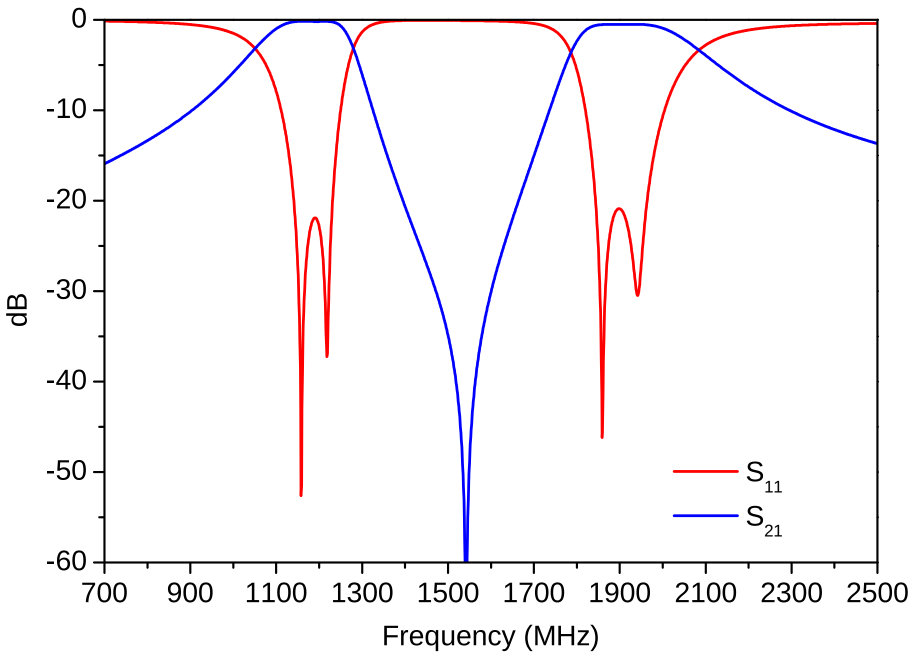

Figure 7.4: Schematic simulation of the proposed dual-band filter.

7.4 Experimental Validation and discussion

For validation of the model, the circuit has been fabricated on an FR4 substrate ($\epsilon = 4.4$, $\tan\delta = 0.02$), and the measured results comply well with the EM simulation results. The experimental result, along with the fabricated prototype, is shown in Fig. 7.5, while the comparison of the EM simulation and the measurement result is shown in Fig. 7.6.

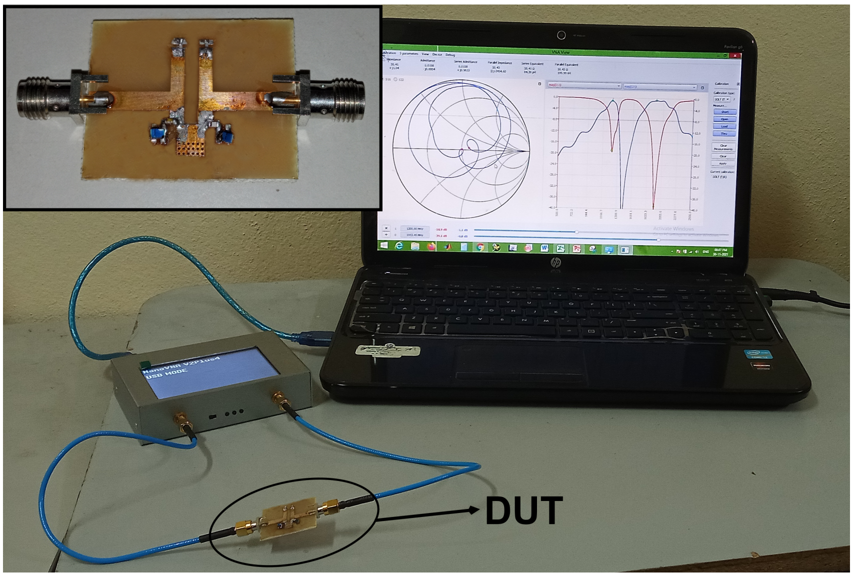

Figure 7.5: The experimental setup and the device under test (inset) with dimensions $W_1 = 2.19$ mm, $W_2 = 2.15$ mm, $W_3 = 4.25$ mm, $W_f = 2.98$ mm, $L_1 = 12.4$ mm, $L_2 = 7.2$ mm, $L_3 = 2.4$ mm, $L_4 = 4.8$ mm, $L_f = 12.5$ mm, $C_p = 0.5$ pF, $C_s = 2.7$ pF, $L_s = 3.9$ nH.

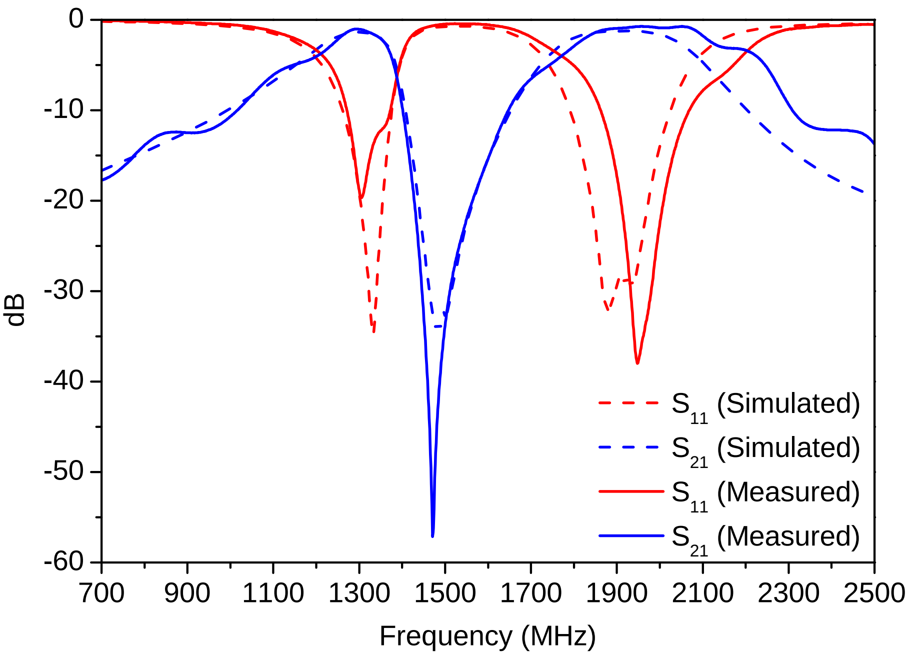

Figure 7.6: Comparison of the EM simulated and the measured results.

The first or the lower band has a bandwidth of approximately 160 MHz and is centered around 1.3 GHz, while the upper band is centered around 1.96 GHz and covers a bandwidth of about 296 MHz. The measured results comply well with the simulation results and incur a maximum IL of 1 dB and 0.63 dB for the first and the second band, respectively, while the return loss (RL) is more than 19.7 dB and 38 dB in the lower and upper band, respectively. Additionally, the use of a series LC resonator inherently generates a transmission zero in between the two bands, thereby preventing any additional source-load coupling circuitry.

Table 7.1: Comparison with other works in the literature

	f_0 **(GHz)**	f_1/f_2	**FB (%)**	**IL**	**RL**	**Size**
[104]	1.57/2.38	1.52	9.9/6.5	1.21/1.95	19/24	1.1×0.48
[109]	8/11.4	1.43	3.01/2.46	2.26/3.07	NA	1.66×1.31
[110]	1.94/4.84	2.49	14.43/2.69	1.26/2.69	15/16	0.179×0.097
[111]	2.45/5.85	2.39	6.5/3	1.06/2.04	NA	0.47×0.56
[113]	2.6/5.8	2.23	10.4/3.6	1.1/2.15	>20	0.26×0.34
[117]	3.5/4.9	1.4	3.7/5	1.1/1.8	NA	0.36×0.65
This work	1.3/1.96	1.5	12.43/15.1	1/0.73	19.7/38	0.34×0.27

IL, RL are in dB scale while size is in terms of $\lambda_g \times \lambda_g$.

A comparative study on the filter characteristics with previously published works is shown in Table 7.1. The compactness of the circuit for very closely spaced bands with the best IL and fractional bandwidth among all the other competitors listed in Table 7.1 adds to the novelty. Although the circuit in [110] excels in compactness, it suffers from higher IL and a considerably

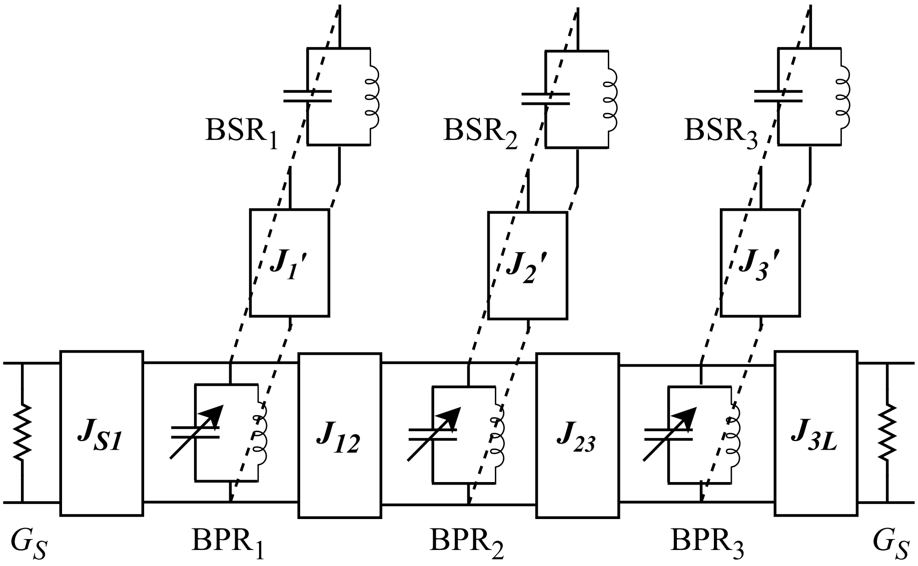

Figure 7.7: Schematic of the proposed configuration.

high passband frequency ratio. There is a slight variation in the bandwidth of the upper band owing to the higher Q of the lumped capacitors used. Although the circuit in [114] excels in passband frequency ratio as well as the compactness, the IL is high, and the measured in-band rejection is only around 22 dB as compared to almost 60 dB in this work. It is observed that the TZ is more distinct in the EM simulated and measured results as compared to the schematic simulation owing to the presence of additional source to load coupling. The presence of a second-order filter structure limits the ability to achieve simultaneous non-reciprocity. This is due to the reduction in the degree of freedom for RF energy to propagate among the harmonics, which is a drawback of the circuit when aiming to demonstrate dual-band simultaneous non-reciprocal response.

7.5 The novel synthesis method for dual-band BPF with manifesting dual-band non-reciprocity

The proposed configuration, as shown in Fig. 7.7, consists of bandstop resonator configurations (BSR$_x$) coupled with bandpass resonators (BPR$_x$), where x ranges from 1 to n and n is the order of the filter, and manifests a dual n^{th}-order bands separated by a sharp transmission zero (TZ). Subsequently, the BPRs are time-modulated to generate non-reciprocal filtering isolation response. Fig. 7.8 shows the frequency translation from the LPP model into a dual-band non-reciprocal BPP model.

The LPP to BPP domain frequency translation for the proposed configuration can be math-

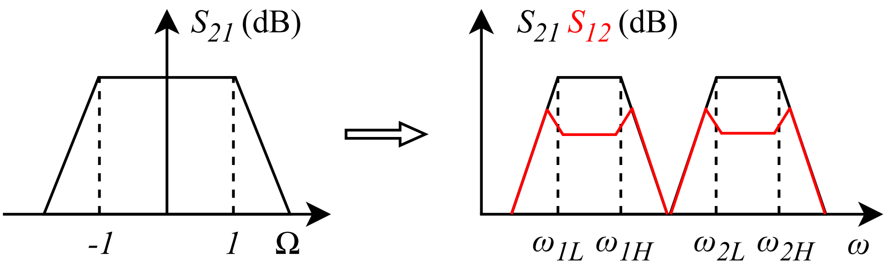

Figure 7.8: LPP to non-reciprocal BPP conversion.

ematically represented by

$$\Omega = \alpha(\varpi) - \beta(\omega) \tag{7.9}$$

where $\alpha(\varpi)$ and $\beta(\omega)$ take into consideration the temporally modulated bandpass resonators and time-invariant bandstop resonators, respectively, the latter can be represented in the form given in (7.10)

$$\beta(\omega) = \frac{b_1}{\left(\frac{\omega}{\omega_1} - \frac{\omega_1}{\omega}\right)} \tag{7.10}$$

where ω_1 and b_1 are the center frequency and susceptance slope parameters of the bandstop resonators, respectively. In contrast, the expression $\alpha(\varpi)$, given in (7.11), is a bit intriguing and incorporates all the spectral harmonics owing to the temporal modulation of the space-separated resonators and generates a non-reciprocal filtering isolation response in both the bands.

$$\alpha(\varpi) = \frac{1}{b_0}\left(\frac{\varpi}{\omega_1} - \frac{\omega_1}{\varpi}\right) = \varpi C_p + \frac{1}{\omega L_p} \tag{7.11}$$

where C_p and L_p are the BPP capacitors and inductors, respectively, and are related to the LPP elemental values by (7.12).

$$C_p = \frac{g}{\Delta\omega} \tag{7.12}$$

$$L_p = \frac{1}{\omega_0^2 C_p} \tag{7.13}$$

7.6 Synthesis of the proposed polynomials

The synthesis approach begins by utilizing the conventional all-pole Chebyshev prototype of order m. As commonly known, this prototype can be represented by connecting shunt capacitances with a unit value through admittance inverters having parameter values $J_{q,q+1} = 1/\sqrt{g_{q,q+1}}$. The conversion from Ω to ω domain, given in (7.9), can be obtained by imposing certain constraints in the mapping between the parameters of the LPP and BPP domain [118, 119]. In particular, the lower band-edges of the BPP domain (ω_{1L} and ω_{2L}), as shown in Fig. 7.8, must be mapped to $\Omega = -1$ in the LPP domain. Similarly, the upper band-edges (ω_{1H} and ω_{2H}) must be mapped to $\Omega = 1$ in the LPP domain. In the reciprocal case, owing to the symmetry in the magnitude of the BPP plane, the following equations hold true.

$$T(-\omega_{1L}) = T(-\omega_{2L}) = T(\omega_{1H}) = T(\omega_{2H}) = 1 \tag{7.14}$$

where $T(\omega) = \alpha(\omega) - \beta(\omega)$ is the reciprocal form of (7.9). Another form of (7.14) can be expressed in the form $U(\omega) = T(\omega) - 1$, whose zeroes are the lower and upper cutoff frequencies (ω_{1L}, ω_{2L}, ω_{1H}, and ω_{2H}) of the BPP model. Therefore $U(\omega)$ can be represented as a ratio of two polynomials and is given by (7.15).

$$U(\omega) = \frac{\omega_4 + \sum_{k=0}^{2m-1} n_k \omega^k}{\sum_{k=0}^{2m-1} d_k \omega^k} \tag{7.15}$$

where m denotes the number of bands in the BPP model while n_k are the coefficients associated with the angular frequency terms ω_k of the polynomial $U(\omega)$. The coefficients of equation (7.15) can be obtained in dual ways. First, it can be constructed directly from (7.9) by substituting $\alpha(\omega)$ and $\beta(\omega)$; secondly, as the zeroes of (7.15) are the lower and upper cutoff frequencies of the BPP model, therefore, the polynomial $U(\omega)$ can be constructed as given by (7.16) and the polynomials can be obtained thereof.

$$U(\omega) = (\omega - \omega_{1H})(\omega - \omega_{2H})(\omega + \omega_{1L})(\omega + \omega_{2L}) \tag{7.16}$$

Equating the terms of $U(\omega)$ obtained from equations (7.9) and (7.16), two sets of equations are obtained; one set correlates the numerator polynomial coefficients of (7.15) with the angular center frequencies (ω_0 and ω_1) and susceptance slope parameters (b_0 and b_1), while the other relates the numerator polynomial coefficients with the BPP cutoff frequencies as given in equations.

$$\begin{aligned}
n_0 &= \omega_0^2 \omega_1^2 \\
n_1 &= \frac{\omega_0 \omega_1^2}{b_0} \\
n_2 &= -\omega_0^2 - \omega_1^2 - \frac{\omega_1 \omega_2}{b_1 b_2} \\
n_3 &= -\frac{\omega_1}{b_1}
\end{aligned} \tag{7.17}$$

$$\begin{aligned}
n_0 &= \omega_{1H}\omega_{2H}\omega_{1L}\omega_{2L} \\
n_1 &= omega_{1H}\omega_{2H}(\omega_{1L} + \omega_{2L}) - \omega_{1L}\omega_{2L}(\omega_{1H} + \omega_{2H}) \\
n_2 &= \omega_{1H}\omega_{2H}\omega_{1L} + \omega_{1H}\omega_{2H}\omega_{2L} - \omega_{1H}\omega_{1L}\omega_{2L} - \omega_{2H}\omega_{1L}\omega_{2L} \\
n_3 &= \omega_{1H}\omega_{2H} - \omega_{1H}\omega_{1L} - \omega_{1H}\omega_{2L} - \omega_{2H}\omega_{1L} - \omega_{2H}\omega_{2L} + \omega_{1L}\omega_{2L}
\end{aligned} \tag{7.18}$$

This set of equations can now be solved to find the values of ω_0, ω_1, b_0, and b_1 and is given in (7.19).

$$\begin{aligned} w_0 &= \sqrt{\frac{-n_0 n_3}{n_1}} \\ w_1 &= \sqrt{\frac{-n_1}{n_3}} \\ b_0 &= \sqrt{\frac{-n_0}{n_1 n_3}} \\ b_1 &= -\frac{w_0 w_1}{b_0(w_0^2 + w_1^2 + n_2)} \end{aligned} \tag{7.19}$$

The admittance inverters (J_{S1}, J_{12}, J_{23}, and J_{3L}) coupling the BPRs and those coupling the BPRs with the BSRs (J_1', J_2', an J_3') are obtained by simple matching networks and are given by (7.20).

$$\begin{aligned} J_{S1} &= \sqrt{\frac{\omega G_S C_{p_1}}{b_0 g_0 g_1}} \\ J_{12} &= \omega_0 \sqrt{\frac{C_{p_1} C_{p2}}{g_1 g_2}} \\ J_m' &= \sqrt{\frac{\omega_0 \omega_1 C_{p_m} C_m'}{b_0 b_1}} \end{aligned} \tag{7.20}$$

where C_{p_1} and C_{p_2} are the capacitors loaded in BPR˙1 and BPR˙2, respectively, m=1 to 3 represent the index of the BSRs and the associated couplings, and the values of J_{23} and J_{3L} are equal to J_{12} and J_{S1}, respectively.

7.6.1 Lumped Reciprocal Dual-Band Filter Synthesis

Based on the procedure and formulas given in the previous sections, a 3^{rd} order lumped element dual-band filter is synthesized with the parameters given below.

$$f_{1L} = 180 \text{ MHz}$$
$$f_{1H} = 190 \text{ MHz}$$
$$f_{2L} = 210 \text{ MHz}$$
$$f_{2H} = 220 \text{ MHz}$$
$$RL = 20 \text{ dB}$$

The LPP or g values corresponding to the Chebyshev response are $g_0 = g_4 = 1$, $g_1 = g_3 = 0.8506$, and $g_2 = 1.1028$. The capacitors (C_{p_m}) of the BPRs are chosen to be 12 pF while the inductors (L_m') of the BSRs are chosen to be 47 nH. The first step involves generating the n_x

values ($x = 0$ to 3) after substituting the cutoff frequencies in (7.18), and are given by (7.21).

$$\begin{aligned} n_0 &= 2.4626 \times 10^{36} \\ n_1 &= 1.9943 \times 10^{26} \\ n_2 &= -3.1701 \times 10^{18} \\ n_3 &= -1.2566 \times 10^{8} \end{aligned} \tag{7.21}$$

Based on these values, the center frequencies and susceptance slope parameters of the BPRs and BSRs are obtained from (7.19) and are given by (7.22).

$$\begin{aligned} \omega_0 &= 1.2457 \times 10^9 \text{ rad/s} \\ \omega_1 &= 1.2598 \times 10^9 \text{ rad/s} \\ b_0 &= 9.9127 \\ b_1 &= 5.0407 \end{aligned} \tag{7.22}$$

Based on these values, the admittance inverter values obtained from (7.20) and the corresponding lumped elements are synthesized (according to the analysis given in Section 3.2.4) and are given in (7.23).

$$\begin{aligned} J_{S1} &= 0.006 \\ J_{12} &= 0.0016 \\ J'_m &= 0.0022 \\ C_{S1_{\text{series}}} &= \frac{J_{S1}}{\omega_0\sqrt{1-\left(\frac{J_{01}}{G_S}\right)^2}} = 5.0073 \text{ pF} \\ C_{S1_{\text{shunt}}} &= \frac{C_{S1_{\text{series}}}}{1+\left(\frac{\omega_0 C_{S1_{\text{series}}}}{G_S}\right)^2} = 4.5634 \text{ pF} \\ C_{12} &= \frac{J_{12}}{\omega_0} = 1.25 \text{ pF} \\ C'_m &= \frac{J'_m}{\omega_1} = 1.7843 \text{ pF} \end{aligned} \tag{7.23}$$

Thus, the final capacitor and inductor values of the BPRs and BSRs are given by (7.24).

$$\begin{aligned} C_{p_1} &= C_{p_m} - C_{S1_{\text{shunt}}} - C_{12} - C'_m = 4.4024 \text{ pF} \\ C_{p_2} &= C_{p_m} - 2C_{12} - C'_m = 7.7159\text{pF} \\ L_p &= \frac{1}{\omega_0^2 C_{p_m}} = 53.7053 \text{ nH} \\ C_s &= \frac{1}{\omega_0^2 L'_m} - C'_m = 11.6223 \text{ pF} \end{aligned} \tag{7.24}$$

It is worthwhile noting that the $C_{p_3} = C_{p_2}$ and $C_{p_4} = C_{p_1}$ owing to the symmetry of the circuit. The reciprocal response using the calculated values of lumped element is shown in Fig. 7.9. The response shows the dual-band response with a sharp TZ at $f_1 = \omega_1/2\pi$.

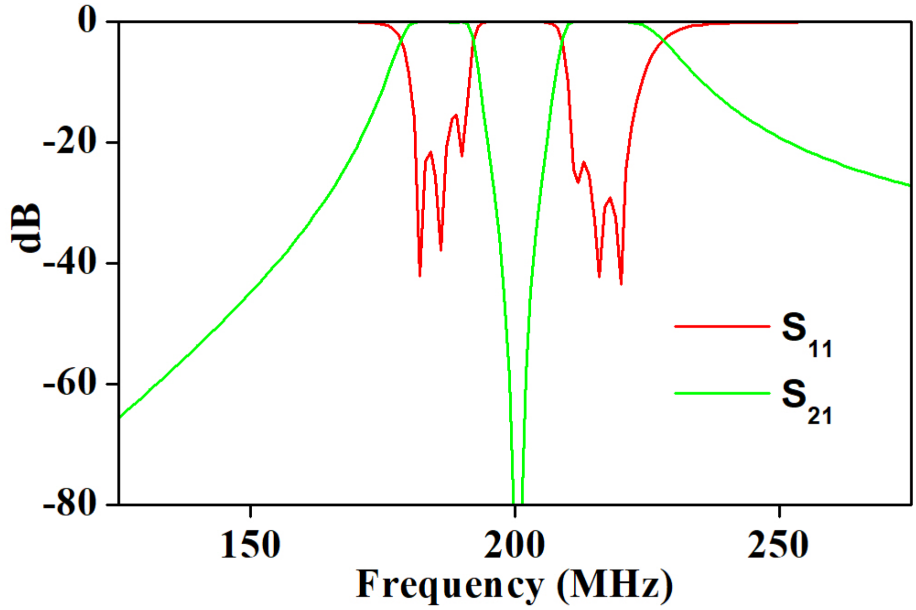

Figure 7.9: The reciprocal response.

7.6.2 The non-reciprocal response

The simultaneous non-reciprocal response can be obtained in both the bands of the dual-band response by splitting the admittance term $\varpi_0 C_P$ in (7.11) into the spectral admittance matrix as given in (7.25).

$$\varpi_0 C_p = C_p \begin{bmatrix} \ddots & \vdots & \vdots & \vdots & \vdots & \vdots & \iddots \\ \cdots & (\omega-\omega_m)\frac{\zeta}{2}e^{j\phi} & (\omega-\omega_m) & (\omega-\omega_m)\frac{\zeta}{2}e^{-j\phi} & 0 & 0 & \cdots \\ \cdots & 0 & \omega\frac{\zeta}{2}e^{j\phi} & \omega & \omega\frac{\zeta}{2}e^{-j\phi} & 0 & \cdots \\ \cdots & 0 & 0 & (\omega+\omega_m)\frac{\zeta}{2}e^{j\phi} & (\omega+\omega_m) & (\omega+\omega_m)\frac{\zeta}{2}e^{-j\phi} & \cdots \\ \iddots & \vdots & \vdots & \vdots & \vdots & \vdots & \ddots \end{bmatrix} \tag{7.25}$$

From the simulation point of view, if the capacitors C_{p_1} and C_{p_2} are replaced with varactor diodes with a series capacitor (C_{DC}) to block the DC and a proper biasing network, as shown in Fig. 7.10, the circuit generates the non-reciprocal response as shown in Fig. 7.11. The DC-blocking capacitors used are 10 pF and 36 pF, respectively, for the first and last resonators and the second resonator. The biasing circuit comprises of a 3^{rd} order LPF having series inductors of values 220 nH and a shunt capacitor of value 150 pF. The DC biasing applied to the first and third resonators are 2.5V, while that for the second resonator is 2 V. The sinusoidal signal amplitudes modulating the first and the third resonators are 1.8 V, while for the second resonator is 0.8V. The modulation frequency (f_m) and the progressive phase shift ($\Delta\phi$) are 9 MHz and 70°. The modulation index (ζ) surfaces from the AC and DC biasing applied to the resonator which generates the capacitance deviation from the nominal value. As can be seen from the

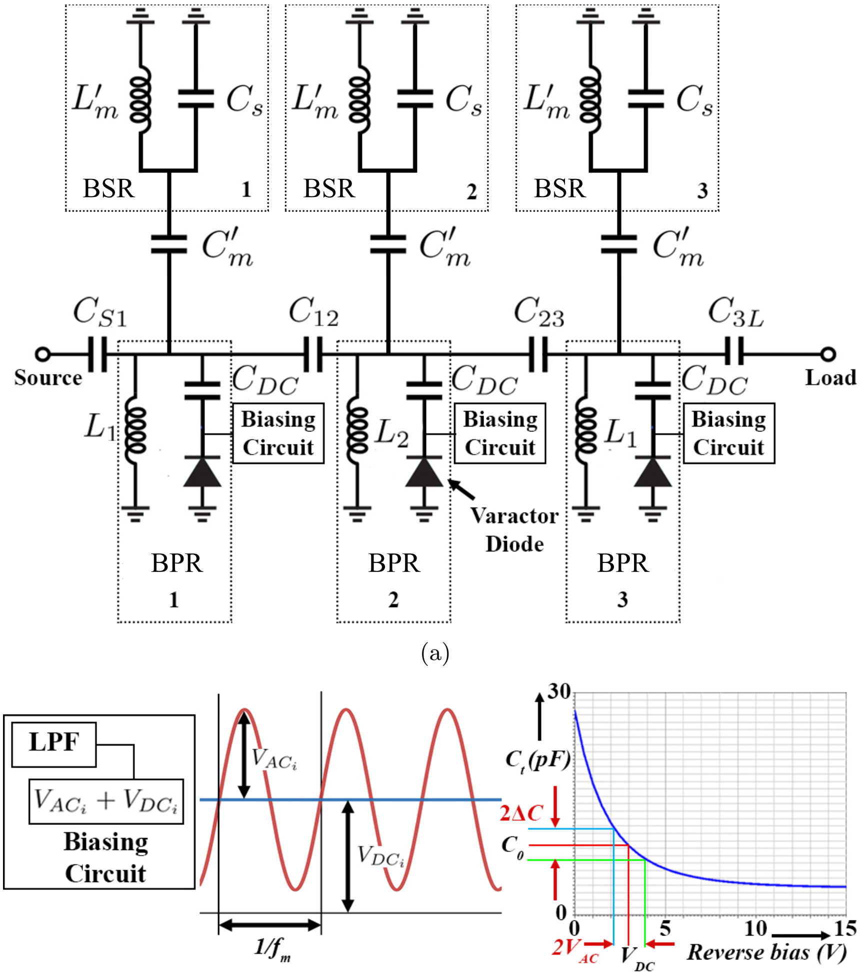

(a)

(b)

Figure 7.10: (a) Schematic of a 3^{rd} order dual-band NR-BPF; (b) the biasing circuit to the varactors and the corresponding generation of time-varying capacitance with the aid of modulation signal having a fixed DC offset.

circuit simulated response, more than 20 dB isolation is achieved in both bands.

7.6.3 Practical realization

The circuit has been fabricated on an FR4 substrate. The varactor diode used is SMV1236, and the DC biasing voltages applied to the diodes are 2.5V, 1.55V, and 2.5V, while the amplitudes of the AC signals are 1.4V, 1V, and 1.4V, starting from the first resonator. Both the BPR as well as the BSR comprise of Coilcraft 1111SQ high Q inductors and Kemet capacitors. The biasing network is again composed of Coilcraft 22SQ high Q inductors. The fabricated prototype and the measurement setup are shown in Fig. 7.12 and Fig. 7.13, respectively, while the comparison of the non-reciprocal simulated and measured results is shown in Fig. 7.14. The EM simulation response has been carried out using Harmonic Balance Simulator in Cadence AWR.

As can be seen from Fig. 7.14, the dual-band non-reciprocal response complies well with the simulated response. Two distinct bands are visible at around 185 MHz and 215 MHz with

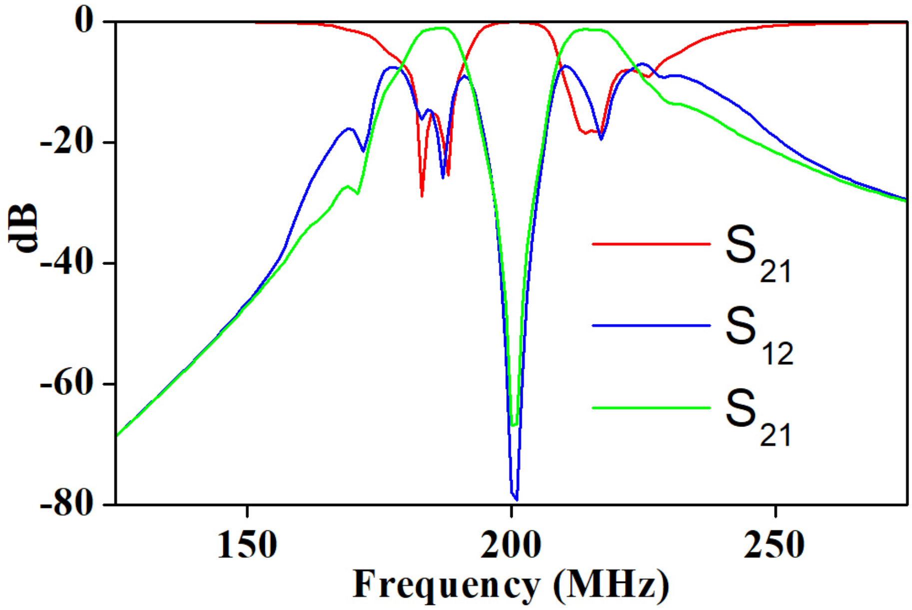

Figure 7.11: The non-reciprocal response.

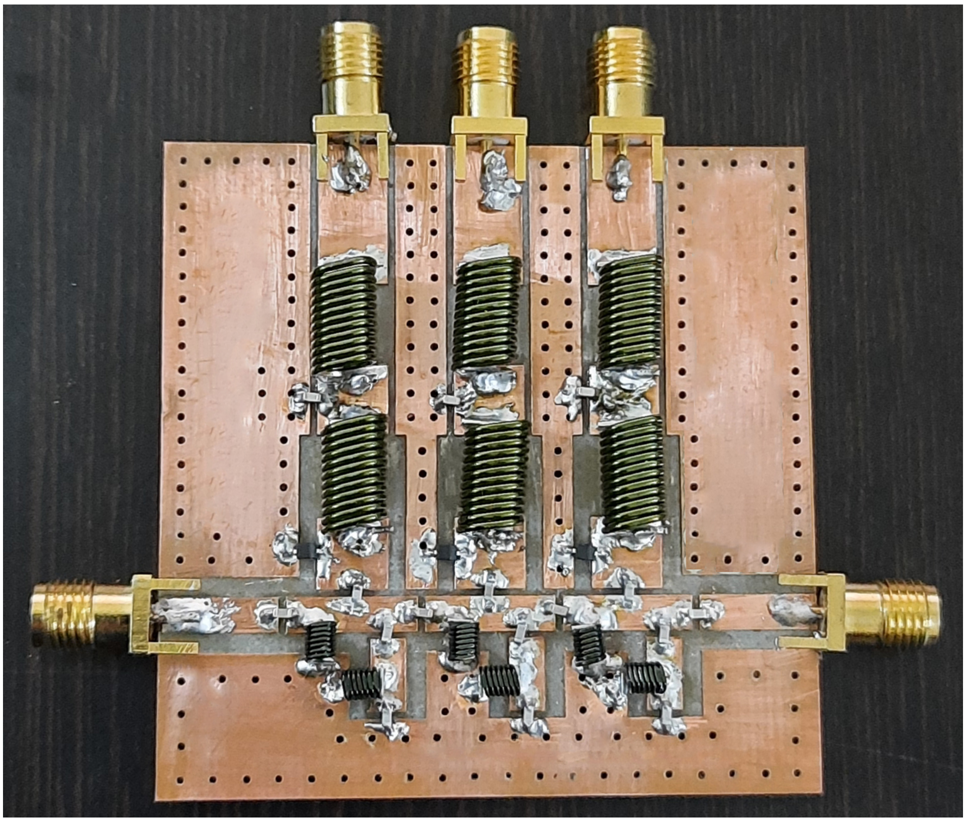

Figure 7.12: The fabricated prototype.

a bandwidth of 10 MHz in both cases. The measured IL in the non-reciprocal case is around 3.9 dB as compared to 3.4 dB in the simulation case for the first band, while, for the second band, the simulated and measured responses are equal to 3.6 dB and 4.1 dB, respectively. The isolation is around 20 dB for the first band, while for the second band, it is somewhat degraded, and the maximum isolation reaches around 14 dB; nevertheless, it provides sufficient isolation for

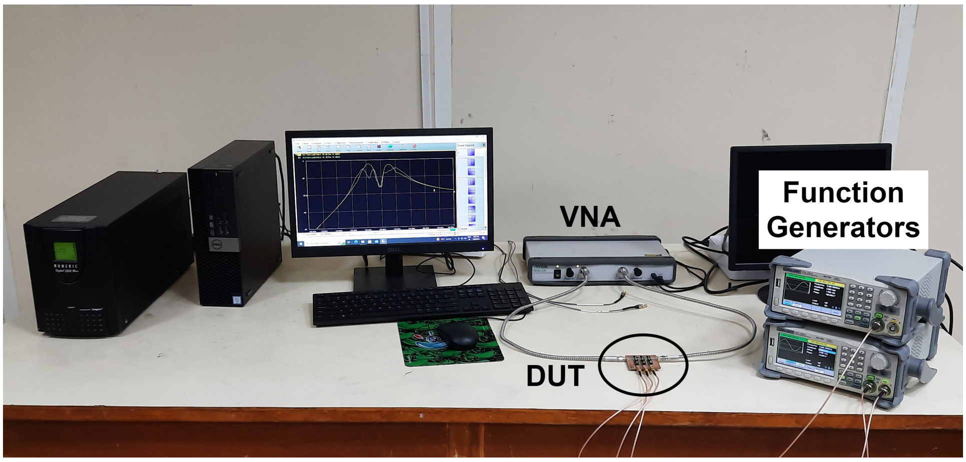

Figure 7.13: The measurement setup.

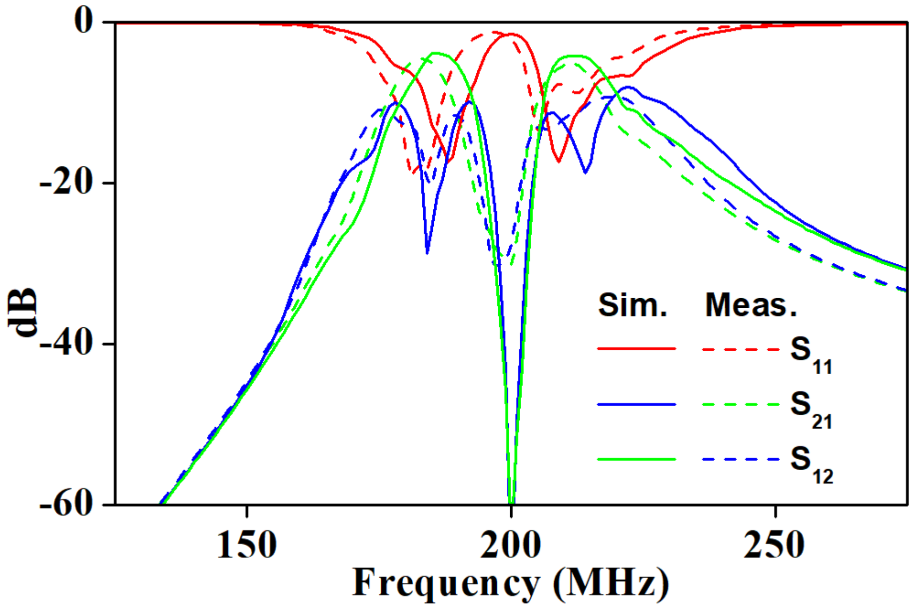

Figure 7.14: The comparison of the simulated and measured non-reciprocal response.

the backward traveling wave. The detailed specification of the dual-band BPF with dual-band non-reciprocal response is given in Table 7.2

Table 7.2: Filter Specifications

Sl. No.	Parameter	Simulation 1st band	Experiment 1st Band	Simulation 2nd band	Experiment 2nd Band
1.	Center Frequency	185 MHz	184 MHz	215 MHz	213 MHz
2.	Bandwidth	≈ 10 MHz	≈ 10 MHz	≈ 10 MHz	≈ 10 MHz
3.	Insertion Loss	3.4 dB	3.9 dB	3.6 dB	4.1 dB
4.	Return Loss	>12 dB	>12 dB	20 dB	11 dB
5.	Isolation	>20 dB	>18 dB	20 dB	14 dB

The comparison conducted with recent works in the literature, as summarized in Table 7.3, serves to emphasize the uniqueness and novelty of the proposed methodical approach in achieving dual-band simultaneous non-reciprocity in closely spaced bands. Notably, this accomplishment is made possible by utilizing only three time-modulating resonators, which in turn requires only three modulation signal sources. This reduction in the number of required resonators and modulation sources significantly reduces complexity and promotes a cost-effective solution. An additional advantage of the proposed approach, distinguishing it from the findings presented in [51], is its ability to avoid spurious responses in the lower and upper skirt frequency ranges. This avoidance of unwanted frequency components further enhances the novelty and practical utility of the proposed method.

Table 7.3: Comparison with other works in the literature

	Techn.	f_0 **(MHz)**	**BW**	**IL**	**D**	**N**	$f_1 : f_{2(3)}$
[97]	Lump. SB	136-163	27.5	<4.1	>20	3	NA
[67]	Dist./SB	960	43.2	4.5	13.8	4	NA
[98]	Dist./SB	1020	65	5.5	≈ 11	2	NA
[50]	Dist./SB	1640-1970	50	4.96-3.94	20	2	NA
[51]	Lump. DB	198 245	14.5 14	3.7 5.5	26.1 35.9	6	1:1.23
[12]	Lump. TB	198-210 247-271 302-369	16.5 23 27.5	4 3.7 3.6	9.4-30.5 9-36.5 8.5-49.8	9	1:1.27 1:1.56
This Work	Lump. DB	185 215	10 10	3.9 ≈ 4.1	20 14	3	1:1.16

IL, RL, and Directivity (D) are in dB, BW is in MHz; SB = Single Band, DB = Dual Band, TB = Triple Band, RB = Reciprocal Band, and N = Time-modulated elements.

7.7 Conclusion

In conclusion, this chapter has focused on the implementation of dual-band bandpass filters with dual-band non-reciprocities, addressing the challenge of achieving simultaneous non-reciprocity in this context. Through the exploration of various design strategies on dual-band bandpass filters and the incorporation of varactor diodes for tunability, an initial approach to generating simultaneous non-reciprocity in the dual-band response has been performed. The failure of the initial approach in achieving dual-band non-reciprocal phenomenon has however led to the development of a novel reciprocal filter configuration in the first part of the chapter, demonstrating closely spaced dual-band response, low-loss characteristics, and substantial rejection between the bands. While non-reciprocity was not achieved due to the filter structure's order, valuable insights were gained.

The second part of the chapter introduced a novel synthesis approach using a dual-band bandpass resonator coupled with bandstop resonators and spatio-temporal modulation. This pioneering method successfully achieved dual-band non-reciprocity by employing only three time-harmonic elements for both bands, a remarkable achievement in the field, which in turn requires only three modulation signal sources. This reduction in the number of required resonators and modulation sources significantly reduces complexity and promotes a cost-effective solution. This approach holds great promise for achieving dual-band filtering isolation in modern transceiver systems with very closely spaced bands.

Overall, this chapter has contributed to the advancement of dual-band bandpass filters and non-reciprocal phenomena. The proposed configurations and innovative techniques have opened up new possibilities and avenues for future research and development. The findings presented herein lay the foundation for further exploration and refinement of dual-band non-reciprocal bandpass filters, enabling enhanced performance and broader applications in advanced communication systems

7.8 Publications

1. **Prantik Dutta**, Gande Arun Kumar, Gopi Ram, Dondapati Suneel Varma, ”A Novel Compact Low-Loss Closely Spaced Dual-Band Filter for Wireless Communications”, *IEEE Microwave and Antenna Propagation Conference, 2023 (Communicated).*

2. **Prantik Dutta**, Gande Arun Kumar, Gopi Ram, ”Dual-band Bandpass Filters with Dual-band Non-reciprocity”, *IEEE Microwave and Wireless Technology Letters (Under Review).*

Chapter 8

Conclusion and Future Scope

In conclusion, this research has successfully addressed the objectives set forth in the introduction, aiming to advance the field of spatio-temporal non-reciprocal bandpass filters (NR-BPFs). Through an extensive literature review and analysis, the origin of non-reciprocity was discussed, leading to the proposal of numerical analysis techniques based on non-conventional filter polynomials. Optimization strategies were developed to enhance the isolation characteristics of the filters, eliminating the need for manual parameter tuning.

Furthermore, the concept of a 3D coupling matrix was introduced to enhance the understanding of spectral resonator generation at harmonic frequencies. Non-conventional S-parameter equations were synthesized to accurately model the behavior of non-reciprocal bandpass filters. The research then expanded to the generation of spatio-temporally modulated dual-band non-reciprocity, incorporating dual-band distributed responses and band tunability.

Finally, a novel synthesis method was proposed for the development of dual-band bandpass filters using lumped elements, demonstrating simultaneous non-reciprocity in both bands with minimal time-modulating elements. This research has contributed to the knowledge in the field of spatio-temporal NR-BPFs by providing novel insights, innovative design approaches, and practical implementations.

The successful implementation of each research objective showcases the potential of spatio-temporal modulation in achieving non-reciprocity in bandpass filters. These advancements offer promising opportunities for the integration of compact and cost-effective non-reciprocal components in modern wireless systems, overcoming the limitations of traditional ferrite-based materials. This research has laid the groundwork for future exploration and development in the field, offering new possibilities and applications in wireless communication technologies. The following areas hold exciting opportunities for further advancement:

Formulation of exact mathematical equations: Future research can focus on formulating precise mathematical equations that govern the placement of in-band transmission zeros (TZs) in the backward isolation response. By understanding the underlying mathematical principles, it will be possible to optimize and fine-tune the performance of NR-BPFs, enhancing their filtering capabilities and isolation characteristics.

Coupling Matrix formulation of dual-band BPF with dual-band non-reciprocity: Another interesting direction for future work is the development of a coupling matrix formulation specifically for dual-band NR-BPFs with dual-band non-reciprocity. This would enable the design and analysis of filters that operate in multiple frequency bands, offering enhanced versatility and functionality in wireless communication systems.

Tunability in center frequency and bandwidth: Exploring methods to achieve tunability in the center frequency and bandwidth of individual bands in dual-band NR-BPFs holds significant potential. By incorporating tunable elements or modulation techniques, it would be possible to dynamically adjust the filter's response to meet varying system requirements and adapt to different frequency ranges.

Compact MMIC designs for 5G bands: As the demand for 5G communication systems continues to grow, future research can focus on developing compact monolithic microwave integrated circuit (MMIC) designs of NR-BPFs specifically tailored for the 5G frequency bands. This would involve optimizing the circuit layout, exploring innovative designs, and leveraging advanced fabrication techniques to achieve compact, high-performance filters suitable for 5G applications.

By pursuing these future research directions, we can further enhance the capabilities and practical applications of spatio-temporal NR-BPFs, contributing to the advancement of wireless communication technologies and meeting the evolving needs of modern communication systems.

Bibliography

[1] X. Wu, X. Liu, M. D. Hickle, D. Peroulis, J. S. Gómez-Díaz, and A. Álvarez Melcón. Isolating bandpass filters using time-modulated resonators. *IEEE Transactions on Microwave Theory and Techniques*, 67(6):2331–2345, 2019.

[2] S. Qin, Q. Xu, and Y. E. Wang. Nonreciprocal components with distributedly modulated capacitors. *IEEE Trans. Microw. Theory Techn.*, 62(10):2260–2272, Oct 2014.

[3] P. K. Tien and H. Suhl. A traveling-wave ferromagnetic amplifier. *Proceedings of the IRE*, 46(4):700–706, 1958.

[4] S. Qin and Y. E. Wang. Parametric conversion with distributedly modulated capacitors (dmc) for low-noise and non-reciprocal rf front-ends. In *2013 IEEE MTT-S International Microwave Symposium Digest (MTT)*, pages 1–3, 2013.

[5] A. Alvarez-Melcon, X. Wu, J. Zang, X. Liu, and J. S. Gomez-Diaz. Coupling matrix representation of nonreciprocal filters based on time-modulated resonators. *IEEE Transactions on Microwave Theory and Techniques*, 67(12):4751–4763, 2019.

[6] D. Simpson and D. Psychogiou. Magnet-less non-reciprocal bandpass filters with tunable center frequency. In *2019 49th European Microwave Conference (EuMC)*, pages 460–463, 2019.

[7] X. Wu, M. Nafe, A. A. Melcón, J. Sebastián Gómez-Díaz, and X. Liu. A non-reciprocal microstrip bandpass filter based on spatio-temporal modulation. In *2019 IEEE MTT-S International Microwave Symposium (IMS)*, pages 9–12, 2019.

[8] X. Wu, M. Nafe, and X. Liu. Non-reciprocal 2nd-order bandpass filter by using time-modulated microstrip quarter-wavelength resonators. In *2019 International Conference on Microwave and Millimeter Wave Technology (ICMMT)*, pages 1–3, 2019.

[9] Xiaohu Wu, Mahmoud Nafe, Alejandro Álvarez Melcón, Juan Sebastián Gómez-Díaz, and Xiaoguang Liu. Frequency tunable non-reciprocal bandpass filter using time-modulated microstrip $\lambda_g/2$ resonators. *IEEE Transactions on Circuits and Systems II: Express Briefs*, 68(2):667–671, 2021.

[10] Dakotah Simpson and Dimitra Psychogiou. Fully-reconfigurable non-reciprocal bandpass filters. In *2020 IEEE/MTT-S International Microwave Symposium (IMS)*, pages 807–810, 2020.

[11] Girdhari Chaudhary and Yongchae Jeong. Nonreciprocal bandpass filter using mixed static and time-modulated resonators. *IEEE Microw. Wireless Compon. Lett.*, 32(4):297–300, 2022.

[12] Dakotah Simpson and Dimitra Psychogiou. Multiband magnetless isolators and circulators with reconfigurable bandpass filtering capabilities. *IEEE Transactions on Microwave Theory and Techniques*, 71(3):1239–1250, 2023.

[13] Richard J. Cameron, Chandra M. Kudsia, and Raafat R. Mansour. *Microwave Filters for Communication Systems: Fundamentals, Design, and Applications.* Wiley, 2018.

[14] C. E. Fay and R. L. Comstock. Operation of the ferrite junction circulator. *IEEE Transactions on Microwave Theory and Techniques*, 13(1):15–27, 1965.

[15] Christophe Caloz, Andrea Alù, Sergei Tretyakov, Dimitrios Sounas, Karim Achouri, and Zoé-Lise Deck-Léger. Electromagnetic nonreciprocity. *Phys. Rev. Applied*, 10:047001, Oct 2018.

[16] Zhanni Wu, Cody Scarborough, and Anthony Grbic. A spatio-temporally modulated metasurface as a free-space n-path system. In *2020 14th European Conference on Antennas and Propagation (EuCAP)*, pages 1–3, 2020.

[17] D. Ramaccia, D.L. Sounas, A. Marini, A. Toscano, and F Bilotti. Achieving electromagnetic isolation by using up- and down-converting time-varying metasurfaces. In *2020 Fourteenth International Congress on Artificial Materials for Novel Wave Phenomena (Metamaterials)*, pages 1–2, 2020.

[18] Ahmed Kord, Dimitrios L Sounas, and Andrea Alù. Achieving full-duplex communication: Magnetless parametric circulators for full-duplex communication systems. *IEEE Microw. Mag.*, 19(1):84–90, 2017.

[19] Toshiro Kodera, Dimitrios L Sounas, and Christophe Caloz. Magnetless nonreciprocal metamaterial (mnm) technology: Application to microwave components. *IEEE transactions on microwave theory and techniques*, 61(3):1030–1042, 2013.

[20] Romain Fleury, Dimitrios L Sounas, Caleb F Sieck, Michael R Haberman, and Andrea Alù. Sound isolation and giant linear nonreciprocity in a compact acoustic circulator. *Science*, 343(6170):516–519, 2014.

[21] Nicholas A Estep, Dimitrios L Sounas, Jason Soric, and Andrea Alù. Magnetic-free nonreciprocity and isolation based on parametrically modulated coupled-resonator loops. *Nature Physics*, 10(12):923–927, 2014.

[22] Negar Reiskarimian and Harish Krishnaswamy. Magnetic-free non-reciprocity based on staggered commutation. *Nature communications*, 7(1):1–10, 2016.

[23] Nicholas Aaron Estep, Dimitrios L Sounas, and Andrea Alù. Magnetless microwave circulators based on spatiotemporally modulated rings of coupled resonators. *IEEE Transactions on Microwave Theory and Techniques*, 64(2):502–518, 2016.

[24] Negar Reiskarimian, Jin Zhou, and Harish Krishnaswamy. A cmos passive lptv nonmagnetic circulator and its application in a full-duplex receiver. *IEEE J. Solid-State Circuits*, 52(5):1358–1372, 2017.

[25] Tolga Dinc, Mykhailo Tymchenko, Aravind Nagulu, Dimitrios Sounas, Andrea Alu, and Harish Krishnaswamy. Synchronized conductivity modulation to realize broadband lossless magnetic-free non-reciprocity. *Nature communications*, 8(1):1–9, 2017.

[26] Ahmed Kord, Dimitrios L Sounas, and Andrea Alù. Magnet-less circulators based on spatiotemporal modulation of bandstop filters in a delta topology. *IEEE Transactions on Microwave Theory and Techniques*, 66(2):911–926, 2017.

[27] Ahmed Kord, Dimitrios L Sounas, and Andrea Alu. Pseudo-linear time-invariant magnetless circulators based on differential spatiotemporal modulation of resonant junctions. *IEEE Transactions on Microwave Theory and Techniques*, 66(6):2731–2745, 2018.

[28] J. Chang, J. Kao, Y. Lin, and H. Wang. Design and analysis of 24-ghz active isolator and quasi-circulator. *IEEE Transactions on Microwave Theory and Techniques*, 63(8):2638–2649, 2015.

[29] Mathew M Biedka, Rui Zhu, Qiang Mark Xu, and Yuanxun Ethan Wang. Ultra-wide band non-reciprocity through sequentially-switched delay lines. *Scientific reports*, 7:40014, 2017.

[30] Dimitrios L Sounas, Jason Soric, and Andrea Alu. Broadband passive isolators based on coupled nonlinear resonances. *Nature Electronics*, 1(2):113–119, 2018.

[31] A. Nagulu, T. Dinc, Z. Xiao, M. Tymchenko, D. L. Sounas, A. Alù, and H. Krishnaswamy. Non-reciprocal components based on switched transmission lines. *IEEE Transactions on Microwave Theory and Techniques*, 66(11):4706–4725, 2018.

[32] D. Correas-Serrano, J. S. Gomez-Diaz, D. L. Sounas, Y. Hadad, A. Alvarez-Melcon, and A. Alù. Nonreciprocal graphene devices and antennas based on spatiotemporal modulation. *IEEE Antennas and Wireless Propagation Letters*, 15:1529–1532, 2016.

[33] S. Taravati and C. Caloz. Mixer-duplexer-antenna leaky-wave system based on periodic space-time modulation. *IEEE Transactions on Antennas and Propagation*, 65(2):442–452, 2017.

[34] J. Wu, X. Yang, S. Beguhn, J. Lou, and N. X. Sun. Nonreciprocal tunable low-loss bandpass filters with ultra-wideband isolation based on magnetostatic surface wave. *IEEE Transactions on Microwave Theory and Techniques*, 60(12):3959–3968, 2012.

[35] Xiao-Hong Li, Hao-Miao Zhou, Qiu shi Zhang, and Wen-Wen Hu. Lumped modeling with circuit elements for nonreciprocal magnetoelectric tunable band-pass filter. *Chinese Physics B*, 25(11):117505, nov 2016.

[36] M. Ghatge, G. Walters, T. Nishida, and R. Tabrizian. A non-reciprocal filter using asymmetrically transduced micro-acoustic resonators. *IEEE Electron Device Letters*, 40(5):800–803, 2019.

[37] J. M. Manley and H. E. Rowe. Some general properties of nonlinear elements-part i. general energy relations. *Proc. IRE*, 44(7):904–913, July 1956.

[38] J. M. Manley and E. Peterson. Negative resistance effects in saturable reactor circuits. *Electrical Engineering*, 65(12):870–881, Dec 1946.

[39] R. V. L. Hartley. Oscillations in systems with non-linear reactance. *The Bell System Tech. Journal*, 15(3):424–440, July 1936.

[40] A. Van Der Ziel. On the mixing properties of non-linear condensers. *Journal of Applied Physics*, 19(11):999–1006, 1948.

[41] L.A. Blackwell and K.L. Kotzebue. *Semiconductor-diode Parametric Amplifiers.* Prentice-Hall electrical engineering series. Prentice-Hall, 1961.

[42] P. K. Tien. Parametric amplification and frequency mixing in propagating circuits. *Jour. Appl. Phys.*, 29(9):1347–1357, 1958.

[43] Y. E. Wang. Non-reciprocity with time-varying transmission lines (tvtls). In *2012 IEEE International Conference on Wireless Information Technology and Systems (ICWITS)*, pages 1–4, 2012.

[44] Y. E. Wang. Time-varying transmission lines (tvtl) - a new pathway to non-reciprocal and intelligent rf front-ends. In *2014 IEEE Radio and Wireless Symposium (RWS)*, pages 148–150, 2014.

[45] D.M. Pozar. *Microwave Engineering, 4th Edition.* Wiley, 2011.

[46] A Atia and A Williams. New types of waveguide bandpass filters for satellite transponders. *Comsat Tech. Review*, 1(1):20–43, 1971.

[47] A. E. Williams and A. E. Atia. Narrow-bandpass waveguide filters. *IEEE Transactions on Microwave Theory and Techniques*, 20(4):258–265, 1972.

[48] H. C. Bell. The coupling matrix in low-pass prototype filters. *IEEE Microwave Magazine*, 8(2):70–76, 2007.

[49] Y. He, G. Wang, and L. Sun. Direct matrix synthesis approach for narrowband mixed topology filters. *IEEE Microwave and Wireless Components Letters*, 26(5):301–303, 2016.

[50] Girdhari Chaudhary and Yongchae Jeong. Frequency tunable impedance matching nonreciprocal bandpass filter using time-modulated quarter-wave resonators. *IEEE Trans. Ind. Electron.*, 69(8):8356–8365, 2022.

[51] Dakotah Simpson, Photos Vryonides, Symeon Nikolaou, and Dimitra Psychogiou. Tunable multi-band non-reciprocal bandpass filters. In *2022 IEEE/MTT-S International Microwave Symposium - IMS 2022*, pages 179–182, 2022.

[52] J. M. Manley. Some general properties of magnetic amplifiers. *Proc. IRE*, 39(3):242–251, March 1951.

[53] Charles F. Spitzer. Sustained subharmonic response in non-linear series circuits. *Jour. Appl. Phys.*, 16(2):105–111, 1945.

[54] A.V. Oppenheim, A.S. Willsky, and S.H. Nawab. *Signals and Systems*. Prentice-Hall signal processing series. Prentice Hall, 1997.

[55] C. Kurth. Steady-state analysis of sinusoidal time-variant networks applied to equivalent circuits for transmission networks. *IEEE Transactions on Circuits and Systems*, 24(11):610–624, 1977.

[56] S. Darlington. Linear time-varying circuits — matrix manipulations, power relations, and some bounds on stability. *The Bell System Technical Journal*, 42(6):2575–2608, 1963.

[57] F. A. Ghaffar, J. R. Bray, M. Vaseem, L. Roy, and A. Shamim. Theory and design of tunable full-mode and half-mode ferrite waveguide isolators. *IEEE Trans. on Magnetics*, 55(8):1–8, 2019.

[58] Nicholas Aaron Estep, Dimitrios L. Sounas, and Andrea Alù. Magnetless microwave circulators based on spatiotemporally modulated rings of coupled resonators. *IEEE Trans. Microw. Theory Techn.*, 64(2):502–518, 2016.

[59] Ahmed Kord, Dimitrios L. Sounas, and Andrea Alù. Magnet-less circulators based on spatiotemporal modulation of bandstop filters in a delta topology. *IEEE Trans. Microw. Theory Techn.*, 66(2):911–926, 2018.

[60] Ahmed Kord, Dimitrios L. Sounas, and Andrea Alù. Pseudo-linear time-invariant magnetless circulators based on differential spatiotemporal modulation of resonant junctions. *IEEE Trans. Microw. Theory Techn.*, 66(6):2731–2745, 2018.

[61] Aravind Nagulu, Tolga Dinc, Zhicheng Xiao, Mykhailo Tymchenko, Dimitrios L Sounas, Andrea Alù, and Harish Krishnaswamy. Nonreciprocal components based on switched transmission lines. *IEEE Trans. Microw. Theory Techn.*, 66(11):4706–4725, 2018.

[62] Sajjad Taravati and Christophe Caloz. Mixer-duplexer-antenna leaky-wave system based on periodic space-time modulation. *IEEE Trans. Antennas Propag.*, 65(2):442–452, 2016.

[63] Andrea Ashley and Dimitra Psychogiou. X-band quasi-elliptic non-reciprocal bandpass filters (nbpfs). *IEEE Trans. Microw. Theory Techn.*, 69(7):3255–3263, 2021.

[64] X. Wu, X. Liu, M. D. Hickle, D. Peroulis, J. S. Gómez-Díaz, and A. Álvarez Melcón. Isolating bandpass filters using time-modulated resonators. *IEEE Trans. Microw. Theory Techn.*, 67(6):2331–2345, 2019.

[65] Prantik Dutta, Gande Arun Kumar, Gopi Ram, and Dondapati Suneel Varma. Spatiotemporal nonreciprocal filters: Theoretical concepts and literature review. *IEEE Microwave Magazine*, 23(6):85–101, 2022.

[66] J. Kennedy and R. Eberhart. Particle swarm optimization. In *Proc. of ICNN'95 - Int. Conf. on Neural Networks*, volume 4, pages 1942–1948, 1995.

[67] A. Alvarez-Melcon, X. Wu, J. Zang, X. Liu, and J. S. Gomez-Diaz. Coupling matrix representation of nonreciprocal filters based on time-modulated resonators. *IEEE Trans. Microw. Theory Techn.*, 67(12):4751–4763, 2019.

[68] A. R. Jordehi. A review on constraint handling strategies in particle swarm optimisation. *Neural Comp. and Appl.*, 26:1265–1275, 2015.

[69] George L. Matthaei, Leo Young, and Edward M. Jones. Microwave filters, impedance-matching networks, and coupling structures. 1980.

[70] J. D. Rhodes. Modern filter theory and design, edited by g. c. temes and s. k. mitra, wiley, new york, 1973. *International Journal of Circuit Theory and Applications*, 3(1):108–108, 1975.

[71] Louis Weinberg. Explicit formulas for tschebyscheff and butterworth ladder networks. *Journal of Applied Physics*, 28(10):1155–1160, 1957.

[72] R. Saal and E. Ulbrich. On the design of filters by synthesis. *IRE Transactions on Circuit Theory*, 5(4):284–327, 1958.

[73] J. D. Rhodes and S. A. Alseyab. The generalized chebyshev low-pass prototype filter. *International Journal of Circuit Theory and Applications*, 8(2):113–125, 1980.

[74] R. J. Cameron. Fast generation of Chebyshev filter prototypes with asymmetrically-prescribed transmission zeros. *ESA Journal*, 6(1):83–95, January 1982.

[75] S. Darlington. Synthesis of reactance 4-poles which produce prescribed insertion loss characteristics: Including special applications to filter design. *Journal of Mathematics and Physics*, 18(1-4):257–353, 1939.

[76] Some recent books. *Journal of the Institution of Electrical Engineers*, 5(53):320–327, 1959.

[77] E.A. Guillemin. *Synthesis of passive networks: theory and methods appropriate to the realization and approximation problems.* Wiley, 1965.

[78] H.W. Bode. *Network Analysis and Feedback Amplifier Design.* Bell Telephone Laboratories series. D. Van Nostrand Company, Incorporated, 1945.

[79] M.E. Van Valkenburg. *Network analysis.* Prentice-Hall, 1974.

[80] W. Saraga. Theory of electrical filters, j. d. rhodes, wiley, london, 1977. *International Journal of Circuit Theory and Applications*, 6(4):409–409, 1978.

[81] R. Baum. Design of unsymmetrical band-pass filters. *IRE Transactions on Circuit Theory*, 4(2):33–40, 1957.

[82] S. B. Cohn. Direct-coupled-resonator filters. *Proceedings of the IRE*, 45(2):187–196, 1957.

[83] Leo Young. Direct-coupled cavity filters for wide and narrow bandwidths. *IEEE Transactions on Microwave Theory and Techniques*, 11(3):162–178, 1963.

[84] R. Levy. Theory of direct-coupled-cavity filters. *IEEE Transactions on Microwave Theory and Techniques*, 15(6):340–348, 1967.

[85] G. Macchiarella. Accurate synthesis of inline prototype filters using cascaded triplet and quadruplet sections. *IEEE Transactions on Microwave Theory and Techniques*, 50(7):1779–1783, 2002.

[86] R. Levy. Synthesis of general asymmetric singly- and doubly-terminated cross-coupled filters. *IEEE Transactions on Microwave Theory and Techniques*, 42(12):2468–2471, 1994.

[87] G. Macchiarella. Synthesis of an in-line prototype filter with two transmission zeros without cross couplings. *IEEE Microwave and Wireless Components Letters*, 14(1):19–21, 2004.

[88] S. Amari. Direct synthesis of folded symmetric resonator filters with source-load coupling. *IEEE Microwave and Wireless Components Letters*, 11(6):264–266, 2001.

[89] G. Macchiarella. Synthesis of prototype filters with triplet sections starting from source and load. *IEEE Microwave and Wireless Components Letters*, 12(2):42–44, 2002.

[90] RJ Cameron. General prototype network-synthesis methods for microwave filters. *ESA JOURNAL-EUROPEAN SPACE AGENCY*, 6(2):193–206, 1982.

[91] A. E. Atia and A. E. Williams. Nonminimum-phase optimum-amplitude bandpass waveguide filters. *IEEE Transactions on Microwave Theory and Techniques*, 22(4):425–431, 1974.

[92] A. Atia, A. Williams, and R. Newcomb. Narrow-band multiple-coupled cavity synthesis. *IEEE Transactions on Circuits and Systems*, 21(5):649–655, 1974.

[93] R. J. Cameron. General coupling matrix synthesis methods for chebyshev filtering functions. *IEEE Transactions on Microwave Theory and Techniques*, 47(4):433–442, 1999.

[94] R. J. Cameron. Advanced coupling matrix synthesis techniques for microwave filters. *IEEE Transactions on Microwave Theory and Techniques*, 51(1):1–10, 2003.

[95] Prantik Dutta, Gande Arun Kumar, and Gopi Ram. Numerical design of non-reciprocal bandpass filters with the aid of 3d coupling matrix for 5g bands. *IEEE Transactions on Circuits and Systems II: Express Briefs*, 69(7):3334–3338, 2022.

[96] Yi-Ting Kuo, Jhe-Ching Lu, Ching-Ku Liao, and Chi-Yang Chang. New multiband coupling matrix synthesis technique and its microstrip implementation. *IEEE Transactions on Microwave Theory and Techniques*, 58(7):1840–1850, 2010.

[97] D. Simpson and D. Psychogiou. Magnet-less non-reciprocal bandpass filters with tunable center frequency. In *2019 49th Eur. Microw. Conf.*, pages 460–463, 2019.

[98] X. Wu, M. Nafe, A. A. Melcón, J. Sebastián Gómez-Díaz, and X. Liu. A non-reciprocal microstrip bandpass filter based on spatio-temporal modulation. In *2019 IEEE MTT-S Int. Microw. Symp.*, pages 9–12, 2019.

[99] Manimala Pal, Rowdra Ghatak, and Pankaj Sarkar. Compact dual-band bandpass filter using asymmetric stepped impedance stub loaded multimode resonator. *International Journal of Microwave and Wireless Technologies*, 9(1):45–50, 2017.

[100] Azita M Moattari, Abolfazl Bijari, and Seyyed Mohammad Razavi. A new compact microstrip dual bandpass filter using stepped impedance and $\lambda/2$ bended resonators. *International Journal of RF and Microwave Computer-Aided Engineering*, 31(4):e22568, 2021.

[101] Songbai Zhang and Lei Zhu. Synthesis design of dual-band bandpass filters with $\lambda/4$ stepped-impedance resonators. *IEEE Trans. Microw. Theory Techn.*, 61(5):1812–1819, 2013.

[102] Wei Jiang, Wei Shen, Tengxing Wang, Yong Mao Huang, Yujia Peng, and Guoan Wang. Compact dual-band filter using open/short stub loaded stepped impedance resonators (oslsirs/sslsirs). *IEEE Microw. Wirel. Compon. Lett.*, 26(9):672–674, 2016.

[103] He Zhu and Amin M. Abbosh. Single- and dual-band bandpass filters using coupled stepped-impedance resonators with embedded coupled-lines. *IEEE Microw. Wirel. Compon. Lett.*, 26(9):675–677, 2016.

[104] Roberto Gómez-García, Li Yang, José-María Muñoz-Ferreras, and Dimitra Psychogiou. Selectivity-enhancement technique for stepped-impedance-resonator dual-passband filters. *IEEE Microw. Wirel. Compon. Lett.*, 29(7):453–455, 2019.

[105] Mingli Sun, Zhijiao Chen, Tao Zuo, Zhaoyu Zuo, and Anxue Zhang. A high selectivity dual-band bandpass filter using quadruple-mode multi-stub loaded ring resonator (slrr). *International Journal of RF and Microwave Computer-Aided Engineering*, 31(7):e22667, 2021.

[106] Zhi-Chong Zhang, Qing-Xin Chu, and Fu-Chang Chen. Compact dual-band bandpass filters using open-/short-circuited stub-loaded $\lambda/4$ resonators. *IEEE Microw. Wirel. Compon. Lett.*, 25(10):657–659, 2015.

[107] Gen-Zhu Liang and Fu-Chang Chen. A compact dual-wideband bandpass filter based on open-/short-circuited stubs. *IEEE Access*, 8:20488–20492, 2020.

[108] Sambaiah Pelluri and Machavaram Venkata Kartikeyan. Widely separated dual-band half-mode siw bandpass filter. *International Journal of RF and Microwave Computer-Aided Engineering*, 30(10):e22360, 2020.

[109] Hao-Wei Xie, Kang Zhou, Chun-Xia Zhou, and Wen Wu. Compact siw diplexers and dual-band bandpass filter with wide-stopband performances. *IEEE Trans. on Circuits and Syst. II: Exp. Briefs*, 67(12):2933–2937, 2020.

[110] Bo Yin and Zhangyao Lin. A novel dual-band bandpass siw filter loaded with modified dual-csrrs and z-shaped slot. *AEU - International Journal of Electronics and Communications*, 121:153261, 2020.

[111] Jian-Xin Chen, Ming-Zhu Du, Yun-Li Li, Yong-Jie Yang, and Jin Shi. Independently tunable/controllable differential dual-band bandpass filters using element-loaded stepped-impedance resonators. *IEEE Trans. Compon. Packag. Manuf. Technol.*, 8(1):113–120, 2018.

[112] Peng Li, Hui Chu, Dan Zhao, and Ru Shan Chen. Compact dual-band balanced siw bandpass filter with improved common-mode suppression. *IEEE Microw. Wirel. Compon. Lett.*, 27(4):347–349, 2017.

[113] Baoping Ren, Haiwen Liu, Zhewang Ma, Masataka Ohira, Pin Wen, Xiaolong Wang, and Xuehui Guan. Compact dual-band differential bandpass filter using quadruple-mode stepped-impedance square ring loaded resonators. *IEEE Access*, 6:21850–21858, 2018.

[114] Li-Tian Wang, Yang Xiong, Li Gong, Man Zhang, Hui Li, and Xin-Jie Zhao. Design of dual-band bandpass filter with multiple transmission zeros using transversal signal interaction concepts. *IEEE Microw. Wirel. Compon. Lett.*, 29(1):32–34, 2019.

[115] Roberto Gómez-García, José-María Muñoz-Ferreras, Wenjie Feng, and Dimitra Psychogiou. Balanced symmetrical quasi-reflectionless single-and dual-band bandpass planar filters. *IEEE Microw. Wirel. Compon. Lett.*, 28(9):798–800, 2018.

[116] Ayan Arora, Abhishek Madan, Sarika, Manoswita Bhattacharjee, Chittaranjan Nayak, Kanaparthi V. Phani Kumar, and Rama Rao Thipparaju. Implementation of a compact dual-band bandpass filter using signal interference technique on paper substrate. *AEU - International Journal of Electronics and Communications*, 123:153262, 2020.

[117] Xuehui Guan, Bo Zhao, and Baoping Ren. Dual-band differential bandpass filters using quadruple-mode stubs-loaded ring resonator with intrinsic common-mode suppression for 5g. *IEEE Access*, 8:205550–205557, 2020.

[118] Xuehui Guan, Zhewang Ma, Peng Cai, Y. Kobayashi, T. Anada, and G. Hagiwara. Synthesis of dual-band bandpass filters using successive frequency transformations and circuit conversions. *IEEE Microwave and Wireless Components Letters*, 16(3):110–112, 2006.

[119] Yi Wu, Erwan Fourn, Philippe Besnier, and Cédric Quendo. Direct synthesis of multiband bandpass filters with generalized frequency transformation methods. *IEEE Transactions on Microwave Theory and Techniques*, 69(8):3820–3831, 2021.

Publications From This Thesis

- Journals

1. **Prantik Dutta**, Gande Arun Kumar, Gopi Ram, Dondapati Suneeel Varma "Spatiotemporal Nonreciprocal Filters: Theoretical Concepts and Literature Review", *IEEE Microwave Magazine*, Vol. 23, Issue 6, 2022 DOI: 10.1109/MMM.2022.3157970.

2. **Prantik Dutta**, Gande Arun Kumar, Gopi Ram, "Numerical Insight into the Origin of Non-reciprocity and Performance Enhancement in Non-reciprocal Bandpass Filters using Evolutionary Algorithm", *IEEE Transactions on Computer-Aided Design of Integrated Circuits and Systems*, 2022, doi: 10.1109/TCAD.2022.3216757.

3. **Prantik Dutta**, Gande Arun Kumar, Gopi Ram, "Numerical Design of Non-Reciprocal Bandpass Filters With the Aid of 3D Coupling Matrix for 5G Bands", *IEEE Transactions on Circuits and Systems II: Express Briefs*, Vol. 69, Issue 7, 2022, doi: 10.1109/TCSII.2022.3157644.

4. **Prantik Dutta**, Gande Arun Kumar, Gopi Ram, "A Novel Compact Closely-spaced Dual-band Bandpass Filter with Non-reciprocal Lower Band and Tunable Reciprocal Upper Band", *IEEE Microwave and Wireless Technology Letters (Under Review).*

5. **Prantik Dutta**, Gande Arun Kumar, Gopi Ram, "Coupling Matrix Representation of Dual-band Bandpass Filter with a Single-band Non-reciprocity", *IEEE Transactions on Microwave Theory and Techniques (Under Review)*

6. **Prantik Dutta**, Gande Arun Kumar, Gopi Ram, "Dual-band bandpass filters with dual-band non-reciprocity", *IEEE Microwave and Wireless Technology Letters. (Under Review)*

- Conferences

1. **Prantik Dutta**, Gande Arun Kumar, Gopi Ram, Dondapati Suneeel Varma, “Magnetless 3-pole Non-reciprocal Bandpass Filter: Numerical Analysis with MATLAB Simulation”, *2021 International Conference on Computing, Communication, and Intelligent Systems (ICCCIS)*, Greater Noida, India, 2021, pp. 810-813, doi: 10.1109/ICCCIS51004.2021.9397139.
2. **Prantik Dutta**, Gande Arun Kumar, Gopi Ram, Dondapati Suneeel Varma, “Non-reciprocal Bandpass Filters: Parametric Simulation”, *2022 IEEE Wireless Antenna and Microwave Symposium (WAMS)*, Rourkela, India, 2022, pp. 1-4, doi: 10.1109/WAMS54719.2022.9848139.
3. **Prantik Dutta**, Gande Arun Kumar, Gopi Ram, Dondapati Suneeel Varma, “Distributed Cross-Coupled Non-Reciprocal Bandpass Filters for Mobile Communications”, *2022 IEEE Wireless Antenna and Microwave Symposium (WAMS)*, Rourkela, India, 2022, pp. 1-2, doi: 10.1109/WAMS54719.2022.9848112.
4. **Prantik Dutta**, Gande Arun Kumar, Gopi Ram, Dondapati Suneeel Varma, “Compact Tunable Non-Reciprocal Bandpass Filter with the aid of Combline Architecture”, *2022 IEEE Microwaves, Antennas, and Propagation Conference (MAPCON)*, Bangalore, India, 2022, pp. 1003-1006, doi: 10.1109/MAPCON56011.2022.10047764.
5. **Prantik Dutta**, Gande Arun Kumar, Gopi Ram, Dondapati Suneeel Varma, “Compact Cross-coupled Tunable Non-Reciprocal Bandpass Filter using Combline Architecture”, *2022 IEEE International Symposium on Smart Electronic Systems (iSES)*, Warangal, India, 2022, pp. 536-539, doi: 10.1109/iSES54909.2022.00117.
6. **Prantik Dutta**, Gande Arun Kumar, Gopi Ram, Dondapati Suneeel Varma, “A Novel 5th order high selective filtering isolator with static and time-modulated resonators”, *Wireless, Antenna and Microwave Symposium (WAMS), 2023*, Gandhinagar. *(Accepted for Presentation)*

Authors Biography

Prantik Dutta was born in West Bengal, India in 1993. He received B. Tech. Degree in Electronics and Communications Engineering from Maulana Abul Kalam Azad University of Technology (formerly West Bengal University of Technology) in 2015, and the M. Tech degree in Radio Physics and Electronics from IRPE, University of Calcutta (CU) in 2018. He is currently a full-time research scholar with the Department of ECE, National Institute of Technology, Warangal, India, with an Institute Fellowship from the Ministry of Human Resource Department (MHRD). His research interests include microwave filters, time-modulated circuits, and solid state devices.